AD-A285 541

THE UNIVERSITY OF

ARIZONA

TUCSON ARIZONA

FINAL TECHNICAL REPORT

**Real-Time Adaptive Control of Mixing in a
Plane Shear Layer**

Submitted by:
Dr. Ari Glezer
Woodruff School of Mechanical Engineering
Georgia Institute of Technology
Atlanta GA 30332-0405
and
Dr. Frank H. Champagne
Department of Aerospace & Mechanical Engineering
College of Engineering & Mines
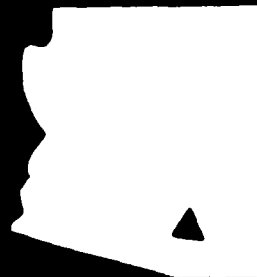The University of Arizona
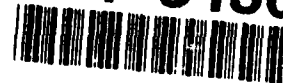Tucson, AZ 85721

DTIC
ELECTE
OCT. 07, 1994
S
B

94-31800

**ENGINEERING EXPERIMENT STATION
COLLEGE OF ENGINEERING AND MINES**

THE UNIVERSITY OF ARIZONA

TUCSON, ARIZONA 85721

REPORT DOCUMENTATION PAGE

1a. REPORT SECURITY CLASSIFICATION Unclassified	1b. RESTRICTIVE MARKINGS
2a. SECURITY CLASSIFICATION AUTHORITY	3. DISTRIBUTION/AVAILABILITY OF REPORT Approved for public release; distribution is unlimited
2b. DECLASSIFICATION/DOWNGRADING SCHEDULE	
4. PERFORMING ORGANIZATION REPORT NUMBER(S) Final Technical	5. MONITORING ORGANIZATION REPORT NUMBER(S) AFOSR-TR- 94 0628

6a. NAME OF PERFORMING ORGANIZATION GTRC	6b. OFFICE SYMBOL (If applicable)	7a. NAME OF MONITORING ORGANIZATION AFOSR
6c. ADDRESS (City, State and ZIP Code) Atlanta, GA 30332		7b. ADDRESS (City, State and ZIP Code) AFOSR/NA Bldg. 410 Bolling AFB, DC 20332-6440

8a. NAME OF FUNDING/SPONSORING ORGANIZATION AFOSR	8b. OFFICE SYMBOL (If applicable) NA	9. PROCUREMENT INSTRUMENT IDENTIFICATION NUMBER AFOSR-89-0465

8c. ADDRESS (City, State and ZIP Code) AFOSR/NA Bldg. 410 Bolling AFB DC 20332-6440	10. SOURCE OF FUNDING NOS.			
	PROGRAM ELEMENT NO. PE-61102F	PROJECT NO. 2307	TASK NO. BS	WORK UNIT NO G-AFOSR 89-0465

11. TITLE (Include Security Classification) Real Time Adaptive Control of Mixing in a Plane Shear Layer

12. PERSONAL AUTHOR(S) A. Glezer

13a. TYPE OF REPORT Final Technical	13b. TIME COVERED FROM 7/15/89 TO 12/14/93	14. DATE OF REPORT (Yr., Mo., Day)	15. PAGE COUNT 223

16. SUPPLEMENTARY NOTATION

17.	COSATI CODES		18. SUBJECT TERMS (Continue on reverse if necessary and identify by block number)
FIELD	GROUP	SUB GR.	mixing, shear layer, feedback control, surface heaters, cold wire sensors, performance measure, mixed fluid temperature, composition, streamwise vorticity, wavelet transform

19. ABSTRACT (Continue on reverse if necessary and identify by block number)

A control system for the enhancement and regulation of mixing in a nonreactive plane shear layer has been developed in a two-stream closed-return water facility. Mixing of a passive scalar is estimated using a thermal analog in which the two streams have uniform, steady temperatures differing by 3 °C. Control is effected via an array of surface heaters flush-mounted on the flow partition and cross-stream temperature distributions are measured with a resolution of 0.03 °C using an array of closely-spaced cold wire sensors. Open-loop forcing is used for the enhancement of mixing in a nonreactive plane shear layer. Mixing of a passive scalar is estimated using a thermal analog to species concentration. From the temperature distributions, a number of mixing performance measures can be calculated to describe the development of mixing with downstream distance. Further, phase-locked measurements are used to study the spatial and temporal structure of the flow and in particular the overall mixedness and composition of the flow as a function of phase in the forcing cycle. In closed-loop experiments, the position of the temperature interface between the two streams is measured in the plane of its cross stream Schlieren image by an optical sensor which is placed upstream of the rollup of the primary vortices. The output from the interface position sensor is fed back to the surface heaters. A transfer function has been developed to predict the effect of feedback on the interface motion. The dependence of various measures of mixing on the feedback gain k and the total delay time Δ between the actuators and the sensors is studied. The feedback gain k is adaptively modified to maximize mixing at a given streamwise station. These experiments indicate that feedback control of the motion of the temperature interface can be used for controlling the nominally 2D entrainment by the primary vortices and thus enhancing mixing.

20. DISTRIBUTION/AVAILABILITY OF ABSTRACT UNCLASSIFIED/UNLIMITED ☒ SAME AS RPT ☐ DTIC USERS ☐	21. ABSTRACT SECURITY CLASSIFICATION
22a. NAME OF RESPONSIBLE INDIVIDUAL Dr. J.M. McMichael	22b. TELEPHONE NUMBER (Include Area Code) (202) 767-4936	22c. OFFICE SYMBOL AFOSR/NA

DD FORM 1473, 83 APR   EDITION OF 1 JAN 73 IS OBSOLETE.

DTIC

INTRODUCTION

A control system for the enhancement and regulation of mixing in a nonreactive plane shear layer has been developed in a two-stream closed-return water facility. Mixing of a passive scalar is estimated using a thermal analog in which the two streams have uniform, steady temperatures differing by 3 ºC. Control is effected via an array of surface heaters flush-mounted on the flow partition and cross-stream temperature distributions are measured with a resolution of 0.03 ºC using an array of closely-spaced cold wire sensors. Open-loop forcing is used for the enhancement of mixing in a nonreactive plane shear layer. Mixing of a passive scalar is estimated using a thermal analog to species concentration. From the temperature distributions, a number of mixing performance measures can be calculated to describe the development of mixing with downstream distance. Further, phase-locked measurements are used to study the spatial and temporal structure of the flow and in particular the overall mixedness and composition of the flow as a function of phase in the forcing cycle.

In closed-loop experiments, the position of the temperature interface between the two streams is measured in the plane of its cross stream Schlieren image by an optical sensor which is placed upstream of the rollup of the primary vortices. The output from the interface position sensor is fed back to the surface heaters. A transfer function has been developed to predict the effect of feedback on the interface motion. The dependence of various measures of mixing on the feedback gain k and the total delay time Δ between the actuators and the sensors is studied. The feedback gain k is adaptively modified to maximize mixing at a given streamwise station. These experiments indicate that feedback control of the motion of the temperature

interface can be used for controlling the nominally 2D entrainment by the primary vortices and thus enhancing mixing.

Part I: OPEN-LOOP CONTROL

1. Introduction

The study of the mechanisms leading to mixing transition in plane and axisymmetric mixing layers owes much of its importance to its technological applications in combustion processes. These processes involve chemical reactions between two or more species in a free turbulent shear flow and depend *crucially* on mixing between the streams, which is induced by a hierarchy of large coherent vortical structures. Thus, development of methods for the control of mixing by manipulation of the instability modes which lead to the formation of these vortical structures will have a direct impact on the performance of propulsion systems from the standpoint of efficient combustion and controllable thrust.

In the plane mixing layer, mixing is accomplished by nominally two-dimensional entrainment of irrotational fluid from both streams by the spanwise vortices, and three-dimensional motion induced by packets of streamwise counter-rotating vortex pairs which form in the region of maximum strain between adjacent spanwise vortices (the "braids"). The mixing process in plane shear layers consists of three distinct stages (Dimotakis 1989): (a) entrainment into the mixing zone, (b) straining of the entrained fluid particles until their spatial scales are comparable with scales at which the kinetic energy diffusive processes take place, and (c) scalar diffusive processes at the molecular level. The amount of mixed fluid which can be produced at any streamwise station is clearly limited by the transverse (cross-stream) extent of the shear layer δ. The composition or volume fraction of fluid from each stream is measured by the volume entrainment ratio E_v, which is the ratio of high-speed fluid to low-speed fluid entrained into the layer. The volume entrainment ratio

is especially important in chemically reacting mixing layers where proper stoichiometry for the reaction is required. Dimotakis (1986, 1989) proposed a model to predict the volume entrainment ratio

$$E_v = s^{1/2} \left(1 + 0.68 \cdot \frac{1-r}{1+r} \right)$$

where $s = \rho_2/\rho_1$ is the density ratio, and $r = U_2/U_1$ is the velocity ratio. Unfortunately, this model does not take into account the effect of external excitation, nor does it predict the total entrainment.

Witte, Broadwell, Shackleford, Cummings, Trost, Whiteman, Marble, Crawford, & Jacobs (1974) presented a simple model relating the distance required for the molecular mixing process to occur to Sc and Re. This idea was further developed in Broadwell & Breidenthal (1982). A model *pdf* was presented in which there were four features: two delta functions at the free-stream concentrations, a delta function at the entrainment ratio E_v, and a U-shaped curve superimposed on the delta functions. This U-shaped curve corresponds to the contributions from laminar diffusion zones ("flame sheets") and may be expected to be negligible if Sc is high. Broadwell & Mungal (1988) extended this analysis to allow the treatment of arbitrary chemical reaction rate. In addition, they presented a formula for the molecularly mixed volume fraction

$$V_m = A + B/(ScRe)^{1/2}$$

for

$$Re \gg 1$$

$$(ScRe)^{1/2} \gg 1$$

$$Re \gg (\ln Sc)^2$$

where A is the contribution from the homogeneous region and $B/(ScRe)^{1/2}$ is the contribution from the laminar diffusion flame sheets. In the experimental data they fitted to this model, A = 0.28 and B = 54.

Kerstein (1989) used a linear-eddy model to reproduce the dependence of the mixing rate on Re and Sc, as well as the qualitative features of the *pdf*. Mixing is modeled as a random walk of fluid particles and molecular diffusion. He attributes the presence of "wings" in the *pdf* of gas-phase mixing layers to mixing which occurs between newly entrained free-stream fluid and fluid which has already been mixed. His model predicts that the area under these wings decreases with increasing Sc and Re. Further, his model was consistent with the Broadwell-Breidenthal picture in terms of product thickness and *pdf* of the concentration field.

There have been a number of numerical studies concerned with secondary instabilities (Metcalfe, Orszag, Brachet, Menon, & Riley 1987; Moser & Rodgers 1991; Rodgers & Moser 1992; Moser & Rodgers 1993; Rodgers & Moser 1993) and mixing and chemical reaction (Riley, Metcalfe, & Orszag 1986; Buell & Mansour 1989; Park, Metcalfe, & Hussain 1994) in the plane mixing layer.

Metcalfe *et al* (1987) used pseudospectral methods to study secondary instabilities (pairing and three-dimensionality) in a temporally developing mixing layer. They showed that, when pairing was suppressed, the Reynolds stresses reverse sign, signifying a transfer of energy from the perturbation field back into the mean flow. During the early stages of the pairing process, however, the Reynolds stresses are large and positive, suggesting a large transfer of energy from the mean flow into the fluctuation field. In addition, the pairing process tends to inhibit the three-dimensional instability. However, they found that the saturated nonpairing

state was highly unstable to three-dimensional perturbations. Hence, the path to turbulence may depend significantly on the amplitudes of subharmonic or three-dimensional modes; or, in experiments, on the forcing waveform.

Moser & Rodgers (1991, 1993) and Rodgers & Moser (1992, 1993), by contrast, assert that mixing transition only takes place when a flow that is already three dimensional begins to pair. The interaction of the three dimensional structures in the two primary vortices brought together by pairing is what triggers the breakdown to small scales. After the second pairing, the transitional flow (with streamwise vortices and pairing) exhibits an increase in their "mixedness" parameter of 0.15 compared to the nontransitional flow (when both are normalized by the ideal, laminar case).

In addition to the above, there have been a small number of works on simulating mixing and chemical reactions in plane shear layers. Riley, Metcalfe, & Orszag (1985) considered direct numerical simulations of a chemically reacting temporal mixing layer. This layer was statistically spanwise and flow-direction uniform. The Reynolds number (based on mean velocity and time) was 92 in all runs. Their results suggest that mean product thickness increases linearly with time, and that concentration data is self-similar. Their data does not show the existence of a "mixing transition", however.

To consider the effects of nonsymmetric entrainment (which cannot be accounted for in a temporally developing mixing layer) Buell & Mansour (1989) used finite difference (in x) methods to simulate a spatially-developing layer. They looked at streamwise structure and passive-scalar mixing in this flow. Their *pdf*s show a peak at the theoretical entrainment ratio for the two-dimensional case and a broader band of mixing (including a secondary peak towards the low-speed concentration) for the three-dimensional case. Thus, the effect of counter-rotating streamwise

vortices is to move the average mixed concentration towards that of the low-speed stream. They attribute this to increased surface area on the low-speed side of the spanwise roller. Interestingly, the streamwise vortices increase the normalized product thickness only for downstream stations; upstream, the effect is negligible. Their average mixture fraction (their figure 11) shows that with increasing streamwise distance, the average mean concentration approaches that of the low-speed concentration for the 3D case and the high-speed concentration for the 2D case.

Park, Metcalfe, & Hussain (1994) used pseudospectral methods in a temporally developing mixing layer to look at mixing and chemical reactions in the presence of streamwise Taylor vortices. The Reynolds number (based on vorticity) varied from 200 initially to 1200 by the end of the simulation (before mixing transition). They emphasized the shape of the *pdf* and the mean-mixed fluid (MMF) concentration curve, finding different shapes due to stirring from the "rolls" (the primary spanwise vortices) and the "ribs" (counter-rotating streamwise vortices). Increasing coherence in the spanwise rolls results in *pdf* peaks which are more stationary. Indeed, roll stirring can even result in an *inverted* MMF S-shaped curve. When roll + rib stirring is considered, it is found that the ribs in the braids region contribute to marching *pdf* peaks (and a "regular" MMF curve which follows the mean concentration).

The disadvantage with these numerical studies is that, due to computational constraints, the Reynolds and Schmidt numbers are restricted to values much lower than those attainable in the laboratory. Also, with the exception of Buell & Mansour (1989), all of these studies have used spectral methods and hence have been temporally-developing mixing layers. The effects of asymmetric entrainment, as well as asymmetry in the primary and secondary structures, are hence eliminated.

A large number of experimental studies have considered entrainment and shear layer growth, as well as secondary instabilities (and the breakdown to small-scale motions) necessary for mixing. In addition, there have been a number of experiments which studied mixing of a passive scalar directly.

Winant & Browand (1973) used a low-speed shear layer with a very thin (splitter plate-induced) wake to study the vortex pairing process. They noted a considerable increase in small-scale motions at the time of the second vortex pairing. They attribute the growth of the layer to entrainment of irrotational fluid by the pairing process. They also presented a model suggesting that the growth rate of the shear layer could be increased by either a more irregular distribution of vortices or a more concentrated vorticity distribution.

Konrad (1976) studied molecular mixing in gas-phase free turbulent shear flows using a high-resolution concentration probe. He also presented a measure of "unmixedness" based on the deviation of the concentration traces from the mean concentration at a given spatial position. The peaks in his *pdfs* of concentration showed little variation in the cross-stream direction. Additionally, shadowgraph evidence shows the development of hairpin (streamwise) vortices above a critical Reynolds number which become rolled up into the primary vortices and thus lead to three-dimensional small scales within the large structures. Finally, Konrad used a model diffusion-limited chemical reaction to apply his results to a chemically-reacting shear layer, plotting the total product in the layer (normalized by the product formed in the equivalent laminar solution) versus downstream distance. He found a jump in this measure at a critical Reynolds number corresponding to mixing transition.

Batt (1977) used a fiber-optics probe to measure NO_2 both as a passive scalar and as a product in a chemically-reacting (nitrogen tetroxide dissociation reaction, i.e. $N_2 + N_2O_4 \longleftrightarrow 2NO_2 + N_2$) mixing layer. The probe measured the shadow caused

by the dark brown NO_2 gas. He found that *pdfs* of concentration showed marching peaks; that is, in cross-stream positions near a given free stream, the peak in the *pdf* is closer to that free stream's concentration. He claims that this result is due to the relative unimportance of large-scale structures in this flow.

A number of researchers have noted the existence of streamwise streaks in plane mixing layers. Breidenthal (1980) used a splitter plate with Lucite extensions to visualize induced streamwise vortices in a reacting flow. He found that spanwise variations in product formation were smoothed out after the first vortex pairing.

Breidenthal (1981) studied mixing in a plane shear layer. A chemical reaction in which phenolphthalein (a pH indicator) reacted with a base (sodium hydroxide) to form a red product was used both to quantify mixing and as a means of flow visualization. Mixing transition was found to occur when wiggles (or streamwise streaks) became apparent in the layer. Mixing transition was complete by $Re_\delta = 10^4$ (consistent with Konrad's data); however, Breidenthal's product thickness was about half Konrad's, despite a difference in Sc of three orders of magnitude. This suggests that, for high Re, mixing is only a weak function of Sc. However, upstream of mixing transition, there is significant product formation in Konrad's gas phase layer, while there is virtually none for Breidenthal's liquid-phase layer. Breidenthal also found that variations in the initial momentum thickness could significantly effect the location of mixing transition.

Bernal (1981) and Bernal & Roshko (1986) studied the topology of the streamwise vortex structure with nonreacting dye. They proposed that the streamwise vortices are part of a continuous vortex line which loops back and forth between two adjacent spanwise vortices. They found that the mean spacing between the pairs of streamwise streaks was 0.67 times the mean spacing of the primary vortices.

Jimenez (1983) showed spanwise variations in longitudinal velocity and turbulence intensity which suggested that his one-stream shear layer as a whole developed an undulation. The variation was up to 0.1 p-p in the mean velocity and 0.03 in the turbulence level, relative to the free stream velocity of the half-jet. In addition, these disturbances had a long spatial coherence: they persisted at the same spanwise locations throughout the streamwise measurement domain.

The amount of reaction product in a reacting mixing layer increases by an order of magnitude downstream of the mixing transition (Roshko 1981). In an experimental investigation of mixing transition in a nonreacting shear layer, Koochesfahani & Dimotakis (1986) used laser induced fluorescence to show a substantial increase in the small-scale motions within the layer. The appearance of the small-scale flow structures marks an important stage in the mixing process because of the increase in the interfacial area between the entrained fluids where efficient mixing at the molecular level can take place. By examining the probability density function $pdf(\xi,y)$ of species concentration ξ at a number of cross-stream elevations they found a substantial increase in concentrations of mixed fluid downstream of mixing transition. The peak of $pdf(\xi,y)$ was found to occur at the same value of ξ at each y elevation. The probability of finding mixed fluid increased with downstream distance x. Furthermore, the expected value of mixed fluid concentration $E(\xi \mid \xi_1 < \xi < \xi_2)$ was found to migrate towards the low-speed concentration with increasing x, suggesting that the initial rollup of the vortices entrained an excess of high-speed fluid.

Matsutani & Bowman (1986) considered mixing and chemical reactions in a gas-phase, pre-mixing transition plane mixing layer. In contrast to the work of Koochesfahani & Dimotakis (1986), they found significant mixed fluid upstream of the mixing transition. They attribute this difference to the increased molecular

diffusivity of a gas relative to liquids. They suggest that mixing in a gas layer takes place in thin diffusion zones which wrap around the primary vortices, as well as in homogeneously mixed zones at the centers of the primary vortices. They note that this is consistent with the Broadwell-Breidenthal model. They also found that, not only is more fluid from the high-speed stream entrained into the layer, but a higher percentage of entrained high-speed fluid than low-speed fluid ends up being mixed, a concept for which they coined the term "mixing efficiency".

Lasheras & Choi (1988) used a corrugated splitter plate to induce the formation of streamwise vortices in a low-speed shear layer. These vortices were then visualized using a number of flow visualization techniques. They attributed the development of streamwise vorticity to the stretching of spanwise vortex lines in the braids region between the primary vortices. These streamwise vortices then cause a spanwise undulation in the primary vortex cores.

Nygaard & Glezer (1991) showed that streamwise vortices of virtually any wavelength could be excited by spanwise-periodic forcing. They showed that these streamwise vortices lead to the development of spanwise inflection points in the mean velocity profiles, which leads to the breakdown to small-scale turbulence. This may be expected to enhance mixing.

A number of experimental investigations have demonstrated that open-loop time harmonic excitation can lead to substantial global flow modifications. For example, Oster & Wygnanski (1982) discovered that forcing a two-dimensional turbulent shear layer produces a "frequency-locked" region in which growth is inhibited, the primary vortices are equally spaced, and their passage frequency is equal to the forcing frequency. However, there has been a dearth of experimental studies on the effects of forcing on mixing in plane shear layers. Roberts (1985) and Roberts & Roshko (1985), as well as Koochesfahani & MacKinnon (1991) and

Katch & Koochesfahani (1993) are the seminal studies in this area. In addition, Wygnanski, Oster, & Fiedler (1980) used temperature as a passive contaminant to study the structure of a forced plane mixing layer.

Roberts & Roshko (1985) conducted experiments in Breidenthal's tunnel, using his absorption technique to quantify mixing. They studied mixing in the three regions of a forced mixing layer defined by Oster & Wygnanski (1982). For high Reynolds number, forcing at a low frequency (3.9 Hz) caused a substantial increase in mixing near the end of region I. Near the end of region I, corresponding to $X_{WO} < 1$ (where X_{WO} is the "Wygnanski-Oster parameter" $X_{WO} = \varepsilon x F / U_c$; $\varepsilon = (U_1 - U_2)/(U_1 + U_2)$, F = forcing frequency, and $U_c = (U_1 + U_2)/2$) the growth rate of the product thickness is enhanced by a factor of two. However, there is no increase in the total mixed fluid until the very end of region I. When the flow is forced at a higher frequency (8 Hz), region II (corresponding to $1 \leq X_{WO} \leq 2$) becomes a frequency-locked region in which the growth rate is inhibited. In fact, their plot of the product thickness δ_{P2} reaches a plateau throughout most of region II. Relative to the unforced case, more mixed fluid is produced upstream of $X_{WO} = 1.12$ and less is produced downstream of this point.

Roberts & Roshko (1985) also considered a low Reynolds number shear layer (by slowing down the free streams) in which mixing transition was just beginning at the end of the test section. In this case, forcing at 4.5 Hz increased the product growth rate in region II (the phase-locked region). The product growth rate remained high until well into region III ($X_{WO} = 2.47$) where it is again decreased. Curiously, the region where product growth decreased in the forced layer is the same region (the beginning of mixing transition) where it *increased* in the unforced layer.

Finally, Roberts & Roshko (1985) plotted their data in "enhancement" plots in which the ratio of forced product thickness to unforced product thickness was

plotted. They show increases of 4-5 in product thickness over the unforced flow at comparable X_{WO}. However, since X_{WO} depends on the forcing frequency, these data points are not all taken at the same streamwise (x) station.

Koochesfahani & MacKinnon (1991) found that forcing well below the natural frequency (by oscillating one free stream) could lead to a small increase in mixing which they attributed to an increase in the layer width due to entrainment and not to increased molecular mixing. They presented *pdf*s of concentration for the forced layer in order to provide complete information about the composition distribution. In the forced layer (as in the unforced layer) the peak in the *pdf* occurs at the same value of concentration at each cross-stream location. Mixing is enhanced preferentially at concentration close to that of the high-speed stream.

In a related work, Katch & Koochesfahani (1993) used a small oscillating airfoil located just downstream of the flow partition to force the flow. They forced the flow at f = 2, 4, and 8 Hz and varied the amplitude of forcing by changing the maximum angle of attack of the airfoil from A = 2°, 4°, 6°, and 8°. (It may be suggested, however, that the forcing level scales with the induced velocity u'~ Af; hence forcing with A = 2° and f = 8 Hz (for example) will have twice the perturbation velocity of A = 2° and f = 4 Hz). They reported that, consistent with Koochesfahani & MacKinnon (1991) forcing well below the natural frequency (of 27 Hz) resulted in an increase in the total amount of mixed fluid (up to a maximum of 30% relative to the unforced flow when A = 6° and f = 8 Hz) while the mixed fluid fraction actually decreased relative to the unforced flow for f = 4 Hz and f = 6 Hz.

The present experiments are conducted in a closed return water shear layer facility using a thermal analog to the concentration measurements normally performed in conventional blowdown chemically reacting shear layer facilities. The thermal analog is based on maintaining the two streams at slightly different constant

temperatures. The performance measures infer the degree of mixing from the history of the temperature distribution.

The previous studies of mixing in a forced mixing layer (with the exception of Wygnanski *et al*) were concerned with the mixing of dye in water. Because in our experiment temperature is being mixed, the Prandtl number (Pr, the ratio of kinematic viscosity to thermal diffusivity) determines the ratio of the smallest velocity scales to the smallest temperature scales. In experiments dealing with the mixing of chemical species, the corresponding relevant parameter is the Schmidt number (Sc, the ratio of kinematic viscosity to chemical diffusivity). Mixing at the smallest scales varies considerably depending upon the value of Sc or Pr. The Schmidt and Prandtl numbers are typically $O(1)$ in air; whereas in water, $Sc = O(1000)$ and $Pr \cong 7$. Hence, the present experiments may be more comparable with mixing in air than with mixing of species in water. By using temperature as a passive scalar, we are able to directly determine the complete composition of the mixed fluid in the form of the *pdf* and quantities derived from it. It takes a large number of runs at different stoichiometries to determine the *pdf* from chemically reacting experiments. There are some resolutions inherent in using passive scalar techniques. Specifically, this technique gives an upper bound on the amount of mixed fluid in the layer. Thus, the measurements presented herein should be used for comparing the forced layer to the unforced layer, rather than to determine absolute levels. The fact that our *pdf*s have non-marching peaks (as will be shown below) also suggests that our resolution is adequate, as marching *pdf* peaks are often the result of inadequate resolution.

Additionally, extensive use in this work is made of spanwise-nonuniform forcing. This type of forcing waveform has the effect of introducing three-dimensional counter-rotating streamwise vortices into the flow. As will be shown below, this substantially enhances the amount of mixed fluid in the layer. All of the

previous studies on mixing in forced shear layers were restricted to spanwise-uniform forcing.

Finally, in this study extensive use is made of phase-locked measurements. This allows us to study the time-dependent structure of the flow and in particular the regions in the flow responsible for mixing. Also, we will present phase-dependent *pdf*s which show the composition of the mixed fluid as a function of phase in the forcing cycle. These measurements are also, to the best of our knowledge, unique.

The experimental apparatus is described in §2. Instantaneous data and time-averaged mixing performance measures are presented in §3. Data taken phase-locked to the forcing signal is presented in §4. Finally, concluding remarks are presented in §5.

Part II of this work, involving linear feedback control to enhance and regulate mixing in a plane shear layer, is detailed in Wiltse & Glezer (1994b). This paper will be referenced hereinafter as WGII.

2. The experimental apparatus and procedure

2.1. The water shear layer facility

The experiments are conducted in a two-stream, closed-return water shear layer facility (figure 1). The velocity of each free stream can be independently varied. In the experiments discussed here, the velocity of the high-speed stream is $U_1 = 36$ cm/s and the velocity of the low-speed stream is $U_2 = 12$ cm/s. Adjustable side walls can be used to adjust the streamwise pressure gradient throughout the test section and in particular along the flow partition.

The facility is substantially modified to provide a constant temperature difference between the two streams. Water from the diffuser downstream of the test section is pumped (at 20 gal/min in the present experiments) through a 63kW circulation heater where the temperature is raised by approximately 10 °C. The water is then injected (using multiple jets to promote mixing) into the low-speed stream well upstream of the turbulence management devices. The temperature of each stream at the entrance of the test section is uniform, and the temperature difference is 3 °C. A chilled-water heat exchanger (operating at nominally 60 gpm at 8 °C in the present experiments) which is built into the facility downstream of the diffuser continuously removes the heat added by the heater. A dedicated PC controls a pump on the chilled water line to maintain the overall temperature of the facility time-invariant to within ±.03 °C. The sensor input to the PC is a platinum thermometer placed in the low-temperature stream. Other platinum thermometers are mounted in various sections of the facility and are continuously scanned using a digital thermometer. For the experiments discussed here, the temperature of the high-speed
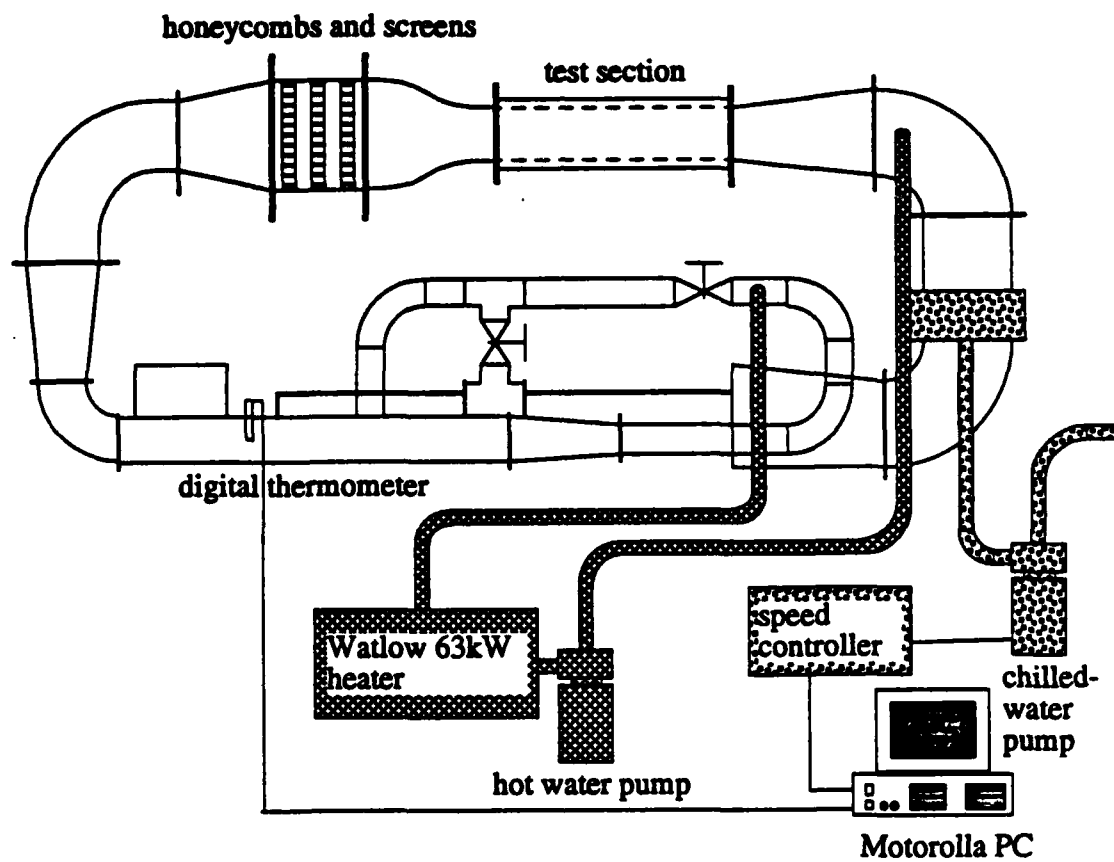
FIGURE 1. The two-stream mixing layer facility.

stream is maintained at $T_1 = 25$ °C and the temperature of the low-speed stream is maintained at $T_2 = 28$ °C.

Excitation of streamwise and spanwise instability modes is accomplished via an array of surface film heating elements mounted on the flow partition (figure 2, see also Nygaard & Glezer 1991). The array is comprised of four spanwise-uniform elements upstream of a single 32-element spanwise row. Each heating element is wired to an individual DC power amplifier. The effect of heating the surface is essentially to introduce three-dimensional vorticity perturbations into the flow-partition boundary layer by exploiting the dependence of the viscosity on temperature (Liepmann, Brown, & Nosenchuck 1982).

2.2. Instrumentation

A Macintosh IIfx programmed in MPW C is used for data acquisition. The temperature distribution between the two streams is measured using a rake of 31 cold wire sensors spaced 2 mm apart (6 cm total). A 32 channel cold wire thermometer (CWT) was designed and built for the purposes of the present experiments. Each CWT channel has an r.m.s. noise fluctuation of approximately .025 °C, and the overall temperature resolution (including switching noise) is 0.03 °C. High-speed internal analog switching allows for scanning of all 31 CWT channels at a maximum frequency of 100 kHz. The CWT is connected to a single A/D channel at the computer which is capable of a maximum sampling frequency of 1 MHz. A separate slave switching box allows for scanning of up to 32 additional analog channels. This slave switch is used to sample the control input to the surface heaters.

A 36 channel, high speed, 12-bit, dual-mode D/A converter (DAC) was designed and built for the present experiments. The DAC can be operated in a signal

control (power to surface heaters)

Flow
Partition

4 spanwise-uniform
heating elements
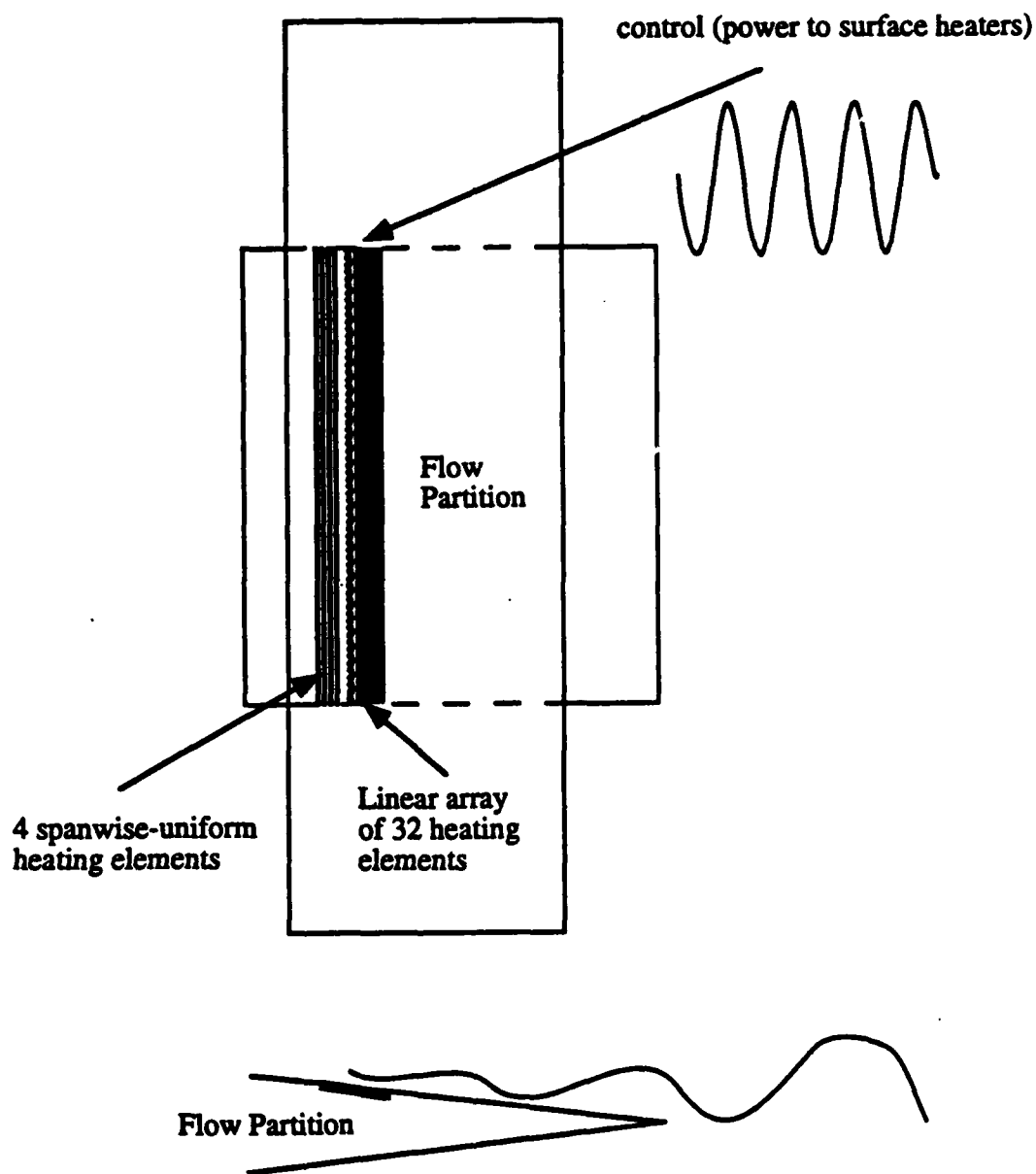
Linear array
of 32 heating
elements

Flow Partition

FIGURE 2. The array of surface heaters.

generator mode for open-loop excitation (and in an update mode for feedback applications, see WGII). In both modes, the DAC is accessed via a parallel interface port. In the update mode, any channel can be randomly addressed and updated at a rate of 2 μs (limited by the present computer). In the signal generator mode, an arbitrary time-periodic waveform can be independently programmed into each of the channels. Each channel contains a 1024 12-bit word dynamic RAM which is loaded from the laboratory computer. Each 12-bit word can be loaded to the output of the respective channel at a maximum rate of 1 MHz.

3. Instantaneous and time-averaged measurements

The present work is concerned with the effect of spanwise uniform and spanwise nonuniform excitation on various measures of mixing performance. Research is continuing (WGII) on the use of linear feedback to enhance mixing in this flow. Although WGII is a natural extension of this work, these results are not directly comparable. However, the open-loop investigations are of interest because there is a substantial body of work concerning mixing of unforced (Koochesfahani & Dimotakis 1986) and forced (Roberts & Roshko 1985) plane shear layers at high Schmidt numbers, while the present research is concerned with mixing of temperature at a low Prandtl number. It will be shown that open-loop forcing can result in a substantial increase in mixing relative to the unforced flow. In the present experiments the excitation is time harmonic. The excitation waveforms are spanwise-uniform (SU) and spanwise-periodic (SP) having a spanwise wavelength of 2.66 cm with a duty cycle of 75%. The SP waveform is synthesized by running every fourth spanwise heater (figure 2) at 4% power. Four cases are reported below: SU and SP at $f = 6$ Hz, and SU and SP at a combination of $f = 3.85$ and 7.7 Hz.

3.1. Mixing in the unforced shear layer

Cross-stream temperature measurements are used to quantify mixing through an instantaneous performance measure pm, an integral performance measure PM, and the probability density function of temperature *pdf*. The instantaneous mixing performance measure pm(x,y,z,t)

$$pm(x,y,z,t) = \frac{(T_2 - T(x,y,z,t))(T(x,y,z,t) - T_1)}{(\Delta T)^2}$$

is a quadratic measure which is zero when the measured temperature $T(x,y,z,t)$ is either T_1 or T_2, and nonzero if $T_1 < T(x,y,z,t) < T_2$ (indicating mixing). It reaches a maximum value of 0.25 at a temperature $T = (T_1 + T_2)/2$, the average temperature of the free streams.

This instantaneous performance measure pm can be integrated in the cross-stream direction to give an integral measure of the amount of mixed fluid in the layer:

$$PM(x,z,t) = \int_{-\infty}^{\infty} pm(x,y,z,t) \; dy.$$

The integral performance measure PM is analogous to the momentum thickness used in velocity measurements, and gives a measure of the overall amount of mixed fluid in the layer. It has dimensions of [length].

The function $pdf(T,x,y,z)$ is the probability density of finding fluid at a temperature T at a location (x,y,z) within the shear layer:

$$P(T_A \leq T \leq T_B) = \int_{T_A}^{T_B} pdf(T,x,y,z) \; dT.$$

Figure 3 is composed of composites taken at three streamwise stations ($x = 10.16$, 15.24, and 20.32 cm) for the unforced shear layer. Each composite includes
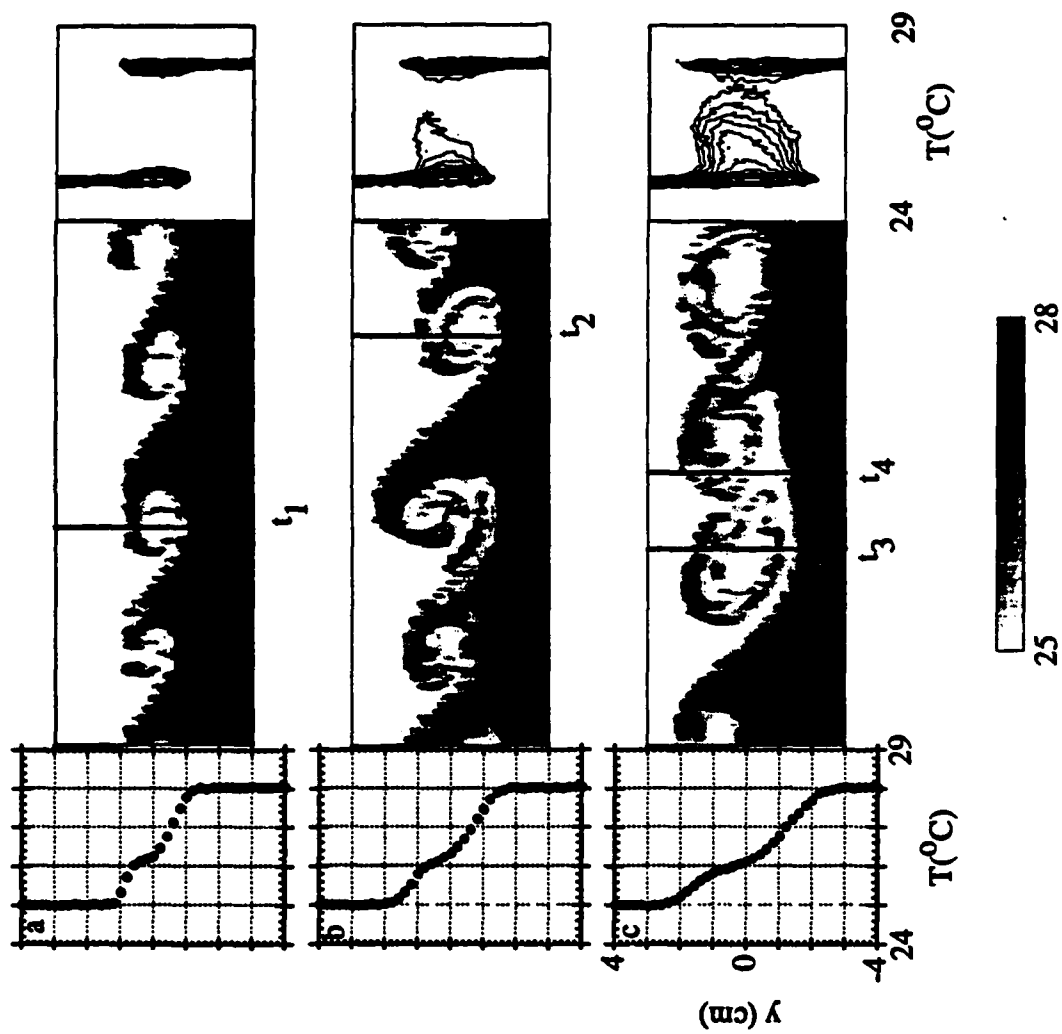
FIGURE 3. T(y), T(y,t), and *pdf*(T,y) for the unforced flow at x = (a) 10.16 cm, (b) 15.24 cm, and (c) 20.32 cm.

the time-averaged temperature $T(y)$, the grayscale raster image of the instantaneous temperature distribution over a period of 0.67 seconds $T(y,t)$, and a contour plot of $pdf(T,y)$ plotted on a logarithmic scale (i.e., $\log_{10}(pdf(T,y))$). The probability density function is shown as a logarithmic plot for two reasons: First, it better elucidates the lower mixing levels which, over a large region, contribute extensively to the mixing. Second, it attenuates the two lobes (at $T_1 = 25$ °C and $T_2 = 28$ °C) corresponding to the two free streams which would otherwise dwarf all else in this plot. The contours of $\log_{10}(pdf(T,y))$ begin at a minimum level of -1.0 $[\log_{10}(°C^{-1})]$ with a contour increment of 0.1 $[\log_{10}(°C^{-1})]$. Sufficient contours are plotted to cover the extent of the data. Other researchers, (Dimotakis 1989), have found that mixing transition in an unforced two-stream shear layer occurs at a Reynolds number of $Re_m = \Delta U \delta / v \approx 10^4$ where $\Delta U = U_1 - U_2$ and $\delta = \delta(x)$ is the local transverse extent of the shear layer. The cross-stream positions in which the fluid is mixed 1% of the time yield $\delta = 2.67$, 3.79, and 5.39 cm at $x = 10.16$, 15.24, and 20.32 cm, respectively. The corresponding local Reynolds numbers are 0.76 x 10^4, 1.08 x 10^4, and 1.63 x 10^4 ($v = .0084$ cm^2/s and $\Delta U = 24$ cm/s). Note that the kinematic viscosity of water decreases by 6.7% between 25 °C and 28 °C. The kinematic viscosity used here is the average of the kinematic viscosities of the two streams.

At $x = 10.16$ cm (figure 3a) the plot of $pdf(T,y)$ shows virtually no mixed fluid. This is to be expected, since the local Reynolds number is well below $Re_\delta = 10^4$. Also of interest is $T(y)$ which shows a distinct concave bend (i.e., towards T_2) near the high speed stream, below which the temperature profile increases almost linearly to T_2. This is contrasted with the cross-stream velocity profile which is similar to a hyperbolic tangent profile. The bend begins above the geometric center of the test section, $y = 0.0$ cm. It is clear that in the absence of mixing, the shape of the mean temperature profile within the shear layer depends on the time fraction that

each of the sensors measures either T_1 or T_2 (for a given sampling period). The concave bend at the present streamwise station is a result of the rollup of the interface between the two streams. The profile appears to be almost linear below the cross-stream domain where the instantaneous temperature profiles become multivalued. Figure 4a-c shows instantaneous temperature profiles $T(y;t_i)$ from figure 3 at representative times t_1, t_2, t_3, and t_4. Figure 4a shows that at this streamwise station, the rollup has progressed to the point that the instantaneous temperature profiles are multivalued and they are being strained by the action of the primary spanwise vortices into thin sheets. The instantaneous temperature distribution in the cores of the spanwise vortices is double-valued at both the high and low free-stream temperatures. These thin sheets of fluid provide the large surface area over which mixing will occur.

There is a small increase in mixing at x = 15.24 cm (figure 3b) as shown by contours of the temperature probability density function *pdf*(T,y). Similar to the mean temperature profile in figure 3a, T(y) at x = 15.24 cm also has a slight slope discontinuity which corresponds to flow regions where the instantaneous temperature profiles are multivalued. The thin sheets which were present in figure 3a have been further strained to the point that each free-stream temperature may be observed 3 or more times in an instantaneous temperature distribution (figure 4b). The presence of the multivalued temperature profiles suggests that the fluid within the primary vortices is rolled into stretched layers which retain their identity. These thin layers, which are continually strained by the action of the large vortices, provide a constantly growing area over which molecular mixing can occur.

At x = 20.32 cm the shear layer appears to undergo mixing transition (figure 3c). The contour map of *pdf*(T,y) has a higher peak near T_1, suggesting that the volumetric mixing ratio of high- to low-speed fluids is greater than 1. However,
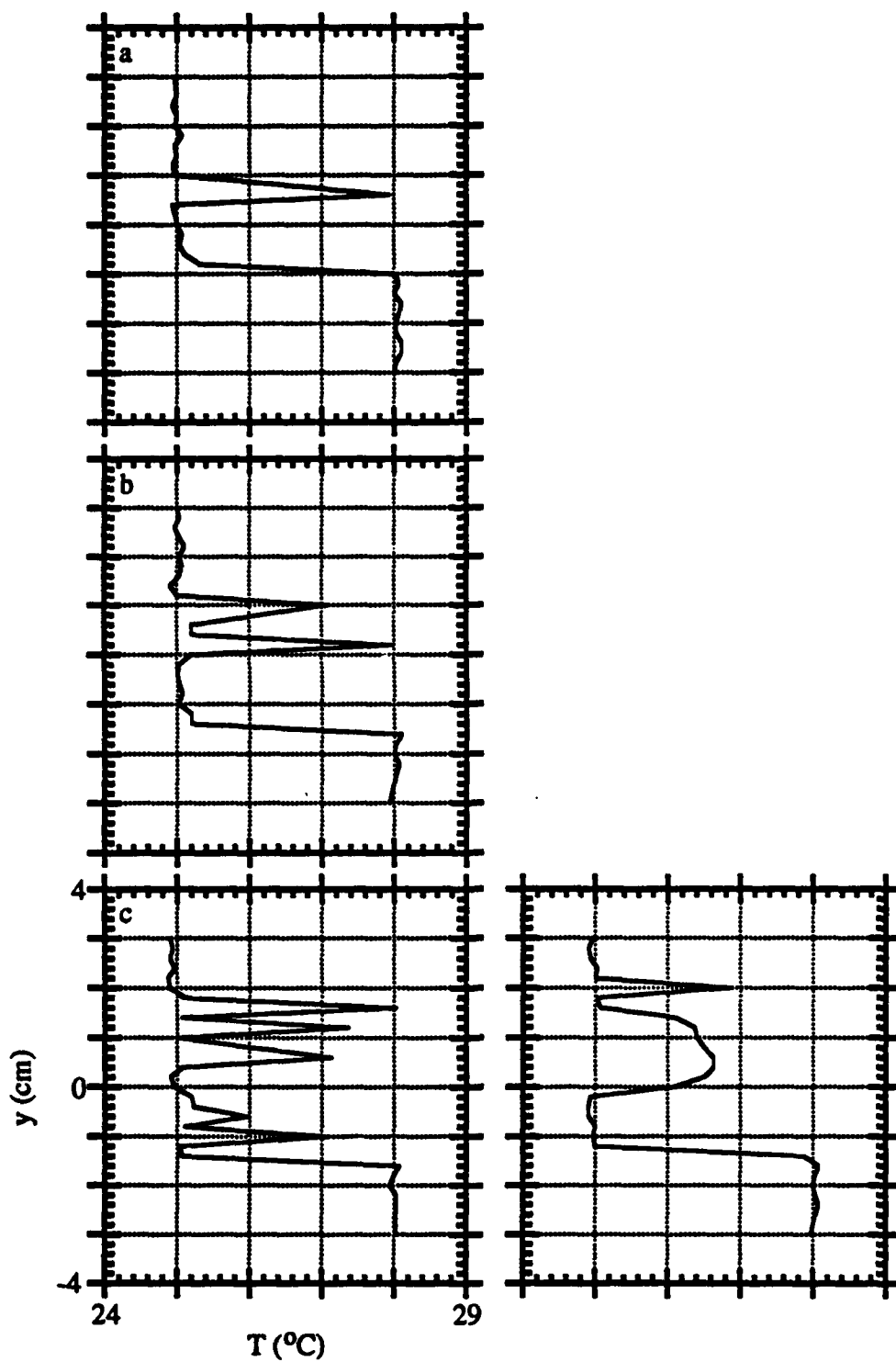
FIGURE 4. Instantaneous temperature profiles T(y) for the unforced flow at x = (a) 10.16 cm, (b) 15.24 cm, and (c) 20.32 cm.

mixed fluid is produced for all $T_1 \leq T \leq T2$. The plot of $T(y,t)$ shows that there are even more diffusion layers than in figure 3b. Also apparent are large regions of mixed fluid which occur primarily around the edges of the spanwise vortices where the thin layers have broken down into mixed fluid. This is illustrated in figure 4c. The left profile $T(y;t_3)$ shows a strong multivalued behavior in that temperatures near that of each free stream can be measured five to six times. The right profile $T(y,t_4)$ shows a case where these layers have broken down into a large patch of mixed fluid, presumably as a result of naturally-occurring three-dimensionality in the flow. Further production of these patches leads to mixing transition in the unforced layer. Koochesfahani & Dimotakis (1986) studied mixing transition in a layer with Sc ≈ 600. Their post-mixing transition (Re = 23,000) *pdf* shows a strong peak at a preferred concentration which is constant throughout the layer. To facilitate comparison with their results, we show the *pdf* of figure 3c in three-dimensional surface format (figure 5, as in their figure 10). In our data, Re = 16,300 and Pr ≈ 7. Although the results are qualitatively similar, there are two primary difference (due to the differences in Re and diffusion coefficients). First, in our case the peak occurs over a broader range of temperatures (concentrations). This is due to the lower value of the diffusion coefficient: there is more "flame sheet" mixing in our case, and relatively more "homogeneous" mixing in their case. Also, their peak appears more prominent than ours. This is due to the difference in Re: natural mixing transition is not completed by the end of our streamwise domain of measurement.

3.2. Instantaneous and time-averaged data for the forced layer

Figures 6 and 8-10 show composites of $T(y)$, $T(y,t)$ and $pdf(T,y)$ as in figure 3. In figures 6a-c (x = 10.16, 15.24 , and 20.32 cm, respectively) the
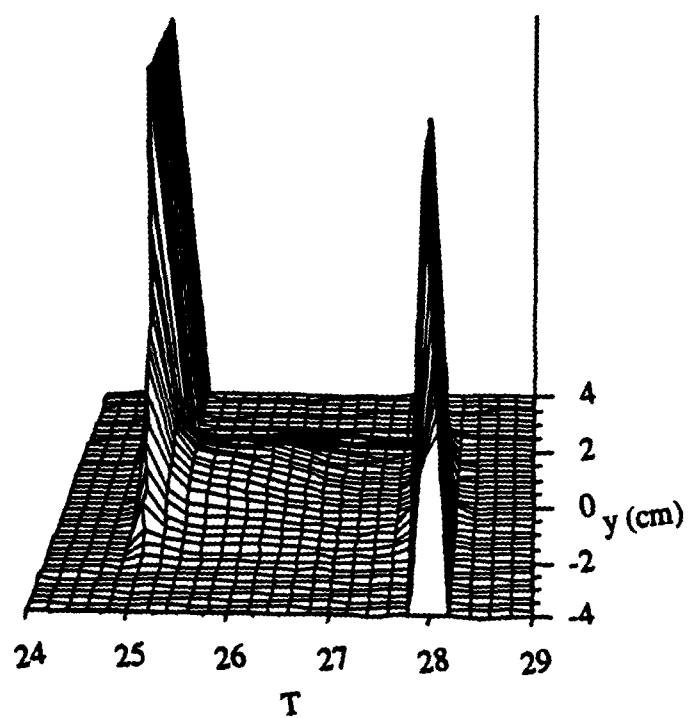
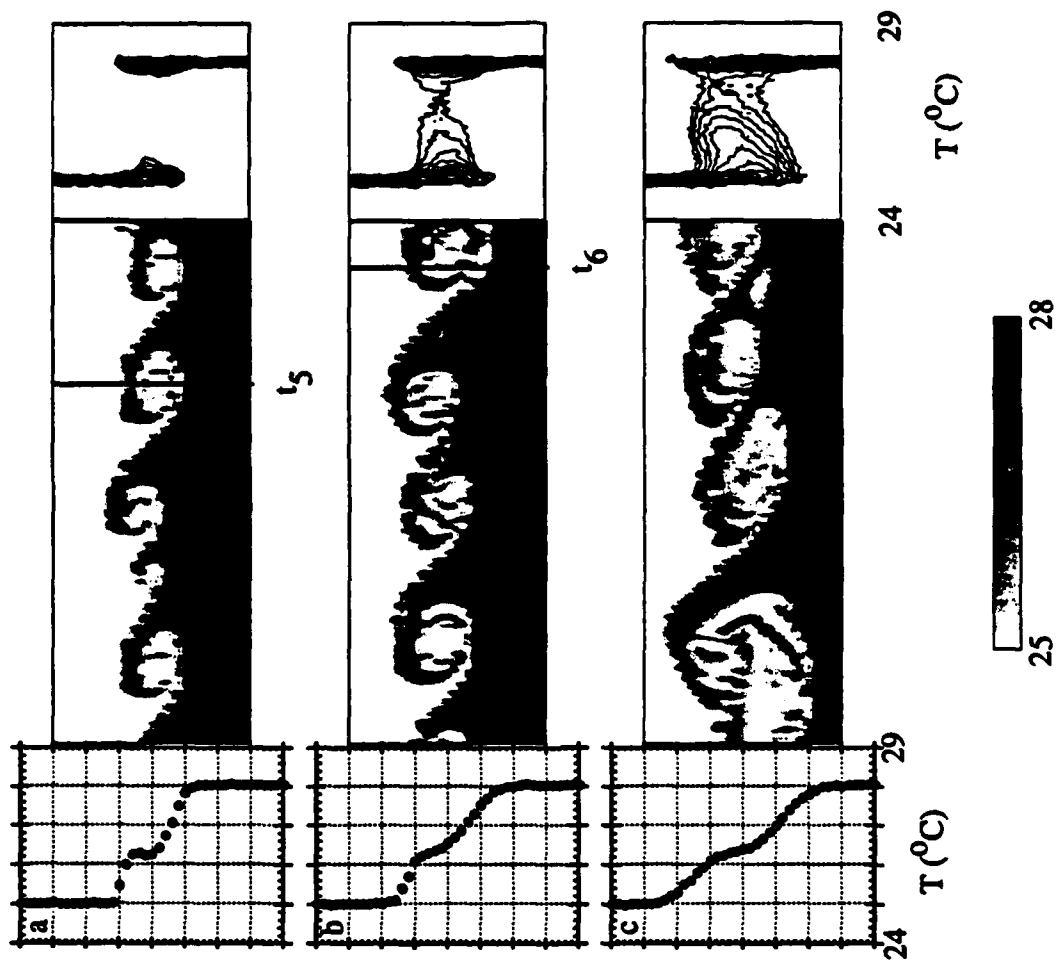FIGURE 5. *pdf*(T,y) for the unforced flow at x = 20.32 cm.

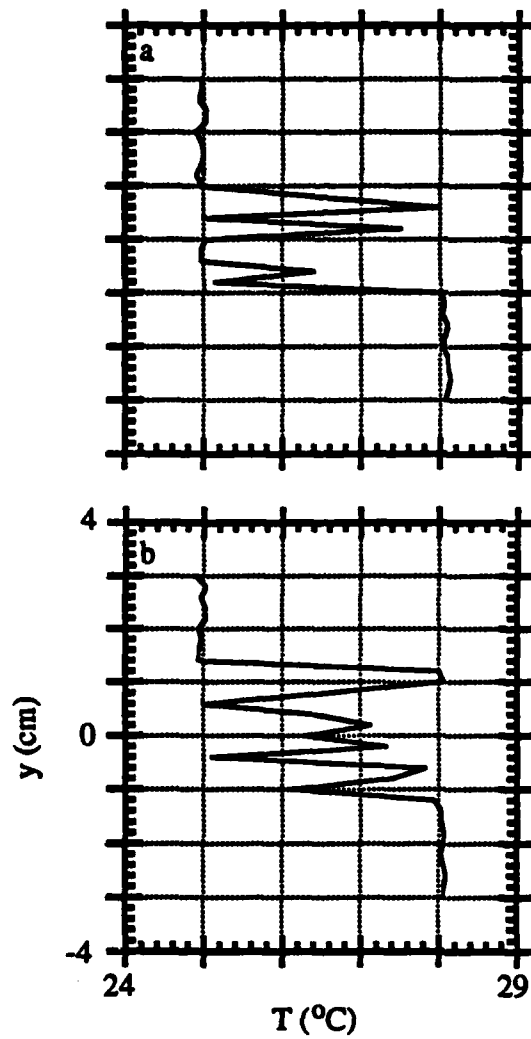FIGURE 6. T(y), T(y,t), and *pdf*(T,y) for SU, f = 6 Hz at x = (a) 10.16 cm, (b) 15.24 cm, and (c) 20.32 cm.

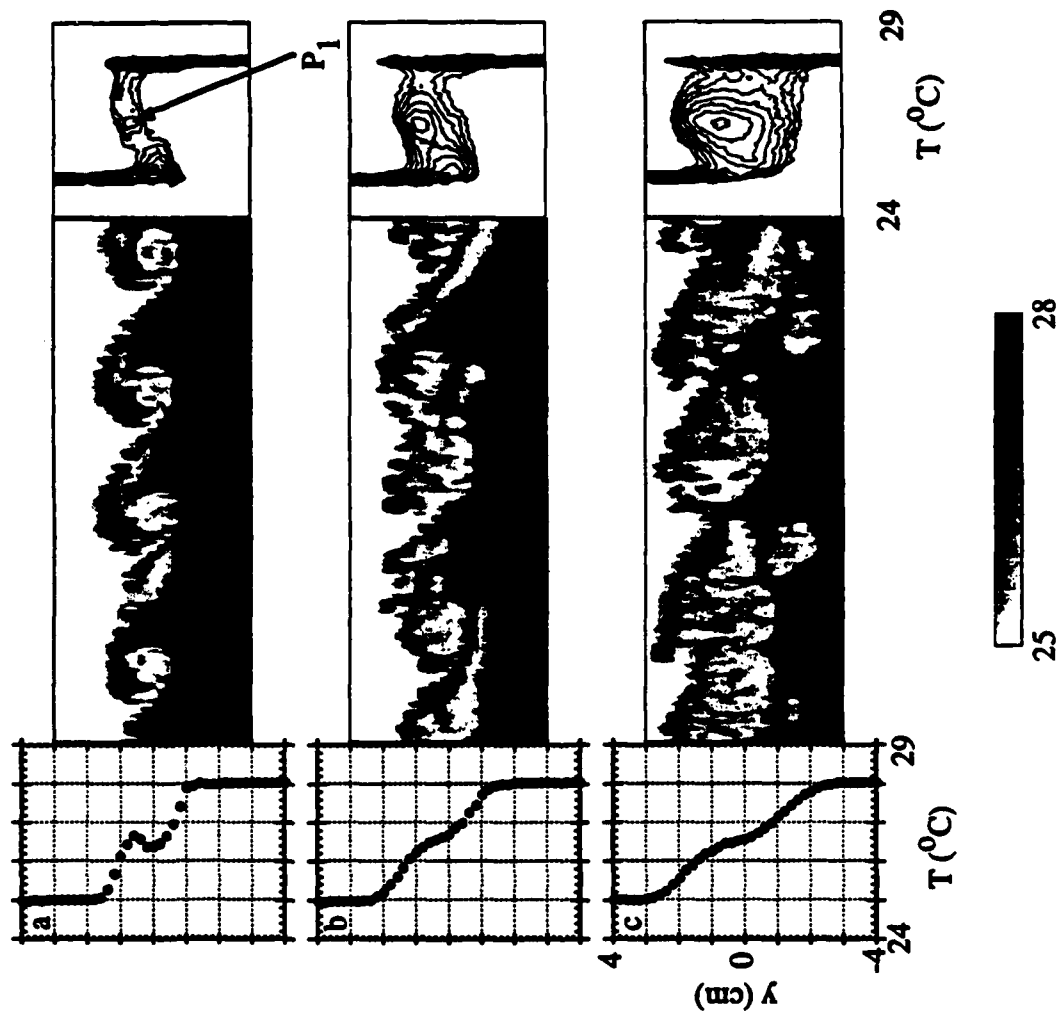FIGURE 7. Instantaneous temperature profiles T(y) for SU, f = 6 Hz at x = (a) 16.24 cm, and (b) 15.24 cm.

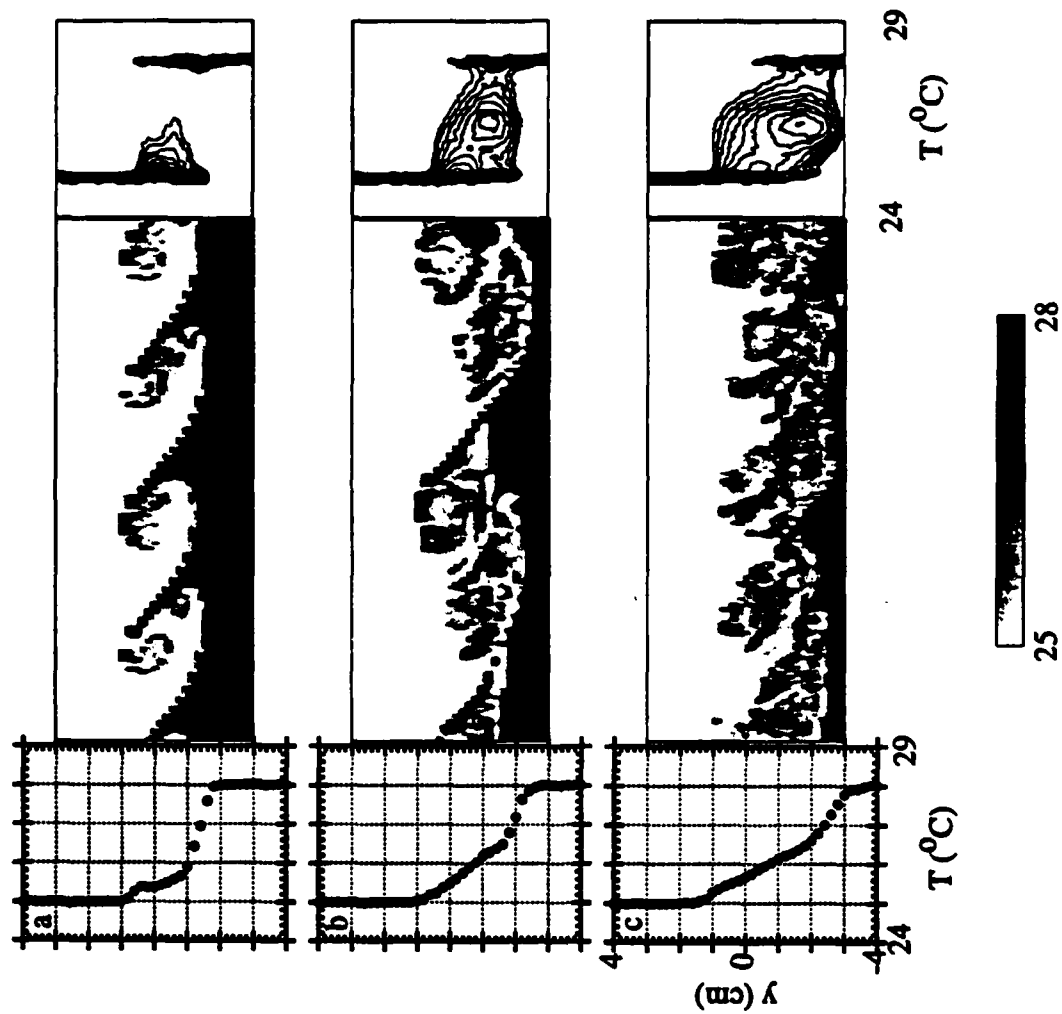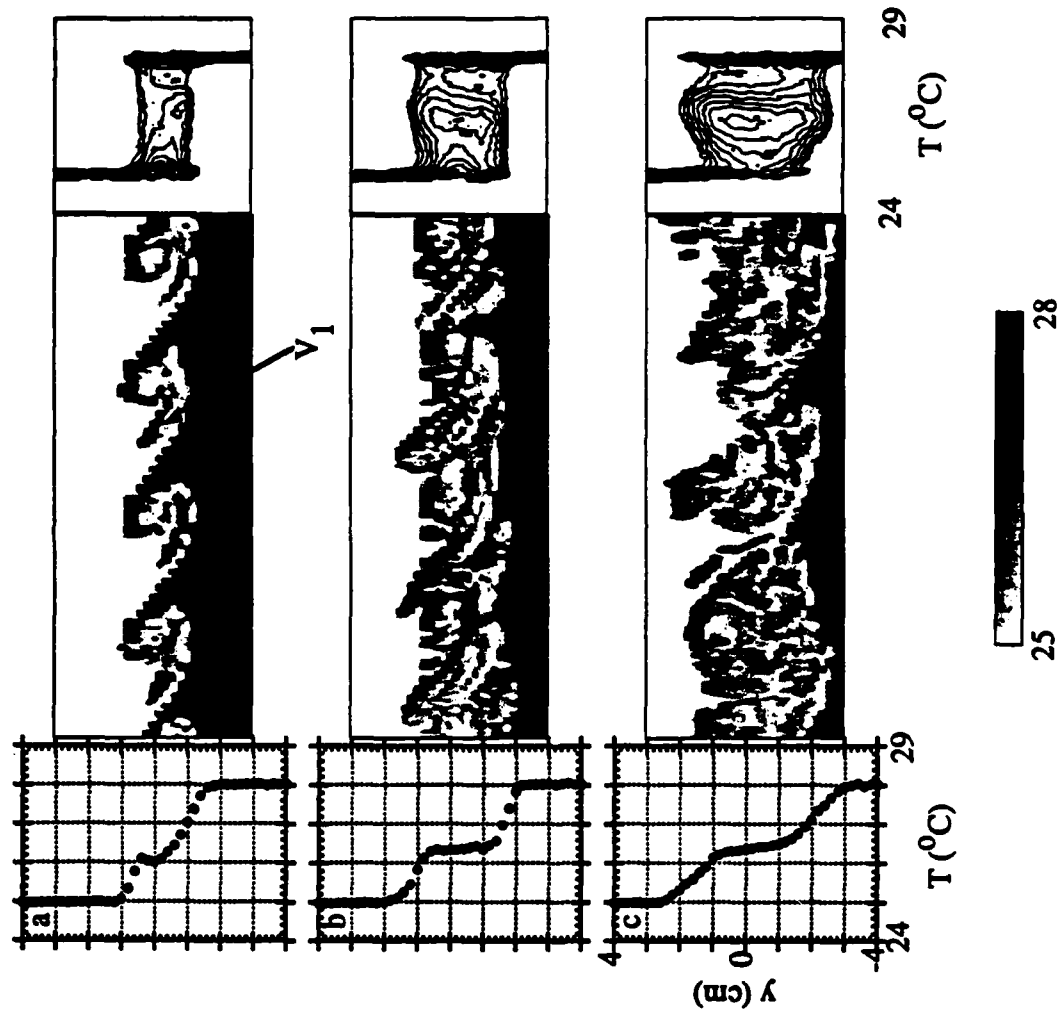FIGURE 8. T(y), T(y,t), and *pdf*(T,y) for SP, f = 6 Hz (head) at x = (a) 10.16 cm, (b) 15.24 cm, and (c) 20.32 cm.

FIGURE 9. T(y), T(y,t), and pdf(T,y) for SP, f = 6 Hz (tail) at x = (a) 10.16 cm, (b) 15.24 cm, and (c) 20.32 cm.

FIGURE 10. T(y), T(y,t), and *pdf*(T,y) for SP, f = 6 Hz (1/2 head/tail) at x = (a) 10.16 cm, (b) 15.24 cm, and (c) 20.32 cm.

excitation waveform is SU, f = 6 Hz. In figures 8-10, the excitation waveform is SP, f = 6 Hz measured at three spanwise positions. The excitation frequency of 6 Hz (close to the natural frequency of 5.66 Hz) is chosen to lock the flow to the forcing frequency. Within the domain of measurement, vortex growth is inhibited and the vortex passage frequency is the forcing frequency (i.e., Oster & Wygnanski 1982). Spanwise-uniform excitation at this frequency leads to mixing enhancement by promoting rollup of the primary vortices closer to the flow partition than in the unforced case (figure 6). Figure 7a-b shows $T(y,t_i)$ at two representative times t_5 (x = 10.16 cm, figure 7a) and t_6 (x = 15.24 cm, figure 7b). Notice the presence of an increased number of thin temperature sheets relative to the unforced case (figure 4a-b). This leads to an earlier appearance of mixed fluid, which is present in $pdf(T,y)$ at x = 10.16 cm (figure 6a). This fluid is localized near the physical center of the test section and is concentrated at temperatures slightly warmer than T_1. At x = 15.24 cm (figure 6b) there is clearly more mixed fluid in $pdf(T,y)$ than in the corresponding case for the unforced flow (figure 3b). The levels of mixing are higher and mixing has become more apparent at warmer temperatures. It is interesting to note, however, that the cross-stream extent of mixing (as designated by the lowest contour, $\log_{10}(pdf) = -1.0$) is actually somewhat narrower in the case of SU, f = 6 Hz forcing than it is for the unforced case; that is, mixing is more localized as a result of the more regular flow in this case. That trend is continued at x = 20.32 cm (figure 6c) where $pdf(T,y)$ shows a peak which is narrower in y than in the unforced case (particularly around temperatures near $(T_1 + T_2)/2$) but which has a higher level of mixing, particularly near T_2. This is an opposite result to that reported by Koochesfahani & MacKinnon (1991), who found that the predominant concentration shifted towards that of the high-speed stream as a result of the forcing. These differences may be explained by the fact that Koochesfahani and MacKinnon forced

the flow well below the natural frequency, while we force it slightly above the natural frequency. Finally, it appears from the plots of T(y,t) (figure 6c) that while there is substantial mixed fluid around the periphery of the primary vortices, there is a substantial amount of unmixed fluid within the cores.

The effect of SP, f = 6 Hz excitation is shown in figures 8-10. This form of forcing introduces packets of counter-rotating streamwise vortices (Nygaard & Glezer 1991) in which there is a large increase in small-scale motion and hence which may be expected to enhance mixing. Streamwise vortices in the plane shear layer are similar to the lambda vortices in boundary layers. The "head" of the lambda-shaped structure is formed at the transition between a heater running at 4% power and one running at full power, and resides on the high-speed side of a spanwise vortex. Its two counter-rotating legs reside in the braids region between this vortex and the one immediately upstream. Its "tail" is the intersection of two adjacent streamwise vortices and resides on the low-speed side of the upstream primary vortex. Measurements are taken at three spanwise positions: the "head" of the streamwise vortex (figure 8), the "tail" of the streamwise vortex (figure 9), and the midpoint between the head and tail, designated "1/2 head/tail" (figure 10).

The triggering of streamwise vortices has a twofold effect on the flow. First, it leads to the appearance of three-dimensional small-scale flow structures and mixing enhancement within the streamwise vortices and eventually within the cores of the primary vortices (Huang & Ho (1990), Nygaard & Glezer (1991)). Second, the rotation of the streamwise vortex pair has the effect of "pumping" high-temperature fluid from the low-speed stream into the high-speed stream at the head, while it pumps low-temperature fluid from the high-speed stream into the low-speed stream at the tail.

At x = 10.16 cm, the streamwise vortices are just beginning to form. It is apparent from T(y,t) at the head (figure 8a) and the tail (figure 9a) that there is significantly more high-temperature fluid entrained into the layer at the head than at the tail. At 1/2 head/tail, T(y,t) shows both the spanwise vortex and a cross-section of the streamwise vortex (designated V_1 in figure 10a). Contour plots of pdf(T,y) indicate a substantial increase in mixing compared to the spanwise-uniform case. Particularly notice the peak P_1 in pdf(T,y) at x = 10.16 cm (head) (figure 8a). This peak (not present in SU, f = 6 Hz, figure 6a) may be attributed solely to mixing within the core of the streamwise vortex. Notice that this peak is not present at the tail of the streamwise vortex (figure 9a), presumably because the streamwise vortex develops fastest at the head and slowest at the tail. This peak (occurring at T = 26.4 °C) is still present at x = 15.24 cm and x = 20.32 cm (figures 8b-c). It appears to broaden in T and y until, by x = 20.32 cm, there is a wide region of mixed fluid over a broad range of temperatures. This mixing may be attributed to the enhancement of small-scale motion which is particularly apparent in T(y,t) in figures 8b-c.

Mixing at the tail of the streamwise vortex (figure 9) is significantly effected by the pumping action of the streamwise vortices. Plane shear layers typically entrain an excess of fluid from the high-speed stream (Dimotakis 1986, 1989). The pumping action of the streamwise vortices at the tail further increases the ratio of high-speed to low-speed fluid. This is demonstrated by T(y,t) at all three streamwise stations (figure 9) which show very little hot fluid in the layer. The stirring action of the streamwise vortices ensures that this fluid is well mixed, however. The plots of pdf(T,y), particularly at x = 15.24 cm and x = 20.32 cm, show a "plateau" of mixed fluid beginning at T_1 and gradually rising to the peak at T = 26.4 °C (the same mixed fluid temperature as at the head, suggesting that the composition is the same throughout the streamwise vortex). At temperatures higher than this, however, there

is a sharp diminution in mixed fluid. Most of the mixed fluid produced at the tail is at lower temperatures than that at the head due to the lack of entrained hot fluid.

Mixing, however, is arguably most effective at 1/2 head/tail. When the cold-wire rake is in this position, it spends virtually all of its time either in a spanwise vortex or an oblique slice through a streamwise vortex. This oblique slice (previously shown as V_1 in figure 10a) contains a large amount of mixed fluid. By x = 15.24 cm (figure 10b), virtually the entire layer contains either mixed fluid from either the spanwise vortex or the streamwise vortex. The peak in the *pdf*(T,y) at T = 26.4 °C now occurs over a significantly broader range in y. Finally, at x = 20.32 cm *pdf*(T,y) there is a large amount of mixed fluid throughout the layer, although it is somewhat more concentrated in low temperatures as was the case at the tail of the streamwise vortex.

Small physical dimensions, either as a result of straining of thin sheets of fluid in the cores of the primary vortices or small-scale three-dimensional motions, are necessary for diffusion processes and molecular mixing. Figures 4 and 7 compared instantaneous temperature profiles $T(y,t_i)$ for unforced and SU, f = 6 Hz. These figures showed how fluid is strained into thin layers which lead to mixing. However, this type of figure is limited by the spatial resolution of measurement of 2 mm, the spacing between the cold wire sensors. It may be more effective to consider the layer spacing in the streamwise dimension. Since the vortical structures are convected with a constant velocity $U_C = (U_1 + U_2)/2$, this is equivalent to considering the time trace $T(y_i,t)$ at a given elevation. To consider the small scales (indicative of thin layers) throughout the flow, the power spectrum of turbulent temperature fluctuations, $S_T(f;y)$, can be considered.

Since mixing occurs where there are strong temperature gradients, it is interesting to consider the scalar dissipation $\nabla T \cdot \nabla T(x,t)$ as a measure of the mixing

rate (i.e., Dahm, Southerland, & Buch (1991)). This scalar energy dissipation comes directly from the scalar energy diffusion equation, and gives the rate at which nonuniformities in temperature are being smoothed by molecular diffusion. In the present experiment the data is in the form $T(y,t)$; it is thus necessary to approximate $\nabla T \cdot \nabla T(x,t) \approx (\partial T/\partial y)^2 + (1/U_C)^2 (\partial T/\partial t)^2$.

Figure 11a-e shows pairs of $S_T(f;y)$ (left) and the scalar dissipation over a period of 0.66s (right) at $x = 17.78$ cm for the unforced flow (figure 11a), SU, $f = 6$ Hz (figure 11b), SP, $f = 6$ Hz (head) (figure 11c), SP, $f = 6$ Hz (tail) (figure 11d), and SP, $f = 6$ Hz (1/2 head/tail) (figure 11e). The power spectra S_T are plotted on a logarithmic scale with arbitrary units. The two contours are at $\log_{10}(S_T) = 0.0$ and $\log_{10}(S_T) = 0.654$. The contours of the scalar dissipation range from a minimum value of 10.0 $[^\circ C/cm]^2$ to a maximum of 210.0 $[^\circ C/cm]^2$ at a contour increment of 40 $[^\circ C/cm]^2$. Comparison of power spectra of the unforced case to that of SU, $f = 6$ Hz shows that the there is more small-scale activity when the flow is forced. However, the region over which it occurs is smaller in the SU, $f = 6$ Hz case, presumably because the flow is locked to the forcing frequency and spreads less. The three SP, $f = 6$ Hz cases show that there is a large increase in small-scale activity at the head of the streamwise vortex (figure 11c). Interestingly, there is very little small-scale activity at the tail of the streamwise vortex (figure 11d). In fact, there appears to be even less than in the unforced case. This is due to the pumping action of the streamwise vortex: there is very little hot fluid in the layer at this spanwise position. The fluid which is in the layer is quite well mixed. Since the layer primarily contains cold fluid with some mixed fluid, there is very little scalar dissipation. This also accounts for the low values of S_T. Finally, at 1/2 head/tail (figure 11e), the magnitude of the temperature fluctuations is approximately the same
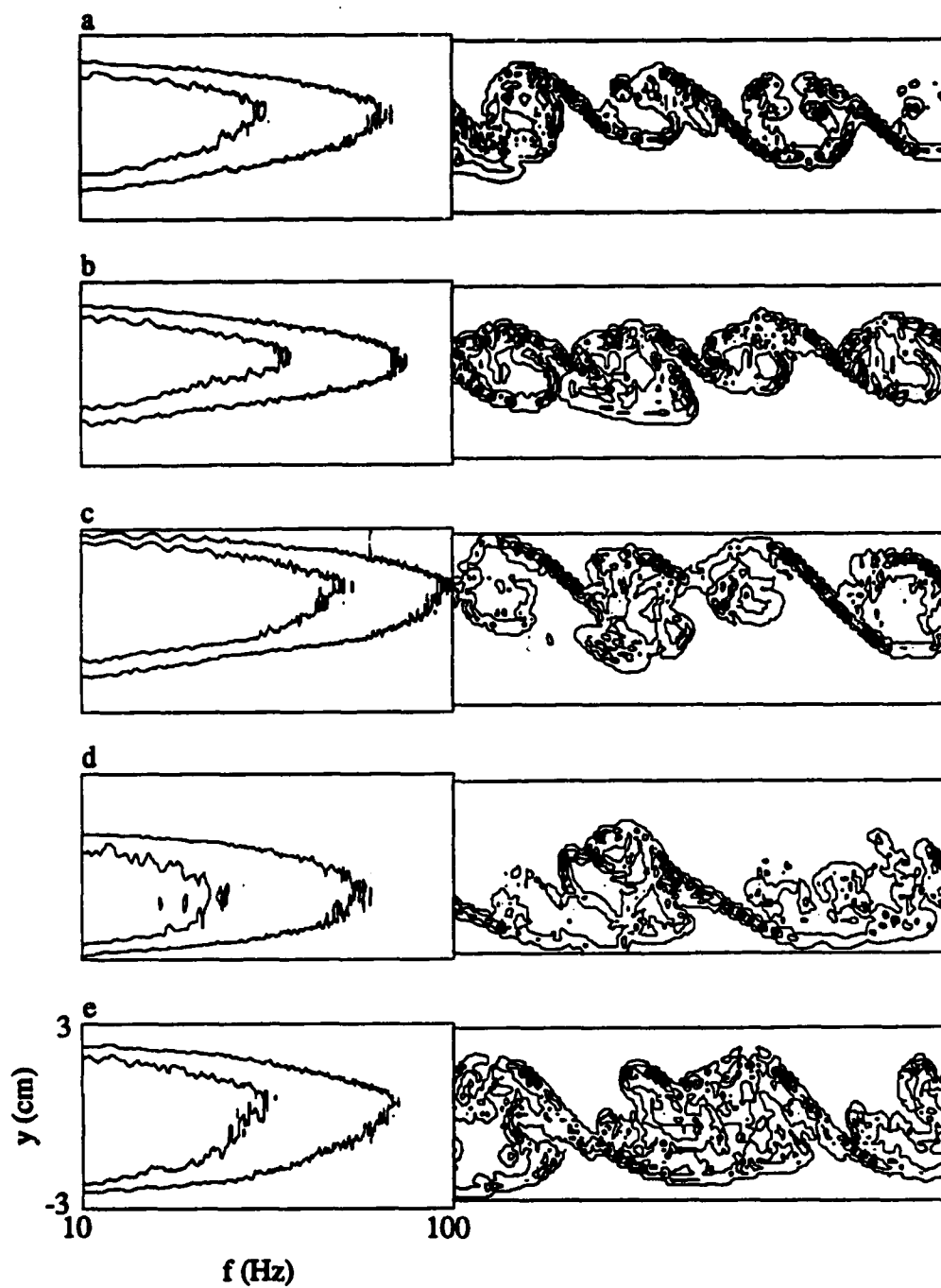
FIGURE 11. Pairs of S_T (left) and scalar dissipation (right) at $x = 17.78$ cm for (a) unforced, (b) SU, $f = 6$ Hz, (c) SP, $f = 6$ Hz (head), (d) SP, $f = 6$ Hz (tail), and (e) SP, $f = 6$ Hz (1/2 head/tail).

as that in the unforced case. However, these fluctuations occur over a broader cross-stream domain.

An increase in the width of the shear layer δ can lead to an increase in the amount of mixed fluid within the layer. When the shear layer is simultaneously forced at a fundamental frequency (f = 7.7 Hz) and its subharmonic (f = 3.85 Hz), controlled pairing of the primary vortices is induced. The pairing process is accompanied by an increase in entrainment and δ. Figure 12 shows the effect of controlled pairing on the mixing. The temperature distribution $<T(y,t)>$ shows that the primary vortices are beginning to pair at x = 10.16 cm (figure 12a) and the process continues through x = 15.24 cm (figure 12b) and is complete at x = 20.32 cm (figure 12c) where the passage frequency of the vortical structures is 3.85 Hz. This pairing of the primary vortical structures results in layer widths of δ = 2.74 cm, 4.17 cm, and 6.05 cm at x = 10.16 cm, 15.24 cm, and 20.32 cm, respectively. This can be contrasted with δ = 2.63 cm, 3.71 cm, and 5.38 cm at the same streamwise stations for SU, f = 6 Hz. In addition, there is an increase in the small-scale motion within the engulfed vortex as the pairing process occurs (V_2 in figure 12b). The thin layers collapse together as the vortices pair, until finally the paired vortex is filled with mixed fluid (figure 12c). Comparisons of $pdf(T,y)$ at x = 15.24 cm and x = 20.32 cm for this case with those of SU, f = 6 Hz forcing (figure 6b-c) show a substantial increase in mixed fluid. In particular, notice the peak at T = 25.5 °C which was not present in the SU, f = 6 Hz case.

Figures 13-15 show the effect of controlled pairing in the presence of streamwise vortices on mixing. These figures document the case SP, f = 3.85, 7.7 Hz at the head (figure 13), the tail (figure 14), and the midpoint between the head and the tail (figure 15). The contour map of $pdf(T,y)$ at x = 20.32 cm exhibits a peak at 26.3 °C which is somewhat broader in the cross stream direction than the peak of the
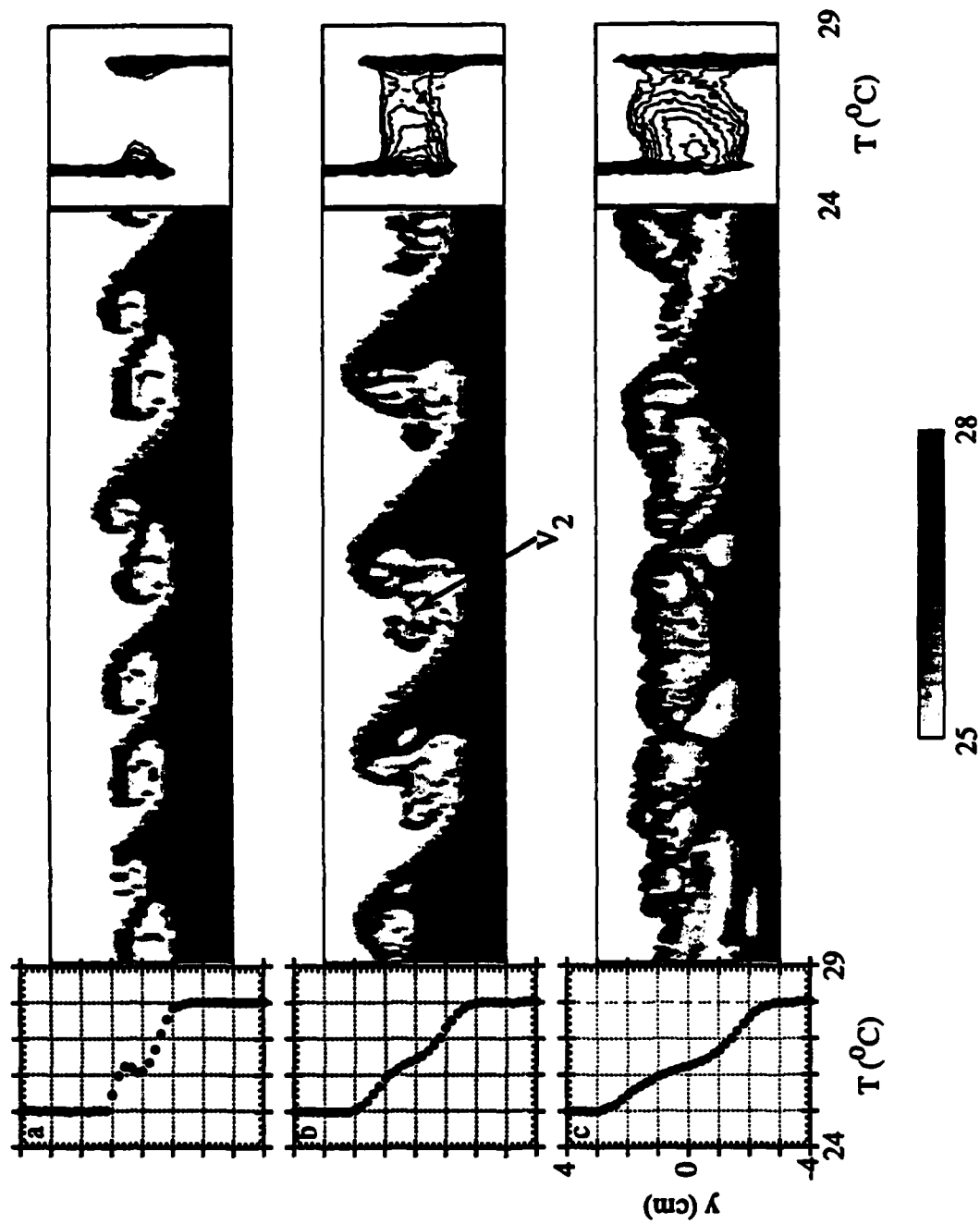
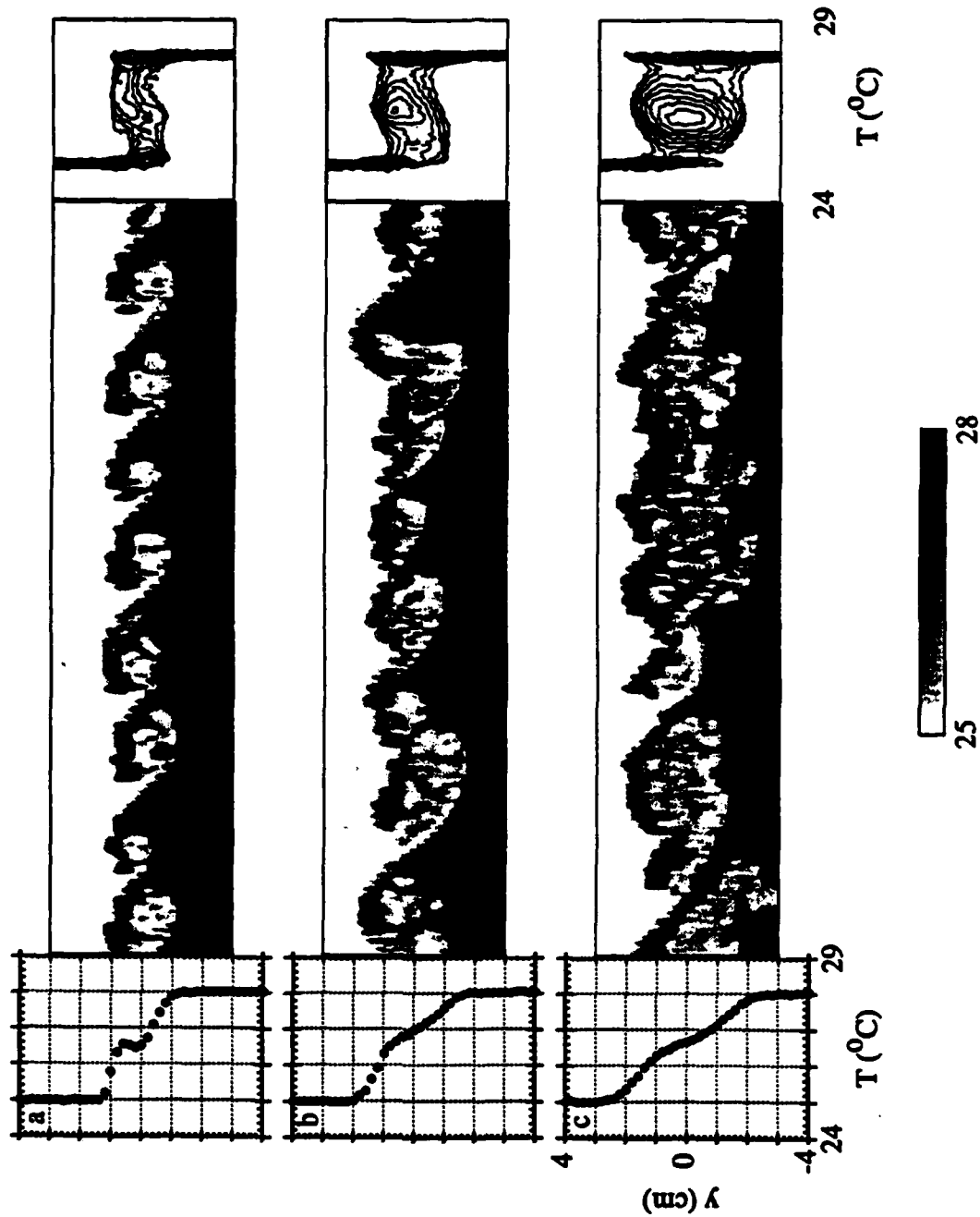FIGURE 12. T(y), T(y,t), and *pdf*(T,y) for SU, f = 3.85, 7.7 Hz at x = (a) 10.16 cm, (b) 15.24 cm, and (c) 20.32 cm.

FIGURE 13. T(y), T(y,t), and *pdf*(T,y) for SP, f = 3.85, 7.7 Hz (head) at x = (a) 10.16 cm, (b) 15.24 cm, and (c) 20.32 cm.
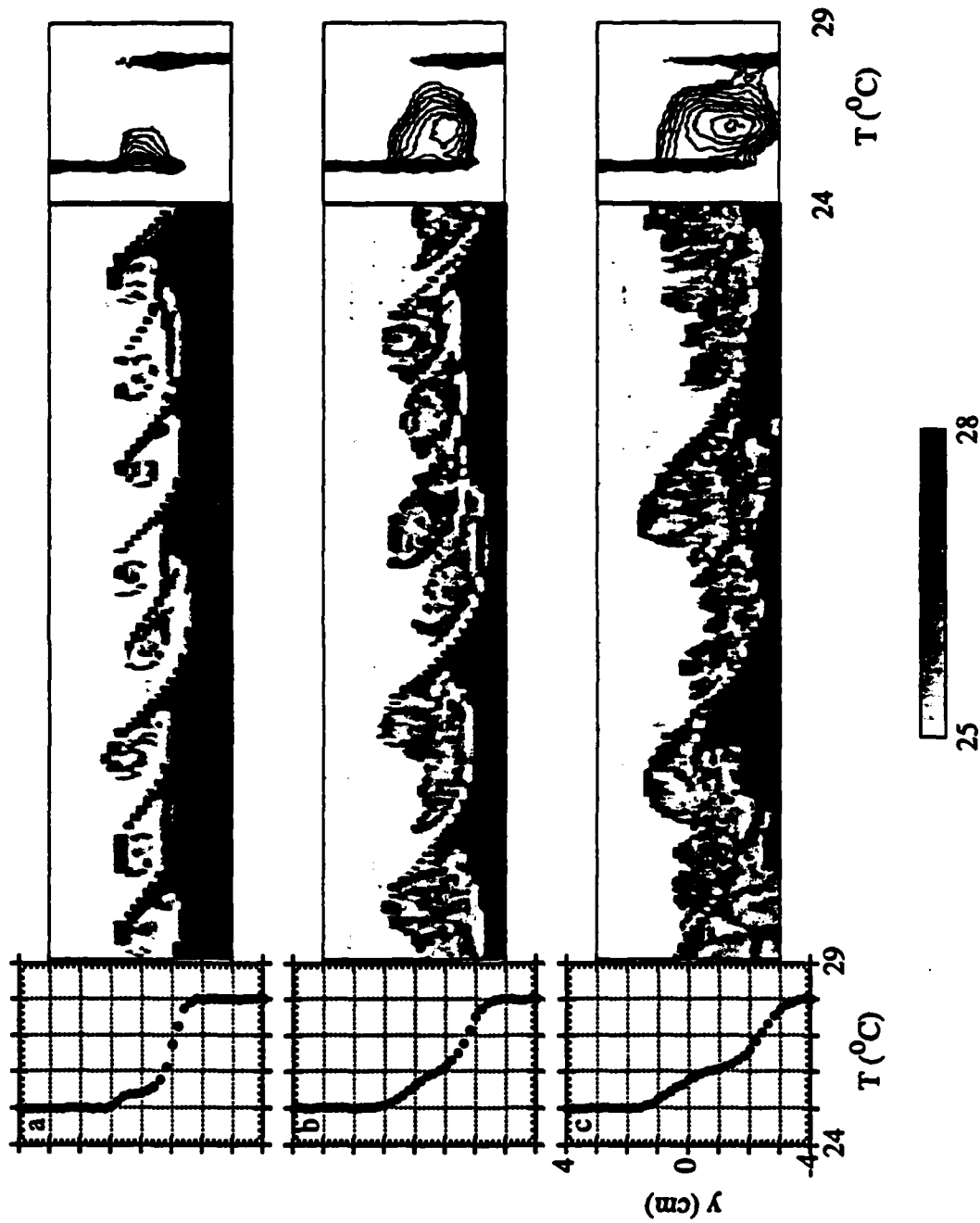
FIGURE 14. T(y), T(y,t), and *pdf*(T,y) for SP, f = 3.85, 7.7 Hz (tail) at x = (a) 10.16 cm, (b) 15.24 cm, and (c) 20.32 cm.

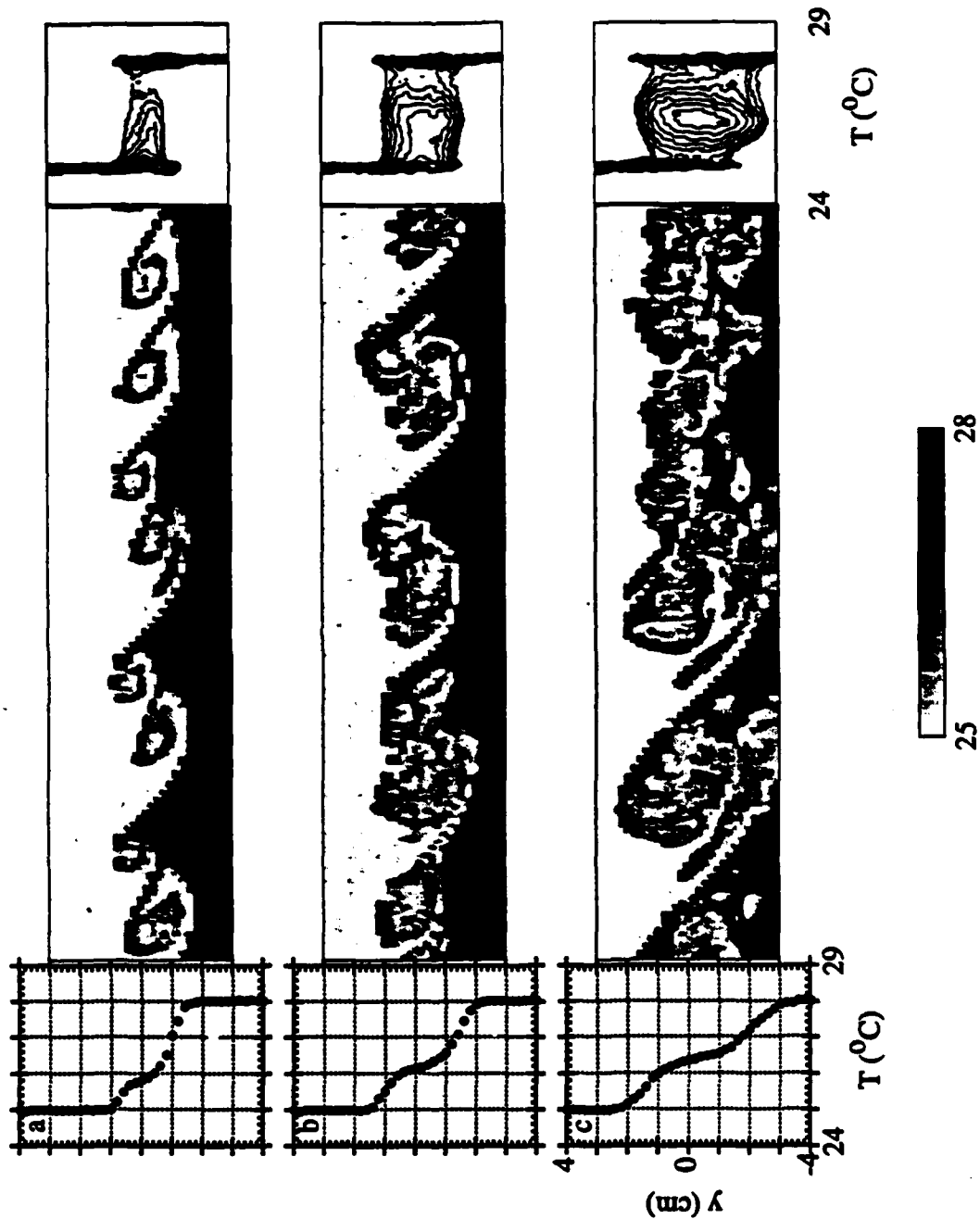FIGURE 15. T(y), T(y,t), and *pdf*(T,y) for SP, f = 3.85, 7.7 Hz (1/2 head/tail) at x
= (a) 10.16 cm, (b) 15.24 cm, and (c) 20.32 cm.

case SP, f = 6 Hz and significantly sharper in T (the mixing is more homogeneous). At the tail of the streamwise vortex (figure 14), the peak in $pdf(T,y)$ is at T = 26.2 °C, significantly cooler than the corresponding SP, f = 6 Hz case. Finally, an interesting thing to notice is that at the midpoint between the head and tail (figure 15) is that mixing (as shown by $pdf(T,y)$) occurs over a *narrower* cross-stream region than in the case of SP, f = 6 Hz. This suggest that the streamwise vortices are not as strong as in the case of SP, f = 6 Hz, presumably because they have been rolled up into the paired spanwise vortices. However, the plots of *pdf* do suggest that this mode of forcing may be as effective at enhancing mixing at the head and tail of the streamwise vortex as SP, f = 6 Hz.

A plot of **PM**(x) is shown in figure 16 for the forcing configurations discussed above. Figure 16a shows **PM**(x) for the unforced flow. There is very little mixed fluid until approximately x = 10 cm, where the flow begins to undergo mixing transition. By x = 22.86 cm, **PM**(x) has reached a value of 0.37 cm, almost an order of magnitude higher than at x ≤ 10 cm. This is consistent with the results of Konrad (1976) (his figure 22) which shows an increase in product formation at Re ≈10^4 at which time the product fraction also increases markedly. Roberts & Roshko (1985) (their figure 2) and other researchers have also found similar results.

Figure 16b shows the percentage change in PM (relative to the unforced case at each streamwise station) for SU, f = 6 Hz and SP, f = 6 Hz at the head, the tail, and 1/2 head/tail. All forms of forcing appear to effect a maximum increase of **PM** between approximately x = 8 cm and x = 12 cm. **PM**(x) for SU, f = 6 Hz reaches a maximum of approximately 37% above the unforced level at x = 8.89 cm. Beyond this point, SU forcing does not significantly increase the level of **PM**. SP forcing, however, does significantly increase the amount of mixed fluid throughout the streamwise domain of measurement. Interestingly, the maximum increase in **PM**
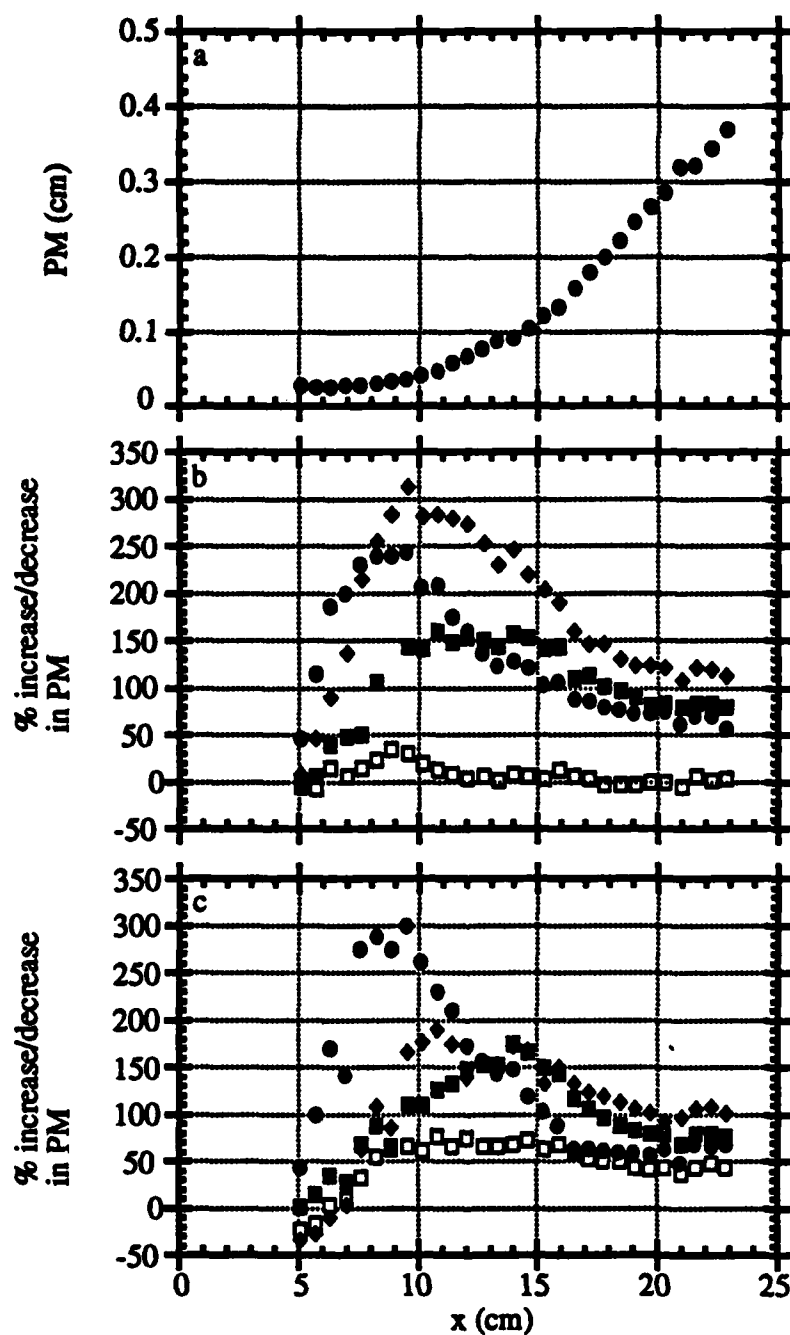
FIGURE 16. (a) PM(x) for the unforced flow, (b) % increase/decrease in PM for SU, f = 6 Hz (□), and SP, f = 6 Hz (head) (●), (tail) (■), and (1/2 head/tail) (◆), (c) % increase/decrease in PM for SU, f = 3.85, 7.7 Hz (□), and SP, f = 3.85, 7.7 Hz (head) (●), (tail) (■), and (1/2 head/tail) (◆).

occurs at 1/2 head/tail. There is an increase of over 300% relative to the unforced case at x = 10.16 cm. The large increase in the performance measure at this spanwise station is due to the fact that at this point, an oblique slice through the induced streamwise vortex results in mixed fluid passing through the measurement station almost continually. At the head of the streamwise vortex, there is a large increase in PM, particularly at upstream locations. Apparently the streamwise vortex is amplified faster at this spanwise position than at the tail of the streamwise vortex. By x = 12.07 cm, PM(x) is actually greater at the tail. By the end of the measurement domain (x = 22.86 cm), PM has reached a value of 55% above the unforced level at the head of the streamwise vortex, 78% above the unforced level at the tail of the streamwise vortex, and 115% at 1/2 head/tail. These increases can be compared to the maximum increase of 22% (in mixed fluid) attained by Koochesfahani & MacKinnon (1991) with a spanwise-uniform, skewed harmonic waveform. Their data was at a local Reynolds number of 6600; in our experiment, the unforced flow reaches this Reynolds number at x ≈ 10 cm.

The configuration SU, f = 3.85, 7.7 Hz results in significantly higher levels of PM than SU, f = 6 Hz. It reaches a level of approximately 50% above the unforced level at all streamwise stations for x ≥ 10 cm. The configuration SP at f = 3.85, 7.7 Hz, by contrast, does not significantly increase PM relative to SP, f = 6 Hz. Indeed, at the tail, the values of PM are approximately the same. However, the mixing at the head of the streamwise vortex appears to increase quicker, while mixing at 1/2 head/tail is significantly lower. This suggests that, while the streamwise vortices may be amplified quicker for SP, f = 3.85, 7.7 Hz forcing, the pairing process may have the effect of reducing the strength of the streamwise vortices in downstream locations. This is similar to the work of Moser & Rodgers

(1993), who found that pairing reduced the growth of three-dimensionality (although they do not actually reduce the overall level of three-dimensionality).

Finally, it is instructive to consider what may broadly be construed as moments of $pdf(T,y)$. The total mixed fluid in the layer is obtained by

$$M^0 = \int_{T_1+\epsilon}^{T_2-\epsilon} \int_{-\infty}^{+\infty} pdf(T,y) \; dy \; dT$$

and has dimensions of [length]. The average temperature of mixed fluid within the layer is obtained by

$$T_{cent} = M_T^1 = \frac{1}{M_0} \int_{T_1+\epsilon}^{T_2-\epsilon} \int_{-\infty}^{+\infty} T \, pdf(T,y) \; dy \; dT.$$

The average y-position of mixed fluid within the layer is obtained by

$$y_{cent} = M_y^1 = \frac{1}{M_0} \int_{T_1+\epsilon}^{T_2-\epsilon} \int_{-\infty}^{+\infty} y \, pdf(T,y) \; dy \; dT.$$

And finally, it is possible to construct higher-order moments ($i > 2$) with respect to T and y in the following manner:

$$M_T^i = \frac{1}{M^0} \int_{T_1+\epsilon}^{T_2-\epsilon} \int_{-\infty}^{+\infty} (T - T_{cent})^i \, pdf(T,y) \; dy \; dT$$

(having dimensions of [(temperature)^i]) and

$$M_y^i = \frac{1}{M^0} \int_{T_1+\varepsilon}^{T_2-\varepsilon} \int_{-\infty}^{+\infty} (y - y_{cent})^i \, pdf(T,y) \, dy \, dT$$

(having dimensions of [(length)^i]). For all of these integrals, $\varepsilon = 0.25$ °C to ensure that the lobes of unmixed fluid do not contribute to the integral. Deemed to be of particular interest are the total mixed fluid (M_0), the average temperature of mixed fluid T_{cent} (M_T^1), the average cross-stream position of mixed fluid y_{cent} (M_y^1), the standard deviation with respect to y, σ_y (($M_y^2)^{1/2}$), the skewness with respect to T, skew$_T$ (M_T^3/σ_T^3), and the kurtosis with respect to T, kurtosis$_T$ (M_T^4/σ_T^4). The standard deviation with respect to T $\sigma_T = (M_T^2)^{1/2}$ (with dimensions of [temperature]) is used to nondimensionalize skew$_T$ and kurtosis$_T$ to give nondimensional measures of the skewness and the flatness of $pdf(T,y)$, respectively.

Figure 17 shows moments of $pdf(T,y)$ for unforced, SU, f = 6 Hz, and SP, f = 6 Hz at the head, the tail, and 1/2 head/tail. The total mixed fluid (figure 17a) shows trends similar to that of PM(x). Thus the integral performance measure used in the current work may be used in comparison with other works which used the total mixed fluid as the primary measure of mixing. Figure 17b shows the average temperature of mixed fluid T_{cent}. Both the unforced flow and SU, f = 6 Hz show a decrease in average mixed fluid temperature from x = 10.16 cm to x = 22.86 cm. By contrast, the three SP, f = 6 Hz cases show an *increase* in mixed fluid temperature with streamwise position. This is consistent with the results found by Buell & Mansour (1989) in their spatially-developing simulation. However, that the T_{cent} moves towards the high-speed concentration with downstream distance for the unforced flow is at odds with the results of Koochesfahani & Dimotakis (1986). They found that the average concentration shifted towards the low-speed
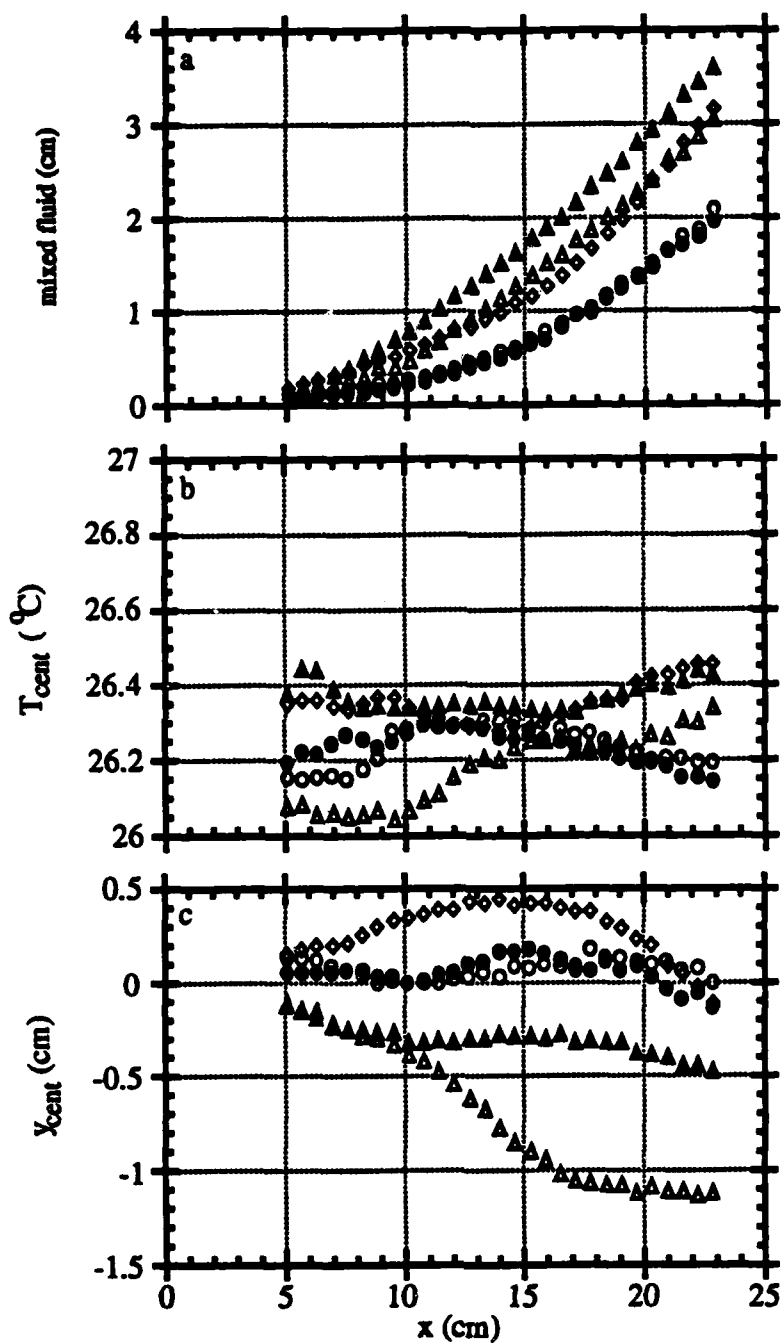
FIGURE 17. (a) total mixed fluid, (b) average temperature of mixed fluid, and (c) average cross-stream position of mixed fluid for unforced (●), SU, f = 6 Hz (○), SP, f = 6 Hz (head) (◊), SP, f = 6 Hz (tail) (Δ), and SP, f = 6 Hz (1/2 head/tail) (▲).
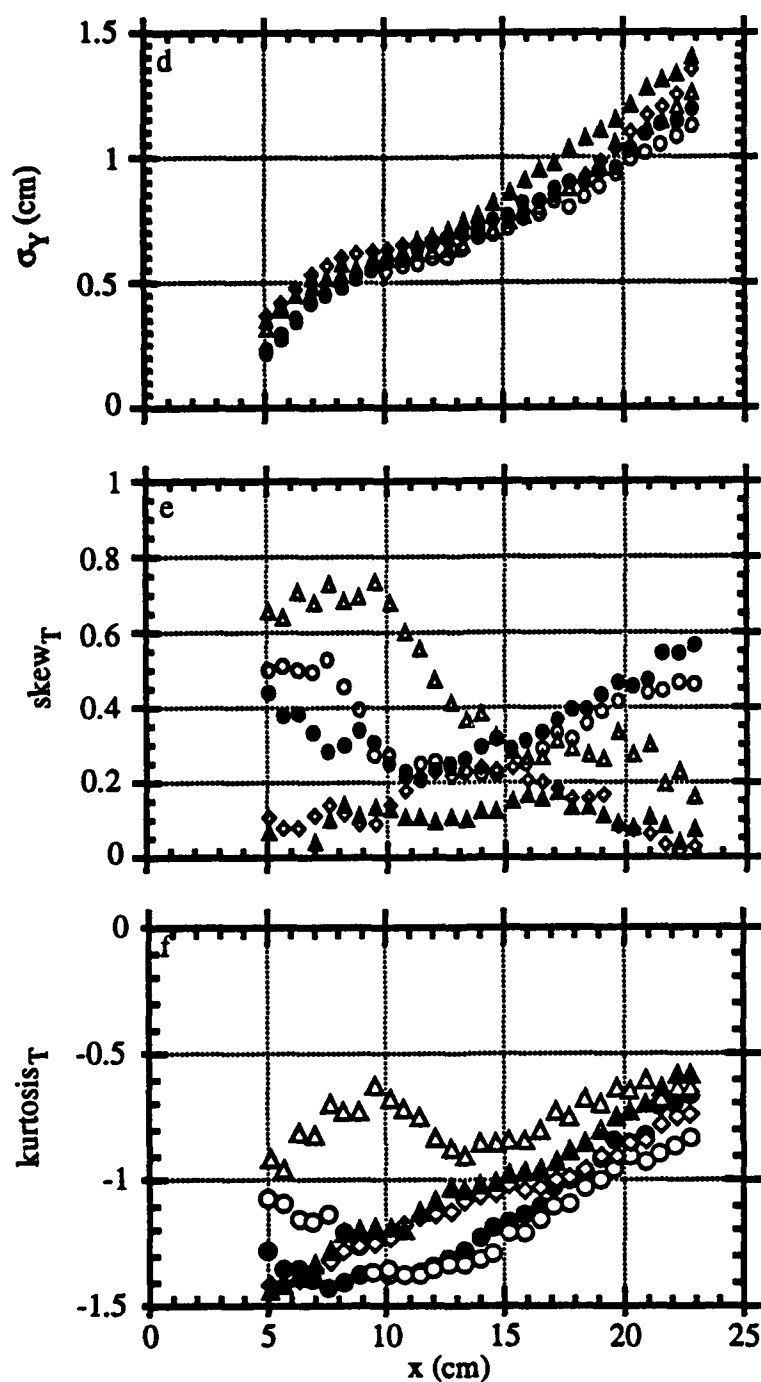
FIGURE 17-*Continued*. (a) σ_Y, (b) skew$_T$, and (c) kurtosis$_T$ for unforced (●), SU, f = 6 Hz (○), SP, f = 6 Hz (head) (◊), SP, f = 6 Hz (tail) (Δ), and SP, f = 6 Hz (1/2 head/tail) (▲).

concentration. They attributed this to an excess entrainment of high-speed fluid during the initial rollup. Our results are contrary to this. In addition, the predicted T_{cent} (from Dimotakis' (1986, 1989) entrainment ratio argument) is 26.28 °C. Our experiments show lower values of T_{cent} than this, with a downward trend at the end of the measurement regime.

As can be expected (due to the pumping action of the counter-rotating streamwise vortices) the average mixed fluid temperature is higher at the head than at the tail. Figure 17c shows the average cross-stream position of mixed fluid y_{cent} for these forcing configurations. Again, due to the pumping action of the streamwise vortices, y_{cent} is displaced upwards at the head and downwards at the tail of the streamwise vortices. Notice that y_{cent} varies by only 1-2 mm around the geometric center of the test section ($y = 0.0$ cm) for the unforced flow and SU, f= 6 Hz. However, it is interesting to note that for $x \geq 17$ cm, y_{cent} begins to decrease at the head and level out at the tail. This suggests a weakening of the streamwise vortices.

The standard deviation with respect to y, σ_y, can be thought of as a measure of the width of the layer over which mixing occurs (figure 17d). Although the layer is widest for the three SP cases, (lead by 1/2 head/tail) the difference does not appear to be enough to account for the large difference in mixing between these cases. Instead, it suggests that the increase in mixing for SP, f = 6 Hz is due to the increased small-scale motions induced by the streamwise vortices, not the increased layer width. Also notice the flat region for all of these cases for 10 cm $\leq$ x $\leq$15 cm. After this region, the layer begins to grow again with the upstream growth rate.

The skewness with respect to T of the *pdf*(T,y) can be used to describe the symmetry of mixing. Figure 17e shows $skew_T(x)$ for unforced, SU, f = 6 Hz, and SP, f = 6 Hz at the head, tail, and 1/2 head/tail. Notice that for both the unforced

flow and SU, f = 6 Hz skew$_T$(x) begins at a positive value, suggesting that there is a long tail in *pdf*(T,y) towards high-temperature fluid. Mixing becomes more symmetric between 10 cm $\leq$ x $\leq$ 15 cm and then becomes progressively skewed towards the high temperature for x > 15 cm, finally reaching a value of 0.45 (unforced) and 0.55 (SU, f = 5.66 Hz) at x = 22.86 cm. At the head of the streamwise vortex for SP, f = 6 Hz, the mixing is quite symmetric except for the range 10 cm $\leq$ x $\leq$ 20 cm, where the skewness reaches a value of 0.25. By contrast, at the tail of the streamwise vortex, the flow is skewed strongly towards the high-temperature side. Skew$_T$ has a value of approximately 0.70 for x $\leq$ 10 cm, then decreases rapidly to a value of 0.15 at x = 22.86 cm. Most symmetric, however, is the *pdf* at 1/2 head/tail. At all streamwise stations, skew$_T$ has a value below 0.20.

A plot of the kurtosis with respect to T, kurtosis$_T$(x) (figure 17f) shows the "flatness factor" of the *pdf* relative to a normal distribution. A negative value of the kurtosis means that the distribution is flatter than a normal distribution, whereas a positive value of the kurtosis implies that the distribution is more peaked than a normal distribution. For the unforced flow, *pdf*(T,y) becomes progressively more peaked in T with increasing streamwise distance, implying that the "preferred" concentration of mixed fluid becomes more so with increased streamwise distance. This trend is similar for the forced cases. Note that kurtosis$_T$(x) is maximized at the tail of the streamwise vortex.

Figure 18 shows the moments of *pdf* for the unforced flow (shown again for reference), SU, f = 3.85, 7.7 Hz, and SP, f = 3.85, 7.7 Hz. As was the case with PM(x), the total mixed fluid (figure 18a) shows less of a difference between the SP cases and the SU case than was the case for forcing at 6 Hz. The average mixed fluid temperature T$_{cent}$ (figure 18b) for SU, f = 3.85, 7.7 Hz is slightly higher than that for SU, f = 6 Hz at all streamwise stations. The corresponding plots for SP, f =
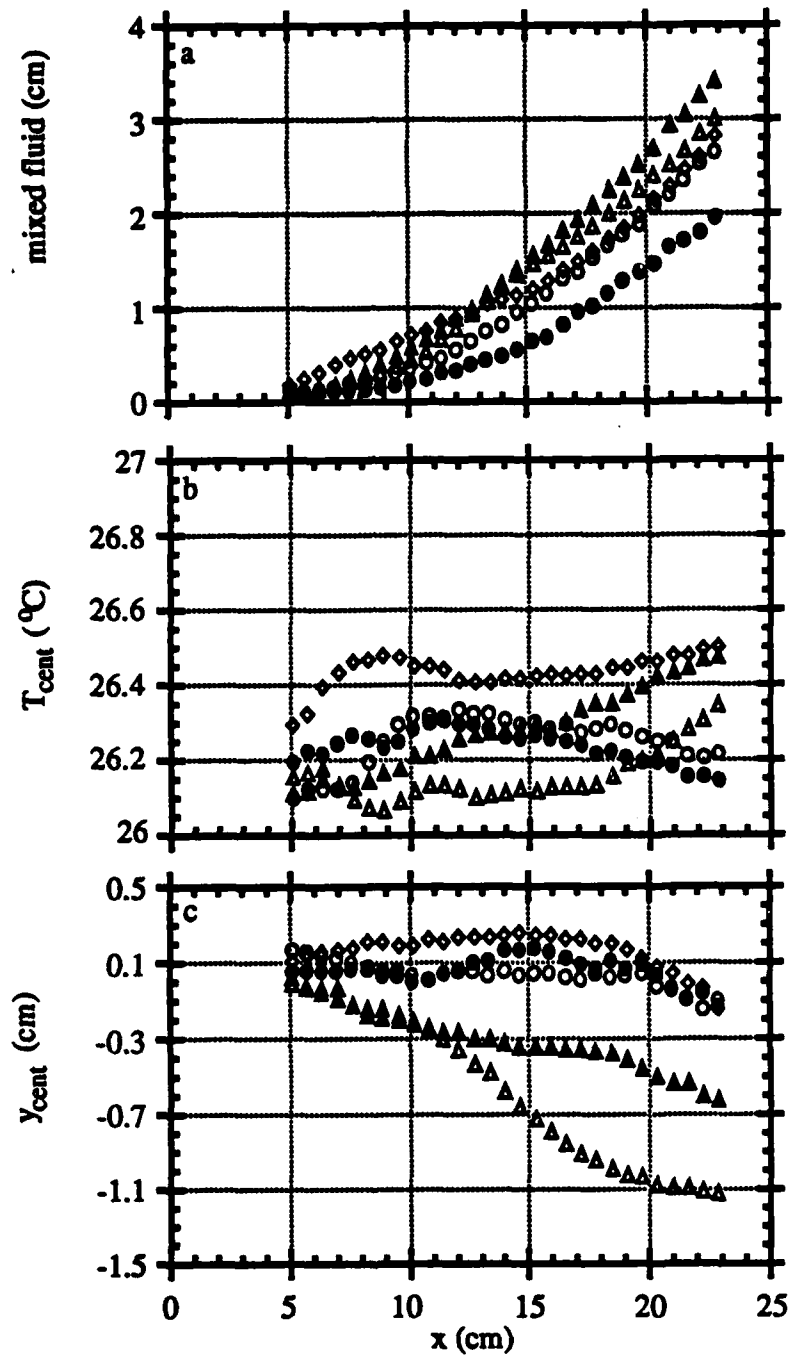
FIGURE 18. (a) total mixed fluid, (b) average temperature of mixed fluid, and (c) average cross-stream position of mixed fluid for unforced (●), SU, f = 3.85, 7.7 Hz (○), SP, f = 3.85, 7.7 Hz (head) (◊), SP, f = 3.85, 7.7 Hz (tail) (△), and SP, f = 3.85, 7.7 Hz (1/2 head/tail) (▲).
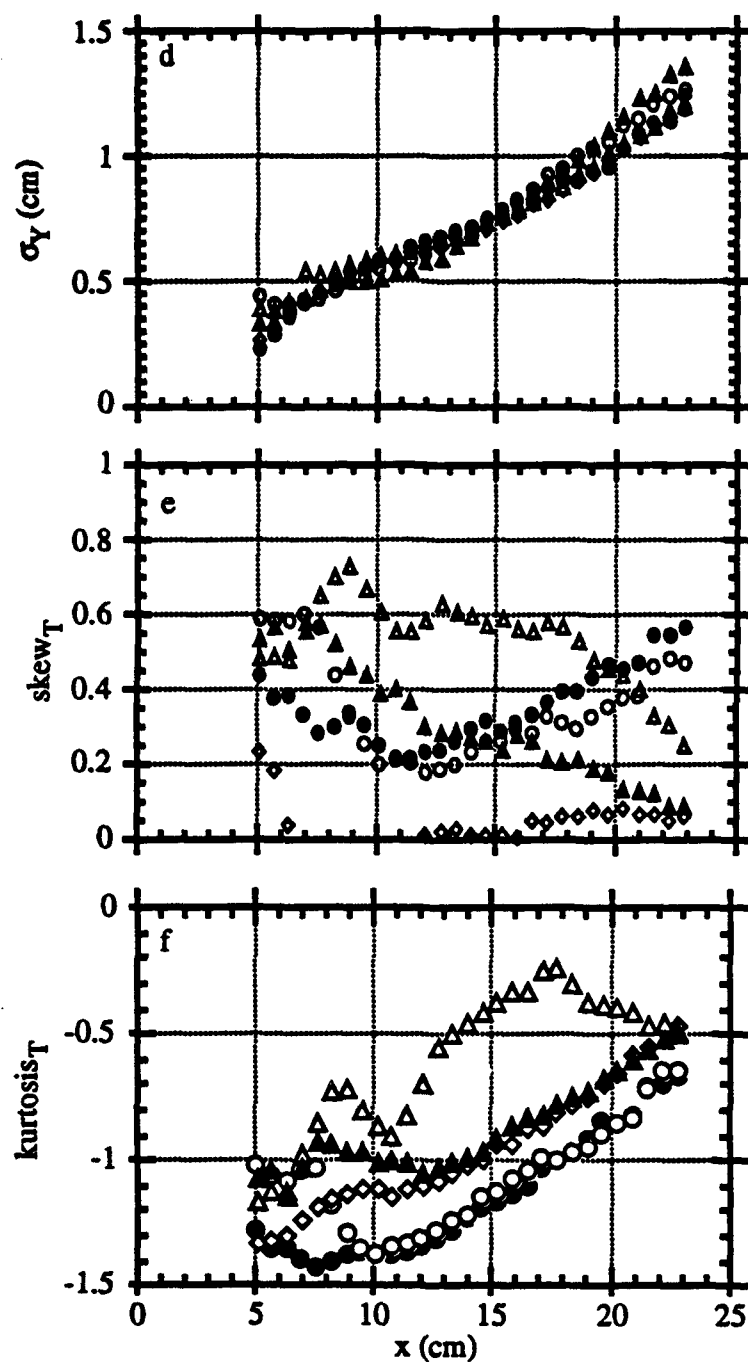
FIGURE 18-*Continued*. (a) σ_Y, (b) skew$_T$, and (c) kurtosis$_T$ for unforced (●), SU, f = 3.85, 7.7 Hz (○), SP, f = 3.85, 7.7 Hz (head) (◊), SP, f = 3.85, 7.7 Hz (tail) (Δ), and SP, f = 3.85, 7.7 Hz (1/2 head/tail) (▲).

3.85, 7.7 Hz are somewhat similar to those for SP, f = 6 Hz. At the head of the streamwise vortex, T_{cent} is significantly higher for the pairing case than for the f = 6 Hz case, particularly at the upstream stations. At the tail of the streamwise vortex, the average mixed fluid temperature is lower for the paring case before approaching that of the single-frequency case further downstream. The greatest difference between the two forcing waveforms, however, is at 1/2 head-tail. At upstream stations, T_{cent} is .3 °C warmer for SP, f = 6 Hz than for SP, f = 3.85, 7.7 Hz. That the greatest differences between the two forcing waveforms occur upstream of the pairing location suggests that the differences may be attributable in significant part to the fact that the fundamental forcing frequency is 7.7 Hz instead of 6 Hz.

The average position of mixed fluid temperature y_{cent} is similar to that for the SU, f = 6 Hz case. However, for SP, f = 3.85, 7.7 Hz case, y_{cent} is lower at the head and higher at the tail than the corresponding SP, f = 6 Hz cases, again suggesting that the streamwise vortices are weaker in this case than in the SP, f = 6 Hz case. This point can be further illustrated by comparing Δy_{cent} (the difference in the average y-location of mixing at the head and the tail) for the two cases. Since the streamwise vortices have the effect of increasing y_{cent} at the head and decreasing y_{cent} at the tail of the streamwise vortex, Δy_{cent} may be indicative of the strength of the streamwise vortices. Figure 19 shows Δy_{cent} for SP, f = 6 Hz and SP, f = 3.85, 7.7 Hz. Notice that at all streamwise stations, Δy_{cent} is greater for SP, f = 6 Hz than for SP, f = 3.85, 7.7 Hz. This suggests that the flow is more three-dimensional in this case, possibly as a result of stronger streamwise vortices. This, in turn, may help explain why PM is higher for SP, f = 6 Hz (particularly at 1/2 head/tail) than for SP, f = 3.85, 7.7 Hz (figure 16).

Finally, plots of $\delta(x)$ (the width of the shear layer) and the mixed fluid fraction (mixed fluid/$\delta(x)$) can be used to determine whether mixing enhancement
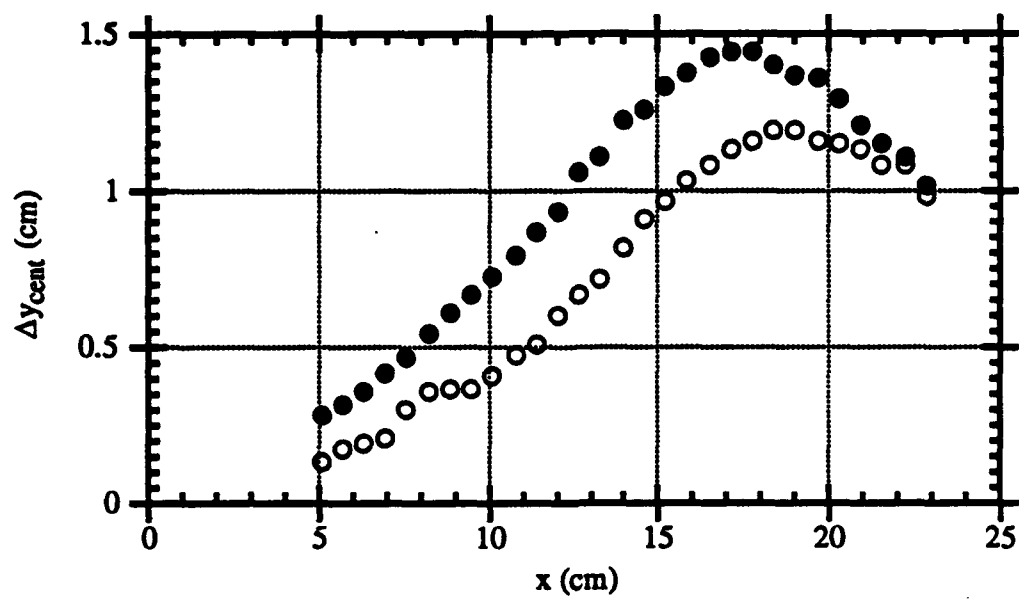
FIGURE 19. $\Delta y_{cent}(x)$ for SP, f = 6 Hz (●) and SP, f = 3.85, 7.7 Hz (○).

occurs because of increased layer width or increased molecular mixing. Figure 20a shows δ(x) for the unforced flow. The layer width increases approximately linearly with downstream distance, reaching a value of 6.3 cm at x= 22.86 cm. Forcing at 6 Hz (figure 20b) has a slight effect on the width of the layer. SU, f = 6 Hz forcing tends to slightly decrease the layer width at the downstream stations. However, its effect on the layer width upstream is minimal. SP, f = 6 Hz forcing increases the layer width. This is expected since the streamwise vortices ride on the outside edges of the primary rollers. Although inducing pairing of the primary vortices by forcing at f = 3.85, 7.7 Hz might be expected to significantly increase the width of the layer, figure 20c shows that this is not the case. Forcing the layer at SU, f = 3.85, 7.7 Hz increases the width of the layer only slightly. In addition, since pairing inhibits the formation of the streamwise vortices, SP, f = 3.85, 7.7 Hz forcing does not significantly enhance the width of the layer at any of the three spanwise positions.

Koochesfahani & MacKinnon (1991) found that most of the increase in mixing in their layer was due to increased layer width. Since forcing does not seem to increase the width of the layer in this case, a different mechanism must be at work. Figure 21a-c shows the mixed fluid fraction for the unforced flow, f = 6 Hz forcing, and f = 3.85, 7.7 Hz forcing, respectively. For the unforced flow (figure 21a), the layer is approximately 5% mixed for x ≤ 10 cm, after which the mixed fluid fraction increases almost linearly to 0.32 at x = 22.86 cm. It is important to note that, since the mixed fluid fraction is *always* ≤ 1.0, this plot implies that mixing transition is not completed by the end of the domain of measurement. Further downstream, it can be expected that the mixed fluid fraction will level off and reach and asymptotic value.

Forcing at SU, f = 6 Hz tends to slightly increase the molecular mixing at all streamwise stations. This may be due to the strong winding of the thin laminar diffusion layers. This increase in molecular mixing accounts for the increase in

mixed fluid at upstream locations when the flow is forced with this waveform. However, further downstream as the growth of the layer is reduced, the overall mixed fluid (and PM) is less than in the unforced case.

For SP, f = 6 Hz forcing, the mixed fluid fraction is highest at 1/2 head-tail. This suggests that as fluid is entrained into the streamwise vortices (which have a small radial dimension than the spanwise vortices) the fluid is mixed immediately. Interestingly, the mixed fluid fraction is lowest at the head of the streamwise vortex, suggesting that there is large amount of additional free-stream fluid entrained at this spanwise position.

Induced pairing due to f = 3.85, 7.7 Hz forcing also increases the level of molecular mixing (figure 21c). However, the high level of the mixed fluid fraction for SU, f = 3.85, 7.7 Hz at streamwise stations upstream of pairing suggests that a significant amount of the increase in mixing in this case may be due to the fundamental f = 7.7 Hz forcing frequency, which results in smaller, more closely-spaced spanwise rollers. This curve begins to level off at x ≈ 15 cm, suggesting a saturation, and then the slope increases slightly as pairing begins. At all streamwise stations, the mixed fluid fraction is significantly higher than that of the unforced flow. Forcing the flow with SP, f = 3.85, 7.7 Hz actually results in *less* molecular mixing for x ≤ 12 cm than the spanwise-uniform case. However, by the downstream locations, the mixed fluid fraction is higher for the spanwise-periodic case.
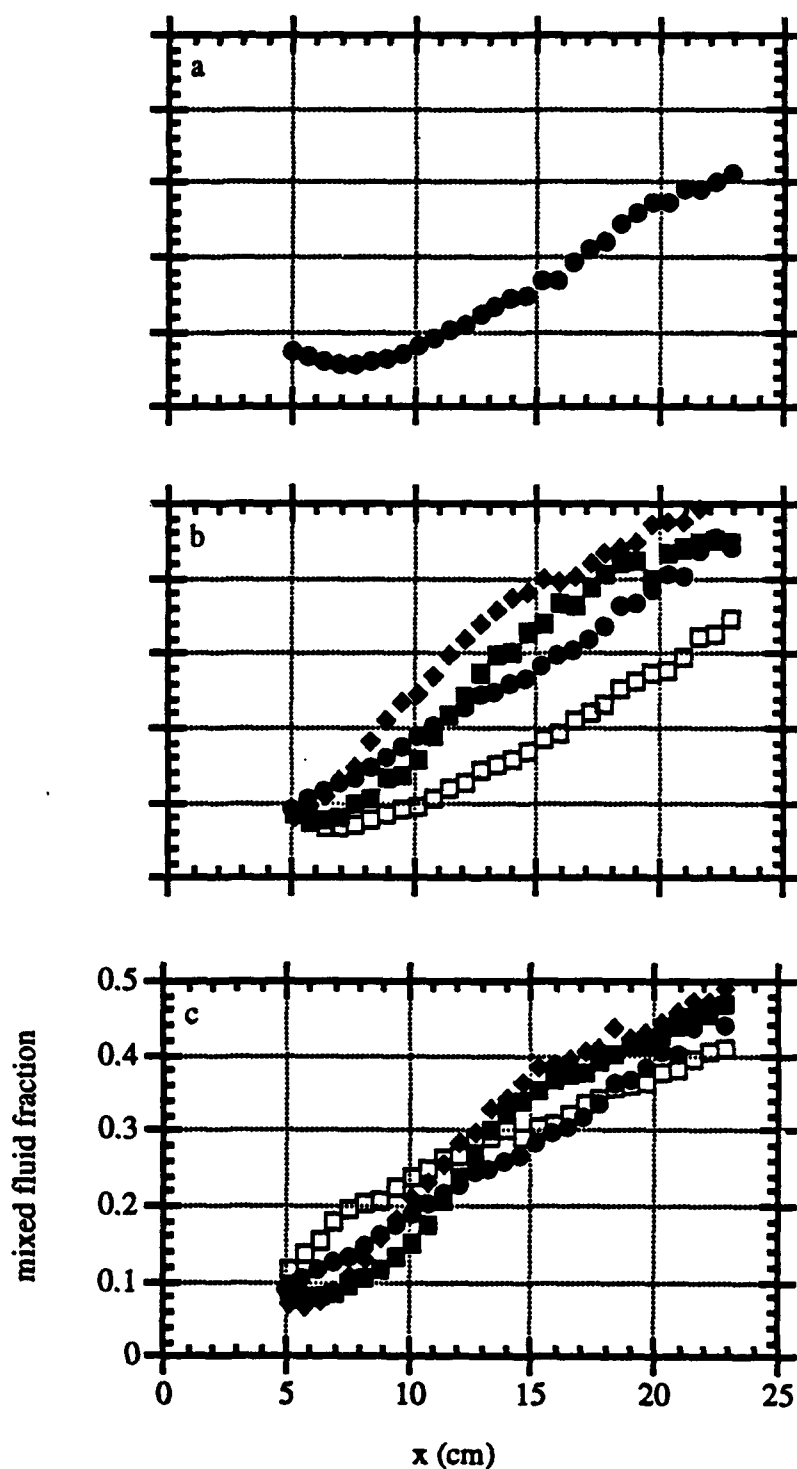
FIGURE 21. (a) mixed fluid fraction for the unforced flow, (b) mixed fluid fraction for SU, f = 6 Hz (□), and SP, f = 6 Hz (head) (●), (tail) (■), and (1/2 head/tail) (◆), (c) mixed fluid fraction for SU, f = 3.85, 7.7 Hz (□), and SP, f = 3.85, 7.7 Hz (head) (●), (tail) (■), and (1/2 head/tail) (◆).

4. Phase-averaged measurements

Given the intermittent nature of the two-dimensional free shear layer, it is clear that mixing in this flow varies significantly with time. The present results demonstrate that most of the mixing occurs within the primary and secondary vortices. Because time-harmonic forcing results in a streamwise domain within which the flow is phase-locked to the forcing signal, it is possible to obtain phase-averaged mixing information which can be directly related to topological features of the vortical structures. In what follows, a comparison is made between forcing configurations SU and SP at f = 6 Hz, as well as SU and SP at f = 3.85, 7.7 Hz. Data is sampled phase-locked to the forcing signal at a sampling rate of 128 points per cycle for the f = 6 Hz cases and at 128 points per low-frequency (3.85 Hz) cycle in the f = 3.85, 7.7 Hz cases. Over 300 cycles are sampled. This data can then be phase-averaged to obtain quantities which are representative of an average cycle of the flow. All phase-averaged quantities are denoted with brackets, i.e. <X(t)> is phase-averaged X(t).

4.1. Phase-averaged mixing

Composites of four pairs (a-d) of grayscale raster images of <T(x,y,t)> and <pm(x,y,t)> for t/T_f = 0, 0.25, 0.5, and 0.75, respectively (T_f is the forcing period) are shown in figures 22a-d and 23a-d for forcing configurations SU and SP (head), respectively, at f = 6 Hz. Each of the phase-averaged plots is synthesized from phase-locked temperature data taken at 29 equally-spaced streamwise stations (5.08 cm $\leq$ x $\leq$ 22.86 cm). The most prominent feature in figures 22 and 23 is that when the shear layer is forced with configuration SP, f = 6

Hz it entrains more fluid from the low-speed stream (at the head), due to the pumping action of the streamwise vortices. This suggests itself as the mechanism by which the peak in $pdf(T,y)$ occurs at higher value of T in the SP cases than in the SU cases.

In the SU configuration, mixing (as measured by the performance measure) first occurs in narrow bands near the perimeter of the primary vortices at $x \approx 13$ cm. The mixing in these regions appears to be connected primarily with stretching of temperature interfaces (figure 22a-d). As the rollup progresses, two larger concentrations (or patches) of mixed fluid appear near the high-and low-speed edges of the primary vortex. The flow undergoes mixing transition when these patches spread towards the centers of the primary vortices ($x \approx 15$ cm) as can be observed on the right hand (downstream) edge of the performance measure plots, particularly figures 22a and 22b. This encroachment of the mixing region towards the cores of the primary vortices is presumably the result of unforced three-dimensional motions. When the flow is subjected to forcing configuration SP, $f = 6$ Hz (figure 23a-d), mixing occurs more rapidly. The performance measure plots show a concentration of mixed fluid near the high-speed side which is where the head of the streamwise vortex forms (figure 23b, $x \approx 9$ cm). This patch of mixed fluid increases in size and migrates towards the center of the primary spanwise vortex as it is advected downstream (figure 23c ($x = 10.5$ cm) and figure 23d ($x = 11.5$ cm)) until (figure 23a ($x = 12.5$ cm)) the entire vortex core consists of mixed fluid.

It is instructive to look at slices of the phase-averaged performance measure $<pm(y,t)>$ for SP, $f = 6$ Hz through the head, tail, and 1/2 head/tail in order to compare it to the case of SU, $f = 6$ Hz. Figure 24a-d shows these cases at $x = 10.16$ cm, 15.24 cm, and 20.32 cm. For the case of SU, $f = 6$ Hz (figure 24a), thin bands of mixed fluid first begin to appear around the cores of the primary vortices at $x =$
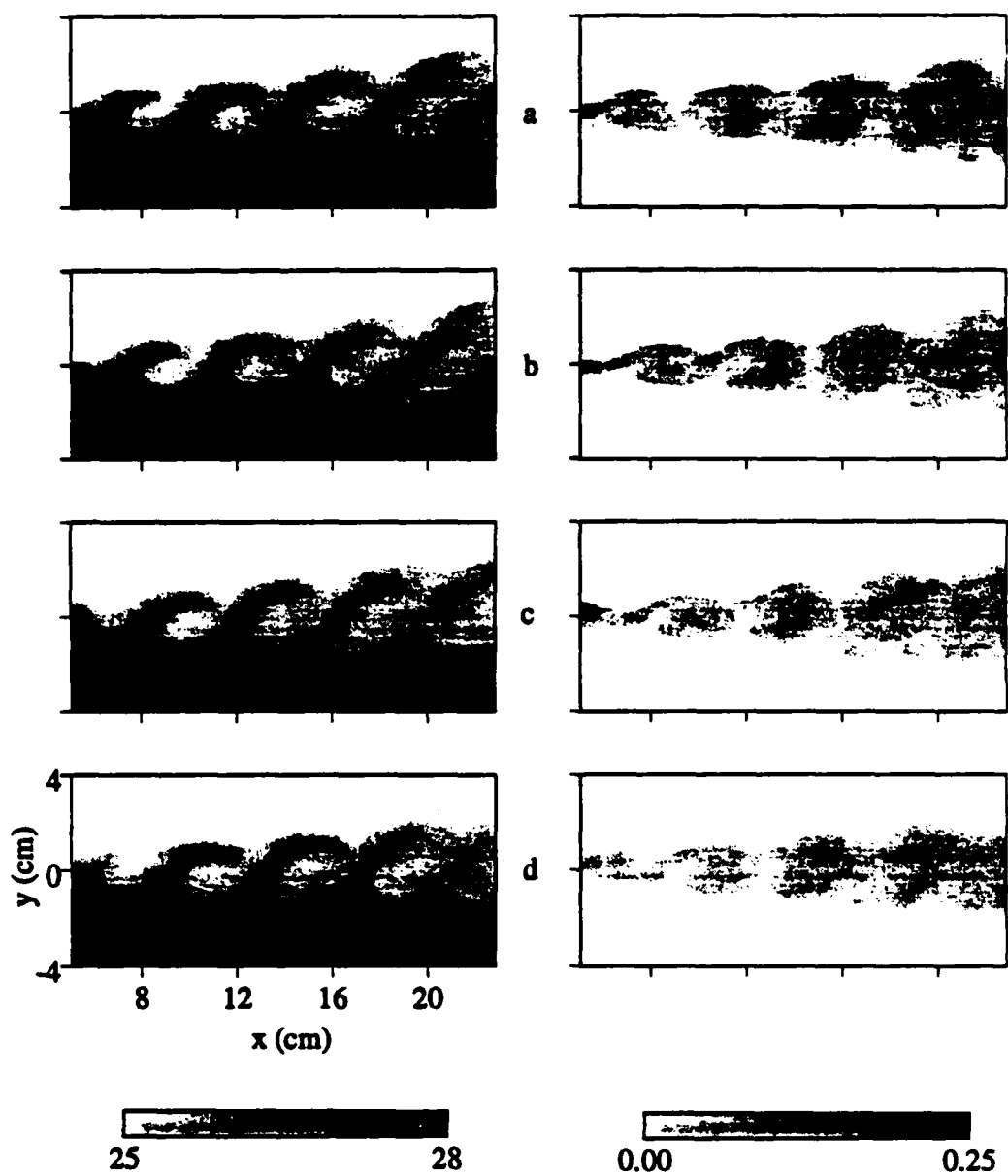
FIGURE 22. $\langle T(x,y,t)\rangle$ and $\langle pm(x,y,t)\rangle$ for SU, f = 6 Hz at times t/T_f = (a) 0.0, (b) 0.25, (c) 0.5, and (d) 0.75.
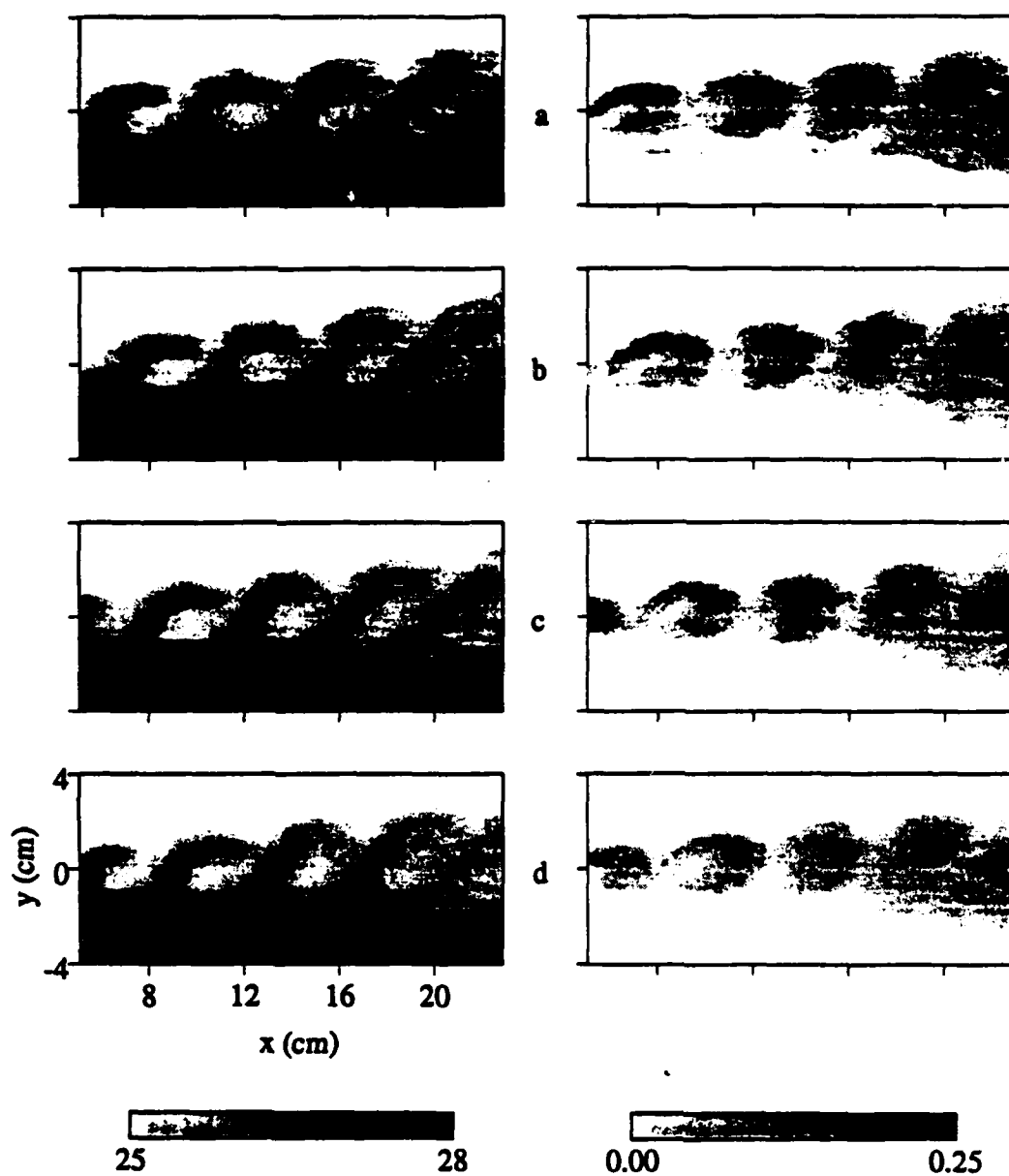
FIGURE 23. $\langle T(x,y,t)\rangle$ and $\langle pm(x,y,t)\rangle$ for SP, $f = 6$ Hz (head) at times $t/T_f = $ (a) 0.0, (b) 0.25, (c) 0.5, and (d) 0.75.
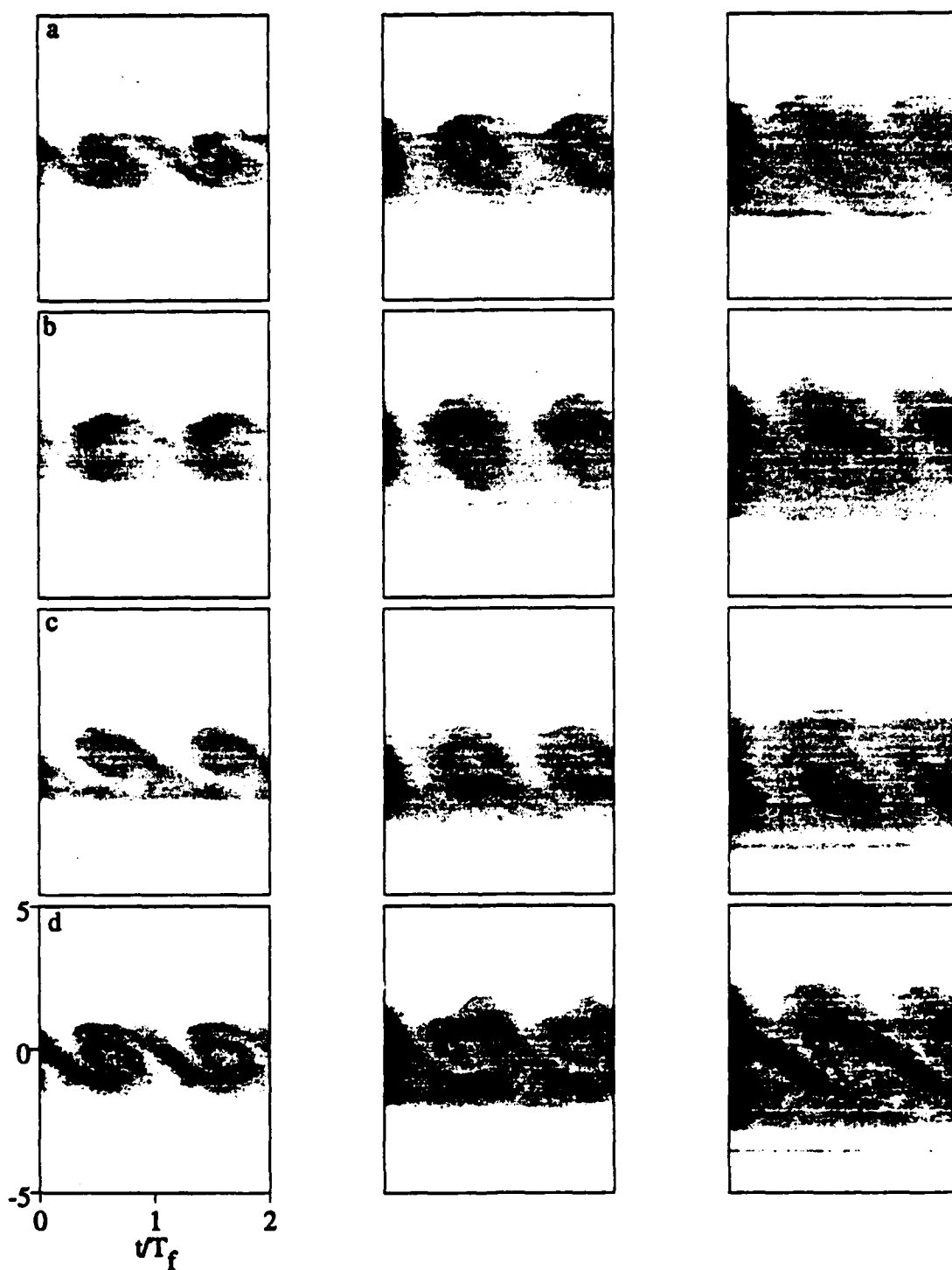
FIGURE 24. <pm(y,t)> at x = 10.16 cm (left), 15.24 cm (center), and 20.32 cm (right) for (a) SU, f = 6 Hz, (b) SP, f = 6 Hz (head), (c) SP, f = 6 Hz (tail), (d) SP, f = 6 Hz (1/2 head/tail).

10.16 cm. By x = 15.24 cm, these bands have converged into two lobes oriented at approximately 135° to the time axis. For the case of SP, f = 6 Hz forcing at the head of the streamwise vortex (figure 24b), there is already a large patch of well-mixed fluid which has formed at approximately 135° relative to the time axis. By x = 15.24 cm, this patch has increased in size until it has filled the cores of the primary vortices. Finally, by x = 20.32 cm, the primary vortices have grown to the point that they have acquired a distinct tilt of 135° relative to the time axis. Again, these structures are filled predominantly with mixed fluid, with a strong concentration at the corresponding location to where the patch of mixed fluid first formed at x = 10.16 cm. At the tail of the streamwise vortex (figure 24c), there is no patch of mixed fluid present at x = 10.16 cm. This is due to the weaker amplification of the streamwise vortices at this spanwise station. However, a large patch of mixed fluid does become apparent near the low-speed side at x = 15.24 cm, and this patch grows to fill much of the layer at x = 20.32 cm. Finally, the slice through 1/2 head/tail (figure 24d) shows that mixed fluid is produced all the way through an oblique slice through a streamwise vortex.

Figures 25a-d and 26a-d show four pairs of grayscale raster images of $<T(x,y,t)>$ and $<(pm(x,y,t)>$ (for t/T_f = 0, 0.25, 0.5, and 0.75, respectively) for the case of controlled pairing in the SU and SP (head) configurations. For the case of SU, f = 3.85, 7.7 Hz (figure 25a-d), the initial passage frequency of the primary vortices is the fundamental forcing frequency 7.7 Hz. At approximately x = 14 cm, the vortices begin to pair (figure 25a). As the upstream vortex resides in higher-speed fluid than the downstream vortex, it begins to overtake and engulf the downstream vortex (figures 25b and 25c). Finally, at x > 20 cm, the spanwise vortices have a passage frequency of 3.85 Hz, the subharmonic forcing frequency. This pairing process is accompanied by an increase in the value of $<pm(x,y,t)>$.

Mixed fluid begins to be formed as the primary vortices pair, i.e. at x ≈ 14 cm in figure 25a. Interestingly, the bulk of the mixed fluid is produced in the downstream vortex as it is being engulfed. This is to be expected since it is the thin laminar sheets in the engulfed vortex which collapse first (i.e., figure 12). As will be shown in §4.3 below, there is an increase in small-scale temperature fluctuations associated with this breakdown.

For the case of SP, f = 3.85, 7.7 Hz (head) (figure 26a-d) the pairing process is similar to the SU case. However, mixed fluid is produced in the induced streamwise vortex, particularly at the head but also in the braids region (figure 26c). This patch of mixed fluid then grows into the core of the primary vortices (figure 26d). As these vortices pair, the two patches of mixed fluid amalgamate and the level of <pm(x,y,t)> increases correspondingly.

Figure 27a-e depicts pairs of <pm(y,t)> for SU, f = 3.85, 7.7 Hz (left) and SP, f = 3.85, 7.7 Hz (right) at x = 10.16 cm, 12.70 cm. 15.24 cm, 17.78 cm, and 20.32 cm, respectively. At x = 10.16 cm (figure 27a) the spanwise rollers are slightly displaced in the cross-stream direction. Note that for the SP case there is more mixed fluid in the streamwise structures (in the braids region) between the two sets of pairing vortices than there is between the pairing vortices themselves. The mixed fluid that is between the two pairing spanwise rollers (and, we conjecture, the streamwise vorticity) is being accumulated into the engulfed roller. This is especially apparent in figure 27b which shows virtually no mixed fluid in the braids region between the pairing rollers; however, there is an intense patch of mixed fluid at the top of the engulfed roller suggesting that the mixed fluid from the braids region now resides there. It is this patch of mixed fluid (as is apparent from figures 27c-e) which accounts for most of the mixing in this forcing configuration. The streamwise vortical structure is absorbed at the head position, thus helping explain why PM(x) is
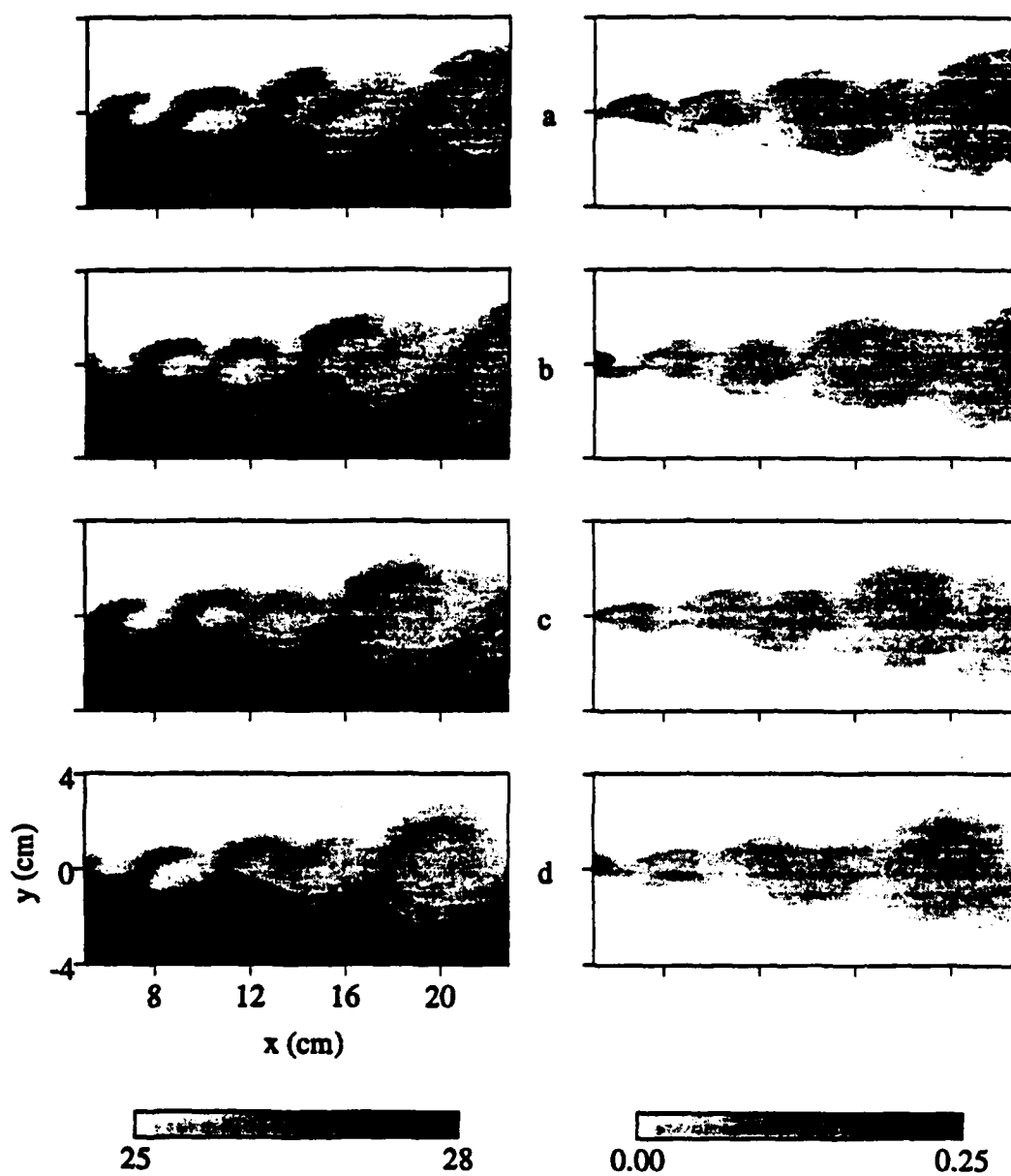
FIGURE 25. <T(x,y,t)> and <pm(x,y,t)> for SU, f = 3.85, 7.7 Hz (head) at times
t/T_f = (a) 0.0, (b) 0.25, (c) 0.5, and (d) 0.75.

FIGURE 26. $\langle T(x,y,t) \rangle$ and $\langle pm(x,y,t) \rangle$ for SP, f = 3.85, 7.7 Hz (head) at times t/T_f = (a) 0.0, (b) 0.25, (c) 0.5, and (d) 0.75.
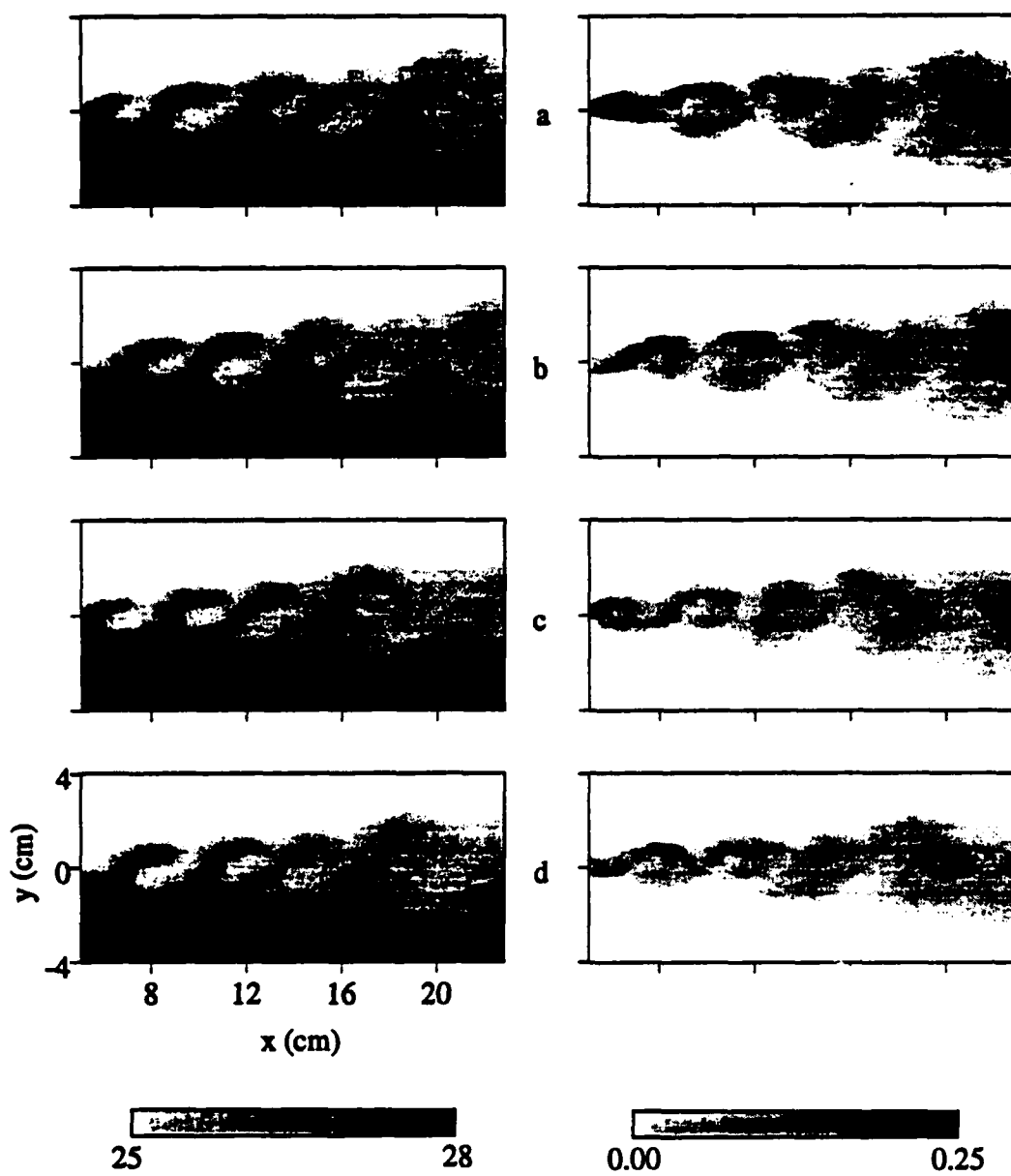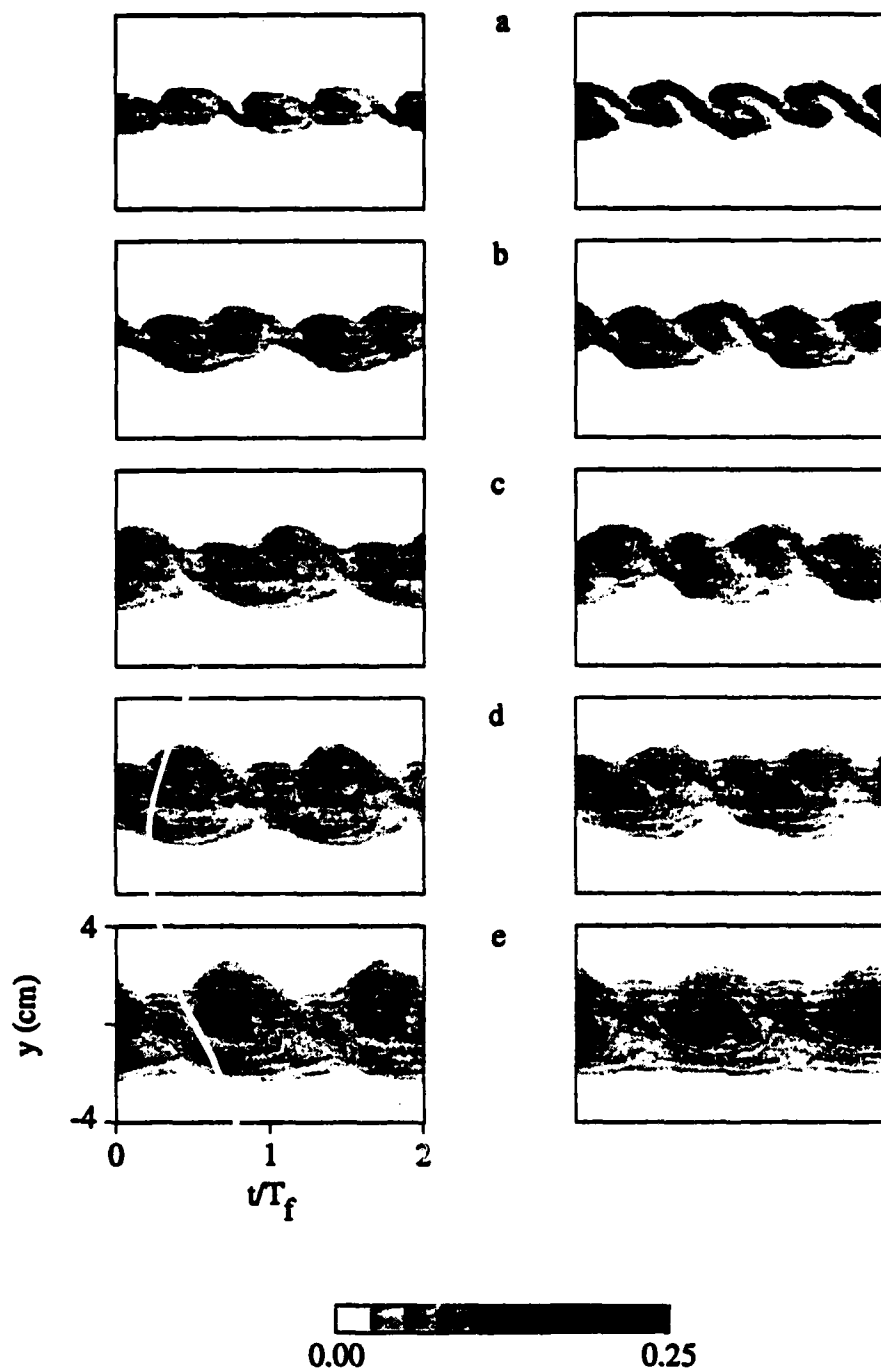
FIGURE 27. <pm(y,t)> for SU, f = 3.85, 7.7 Hz (left) and SP, f = 3.85, 7.7 Hz (right) at x = : (a) at x = 10.16 cm, (b) 12.70 cm, (c) 15.24 cm, (d) 17.78 cm, and (e) 20.32 cm.

significantly higher at upstream locations for SP, f = 3.85, 7.7 Hz (head) than for SP, f = 6 Hz (head) while SP, f = 6 Hz has higher levels of PM at other spanwise positions (see figure 16b-c). Finally, it is important to notice that for both the SU and SP cases, there appears to be an "ejection" of mixed fluid into the braids region after the pairing process is complete (x = 20.32 cm, figure 27e). Moser & Rodgers (1993), among others, have noted an ejection of spanwise vorticity from the vortex cores after pairings. It may be that the re-entry of mixed fluid into the braids region after pairing is a manifestation of the same phenomenon.

The probability density function of temperature can be calculated as a function of phase in the forcing cycle for these forcing configurations. This gives a measure of the composition and total mixed fluid in different parts of the layer. In what follows, the phase-averaged $<pdf(T,y,t)>$ is presented for SU and SP, f = 6 Hz, and SU and SP, f = 3.85, 7.7 Hz. Because of the enormous amount of data required (and the enormous amount of time involved in acquiring it) to produce statistically meaningful pdfs when only 1 of 128 data points can be used for each pdf, only one streamwise station was considered. Because x = 15.24 cm corresponds to a location well within natural mixing transition (figure 16a) and where the primary rollers are beginning to pair when forced with the $f = 3.85$, 7.7 Hz waveforms, this location was used for all the $<pdf(t,y,t)>$ measurements.

Figure 28a-d shows $<pdf(T,y,t)>$ (plotted on the same logarithmic scale as in figures 3 et al) at x = 15.24 cm for $t/T_f = 0.0156$, 0.2656, 0.5156, and 0.7656, respectively, for SU, f = 6 Hz. Grayscale raster images of two cycles of the phase-averaged temperature $<T(y,t)>$ are shown for reference. Times corresponding to contour plots of $<pdf(T,y,t)>$ are indicated by a dark line at the center of each frame of $<(T(y,t)>$. The temperature data $<T(y,t)>$ is shifted in time so that the time of interest is at the center of the grayscale image. For the SU configuration, there is

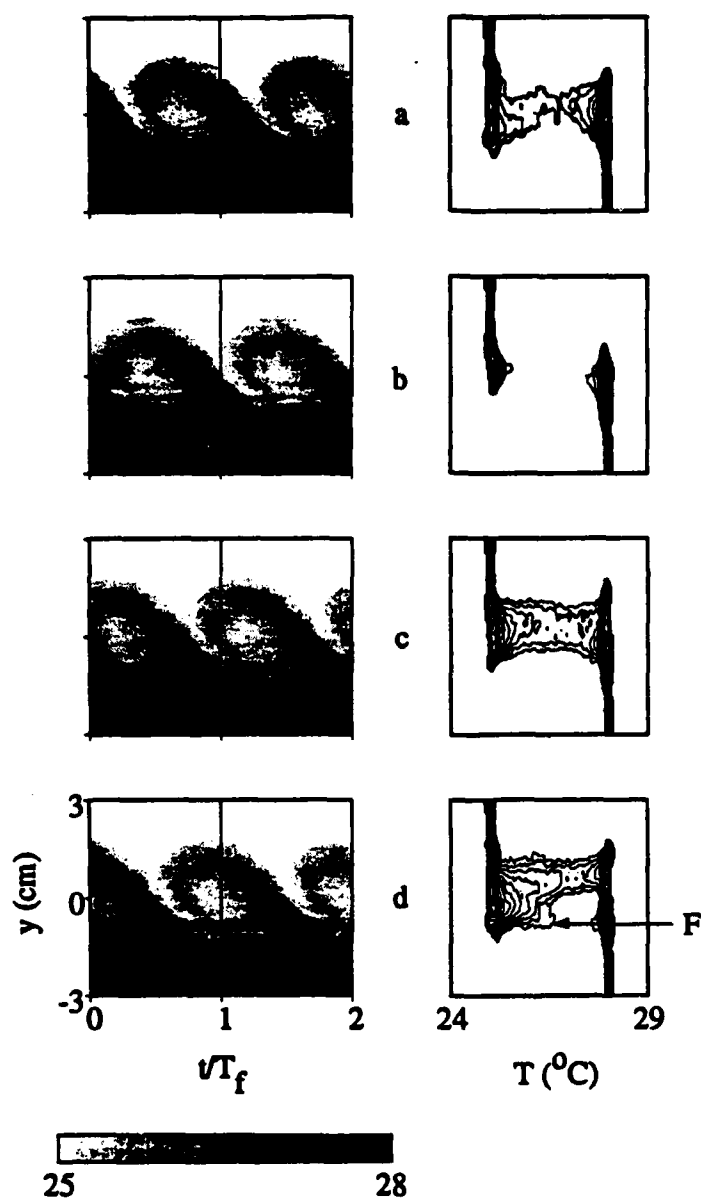FIGURE 28. $<T(y,t)>$ and $<pdf(T,y,t)>$ at $x = 15.24$ cm for SU, $f = 6$ Hz at times $t/T_f = $ (a) 0.0156, (b) 0.2656, (c) 0.5156, and (d) 0.7656.

little mixing within the braids region; mixing is clearly confined to a region within the primary vortex (e.g., compare $t/T_f = 0.7656$ to $t/T_f = 0.2656$). This mixing occurs around the periphery of the spanwise roller due to the collapse of the strained layers. The probability density $<pdf(T,y)>$ at the beginning (figure 28c), through the center (figure 28d), and at the end (figure 28a) of the spanwise roller shows mixed fluid being produced at all temperatures (although weighted towards the high-speed temperature) both at the beginning and the end of the roller. Through the center of the roller, however, there is a fork (denoted "F" in figure 28d) in the pdf corresponding to the mixing zones at the top and the bottom of the roller and the lack of mixing through the center.

In the SP configuration (figure 29) the peak in pdf as a result of the head of the streamwise vortex is visible in figure 29d. There is a large patch of mixed fluid at $y \approx 1.0$ cm at a temperature of 26.4 °C. Clearly the streamwise vortex is responsible for the fluid being mixed at intermediate temperatures in this forcing configuration. Notice also the double-peak structure apparent in pdf in figure 29d. The high temperature peak due to the influence of the streamwise vortex is still present P_2, but there is also a low-temperature peak resulting from the core of the primary vortex P_3. This latter peak is also apparent in the SU, $f = 6$ Hz case (figure 29d).

The probability density function of temperature can also be calculated for configurations SU and SP (head) at $f = 3.85$, 7.7 Hz as a function of phase at a given streamwise station. Figure 30a-h shows $<pdf(T,y,t)>$ at $x = 15.24$ cm for t/T_f = 0.0781, 0.2030, 0.3281, 0.4530, 0.5781, 0.7030, 0.8282, and 0.9530, respectively, for SU, $f = 3.85$, 7.7 Hz. Eight points in phase are shown for these cases instead of four for the previous cases since there are two primary vortices in each cycle of the forcing. Raster plots of two cycles of the phase-averaged temperature $<T(y,t)>$ are shown for reference. Times corresponding to contour plots

of $<pdf(T,y,t)>$ are indicated by a dark line at the center of each frame of $<T(y,t)>$. For the SU configuration, the mixing occurs in the cores of the two pairing primary vortices. In the engulfing vortex (figure 30a-d) a small amount of mixed fluid is produced near the center of the vortex. Notice that the level of mixing $\log_{10}(<pdf(T,y,t)>) \leq -0.6$ [$\log_{10}(^oC^{-1})$] throughout. Also notice that in the braids region between the pairs of pairing spanwise vortices (figures 30d and 30e) there is no mixed fluid apparent. In the engulfed vortex (figures 30f-h) there is significantly more mixed fluid being produced than in the engulfing vortex. For example, in figure 30g $\log_{10}(<pdf(T,y,t)>) \approx -0.4$ [$\log_{10}(^oC^{-1})$] at a cross-stream location corresponding to the center of this vortex. Apparently, then, mixed fluid is produced in the low-speed vortex as it is being engulfed by the high-speed vortex due to the collapse of the laminar layers in the pairing process.

For the case of SP, f = 3.85, 7.7 Hz (head) figure 27 depicted the method by which the streamwise vortex in the braids region between the two pairing rollers was absorbed into the engulfed roller before pairing while the other streamwise vortex strengthened. Thus, in the high-speed vortex (figures 31a-d) there is mixed fluid produced corresponding primarily to the head of the streamwise vortex (figures 31b and c). However, the level of mixing is again quite low: $\log_{10}(<pdf(T,y,t)>) \approx -0.6$ [$\log_{10}^oC^{-1}$]. In the braids region between the pairs of pairing vortices (figures 31d and e), there is a sharp peak in $<pdf(T,y,t)>$ at x = 0.5 cm and T = 26.25 ^oC. This was not the case for SU forcing, and may be attributed to the effect of the streamwise vortices. In the low-speed (engulfed) vortex, there is substantially more mixing than in the high-speed (engulfing) vortex resulting from the increased three-dimensionality due to the absorbed streamwise vortex. At the top of the low-speed vortex (figure 31g) $\log_{10}(<pdf(T,y,t)>) \approx -0.3$ [$\log_{10}(^oC^{-1})$]. In addition, this

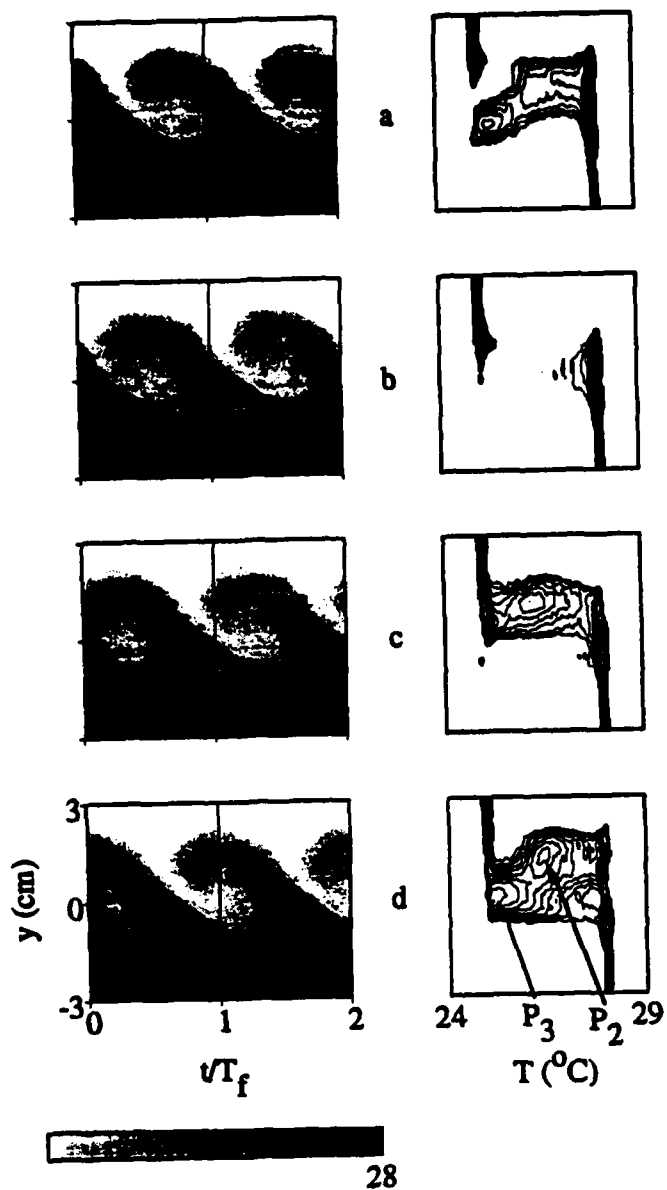peak occurs at a value of T = 26.4 °C, which is almost exactly the mean temperature of the two free streams.

FIGURE 29. $<T(y,t)>$ and $<pdf(T,y,t)>$ at $x = 15.24$ cm for SP, $f = 6$ Hz (head) at times t/T_f = (a) 0.0156, (b) 0.2656, (c) 0.5156, and (d) 0.7656.
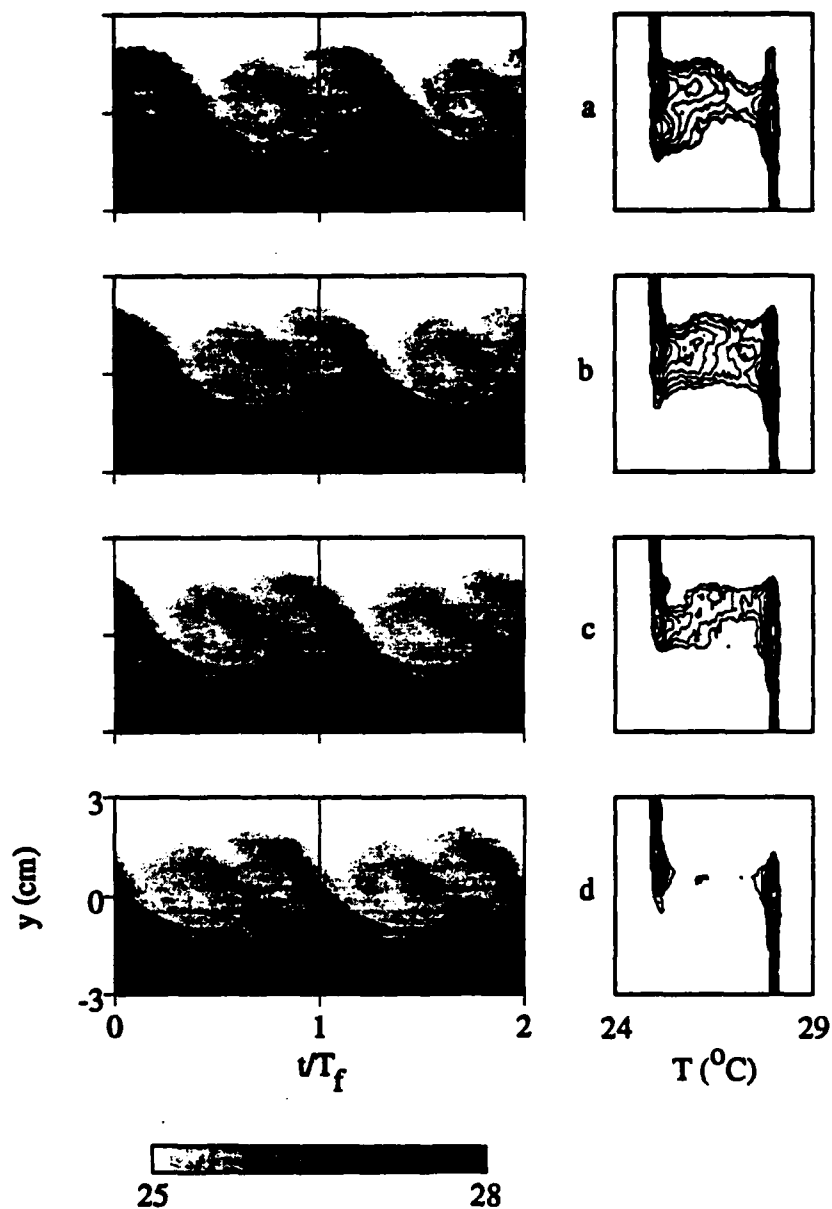
FIGURE 30. $\langle T(y,t)\rangle$ and $\langle pdf(T,y,t)\rangle$ at x = 15.24 cm for SU, f = 3.85, 7.7 Hz at times t/T_f = (a) 0.0781, (b) 0.2030, (c) 0.3281, and (d) 0.4530.
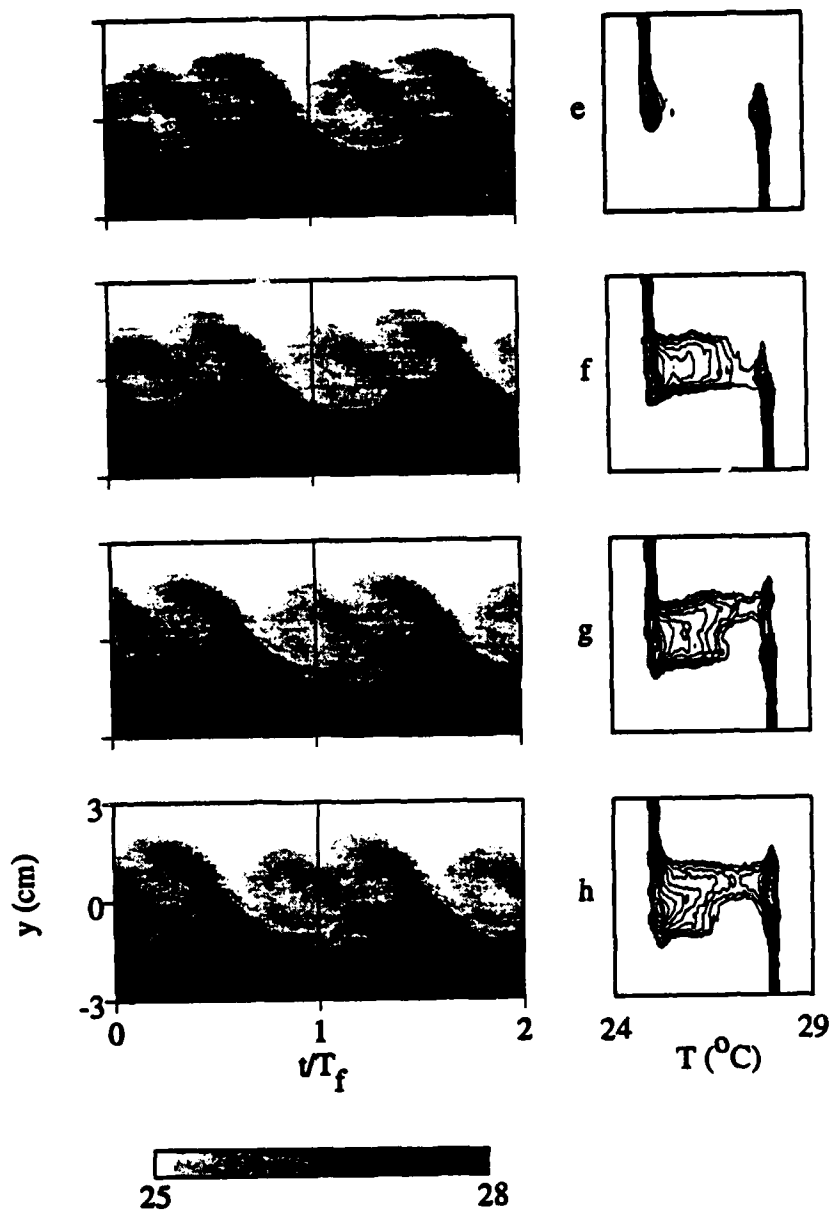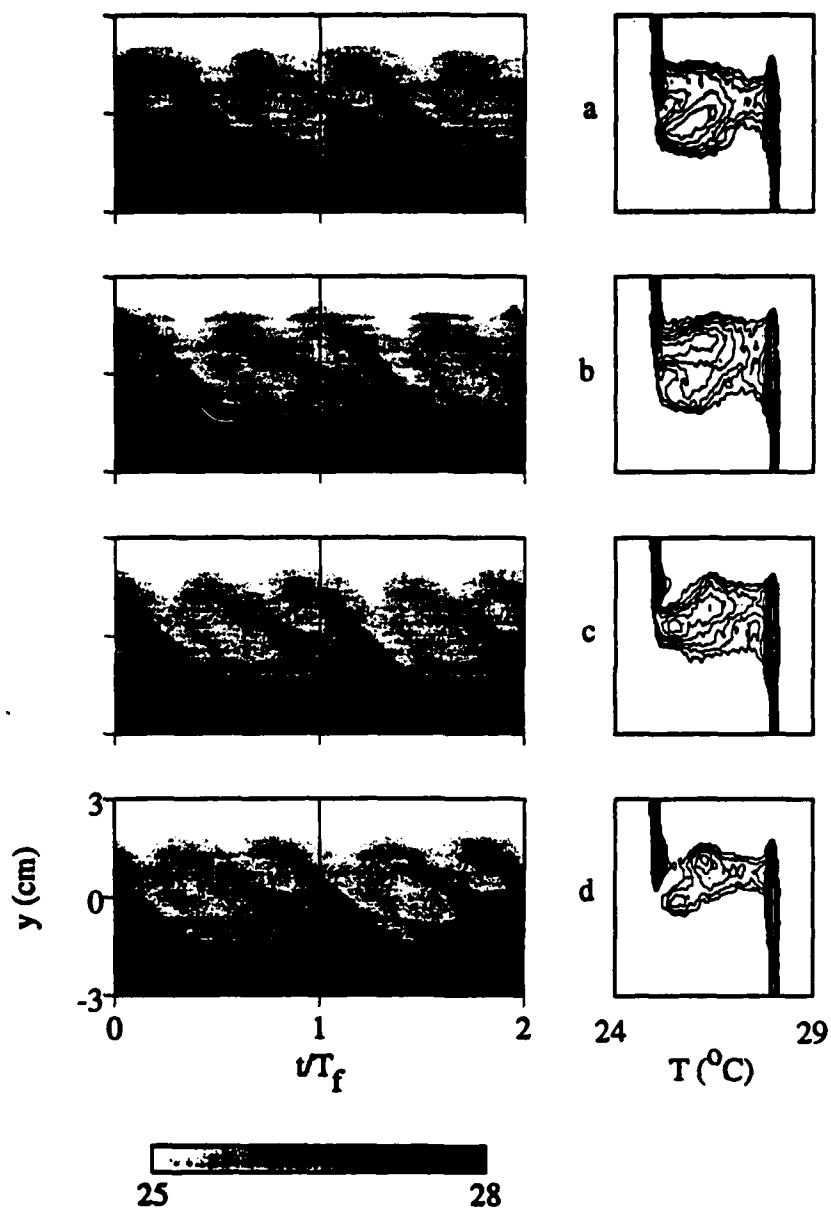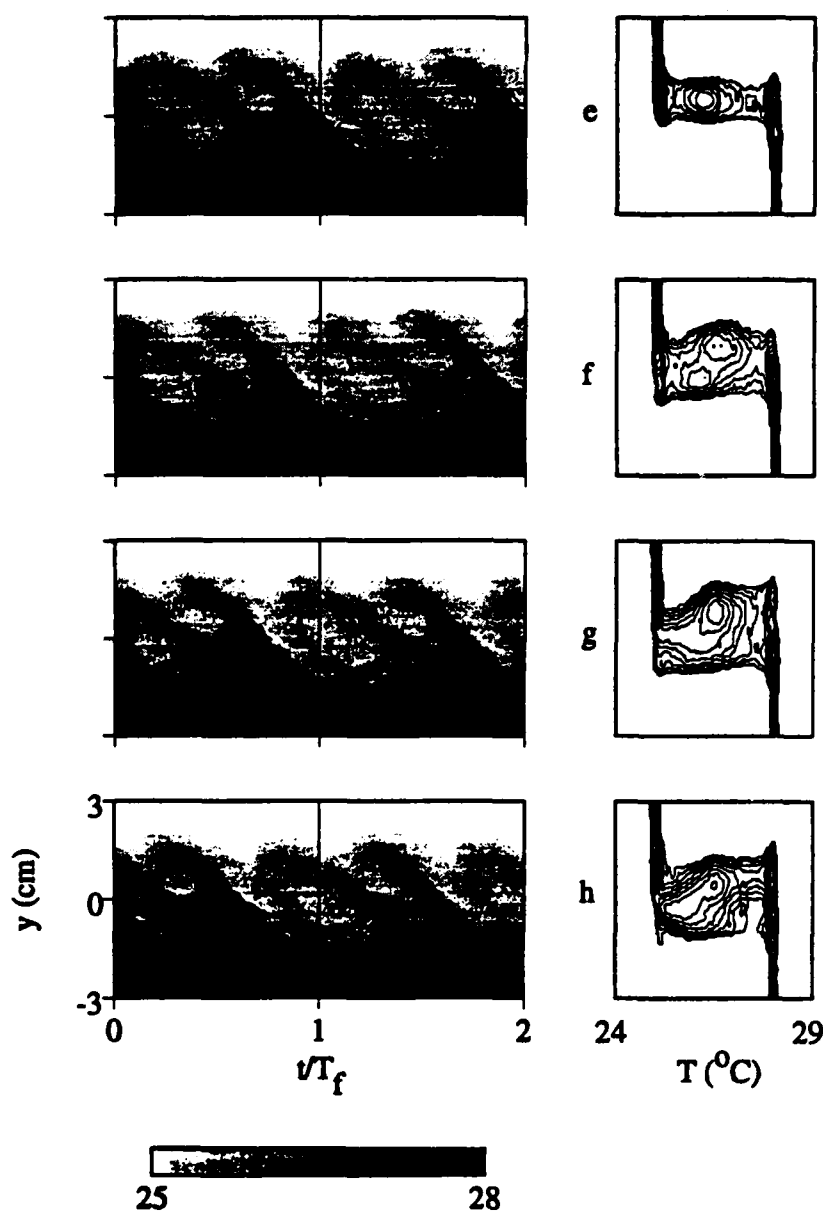
FIGURE 30-*Continued.* $\langle T(y,t)\rangle$ and $\langle pdf(T,y,t)\rangle$ at x = 15.24 cm for SU, f = 3.85, 7.7 Hz at times t/T_f = (e) 0.5781, (f) 0.7030, (g) 0.8281, and (h) 0.9530.

FIGURE 31. $\langle T(y,t)\rangle$ and $\langle pdf(T,y,t)\rangle$ at $x = 15.24$ cm for SP, $f = 3.85, 7.7$ Hz (head) at times $t/T_f =$ (a) 0.0781, (b) 0.2030, (c) 0.3281, and (d) 0.4530.

FIGURE 31-*Continued.* $<T(y,t)>$ and $<pdf(T,y,t)>$ at x = 15.24 cm for SP, f = 3.85, 7.7 Hz (head) at times t/T_f = (e) 0.5781, (f) 0.7030, (g) 0.8281, and (h) 0.9530.

Figures 32-35 show $<T(y,t)>$, $<$mixed fluid(t)$>$, $<T_{cent}(t)>$, $<y_{cent}(t)>$, $<\sigma_y(t)>$, and $<$skew(t)$>$ at x = 15.24 cm. Shown are SU, f = 6 Hz (left) and f = 3.85, 7.7 Hz (right) (figure 32), SP, f = 6 Hz (head) (left) and f = 3.85, 7.7 Hz (head) (right) (figure 33), SP, f = 6 Hz (tail) (left) and f = 3.85, 7.7 Hz (tail) (right) (figure 34), and SP, f = 6 Hz (1/2 head-tail) (left) and f = 3.85, 7.7 Hz (1/2 head-tail) (right) (figure 35).

For SU, f = 6 Hz forcing (figure 32, left), $<$mixed fluid(t)$>$ can be seen to show an almost sinusoidal variation in time, with a maximum level of 1 cm in the cores of the primary vortices and a minimum level of 0.3 cm in the braids region. The maximum in $<T_{cent}(t)>$, however, occurs in the braids region while the minimum occurs in the cores of the primary vortices. Not surprisingly, the maximum in $<\sigma(t)>$ (a measure of the width over which mixing occurs) occurs within the cores of the primary vortices with a minimum in the braids region. The skewness with respect to temperature $<$skew$_T$(t)$>$ shows that in the braids region mixing is quite symmetric ($<$skew$_T$(t)$> \approx 0$). In the cores of the primary vortices, $<$skew$_T$(t)$> \approx 0.4$ as the mixing is skewed towards the concentration of the low-speed stream. For the corresponding pairing case (figure 32 right), the primary difference is that the pairing spanwise vortices (due to the collapse of the laminar diffusion sheets) allow for core mixing to occur relative to braid mixing. Thus, while there is more mixing in the cores (figure 32b, right) there is less in the braids region. It is also important to note that the level of $<$mixed fluid(t)$>$ is greater at the time corresponding to the low speed, engulfed vortex than the high speed, engulfing vortex. In addition, $<T_{cent}(t)>$ is lower at all points in phase than the SU, f = 6 Hz case while $<$skew$_T$(t)$>$ is higher, indicating more mixing at lower temperatures and longer tails into higher temperatures. This is ostensibly a result of the increased core mixing relative to braid ("flame sheet") mixing. Finally, there is an increased
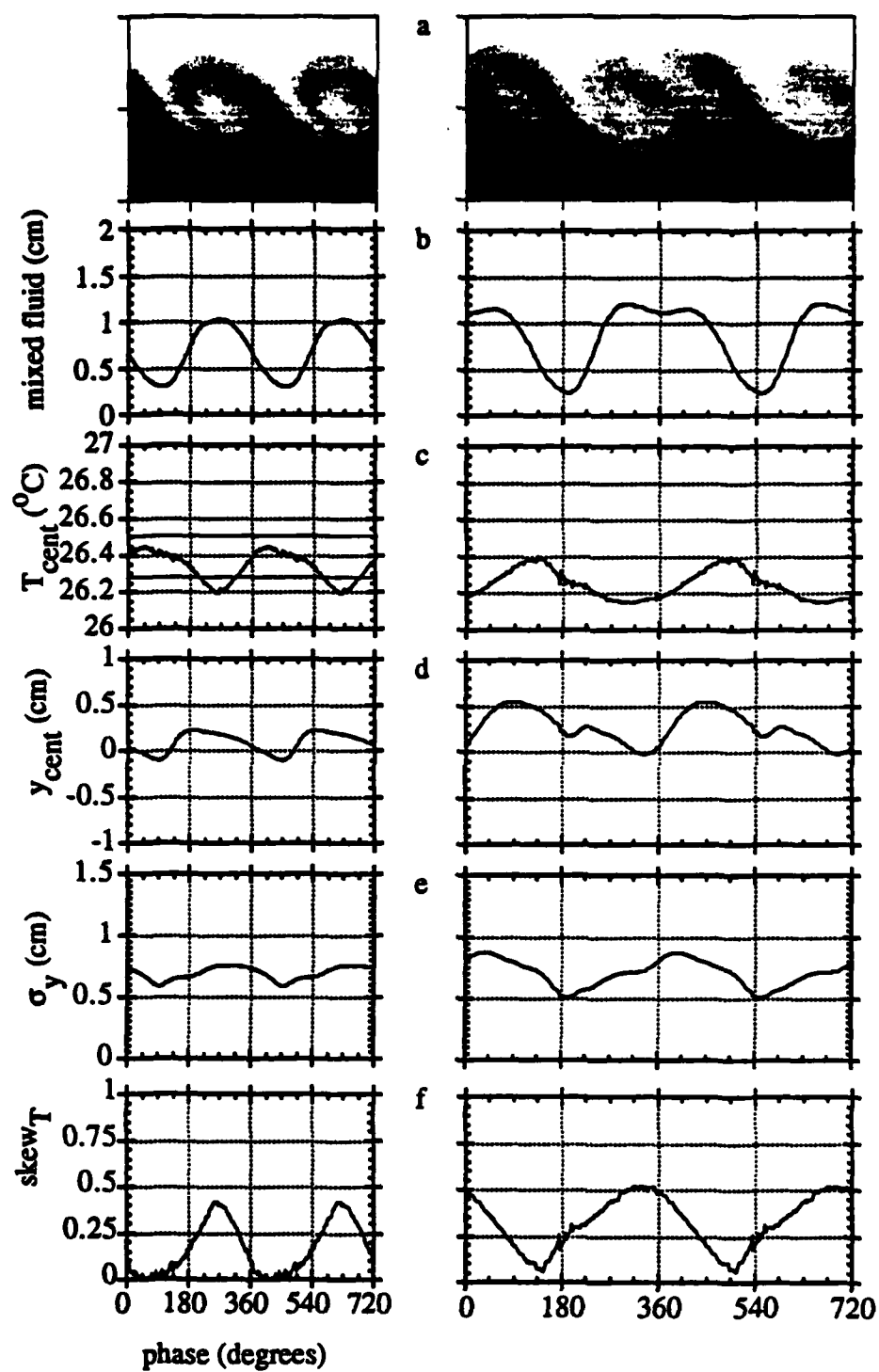
FIGURE 32. (a) <*T*(y,t)>, (b) <mixed fluid(t)>, (c) <*T*cent(t)>, (d) <ycent(t)>, (e) σy(t), and (f) <skewT(t)> for SU, f = 6 Hz (left) and SU, f = 3.85, 7.7 Hz (right).

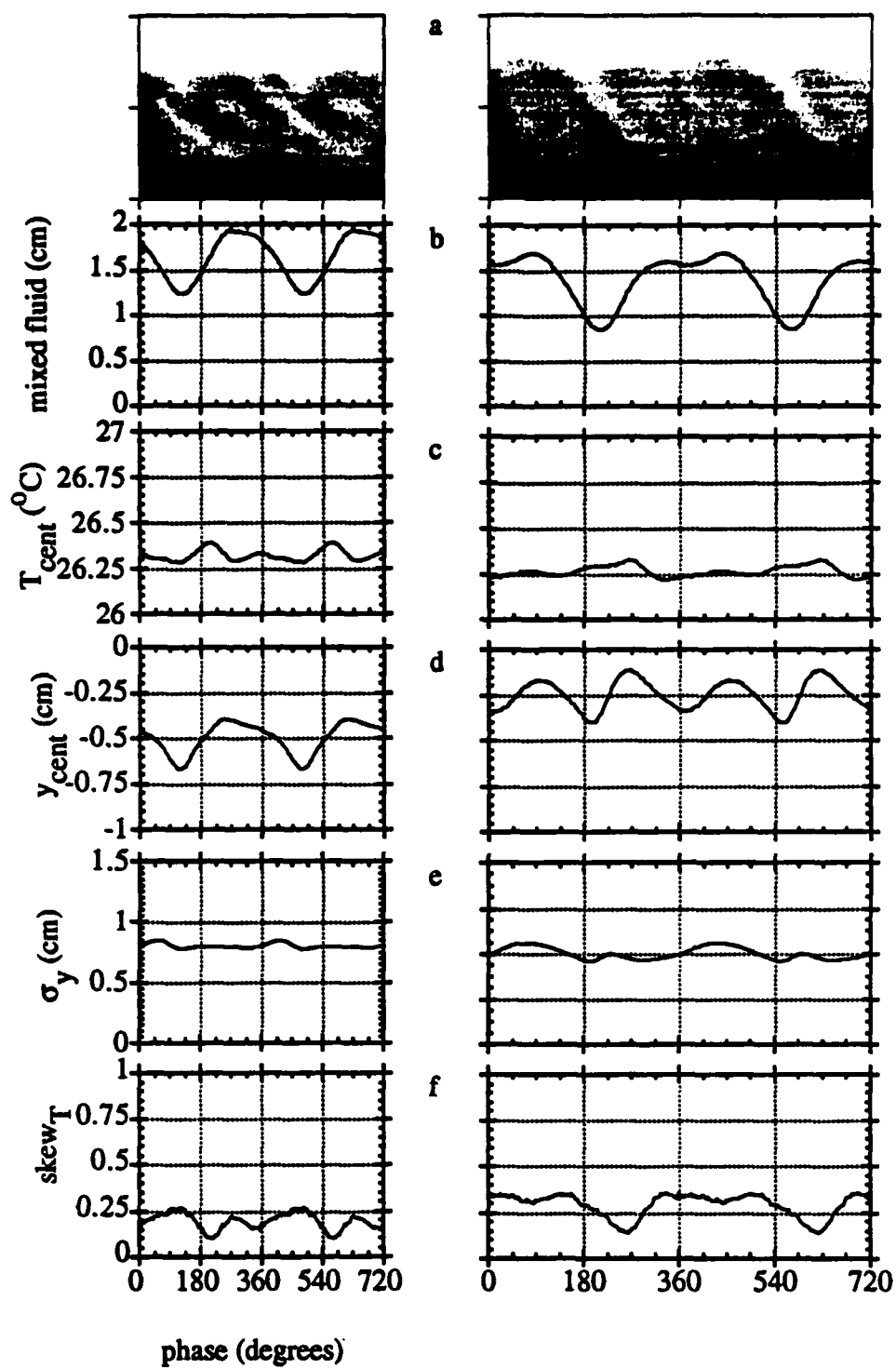FIGURE 33. (a) $\langle T(y,t)\rangle$, (b) $\langle$mixed fluid(t)$\rangle$, (c) $\langle T_{cent}(t)\rangle$, (d) $\langle y_{cent}(t)\rangle$, (e) $\sigma_y(t)$, and (f) $\langle skew_T(t)\rangle$ for SP, f = 6 Hz (head) (left) and SP, f = 3.85, 7.7 Hz (head) (right).

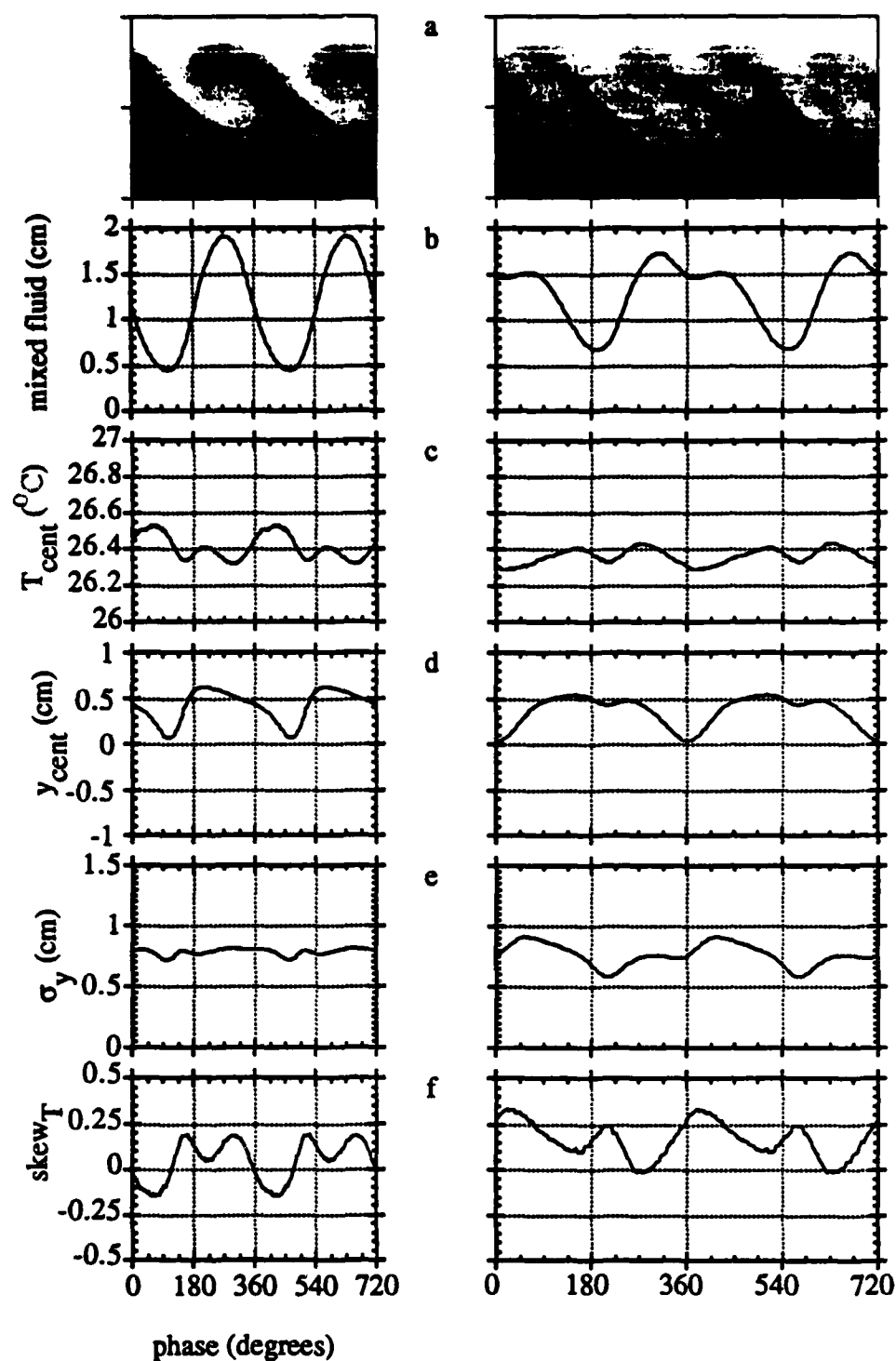FIGURE 34. (a) $<T(y,t)>$, (b) $<$mixed fluid(t)$>$, (c) $<T_{cent}(t)>$, (d) $<y_{cent}(t)>$, (e) $\sigma_y(t)$, and (f) $<skew_T(t)>$ for SP, f = 6 Hz (tail) (left) and SP, f = 3.85, 7.7 Hz (tail) (right).
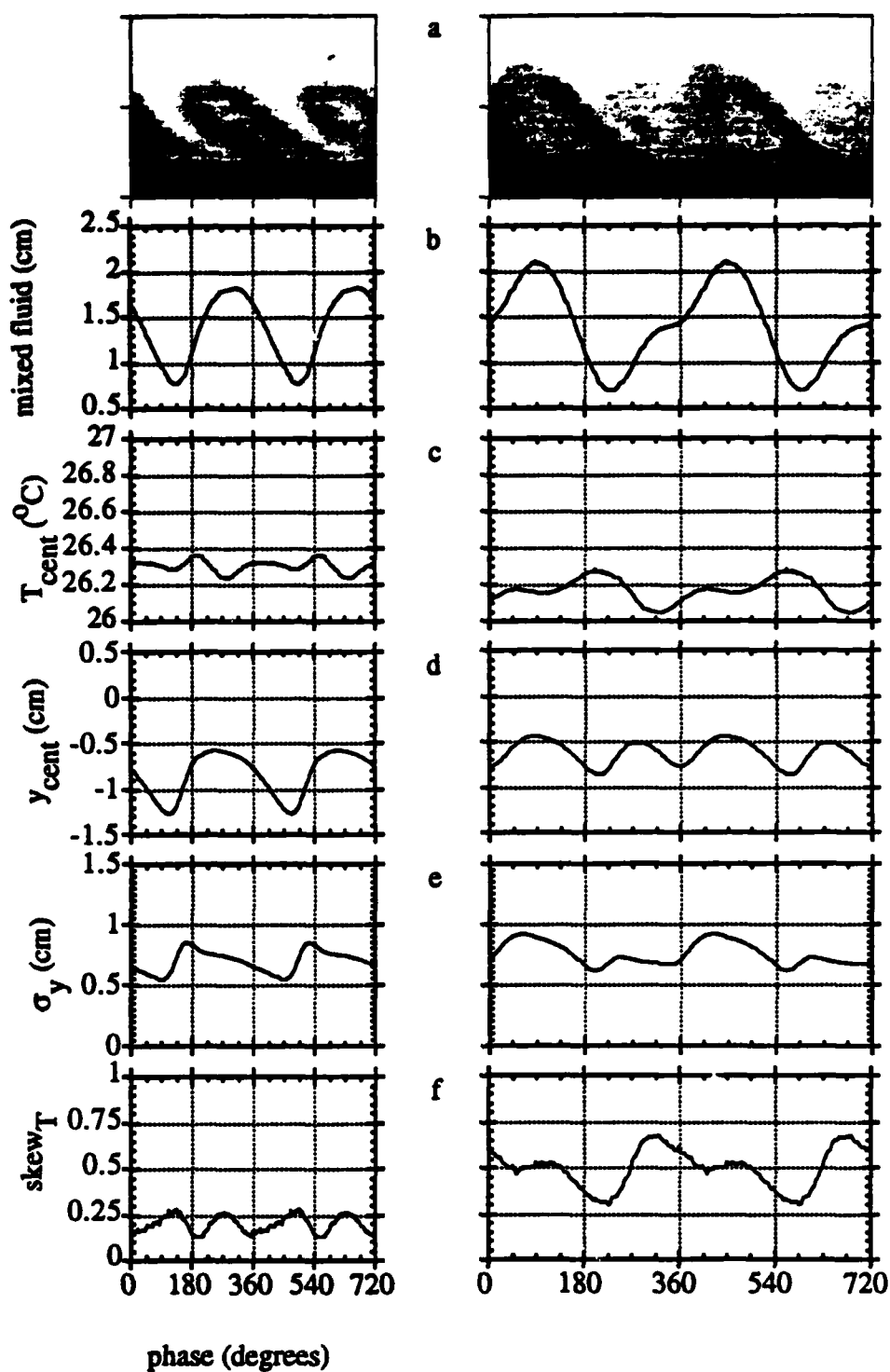
FIGURE 35. (a) $\langle T(y,t)\rangle$, (b) $\langle$mixed fluid(t)$\rangle$, (c) $\langle T_{cent}(t)\rangle$, (d) $\langle y_{cent}(t)\rangle$, (e) $\sigma_y(t)$, and (f) $\langle$skew$_T(t)\rangle$ for SP, f = 6 Hz (1/2 head-tail) (left) and SP, f = 3.85, 7.7 Hz (1/2 head-tail) (right).

variation in $<\sigma_y(t)>$ relative to the nonpairing case. This may be explained by the fact that, after pairing, the proportion of vortical fluid in the layer decreases (the area doubles, hence the radial dimension of the paired vortex increases by $2^{1/2}$; however, the spacing between the vortices doubles). Thus, the region over which mixing occurs should be lower in the braids after pairing and higher in the cores.

The effects of spanwise-periodic forcing are assessed in figures 33-35 at spanwise positions corresponding to the head, the tail, and 1/2 head tail, respectively. At the head, the peaks in <mixed fluid(t)> occur at approximately the same points in phase as in the SU case. The peaks corresponding to the centers of the spanwise vortices occur at a higher level, however. As has been previously noted, the effect of streamwise vortices on mixing is less in the presence of pairing. For example, introducing the streamwise vortices increases the maximum value of <mixed fluid(t)> from approximately 1 cm to 1.9 cm in the single frequency case. In the pairing case, however, the peak corresponding to the engulfed vortex increases from 1.2 cm to 1.7 cm, while the peak in the high-speed engulfing vortex increases from 1.15 cm to 1.55 cm. As can be seen from the three spanwise positions, the greatest increase in mixing is attributable to the effects of the streamwise vortices between the pairing spanwise vortices. This may seem counterintuitive, as these streamwise vortices are being compressed rather than stretched, however, it can be argued that the mixed fluid within the cores of these streamwise vortices is being concentrated in patches of smaller streamwise extent. Hence, the largest peak in <mixed fluid(t)> occurs at times corresponding to the engulfed vortex (at the head) and the engulfing vortex (at the tail). This is consistent with the idea that large patches of mixed fluid are being produced in the compressed streamwise vortices

(which have their heads on the engulfed vortex and their tails under the engulfing vortex).

The effect of the streamwise vortices is to increase $<T_{cent}(t)>$ at the head of the streamwise vortex and lower $<T_{cent}(t)>$ at the tail. An additional trend is that, whereas in the SU case the maximum in $<$mixed fluid$(t)>$ roughly corresponded to a minimum in $<T_{cent}(t)>$, this is not the case when the flow is forced with SP, $f = 6$ Hz or SP, $f = 3.85, 7.7$ Hz. Indeed, a secondary maximum can be seen in $<T_{cent}(t)>$ at the center of the spanwise vortex, corresponding time of maximum mixing. This is a direct result of the more symmetric entrainment by the streamwise vortex. This feature is also apparent in $<T_{cent}(t)>$ for SP, $f = 3.85, 7.7$ Hz (head), as well as the corresponding plots at the tails of the streamwise vortices. At 1/2 head-tail (figure 35c), there are large flat regions in $<T_{cent}(t)>$ owing to the uniform mixed temperature within the slice through the streamwise vortex.

Finally, the plots of $<\sigma_y(t)>$ show trends quite dependent on spanwise position. There is very little variation in $<\sigma_y(t)>$ at the 1/2 head-tail for either SP, $f = 6$ Hz or SP, $f = 3.85, 7.7$ Hz. However, at the tail of the streamwise vortex, there are strong variations. This may be attributed to the increased entrainment asymmetry at this spanwise location; hence most of the layer is unmixed, high-speed fluid.

4.3. Composition of mixed fluid

It is instructive to consider the average temperature of mixed fluid as a function of streamwise position and forcing waveform. The average composition of mixed fluid may be equally as important as the amount of mixed fluid from the point of view of combustion and other chemical reactions where precise stoichiometry is required. In this section, the average temperature of mixed fluid is calculated as follows:

$$T_{mixed}(y) = \frac{\int_{T_1+\epsilon}^{T_2-\epsilon} T pdf(T,y) \, dT}{\int_{T_1+\epsilon}^{T_2-\epsilon} pdf(T,y) \, dT}$$

for

$$\int_{T_1+\epsilon}^{T_2-\epsilon} T pdf(T,y) \, dT \geq 0.1.$$

Importantly, $T_{mixed}(y) \neq T(y)$ since pure unmixed fluid from the free streams is not considered in the average. Note that this provides a convenient way of checking the existence of "marching" *pdfs*, over which there has been much debate (i.e., Batt 1977 (marching), Konrad 1976 (non-marching)). Also, results can be compared with the numerical results of Park, Metcalfe, & Hussain (1994) as well as the experimental research of Konrad (1976) and Koochesfahani & Dimotakis (1986).

Figure 36a-c shows T_{mixed} for the unforced flow at x = 10.16 cm, 15.24 cm, and 20.32 cm. The average temperature profile T(y) is shown for comparison. For the unforced flow, the profile of T_{mixed} shows little variation with cross-stream position. Indeed, there is a slight tendency for the minimum value of T_{mixed} to occur near the center of the layer with slightly higher values toward the outside edges. The minimal variation is similar to that found by Konrad (1976) in a gas layer and Koochesfahani & Dimotakis (1986) in a liquid layer, but unlike that of Batt's (1977) gas layer.

Figure 37a-c shows pairs of T_{mixed} for SU, f = 6 Hz (left) and SU, f = 3.85, 7.7 Hz (right) at x = 10.16 cm, 15.24 cm, and 20.32 cm. The composition for SU, f = 6 Hz is virtually the same as that for the unforced flow at all three streamwise
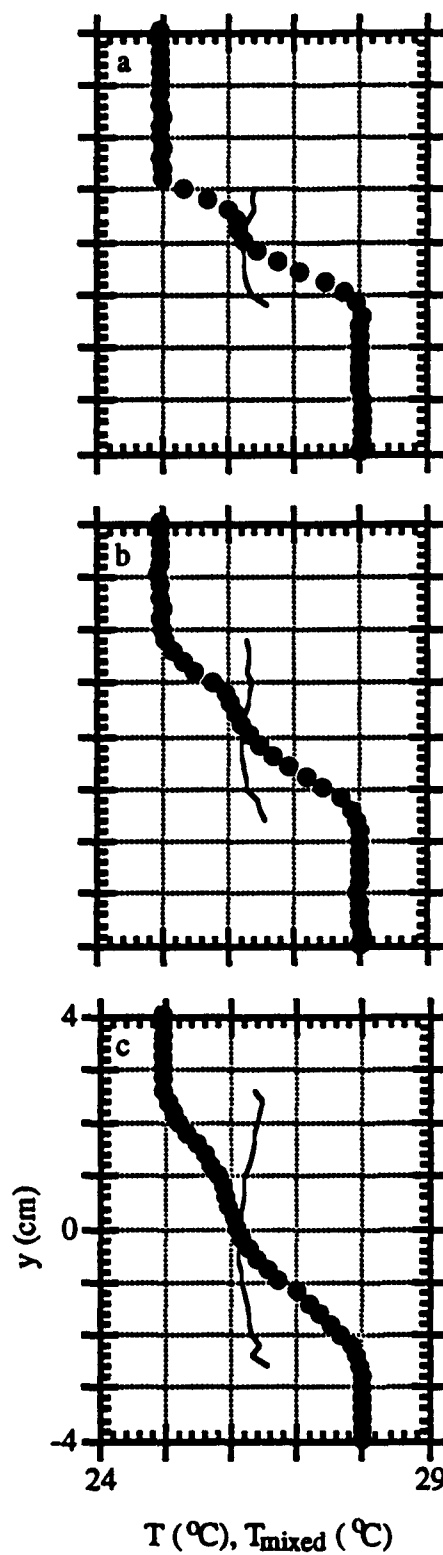
FIGURE 36. $T_{mixed}(y)$ (—) and $T(y)$ (●) for the unforced flow at x = : (a) 10.16 cm, (b) 15.24 cm, and (c) 20.32 cm.
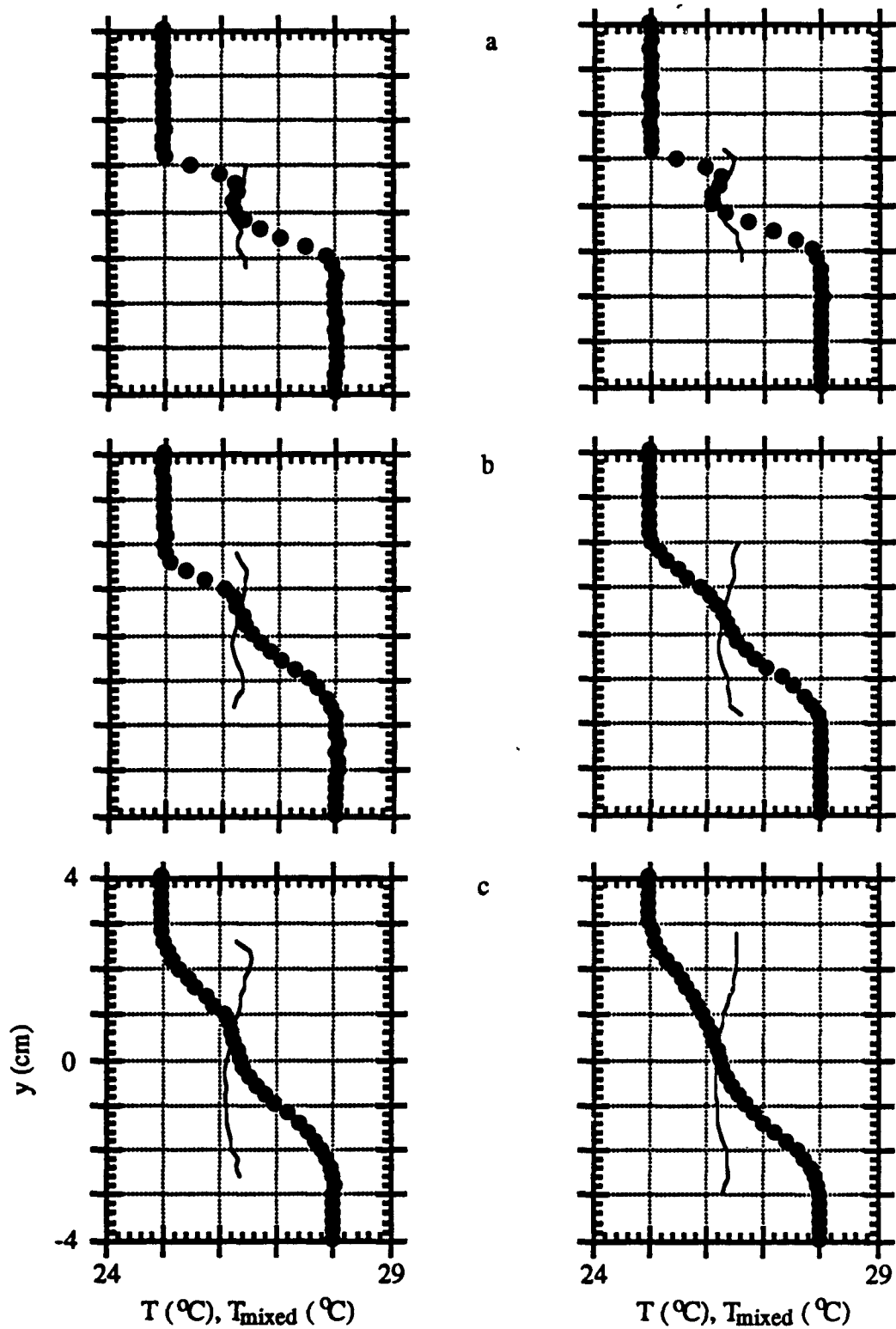
FIGURE 37. Pairs of $T_{mixed}(y)$ (—) and $T(y)$ (•) for SU, f = 6 Hz (left) and SU, f = 3.85, 7.7 Hz (right) at x = : (a) 10.16 cm, (b) 15.24 cm, and (c) 20.32 cm.

stations. By contrast, T_{mixed} for SU, f = 3.85, 7.7 Hz shows that the average temperature of mixed fluid is slightly warmer than the unforced flow, particularly near the low-speed side of the layer at x = 10.16 cm and near the high-speed side of the layer at x = 15.24 cm and x = 20.32 cm. This is consistent with the plot of T_{cent} (figure 18) which showed that T_{cent} was ~0.1 °C warmer for SU, f = 3.85, 7.7 Hz than for the unforced flow.

Figures 38a-c, 39a-c, and 40a-c show pairs of T_{mixed} for SP, f = 6 Hz (left) and SP, f = 3.85, 7.7 Hz (right) at the head, the tail, and 1/2 head-tail, respectively. The effect of the streamwise vortices is to reduce the cross-stream homogeneity of the T_{mixed} profiles. These profiles are all quite interesting, particularly the ones at x = 10.16 cm. At the head of the streamwise vortex (figure 38), the profiles for both the single-frequency case and the two-frequency case show a zig-zag profile which has a maximum temperature towards the high-speed (low-temperature) side of the layer, and a minimum towards the low-speed (high-temperature) side of the layer. This may be attributed to the pumping action of the streamwise vortices which brings hot fluid into the layer at the head. At x = 15.24 both the single-frequency and the two-frequency case have T_{mixed} profiles which show increases in mixed fluid temperature towards the head of the streamwise vortex, while at x = 20.32 cm downstream, this effect has spread throughout the layer. At the tail of the streamwise vortex (figure 39a-c), there are sharp bends in the T_{mixed} profile at x = 10.16 cm. At the two downstream locations, the bend has straightened out considerable. However, in contrast to the other T_{mixed} profiles, the profile is considerable tilted in the direction of the mean temperature gradient. For example, at x = 20.32 cm (figure 39c), $T_{mixed} \approx 26$ °C at the high-speed side of the layer for both SP, f = 6 Hz and SP, f = 3.85, 7.7 Hz. At the low-speed side of the layer, $T_{mixed} \approx 26.5$ °C. Finally, at 1/2 head-tail (figure 40a-c), both forcing schemes result in a relatively flat
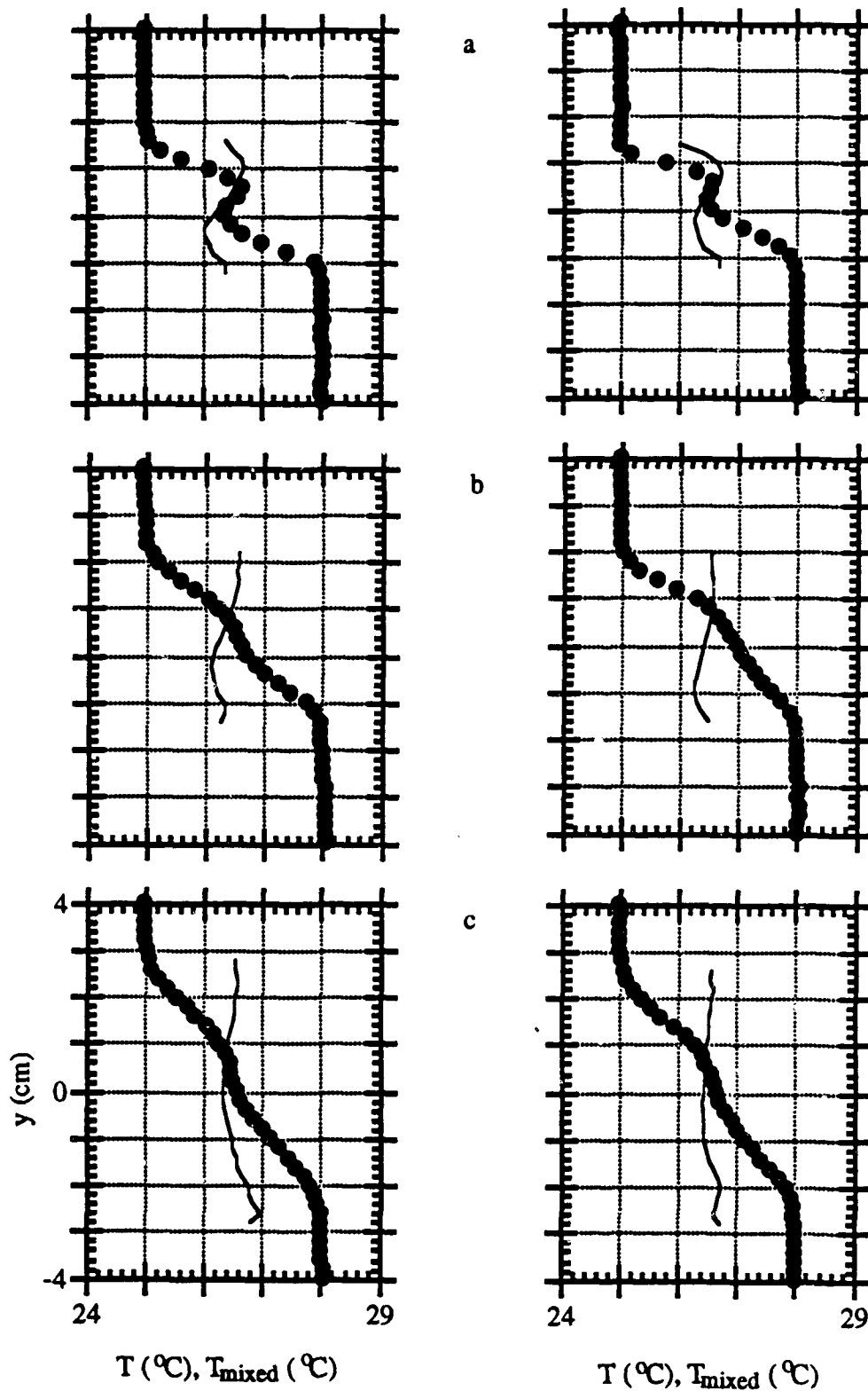
FIGURE 38. Pairs of $T_{mixed}(y)$ (—) and $T(y)$ (•) for SP, f = 6 Hz (head) (left) and SP, f = 3.85, 7.7 Hz (head) (right) at x = : (a) 10.16 cm, (b) 15.24 cm, and (c) 20.32 cm.
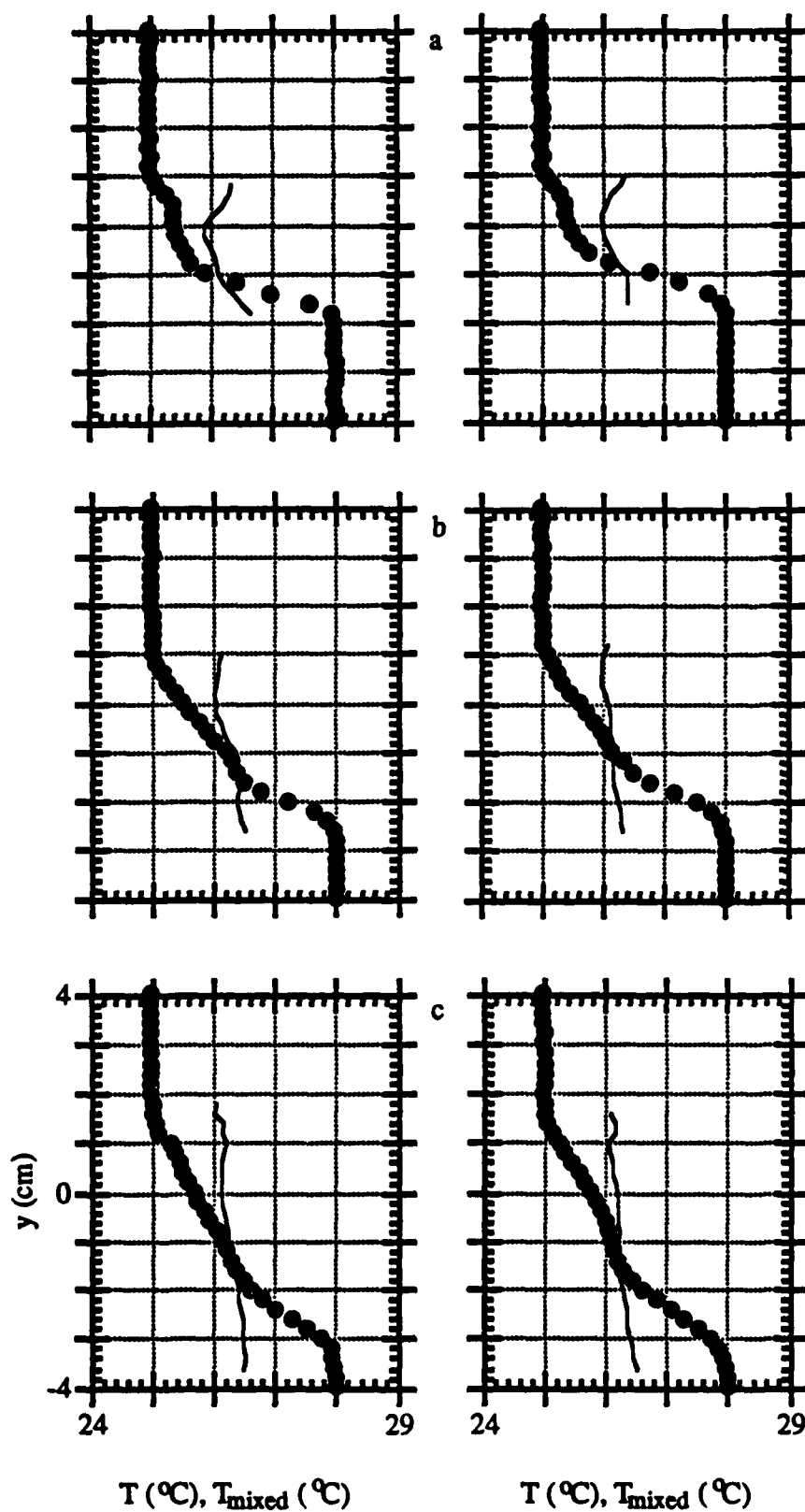
FIGURE 39. Pairs of $T_{mixed}(y)$ (—) and $T(y)$ (•) for SP, f = 6 Hz (tail) (left) and SP, f = 3.85, 7.7 Hz (tail) (right) at x = : (a) 10.16 cm, (b) 15.24 cm, and (c) 20.32 cm.
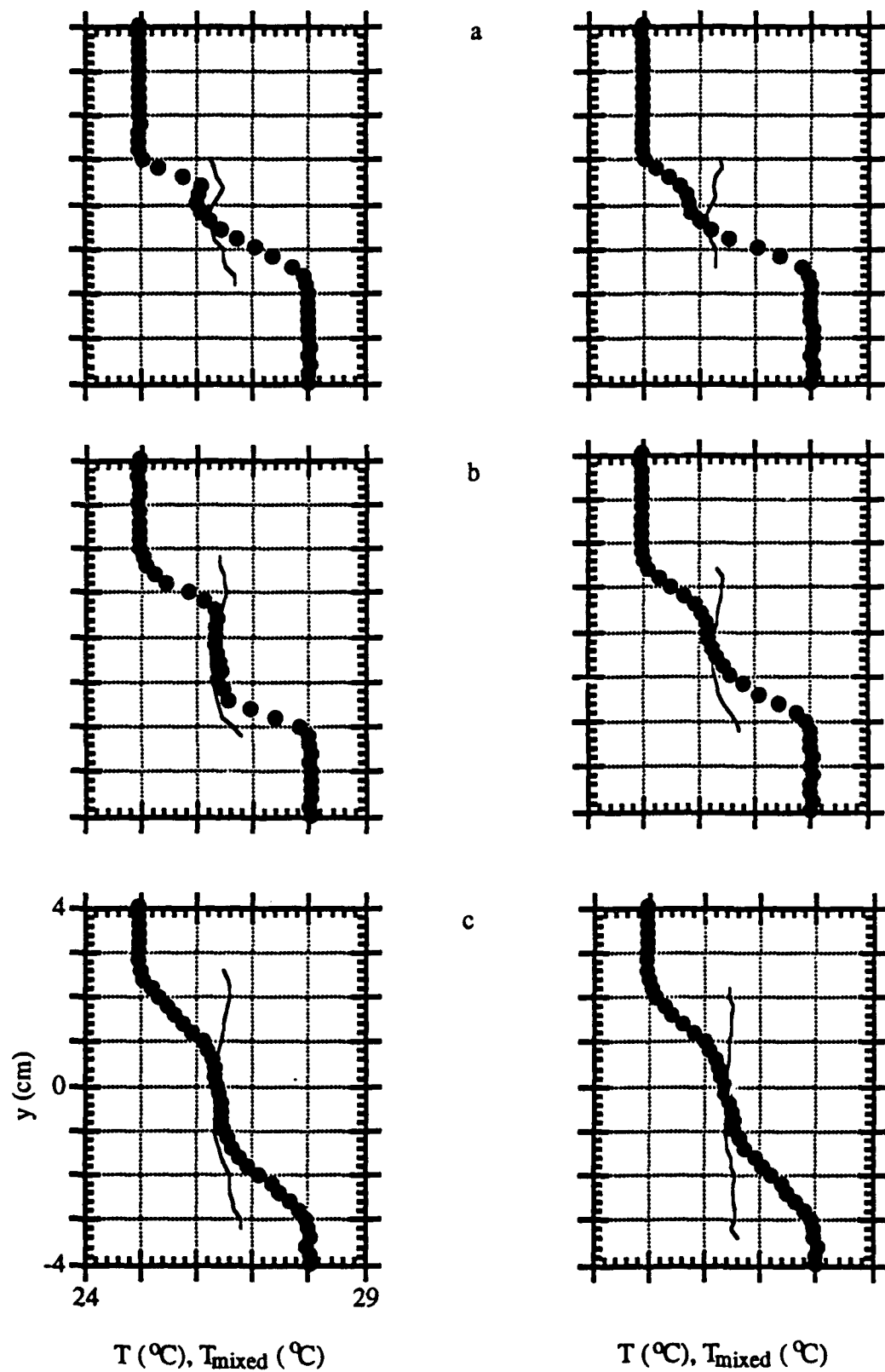
FIGURE 40. Pairs of $T_{mixed}(y)$ (—) and $T(y)$ (•) for SP, $f = 6$ Hz (1/2 head-tail) (left) and SP, $f = 3.85$, 7.7 Hz (1/2 head-tail) (right) at $x = $: (a) 10.16 cm, (b) 15.24 cm, and (c) 20.32 cm.

T_{mixed} profile centered around 26.5 °C, the average temperature of the two free streams.

The shape of these T_{mixed} profiles can be explained by considering plots of the phase-averaged T_{mixed}, $<T_{mixed}(y,t)>$. Figure 41a-d shows pairs (f = 6 Hz, left; f = 3.85, 7.7 Hz, right) of grayscale raster plots of $<T_{mixed}(y,t)>$ at x = 15.24 cm for SU, SP (head), SP (tail), and SP (1/2 head-tail), respectively. For SU, f = 6 Hz forcing (figure 41a) an interesting result is that there is an "island" of cool mixed fluid at the center of the spanwise vortices, everywhere surrounded by warmer fluid. There are two possible explanations for this. The first is that there is an excess of high-speed fluid entrained into the layer during the initial roll-up. The second possible explanation is that fluid which is entrained into the core of the spanwise vortex proper mixes at a temperature controlled by the large-scale entrainment ratio, while fluid in the braids region mixes at a temperature much closer to the mean temperature of the free streams. This mixed fluid from the braids region is then wrapped around the cores of the primary vortices as they are advected downstream. Note that in this scenario, the fluid from the braid region corresponds to the "flame sheet" of the Broadwell-Breidenthal model, while the mixed fluid at the cores of the primary vortices is the "homogenous" fluid.

Figures 41b-d show $<T_{mixed}(y,t)>$ for SP, f = 6 Hz (left) and SP, f = 3.85, 7.7 Hz (right) at the head, tail, and 1/2 head-tail, respectively. Note that, since the streamwise vortices form in the braid region, their average mixed fluid temperature should be approximately the average of the two free streams. Indeed, if the streamwise vortices "entrain" fluid like the spanwise vortices, there is no reason for them to prefer one free stream over the other! This increase in temperature is most apparent at the head of the streamwise vortex for SP, f = 6 Hz (figure 41b, left). There is a large warm region (corresponding to the head of the streamwise vortex)
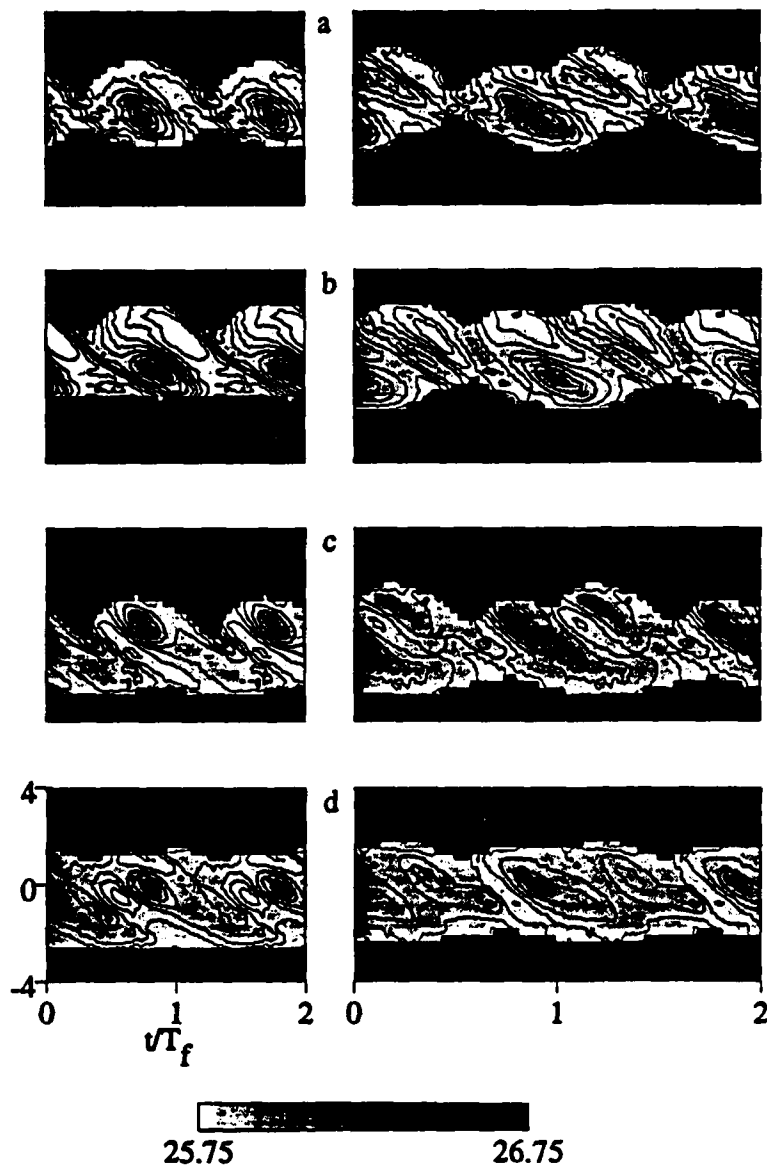
FIGURE 41. Pairs of $\langle T_{mixed}(y,t)\rangle$ at $x = 15.24$ cm for (a) SU, $f = 6$ Hz (left) and SU, $f = 3.85, 7.7$ Hz (right), (b) SP, $f = 6$ Hz (head) (left) and SP, $f = 3.85, 7.7$ Hz (head) (right), (c) SP, $f = 6$ Hz (tail) (left) and SP, $f = 3.85, 7.7$ Hz (right), and (d) SP, $f = 6$ Hz (1/2 head-tail) and SP, $f = 3.85, 7.7$ Hz (right).

located on the high-speed side of the cooler primary core. Figure 41c (left) shows $<T_{mixed}>$ at the tail of the streamwise vortex. A smaller region, which is somewhat less warm than that at the head, can be seen below the spanwise vortex. And at 1/2 head-tail (figure 41d, left), this region is at approximately the same cross-stream location as the primary vortex core. This case is also of interest because it is similar to the case considered by Park, Metcalfe, and Hussain (1994). In their figure 27, they show conditionally averaged (over the "braid" and "roll" regions) mixed mean fluid (MMF) profiles (analogous to our T_{mixed} profiles). They show a MMF profile which follow the mean concentration profile almost exactly in the braid region, and a flat MMF profile in the core region. Although it can be seen that there is considerable structure in $<T_{mixed}(y,t)>$, conditionally averaged plots in the core and the braid region (not shown) are almost identical (and look like the mean T_{mixed} profile, figure 40c, left). However, it is important to note that the average temperature profile $T(y)$ is also constant over a wide range of y for this case. For SP, f = 3.85, 7.7 Hz forcing (figure 41b-d, right) the effect is less dramatic. Again, this reasserts the conjecture that the streamwise vortices are inhibited by the pairing process.

Figure 42a-c shows $<T_{mixed}(x,y;t)>$ for SU, f = 6 Hz, SP, f = 6 Hz (head), and SU, f = 3.85, 7.7 Hz, respectively. These instantaneous snapshots in the x-y plane show the development of the mean mixed temperature with streamwise distance. Notice that in the case of SU, f = 6 Hz forcing, the "islands" of cool fluid in the center of the primary vortices suffer no diminution with downstream distance. This tends to refute the argument that their existence owes to an excess entrainment of high-speed fluid during the initial roll-up. SP, f = 6 Hz forcing (figure 42b) shows a different picture. At upstream locations ("U" in the figure) there is a strong temperature gradient between the head of the streamwise vortex and the core of the spanwise roller. Further downstream, however ("D" in the figure) the streamwise
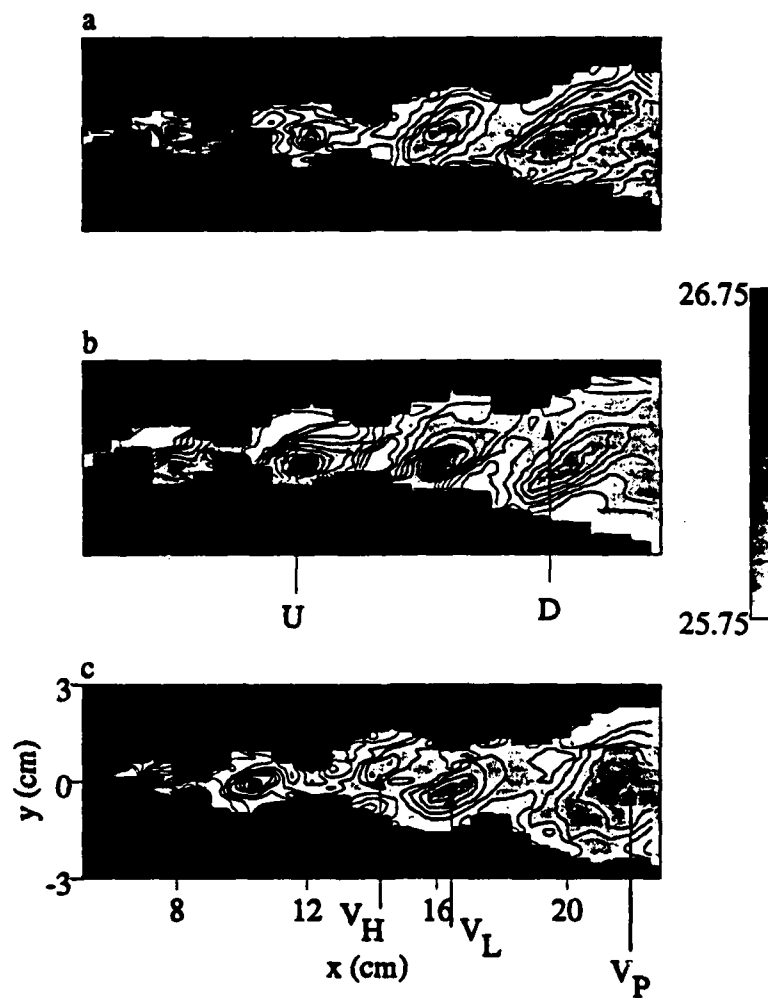
FIGURE 42. $<T_{mixed}(x,y,t)>$ at $x = 15.24$ cm for (a) SU, $f = 6$ Hz, (b) SF, $f = 6$ Hz (head), and (c) and SU, $f = 3.85, 7.7$ Hz.

vorticity has caused a breakdown to small scales of the primary vortex and mixing has moved towards the core of the roller. Concomitant with this, the temperature at the core of the roller has increased significantly, while the temperature in the streamwise vortex has been reduced. This increase homogeneity is a further manifestation of the increased mixing.

Finally, figure 42c shows the case of SU, f = 3.85, 7.7 Hz forcing. The high-speed vortex (V_H in the figure) has a low-temperature island that is slightly warmer than that of the low-speed vortex (V_L in the figure). As they pair, their temperatures equilibrate until there is one large, paired vortex (V_P in the figure) whose temperature is approximately the mean temperature of V_L and V_H.

4.3. Wavelet analysis

It is possible to use a one-dimensional wavelet transform to consider the frequencies associated with mixing as a function of phase within the forcing cycle. Since mixing transition is associated with the breakdown of the primary vortical structures into turbulence, it is expected that regions within the flow where mixing occurs will correlate with those regions where there is a high level of turbulent temperature fluctuations. In this section, the following cases are considered: SU, f = 6 Hz; SP, f = 6 Hz (head); SU, f = 3.85, 7.7 Hz; and SP, f = 3.85, 7.7 Hz (head).

The wavelet transform of a time series f(t), defined here as W(a,b), is obtained by convoluting an analyzing wavelet, g(t), with f(t). More precisely,

$$W(a,b) = \int_{-\infty}^{\infty} f(t)\, g\left(\frac{t-b}{a}\right)\, dt$$

The form of the wavelet g can be chosen arbitrarily. However, it is important to note that the result of the wavelet transform W(a,b) depends equally on the analyzing wavelet g(t) and the data f(t).

The form of the wavelet used here is a complex exponential with gaussian damping (the Morlet wavelet), defined as

$$g(t) = \exp(-\frac{1}{2\sigma} t^2) \exp(i2\pi t).$$

The factor σ determines the number of waves in the convoluting wave packet and hence the frequency and time resolution of the transform: low values of σ give a wave packet of short duration and hence good time resolution, whereas larger values of the damping σ give a longer wave packet and more frequency resolution. The convolution of the signal f(t) with the analyzing wavelet $g(\frac{t-b}{a})$ gives the contribution to the signal at a frequency f_{Ny}/a (where f_{Ny} is the nyquist frequency, or 1/2 of the sampling frequency) at a time t = b. Hence the wavelet transform W(a,b) can be thought of as a localized frequency analysis.

The convolution to calculate W(a,b) can most easily be done in the frequency domain where

$$W(a,b) = \int_{-\infty}^{\infty} f(t) \ g(\frac{t-b}{a}) \ dt$$

$$= F^{-1}\{\hat{f}(\omega) \ a \ \hat{g}(a\omega)\}$$

The common procedure is to take the Fourier transform of f(t) using an FFT routine, multiply it by an analytical expression for $\hat{g}(a\omega)$, and then perform the inverse FFT to obtain W(a,b). In this case, for $g(t) = \exp(-\frac{1}{2\sigma} t^2) \exp(i2\pi t)$,

$$\hat{g}(\omega) = \int\limits_{-\infty}^{\infty} \exp(i\omega t) \exp(-\frac{1}{2\sigma} t^2) \exp(i2\pi t) \, dt$$

or

$$\hat{g}(\omega) = \int\limits_{-\infty}^{\infty} \exp(i(\omega+2\pi)t) \exp(-\frac{1}{2\sigma} t^2) \, dt$$

and finally

$$\hat{g}(\omega) = \int\limits_{-\infty}^{\infty} \exp(i(\omega+2\pi)t - \frac{1}{2\sigma} t^2) \, dt \ .$$

Completing the square gives

$$\hat{g}(\omega) = \int\limits_{-\infty}^{\infty} \exp(-\frac{1}{2\sigma}(t-\sigma(\omega+2\pi))^2 - \frac{\sigma}{2}(\omega + 2\pi)^2) \, dt$$

$$= \exp(-\frac{\sigma}{2}(\omega + 2\pi)^2) \int\limits_{-\infty}^{\infty} \exp(-\frac{1}{2\sigma}(t-\sigma(\omega+2\pi))^2) \, dt$$

$$= \sqrt{2\pi\sigma} \exp(-\frac{\sigma}{2}(\omega + 2\pi)^2).$$

The wavelet $\hat{g}(a\omega)$ is normalized such that the real part of the wavelet transform W(a,b) of a harmonic signal f(t) is the same as f itself (when a is chosen to correspond to the frequency of f(t)).

In what follows, the wavelet transform is used to analyze a single temperature time trace taken on the centerline $y = 0$ ($f(t) = T(y = 0, t)$). Since the wavelet transform $W(a,b)$ of a signal is in general complex, the squared magnitude of $W(a,b)$ is plotted. Figure 43a-c shows $<T(y,t)>$ (for comparison) and $\log_{10}(<|W(a,b)|^2>)$ for SU, $f = 6$ Hz forcing at $x = 10.16$ cm (figure 43a), 15.24 cm (figure 43b), and 20.32 cm (figure 43c). The wavelet transform $\log_{10}(<|W(a,b)|^2>)$ at the centerline position $y = 0$ is shown as a grayscale raster plot as a function of b (the "time" coordinate, horizontal axis) and n_a (the "frequency" coordinate, where $a = 2^{n_a}$, vertical axis). The frequency coordinate n_a is plotted from $n_a \approx 6$ (six octaves lower than the nyquist frequency, corresponding to the forcing frequency $f = 6$ Hz) at the bottom of the plot, to $n_a = 0$ (corresponding to the nyquist frequency $f_{Ny} = 384$ Hz) at the top of the plot. Since the data is phase-averaged (at 128 points per cycle), frequencies corresponding to lower than $n_a = 6$ (or $a = 64$) will show no variation in time.

At a streamwise station characterized by very little mixing ($x = 10.16$ cm, figure 43a), there are two dominant features. The first is the protrusion into the small-scale region ($0 \leq n_a \leq 3.5$) at approximately $t/T_f = 0.3$. This appears to correspond to the region in $<T(y,t)>$ where the entrained low-speed fluid has been strained into a thin sheet, and the scales are small enough that mixing can take place. At approximately the opposite end of this structure, or $t/T_f = 0.8$, there is a smaller concentration of small scales. In addition, there is a large, broad peak at $n_a \approx 4$. This peak is apparently indicative of the entrainment of high-temperature fluid into the low-temperature stream: this tongue of high-temperature unmixed fluid in the cold stream essentially creates a square wave in the temperature record $T(y = 0, t)$, and $\log_{10}(<|W(a,b)|^2>)$ shows the higher harmonics of the forcing frequency. By $x = 15.24$ cm (figure 43b), the protrusions into the small-scale region at the beginning
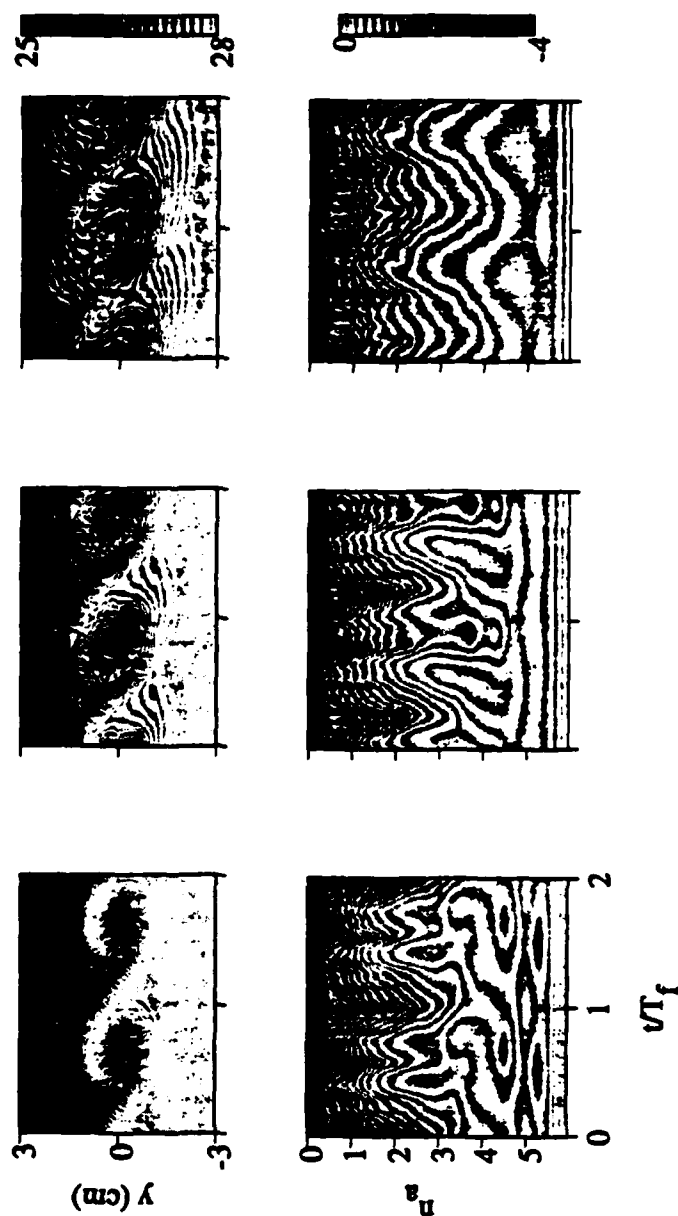
FIGURE 43. $\langle T(y,t) \rangle$ and $\log_{10}(\langle |W(a,b)|^2 \rangle)$ for SU, $f = 6$ Hz (head) at x = (a) 10.16 cm, (b) 15.24 cm, and (c) 20.32 cm.

and end of the spanwise vortices (now at t/T_f = 0.48 and 0.98, respectively) have begun to broaden somewhat as the breakdown of the primary vortices continues. Bye x = 20.32 cm (figure 43c) the two protrusions into the low values of n_a (at the beginning and end of the spanwise vortex) have merged as the turbulent temperature fluctuations around the edges of the roller have moved towards the center of the roller. The vortex core has broken down into turbulence.

Figure 44a-c shows $<T(y,t)>$ and $\log_{10}(<|W(a,b)|^2>)$ at y = 0.0 for the case of SP forcing at f = 6 Hz. The measurements are taken at a spanwise position corresponding to the head of a streamwise vortex. In contrast to the SU case (figure 43a), the plot of $\log_{10}(<|W(a,b)|^2>)$ for the SP case (figure 44a) at x = 10.16 cm has much broader protrusions into the small-scale regions, particularly at the beginning of the roller (t/T_f = 0.3). This is indicative of the increased small-scale activity induced by the streamwise vortices. At 15.24 cm, these protrusions have smoothed out even further. It is interesting to note that, while in the SU case the highest frequencies occur at the beginning of the spanwise vortex and frequencies two octaves above the forcing frequency occur at the end of the vortex, in the SP case nearly all these higher frequencies occur at the same phase point, corresponding to the beginning of the spanwise vortex. By x = 20.32 cm (figure 44c) the protrusions have smoothed to the point that there is very little variation with time of the spectral contents of this temperature record. In addition, the overall level of temperature fluctuations has been raised to a level higher than in the SU, f = 6 Hz case.

Figure 45a-c shows sets of $<T(y,t)>$ (top) and $\log_{10}(<|W(a,b)|^2>)$ (at y = 0.6 cm (center) and y = 0.0 cm (bottom)) at x = 10.16 cm, 15.24 cm, and 20.32 cm, respectively, for SU, f = 3.85, 7.7 Hz. The two cross-stream positions correspond to the center of the high-speed vortex and the center of the low-speed vortex. At a streamwise station characterized by very little mixing (x = 10.16 cm, figure 45a), the
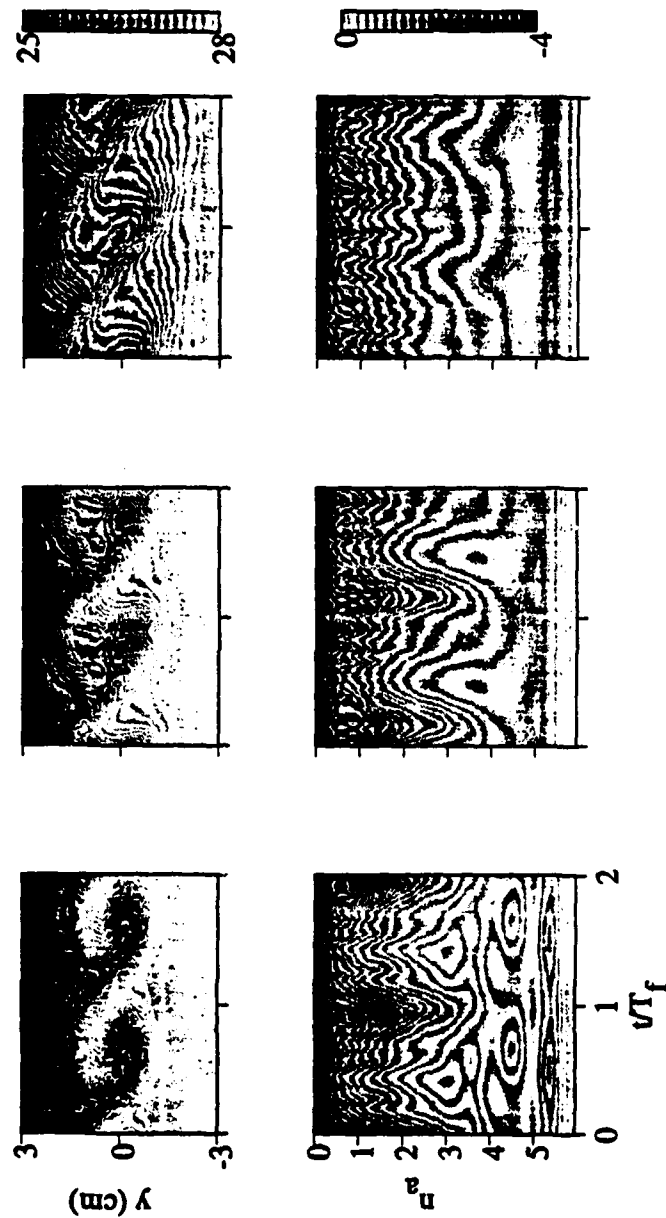
FIGURE 44. $\langle T(y,t) \rangle$ and $\log_{10}(\langle |W(a,b)|^2 \rangle)$ for SP, $f = 6$ Hz (head) at $x =$ (a) 10.16 cm, (b) 15.24 cm, and (c) 20.32 cm.
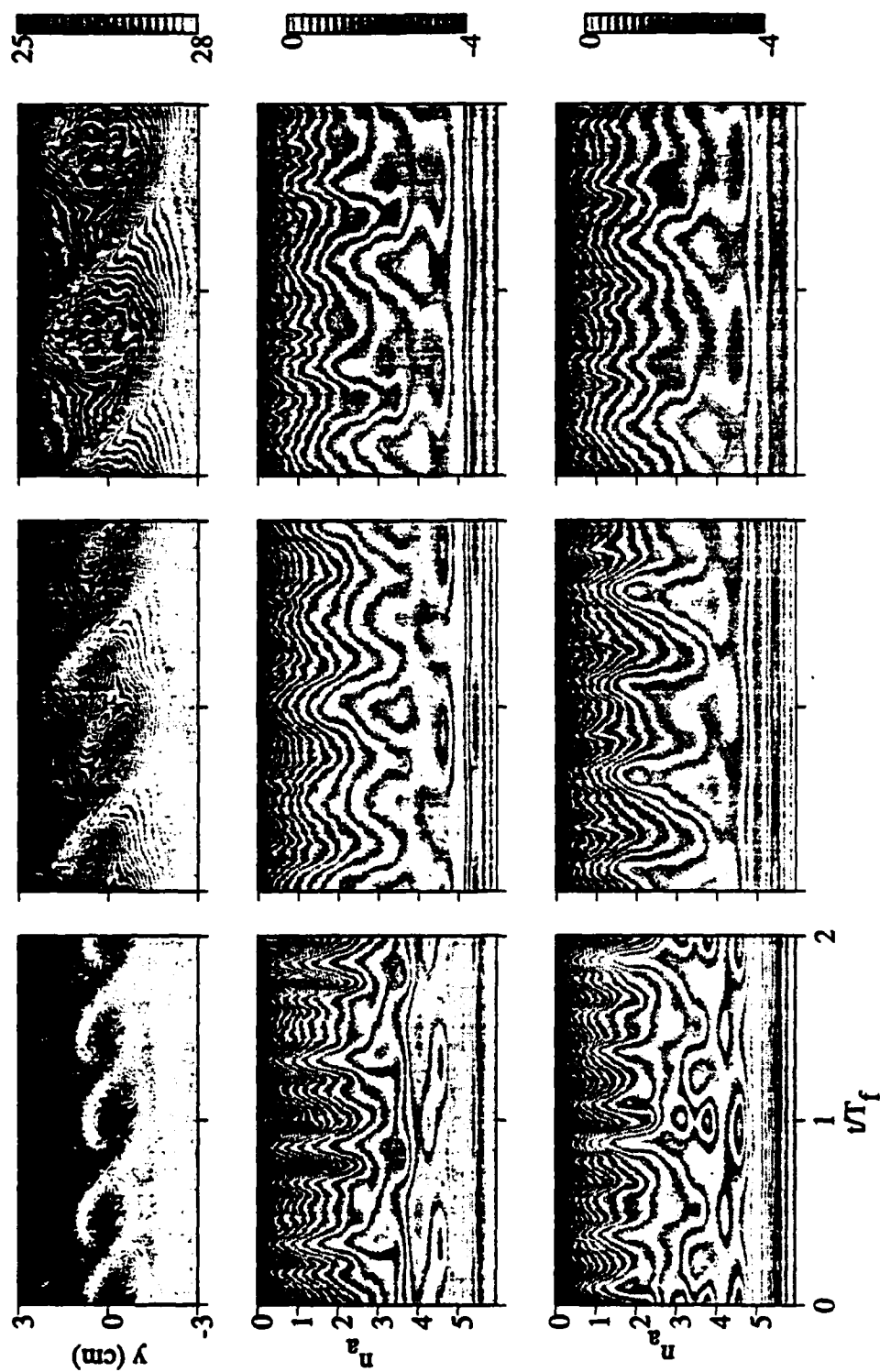
FIGURE 45. $\langle T(y,t) \rangle$ (top) and $\log_{10}(\langle |W(a,b)|^2 \rangle)$ at $y = 0.6$ cm (center) and $y = 0.0$ cm (bottom) for SU, $f = 3.85$, 7.7 Hz at $x = $ (a) 10.16 cm, (b) 15.24 cm, and (c) 20.32 cm.

dominant feature is the protrusion into the small-scale region ($0 \le n_a \le 3.5$) where the entrained low-speed fluid has been strained into a thin sheet, and the scales are small enough that mixing can take place. Note that there are two of these protrusions, at $t/T_f = 0.33$ and at $t/T_f = 0.87$, corresponding to the high-speed and low-speed vortex, respectively. The protrusion at $t/T_f = 0.87$ is more prominent in the plot of $\log_{10}(<|W(a,b)|^2>)$ at y = 0.0 cm whereas the protrusion at $t/T_f = 0.33$ is more prominent in the plot of $\log_{10}(<|W(a,b)|^2>)$ at y = 0.6 cm. By x = 15.24 cm (figure 45b), the two protrusions are of approximately equal amplitude and occur over the same (a,b) space at both cross-stream locations. Hence, at this streamwise station there is approximately the same level of small-scale motion in both the high-speed and low-speed vortices. Figure 45c depicts the wavelet transforms at x = 20.32 cm. There is even less difference between the cross-stream stations y = 0.6 cm and y = 0.0 cm than there is at x = 15.24 cm (figure 45b). Notice that there is one prominent protrusion of small-scale activity at this streamwise station, and that is occurs not at the center of the paired vortices, but just outside of it. Plots of <pm(y,t)> (not shown) show that this is a region containing a small amount of mixed fi_.d (which makes little contribution to <PM(t)>). We speculate that this region is due to the ejection of spanwise vortical fluid from the core of the paired vortex back into the braids region. This region contains significant turbulent temperature fluctuations.

Figure 46a-c shows <T(y,t)> (top), and $\log_{10}(<|W(a,b)|^2>)$ at y = 0.6 cm (center) and y = 0.0 cm (bottom) for the case of SP forcing at f = 3.85, 7.7 Hz. Again, the measurements are taken at a spanwise position corresponding to the head of a streamwise vortex. As was the case for f = 6 Hz, the plot of $\log_{10}(<|W(a,b)|^2>)$ for the SP case (figure 46a) at x = 10.16 cm has much broader protrusions into the small-scale regions than the SU case. This is indicative of the increased small-scale activity induced by the streamwise vortices. However, at 15.24 cm (figure 46b) and
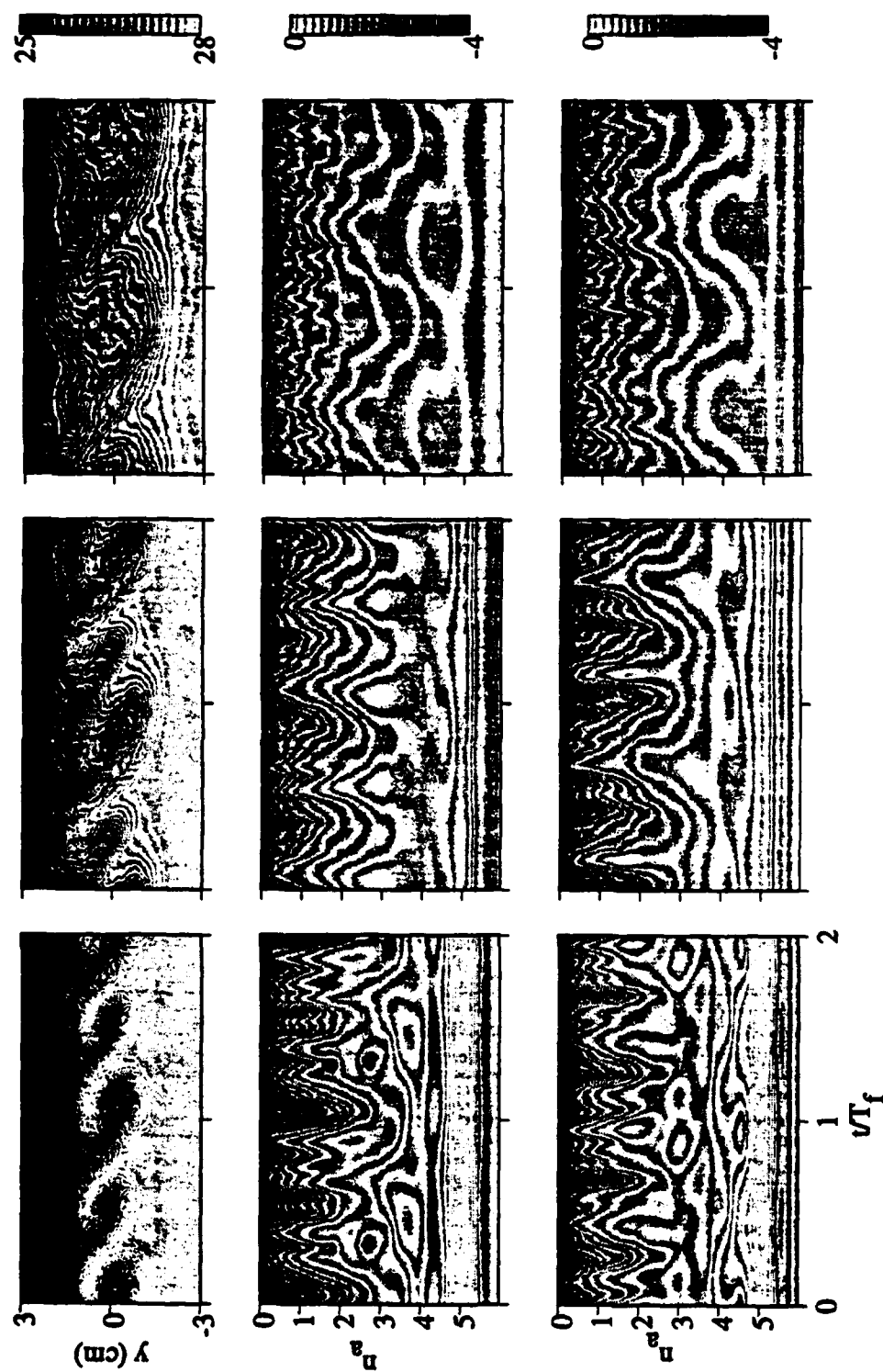
FIGURE 46. $\langle T(y,t)\rangle$ (top) and $\log_{10}(\langle |W(a,b)|^2\rangle)$ at $y = 0.6$ cm (center) and $y = 0.0$ cm (bottom) for SP, $f = 3.85$, 7.7 Hz (head) at $x = $ (a) 10.16 cm, (b) 15.24 cm, and (c) 20.32 cm.

x = 20.32 cm (figure 46d), these protrusions appear similar to those in the SU case. It appears that in the case of pairing, the introduction of streamwise vortices does not significantly effect the level of small-scale temperature fluctuations. This further explains why SP, f = 3.85, 7.7 Hz does not have a significantly higher level of PM than SU, f = 3.85, 7.7 Hz. Also notice that, as in the SU case, the largest concentration of small-scale temperature fluctuations occurs at the region in $<T(y,t)>$ where the remains of the low-speed vortex are located.

It is also useful to consider slices of $<|W(a,b)|^2>$ at individual phase points b. Plots of this type can show the slope of the power spectrum of a given signal at certain points in phase. For the case of SP, f = 6 Hz (head) forcing (deemed to be the most interesting of the cases because of its higher level of small-scale activity), figures 47a-d (x = 15.24 cm) and 48a-d (x = 20.32 cm) show $|W(a)|^2$ at y = 0 for t/T_f = 0.03125, 0.28125, 0.53125, and 0.78125, respectively. Also shown for reference in all the plots is a line of slope -5/3. In a fully turbulent, high Reynolds number flow, there should be an inertial-convective subrange in which the power spectra of the temperature fluctuations (when plotted on a log-log graph) have a slope of -5/3 (Tennekes & Lumley 1972). Due to the intermittent nature of the plane shear layer, normal FFT methods may not reflect this. However, it is possible by using the wavelet transform to look at the power spectra at each point in time - thus providing a more accurate test of these scaling laws than normal power spectra. Figure 47 shows that at a comparatively upstream location, the only phase point at which there is a significant inertial-convective subrange is at t/T_f = 0.28125 (figure 47b), which corresponds to the beginning of the spanwise vortex and the head of the streamwise vortex. By x = 20.32 cm (figure 48) all four phase points begin to show a significant inertial-convective subrange. This reflects the smoothing-out in time of the small scales evident in figure 44c.
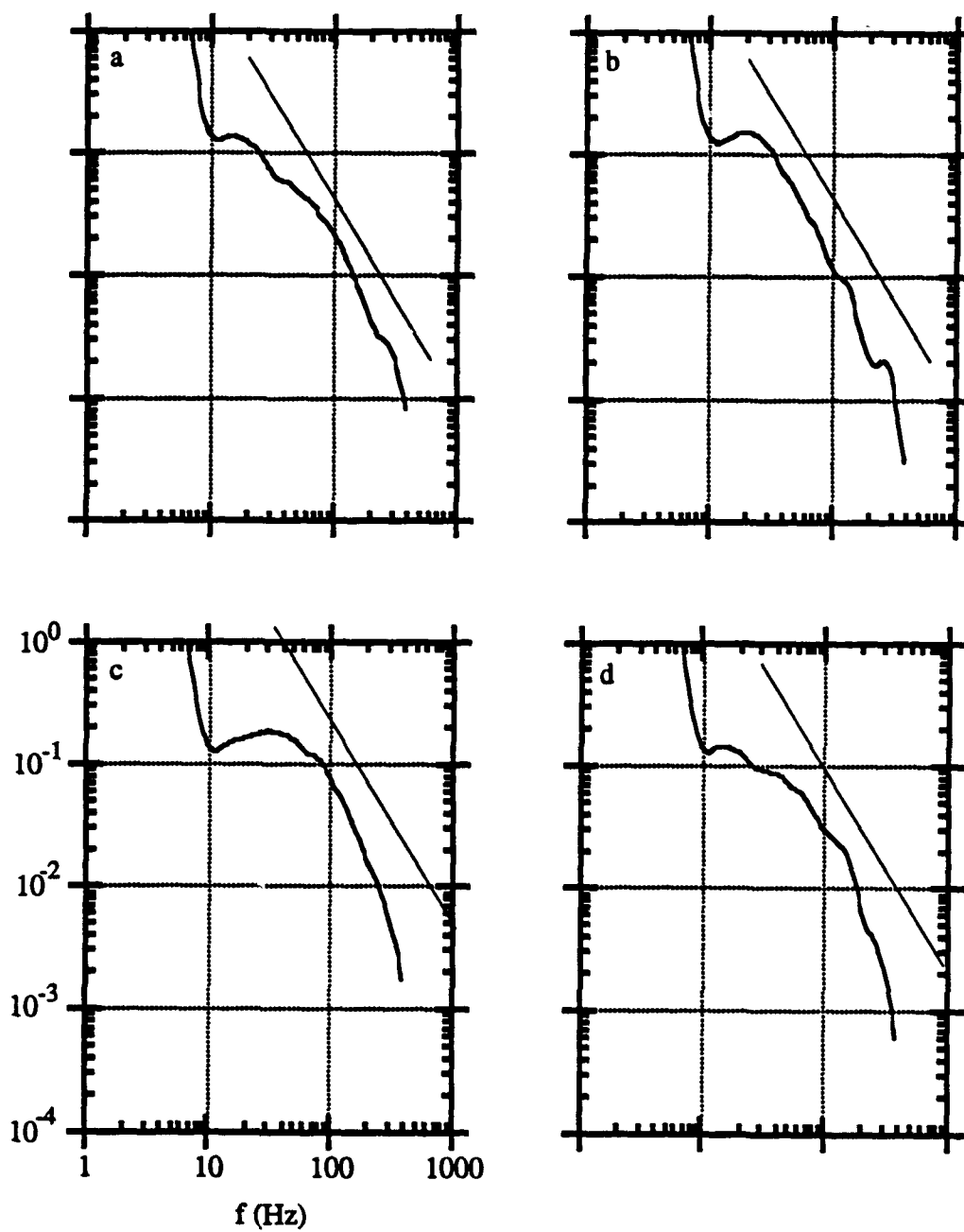
FIGURE 47. $|W(a)|^2$ for SP, f = 6 Hz (head) at x = 15.24 cm for t/T_f = (a) 0.0156, (b) 0.2656, (c) 0.5156, and (d) 0.7656.
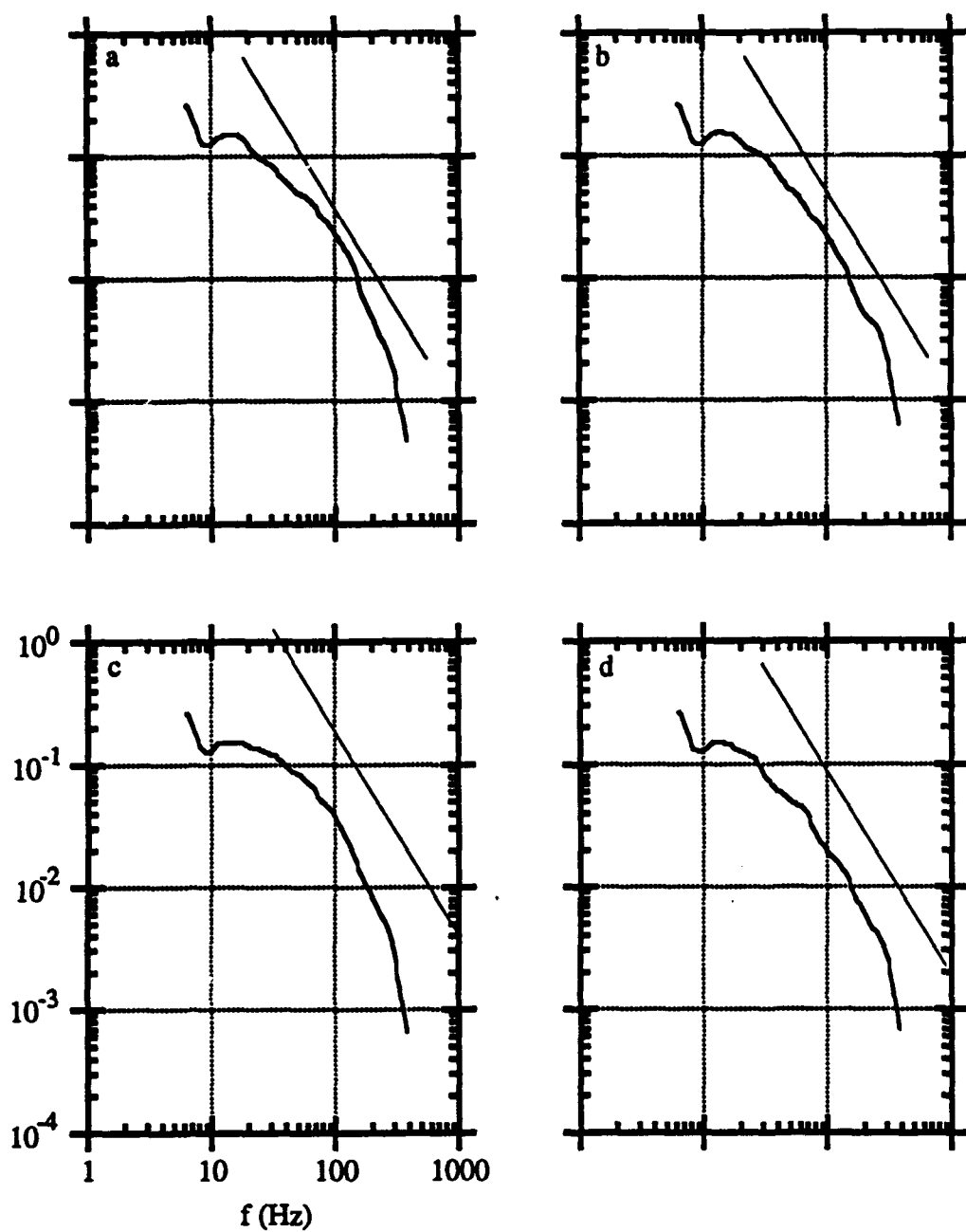
FIGURE 48. $|W(a)|^2$ for SP, $f = 6$ Hz (head) at $x = 20.32$ cm for $t/T_f =$ (a) 0.1484, (b) 0.3984, (c) 0.6484, and (d) 0.8984.

4.4. Spanwise structure

It is instructive to consider mixing as a function of spatial (and particularly spanwise) position in the layer for a number of different forcing schemes. In what follows, phase-locked measurements are used to construct the flow field in y-z planes normal to the x-axis. The following forcing configurations are considered: SU, f = 6 Hz; SP, f = 6 Hz (with a spanwise wavelength of λ_z = 2.66 cm and a duty cycle of .75); SU, f = 3.85, 7.7 Hz; and SP, f = 3.85, 7.7 Hz (also with a spanwise wavelength of λ_z = 2.66 cm and a duty cycle of .75). Evolution through the mixing transition region is studied by considering data at x = 10.16 cm, 15.24 cm, and 20.32 cm.

Figure 49a-c are pairs of isosurface plots of the phase-averaged performance measure <pm(y,z,t)> at x = 10.16 cm, 15.24 cm, and 20.32 cm, respectively, for SP, f = 6 Hz (left) and SU, f = 6 Hz (right). In figure 49 as in figures 50-52, the phase in the forcing cycle is shifted for convenience in viewing the structure of the flow. Here y and z are the cross-stream (vertical) and spanwise (horizontal) coordinates, respectively, and time increases into the page (analogous to a spatially-developing flow coming out of the page). Two periods of the excitation waveform and two wavelengths of the spanwise waveform are shown. The reference cube is a volume consisting of a 6 cm x 6 cm grid in the y-z plane and a length proportional to the convection velocity (24 cm/s) divided by the forcing frequency. The level of pm increases from 0.0 (white) to 0.25 (black). Note that pm = 0.25 indicates that the fluid is fully mixed at the mean temperature of the two free streams. This scale is the same in all figures; however, to accentuate the features of the flow the isosurface level is chosen on a case-by-case basis.
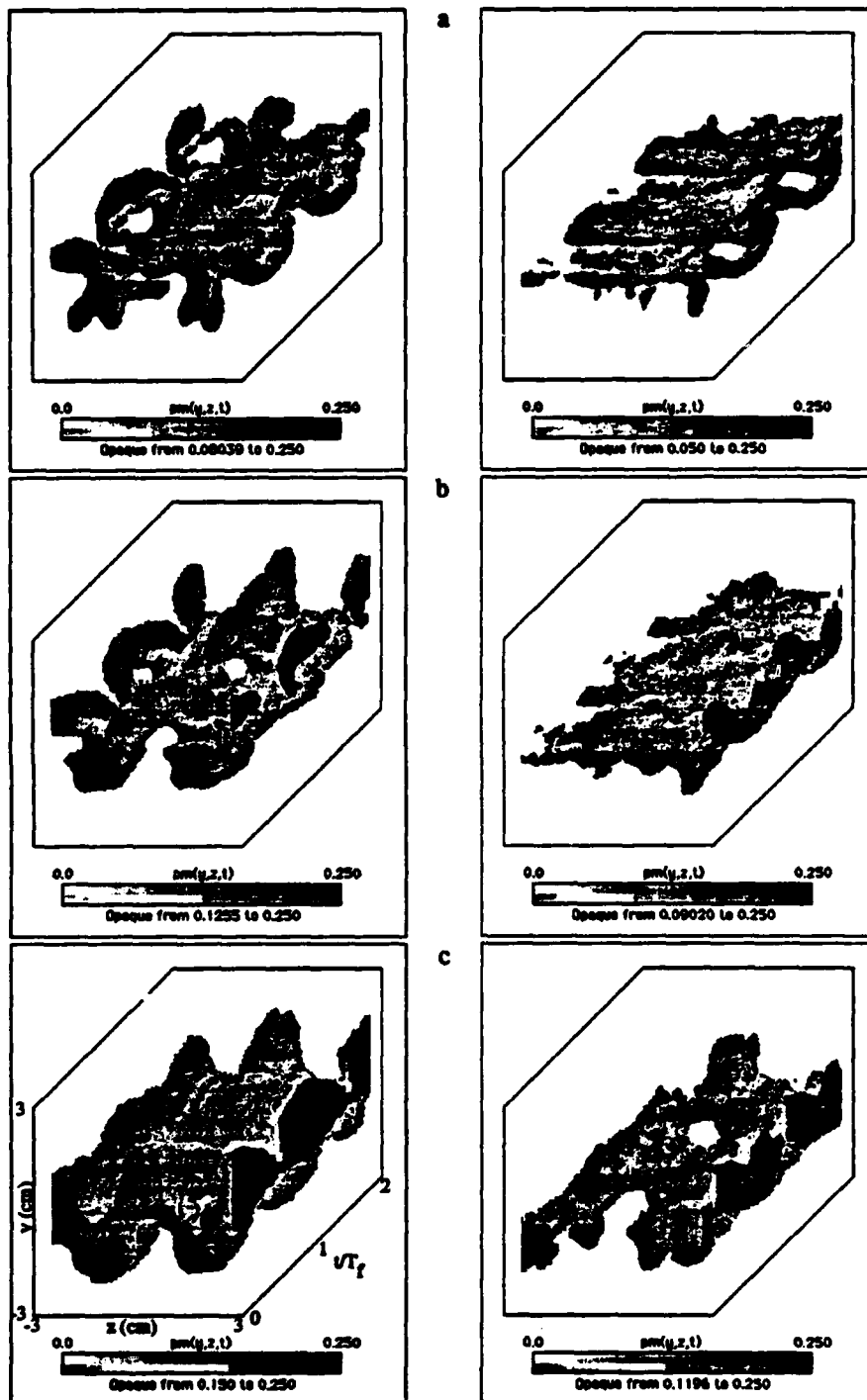
FIGURE 49. Pairs of <pm(y,z,t))> for SP, f = 6 Hz (left) and SU, f = 6 Hz (right)
at x = (a) 10.16 cm, (b) 15.24 cm, and (c) 20.32 cm.

Upstream of the mixing transition (figure 49a) there is very little mixed fluid within the co.cs of the primary (spanwise) vortices, but the streamwise vortices in the SP case induce substantial mixing. Indeed, at the center of these vortices, the fluid is almost completely mixed. However, the volume over which mixing takes place is quite small. By contrast, there is very little mixing at all in the SU case. What mixing there is occurs either in the cores of the primary vortices or in naturally occurring streamwise vortices. At x = 15.24 cm (figure 49b) the overall structure of the flow is unchanged from the upstream case. However, the level of mixedness in the streamwise vortices in the SP has increased significantly and the size of these vortices (as can be determined by the region over which mixing occurs) has increased. In the SU case, the level of mixing has also increased due to naturally occurring mixing transition. Notice the essential three-dimensionality of the flow, even though if was forced with a two-dimensional waveform. This reinforces the idea that mixing is by its nature a three-dimensional phenomenon and that the naturally-occurring streamwise vortices are absolutely essential to the mixing process. By x = 20.32 cm (figure 49c) the streamwise vortices induced by the SP forcing have increased to such a spatial extent that nearly the entire layer is filled with mixed fluid. However, the spanwise structure of the flow is still essentially the same as it was in the two upstream locations. These streamwise vortices do not appear to weaken or smear out with downstream distance. In fact, as can be seen from the SU case, they may actually be amplified. At this streamwise station, the flow appears to have nearly as much three-dimensional structure when the flow is forced SU as when it is forced SP, although this structure is not as coherent as in the SP case. There is substantial mixedness, and most of it occurs in the braids region between two adjacent primary vortices.

Figure 50a-b is analogous to figure 34a-c with the exception that the forcing waveforms are SP, f = 3.85, 7.7 Hz (left) and SU, f = 3.85, 7.7 Hz (right). Two cycles of the low-frequency excitation waveform are shown. Figure 50a is taken at x = 15.24 cm and figure 50b corresponds to x = 20.32 cm. In contrast to the case with a single forcing frequency, the effect of the pairing in this case is to essentially roll the mixed fluid up into the large, low-frequency spanwise vortices. As the pairing process is beginning (figure 50a) there are distinct streamwise vortices for the SP case, particularly between the sets of pairing rollers. The streamwise vortices between the two pairing vortices are compressed as they are rolled into the amalgamated vortex. By contrast, the streamwise vortices between two primary vortices which are not pairing are stretched longitudinally so that their radial dimension is diminished. Immediately after the pairing process is complete (figure 50b), there is almost no mixed fluid in the braids region between the primary vortices. However, the spanwise structure is apparent in the *shape* of the primary vortices: they are distorted towards the high-speed stream in the spanwise location corresponding to what was the head of a streamwise vortex, and distorted towards the low-speed stream in the spanwise location where the tail of a streamwise vortex used to be. Correspondingly for the SU case, there is very little mixed fluid in the braids region after mixing is completed (figure 50b); however, there spanwise vortices themselves are significantly more distorted and three-dimensional than in the case of SU, f = 6 Hz.

From the above measurements it is possible to integrate <pm(y,z,t)> in y to obtain the phase-averaged integral performance measure <PM(z,t)>. This gives the overall amount of mixed fluid in the layer as a function of the spanwise position z and time t. Figure 51a-c shows pairs of contour plots of <PM(z,t)> for SP, f = 6 Hz (left) and SU, f = 6 Hz at x = 10.16 cm, 15.24 cm, and 20.32 cm, respectively.

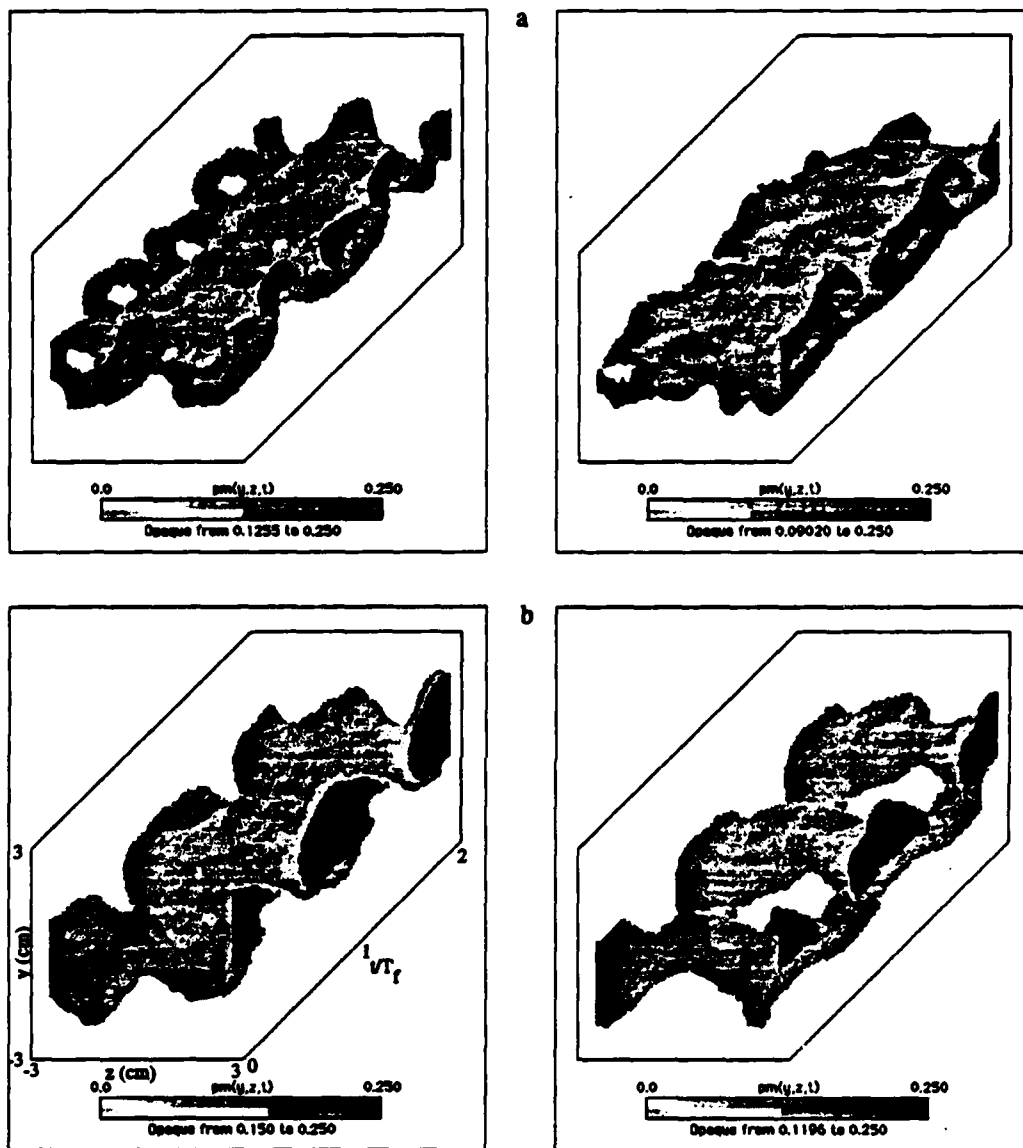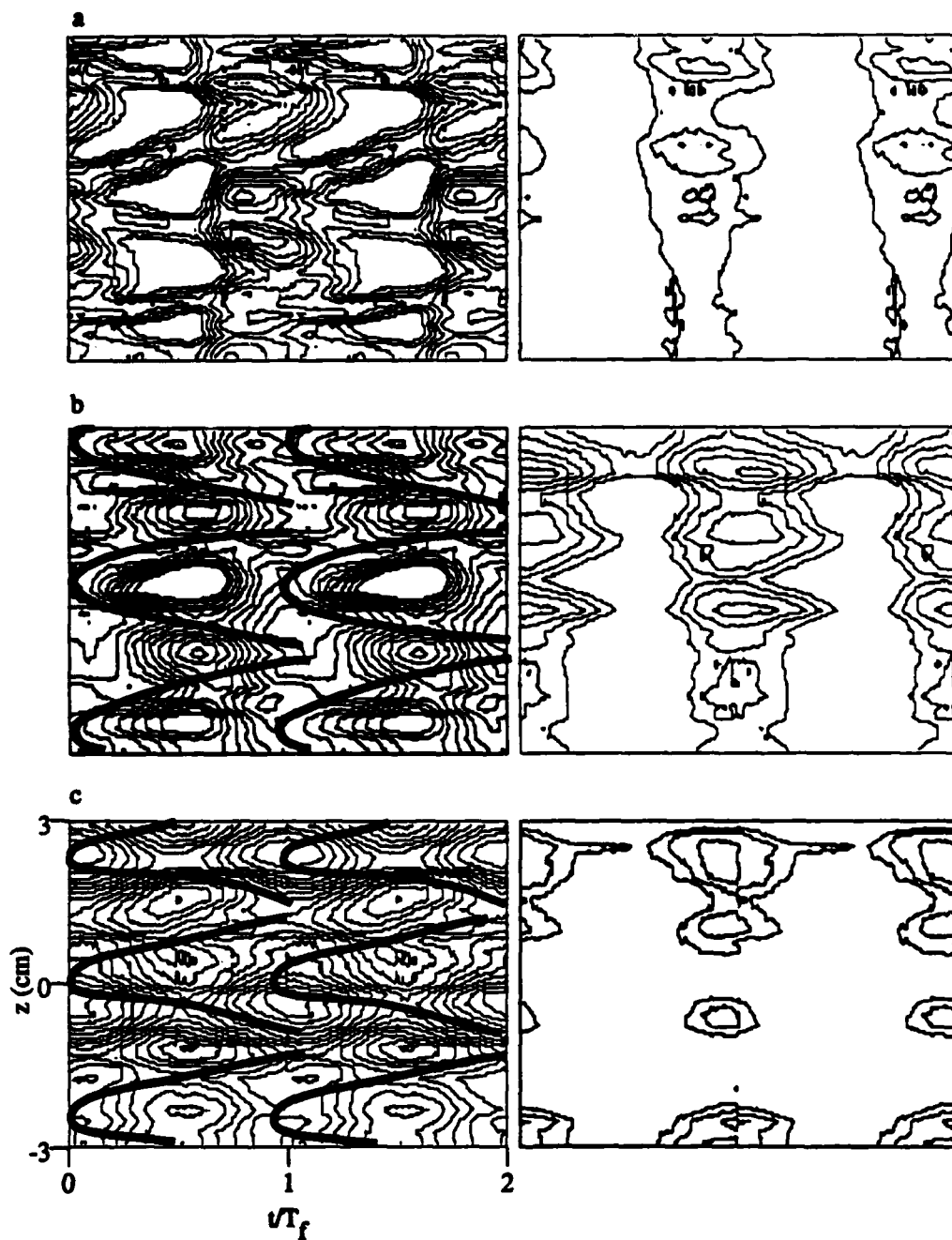FIGURE 50. Pairs of <pm(y,z,t)> for SP, f = 3.85, 7.7 Hz (left) and SU, f = 3.85, 7.7 Hz (right) at x = (a) 15.24 cm, and (b) 20.32 cm.

FIGURE 51. Pairs of <pm(z,t)> for SP, f = 6 Hz (left) and SU, f = 6 Hz (right) at x = (a) 10.16 cm, (b) 15.24 cm, and (c) 20.32 cm.

The minimum contour level is always the same for each pair; however, to account for the increase in PM with downstream distance, the minimum contour level is 0.05 cm for 51a, 0.15 cm for figure 51b, and 0.35 for 51c. The contour increment is 0.025 cm throughout. For clarity, a cartoon representing the streamwise vortex structure is superimposed upon the contours at the two downstream stations (figures 51b-c). This plot illustrates two points which were made previously. First, mixing induced by the streamwise vortices grows in spatial extent until it fills the layer (figures 51a-c, left). Second, even when the flow is forced SU (figures 51a-c, right), much of the mixed fluid tends to form in unforced streamwise streaks. That is, mixing is an inherently three-dimensional process.

Figure 52a-b depicts pairs of $PM(z,t)$ for SP, $f = 3.85, 7.7$ Hz (left) and SU, $f = 3.85, 7.7$ Hz (right) at $x = 15.24$ cm and $x = 20.32$ cm, respectively. The most interesting feature of these figures is that there is no mixed fluid in the braids regions between the paired spanwise vortices (figure 52b). Furthermore, even for SP, $f = 3.85, 7.7$ Hz at $x = 15.24$ cm (figure 52a), there is significantly less mixed fluid in the braids region than for the corresponding SP, $f = 6$ Hz case.

Finally, it is possible to time-average $<PM(z,t)>$ to obtain $PM(z)$. This measure gives an integrated measure of the mixed fluid throughout the layer as a function of spanwise position. Figure 53a-d depicts the percentage increase of $PM(z)$ (relative to the unforced flow at the centerline of the test section, $y = 0.0$ cm) at $x = 10.16$ cm, 15.24 cm, and 20.32 cm for SP, $f = 6$ Hz (figure 53a); SU, $f = 6$ Hz (figure 53b); SP, $f = 3.85, 7.7.$ Hz (figure 53c); and SU, $f = 3.85, 7.7$ Hz (figure 53d). In the SP cases, $z = 0.0$ corresponds to the head of a streamwise vortex and $z = \pm 2.66$ cm corresponds to the tail of a streamwise vortex. Figures 53b and 53d show that even when the flow is excited with a two-dimensional
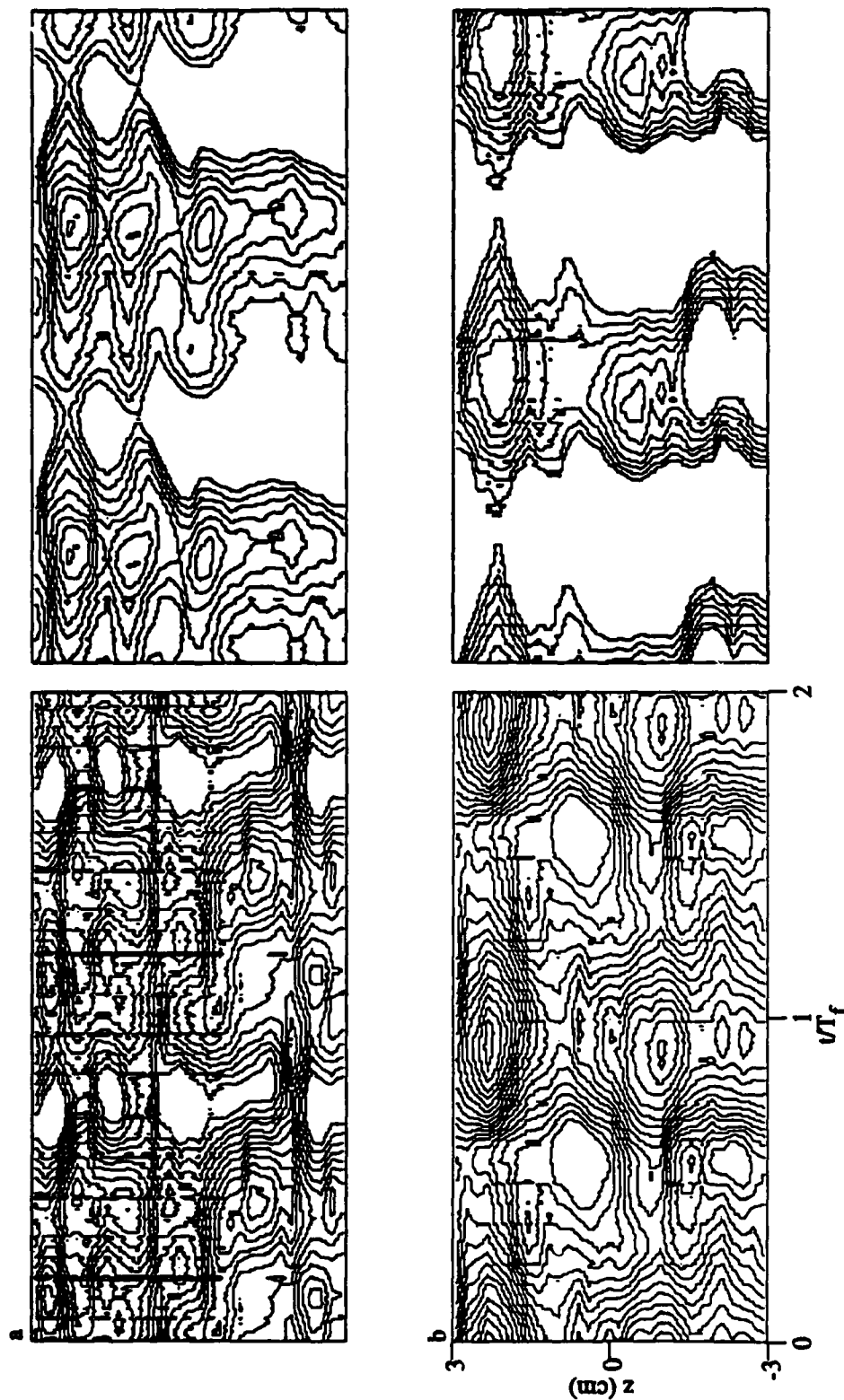
FIGURE 52. Pairs of $\langle pm(z,t) \rangle$ for SP, f = 3.85, 7.7 Hz (left) and SU, f = 3.85, 7.7 Hz (right) at x = (a) 15.24 cm, and (b) 20.32 cm.
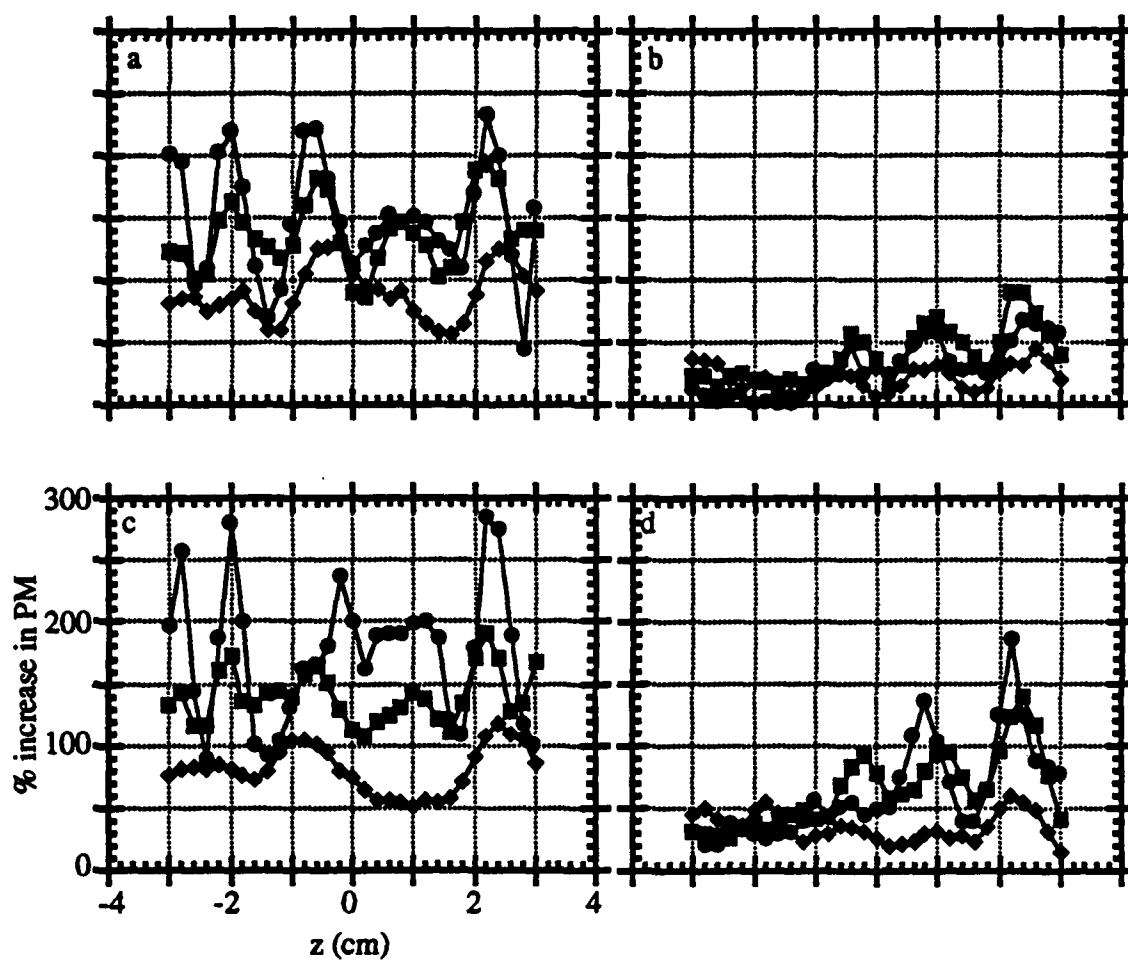
FIGURE 53. PM(z) at x = 10.16 cm (●), 15.24 cm (n), and 20.32 cm (u) for (a) SP, f = 6 Hz, (b) SU, f = 6 Hz, (c) SP, f = 3.85, 7.7 Hz, and (d) SU, f = 3.85, 7.7 Hz.

waveform, three-dimensionality develops with downstream distance. Note, however, that by x = 20.32 cm the percentage variation with z is somewhat smaller.

For the SP cases, there is a definite variation in PM with period λ_z = 2.66 cm. As was noted in §3.2, the maximum in PM corresponds to the spanwise position 1/2 head/tail due to an oblique slice of the streamwise vortex passing through the measurement station. For SP, f = 6 Hz (figure 53a) there are definite peaks at z = ± 0.675 cm and z = ±2.02 cm corresponding to midpoints between heads and tails of streamwise vortices. Note that the peak at z = +0.675 cm is considerably weaker but broader than the other three. This is apparently due to the angle of the streamwise vortex with respect to the time axis. Figure 51a clearly shows that this streamwise vortex is less parallel to the time axis (and hence the x axis) than the other three vortices.

Finally, it is interesting to note that the value of PM at the three head positions is significantly higher for SP, f = 3.85, 7.7 Hz than for SP, f = 6 Hz at x = 10.16 cm. This is due to the accumulation of the streamwise vorticity into low-speed roller at the head position.

4.5. Mixing as a function of open-loop forcing frequency

In the above sections, the flow was forced either at f = 6 Hz (for the case of a single frequency), or at f = 3.85, 7.7 Hz (for the case of two frequencies). These frequencies were chosen because they resulted in a flow which was quite well locked, allowing details of the flow to be shown with phase-locked measurements. However, there is no reason to believe that these frequencies are optimal from the point of view of optimizing mixing; and there is considerable reason to believe that

the amount of mixed fluid produced will vary with the frequency with which the flow is forced.

The dependence of PM on the forcing frequency is studied at x = 15.24 cm, a station solidly in the region of unforced mixing transition. The waveform is SU in all cases, and only the case of a single frequency is considered. Figure 54 shows PM(f) as f is varied from f = 3 Hz to f = 10 Hz. The nature of the forcing in this experiment precludes effective forcing at frequencies significantly above 10 Hz or below 3 Hz. There are two broad peaks in PM(f), centered at approximately f = 4.25 Hz and f = 8.5 Hz. Between these peaks there is a depression between f = 5 Hz and f = 7 Hz, with a value of PM which is which is nominally 5% above the unforced level. It should be noted that this coincides well with figure 16b, which shows PM(x) for SU, f = 6 Hz. Presumably this corresponds to the region where entrainment and pairing are suppressed and little mixed fluid is produced. Mixing is most effectively accomplished at f = 8.5 Hz (at this streamwise station) with an increase in PM of 60% over the unforced flow. At the lower peak, there is an increase of 25% over the unforced flow at f = 4.25 Hz. Because the two peak frequencies are harmonics, it is postulated that a pairing process is responsible for the increase in mixed fluid at f = 4.25 Hz. Indeed, the increase in PM at f = 8.5 Hz (60%) is approximately the same level as is obtained with SU, f = 3.85, 7.7 Hz (figure 16c).

Figure 55a-f depicts the moments of pdf(T,y) (i.e., figures 17-18) as a function of the forcing frequency f. The unforced levels are shown by dashed lines in all plots. The plots of T_{cent} and skew$_T$ (figures 55b and e) suggest that fluid is mixed more uniformly (i.e., closer to the average temperature of the two free streams) at f ≈ 6.75 Hz, a frequency at which the flow is very well locked. Above or below this frequency, the fluid mixes at a cooler temperature much like that of the
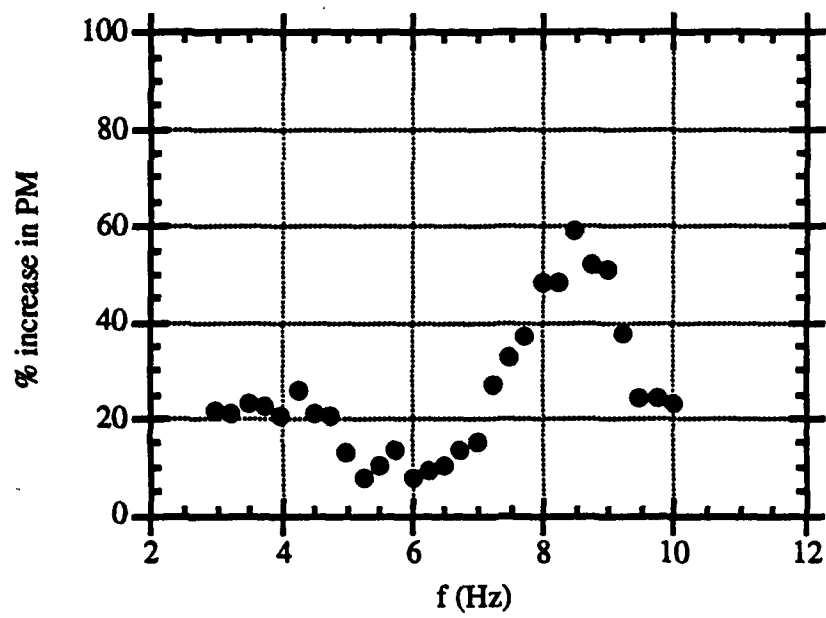
FIGURE 54. Integral performance measure PM as a function of the forcing frequency f, for the case of SU forcing at x = 15.24 cm.
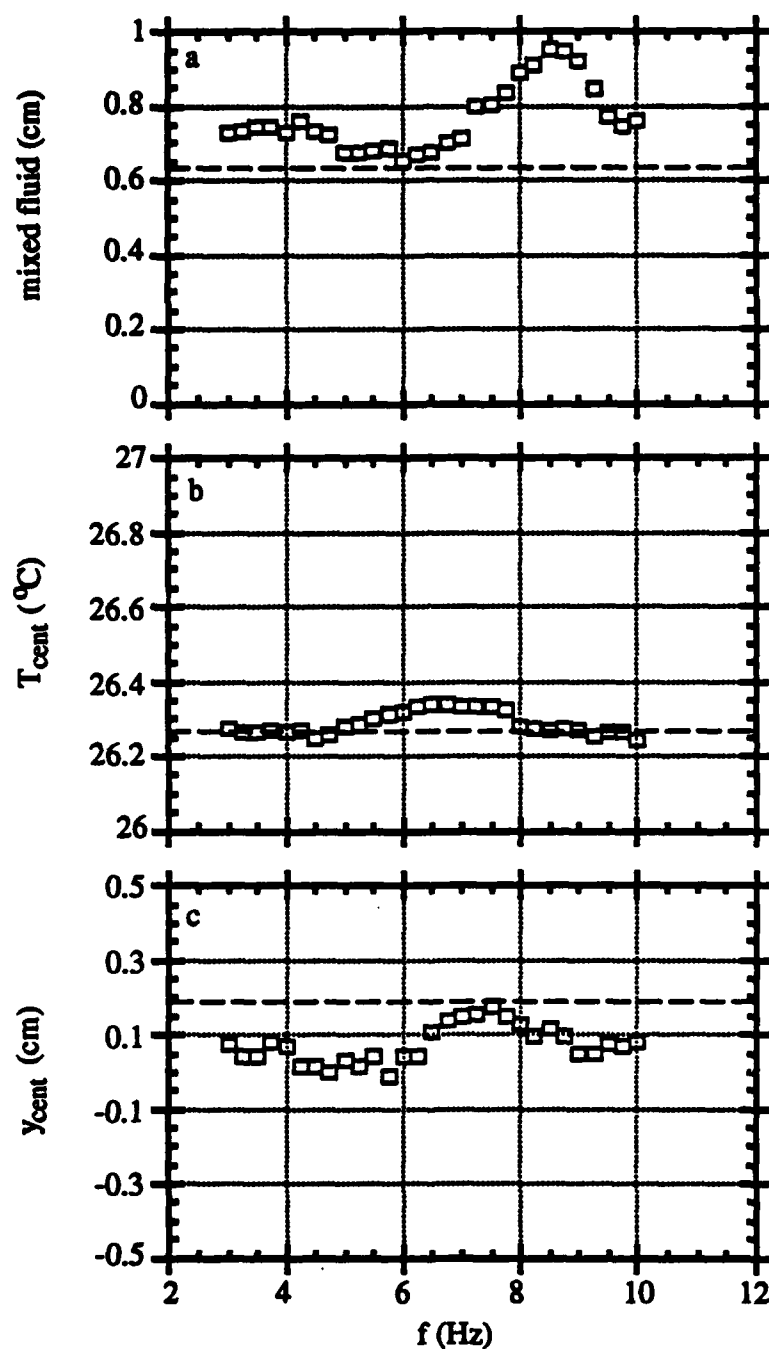
FIGURE 55. (a) total mixed fluid, (b) average temperature of mixed fluid, and (c) average cross-stream position of mixed fluid for SU at x = 15.24 cm. Unforced levels are denoted by dashed lines.
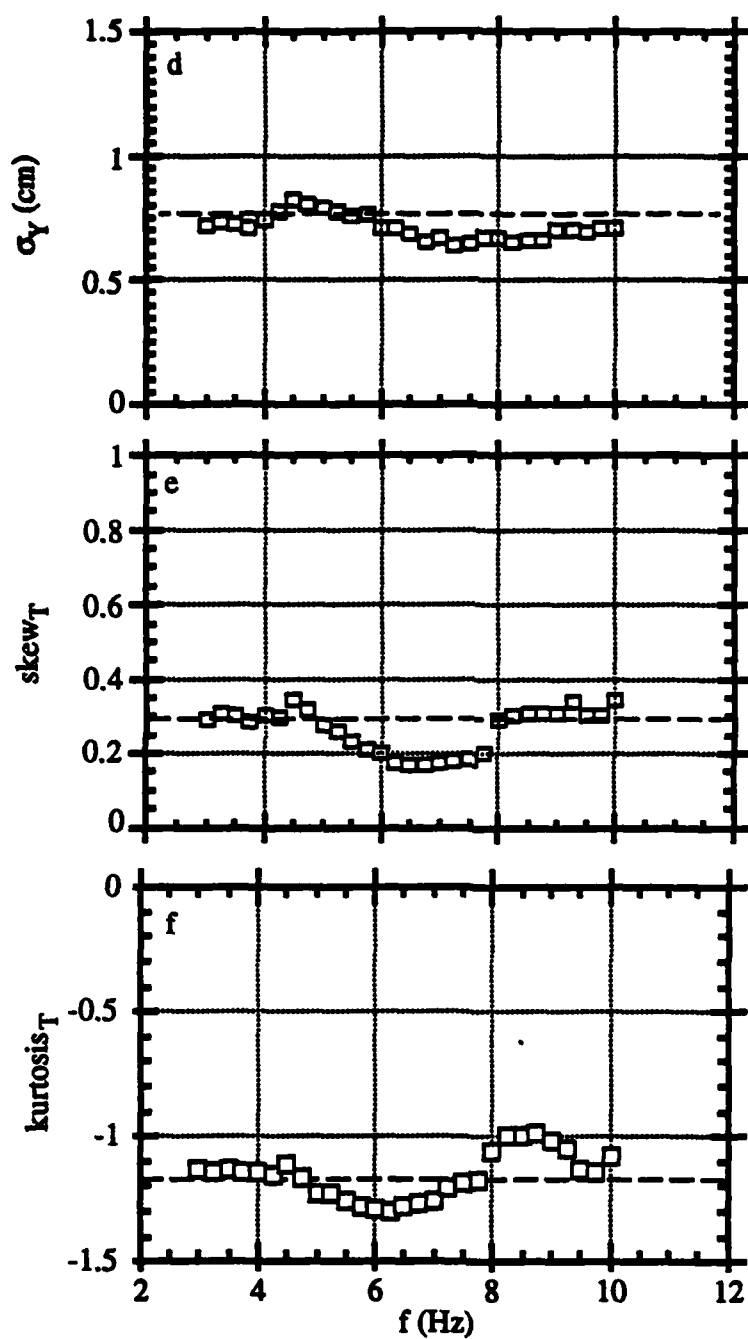
FIGURE 55-*Continued*. (d) σ_Y, (e) skew$_T$, and (f) kurtosis$_T$ for SU at x = 15.24 cm. Unforced levels are denoted by dashed lines.

unforced flow. Finally, the plot of kurtosis$_T$ shows that the *pdf*s of temperature are more peaked at the two regions where mixing is enhance, and flatter over the middle frequency range where mixing is suppressed.

5. Summary and conclusions

The present work focuses on a plane shear layer in which, far upstream of the flow partition, the high- and low-speed streams have uniform, steady temperatures differing by 3 °C. Downstream of the flow partition the temperature distribution is sensed by a rake of cold wire thermometers. Mixing can be inferred by the resulting instantaneous temperature distributions.

The actuators are chosen as surface film heaters flush-mounted on the high-speed side of the flow partition. The heaters are arranged in an array consisting of four spanwise-uniform elements upstream of a 32-element spanwise row. The spanwise-uniform heaters provide the control authority for influencing the nominally two-dimensional rollup and entrainment in the shear layer. The 32-element spanwise nonuniform array provides the capability to introduce a high degree of three-dimensionality into the flow.

Four primary means of forcing the flow have been studied: spanwise uniform (SU) and spanwise periodic (SP) at f = 6 Hz, and SU and SP at f = 3.85, 7.7 Hz. SU, f = 6 Hz forcing can increase the level of mixed fluid (as quantified by the integral performance measure PM) by a significant degree by promoting earlier roll-up of the primary spanwise vortices. However, this effect is attenuated with downstream distance, where the flow relaxes back to the unforced level. SP, f = 6 Hz forcing, on the other hand, leads to a more substantial increase in PM. Mixed fluid is produced within the cores of the *streamwise* vortices. As these vortices increase in spatial extent, mixed fluid fills a significant portion of the layer. Oblique slices through the streamwise vortices (as can be observed at the midpoint between the head and the tail) lead to the largest increase in PM.

SU, f = 3.85, 7.7 Hz forcing also tends to increase the production of mixed-fluid. A large increase in small-scale motions (and hence mixing) is observed in the low-speed (engulfed) vortex as the pairing process occurs. An increase in PM of 40-70% over the unforced flow was observed at downstream stations. The introduction of streamwise vortices to the pairing process (SP, f = 3.85, 7.7 Hz) had a smaller effect on PM than the corresponding f = 6 Hz case. The streamwise vortices tended to be absorbed into the paired primary vortices, resulting in an undulation at the spanwise wavelength but very little streamwise vorticity in the braids region at downstream locations. Hence, the levels of PM for SP, f = 3.85, 7.7 Hz were less than for SP, f = 6 Hz.

Generally, then, the results may be summarized as follows: Mixing is greatest for SP, f = 6 Hz, followed, in order, by SP, f = 3.85, 7.7 Hz, SU, f= 3.85, 7.7 Hz, SU, f = 6 Hz, and the unforced flow.

Part II. FEEDBACK CONTROL

1. Introduction

A number of experimental studies have been conducted to study the effect of open-loop forcing on the development of free shear flows, and more specifically on the effect of forcing on the production of mixed fluid in plane shear layers. This type of forcing can have a significant effect in technological applications from the point of view of enhancing mixing, chemical reactions, and thrust. A survey of this literature is presented in Part I of this work (Wiltse & Glezer 1994a, herein after referenced as WGI).

In addition to previous investigations involving manipulation of free and wall bounded shear flows, there have been a number of previous attempts to control these flows using various forms of feedback. Wehrmann (1965a, 1965b, 1967a, 1967b) investigated the effect of feedback on a cylinder wake (1965a, 1967a) and a flat plate boundary layer (1965b, 1967b). In the wake experiments, an oblong piezoelectric cylinder was used as the body and the actuator. A hot wire located 2.5 wavelengths downstream of the cylinder was used as the sensor. The signal from the hot wire was fed back into the piezoelectric cylinder, inducing vibrations. Wehrmann reported a reduction in the magnitude of the Kármán vortex street fluctuations of 72% relative to the level without feedback.

In the boundary layer experiments he utilized successfully an active flexible wall driven by piezoelectric actuators and located immediately downstream of a hot wire sensor to suppress Tollmien-Schlichting (T-S) waves introduced by a vibrating ribbon. In the open-loop experiment, Wehrmann (1965b) found that by adjusting the phase of the active wall relative to the upstream vibrating ribbon, it was possible to

either decrease (by 10% integrated over the entire layer) or increase the magnitude of the Tollmien-Schlichting instability. In a later experiment using more advanced electronics, (Wehrmann 1967b) reported a reduction of 476 dB/m in the open-loop suppression experiments. In addition, he used a closed-loop feedback mode to suppress *naturally-occurring* Tollmien-Schlichting wave. In this mode, he also reported a damping of 476 dB/m.

In a similar experiment, Nosenchuck (1982) used surface-mounted strip heaters and hot film probes for the suppression of T-S waves in a flat-plate boundary layer. In open-loop experiments, a downstream heater running at 31 Hz was used to cancel (or enhance) the T-S waves introduced by an upstream heater, also running at 31 Hz. In closed-loop experiments, a single hot film probe (located downstream of the actuator, a single surface strip heater) was used to suppress naturally-occurring T-S waves. Unlike the Wehrmann's (1967b) experiment, the sensor (downstream of the actuator) acted like an error signal. A harmonic forcing waveform was synthesized and the phase was continuously updated by the feedback mechanism. Attenuating the T-S waves had the effect of significantly delaying the transition to turbulence.

In the present experiment, the actuators are located *upstream* of the sensors. Hence, the controller affects states which are not yet measured by the sensors. This is similar to the configuration employed by Reisenthel (1988), who studied the effect of pressure feedback on the global instability of an axisymmetric jet. Reisenthel measured velocity fluctuations with a single hot wire sensor placed downstream of the jet nozzle. The hot wire signal was fed back (with various gains and delays) using a loudspeaker placed downstream of the jet exit plane. Hence, in a manner similar to the present experiment, the sensor was placed downstream of the actuator. Reisenthel found that the signal of a separate hot wire sensor placed downstream of

the nozzle contained a series of spectral peaks (dubbed "eigenfrequencies"). The period associated with each spectral peak was an integer submultiple of a delay time (the loop delay) which included the effect of flow and electronic delays. This eigenfrequency structure can be expected in any feedback system with delays, as will be shown in §2 below.

Gaster (1986) developed linear and quadratic transfer function descriptions to predict the effects of open-loop forcing in a boundary layer. These transfer functions considered a "black box" between the actuator (a microphone) and a sensor (a hot wire). For several different forcing frequencies, Gaster mapped the response (gain and phase). In §3.1 below, we present a linear transfer function to predict the effects of closed-loop feedback on the temperature interface between the two streams of the plane shear layer upstream of the first rollup of the primary vortices.

In summary, then, closed-loop feedback has never been used to attempt mixing enhancement. Instead, the uses of feedback in flow control has focused on transition control (particularly in boundary layers), suppression of vortices in wakes (particularly the Kármán vortex street), and separation control. As will be shown below, closed-loop linear feedback can accrue significant gains in mixing relative to open-loop forcing like the type discussed in WGI. In §2, we describe the experimental apparatus, including the control system hardware. In §3, we describe the transfer function used to represent the plant and the feedback control scheme used. in §4 we describe the effects of spanwise-uniform feedback on the flow while in §5 we describe the effects of spanwise-periodic feedback on the flow. Finally, conclusions are presented in §6.

2. The experimental apparatus

2.1. The water shear layer facility

The facility and some of the auxiliary equipment used in the present experiments are described in Nygaard & Glezer (1991) and in WGI. The forcing scheme consists of using the boundary layer along the flow partition to amplify disturbances introduced by the heater array before they reach the plane shear layer flow. The test section was equipped with adjustable side walls which could manipulate the pressure gradient along this boundary gradient with great versatility. Because the open-loop measurements in WGI were predicated on effectively phase-locking the flow to the forcing frequency, the side walls were set to provide a minimal adverse pressure gradient.

For the closed-loop measurements reported here, it was necessary to have amplification in a broader range of frequencies. Thus, the side walls were set to a significantly more adverse pressure gradient. This had a pronounced effect on the frequency response of the flow to the forcing (as intended) but it also resulted in a more three-dimensional flow (and more mixing between the two streams). Hence, the measurements in WGI are only indirectly comparable to those in this manuscript (denoted WGII).

2.2. Control system hardware

A 36 channel, high speed, 12-bit, dual-mode D/A converter (DAC) was designed and built for the present experiments. The DAC can be operated in an update mode for closed-loop feedback applications (and in a signal-generator mode

for open-loop applications). Each channel can be accessed and updated at a rate of 2 μs (limited by the present computer and parallel interface board).

The closed-loop feedback control scheme used in the present experiments is predicated on measurements of the position and velocity of the interface between the two streams (upstream of the first rollup of the primary vortices) as inputs to a digital controller. To this end, an optical Schlieren system is used to determine the instantaneous position of the interface in the cross-stream direction. As shown in figure 1, this system differs from conventional Schlieren systems in that all light rays which are not deflected by index of refraction gradients (resulting from temperature gradients) are removed by the knife edge. The large temperature gradient across the interface between the two streams downstream of the flow partition but before the rollup of the primary vortices appears as a bright spot in the Schlieren image (when the flow field is isothermal the Schlieren image is completely dark). A segment of the interface within this streamwise domain is imaged onto a linear optical position sensor which is aligned in the cross stream direction. The output voltage of the sensor is proportional to the position of the interface and is recorded by the laboratory computer. Accurate measurement of this interface position is crucial, since the linear model described below controls the motion of this interface.

The complete control system is shown in figure 2. The output of the system is the interface position $y(t)$ which can be normalized by the r.m.s. motion for the unforced flow, i.e. $Y(t) = y(t)/y_{r.m.s.}$. In addition, the instantaneous temperature distribution across the layer $T(y,t)$ is sampled at given streamwise and spanwise positions. As described in WGI§2.1, the actuators are an array of surface film heaters flush mounted on the high speed side of the flow partition and driven by DC power amplifiers. The control input $u(t)$ is proportional to $Y(t-\Delta)$ and $\dot{Y}(t-\Delta)$ where Δ is a time delay which is added in software. The reason for the delay is discussed

in §3.1. The present controller is characterized by three parameters: k_1 and k_2 (the gains for $Y(t-\Delta)$ and $\dot{Y}(t-\Delta)$, respectively), and the software delay time Δ.
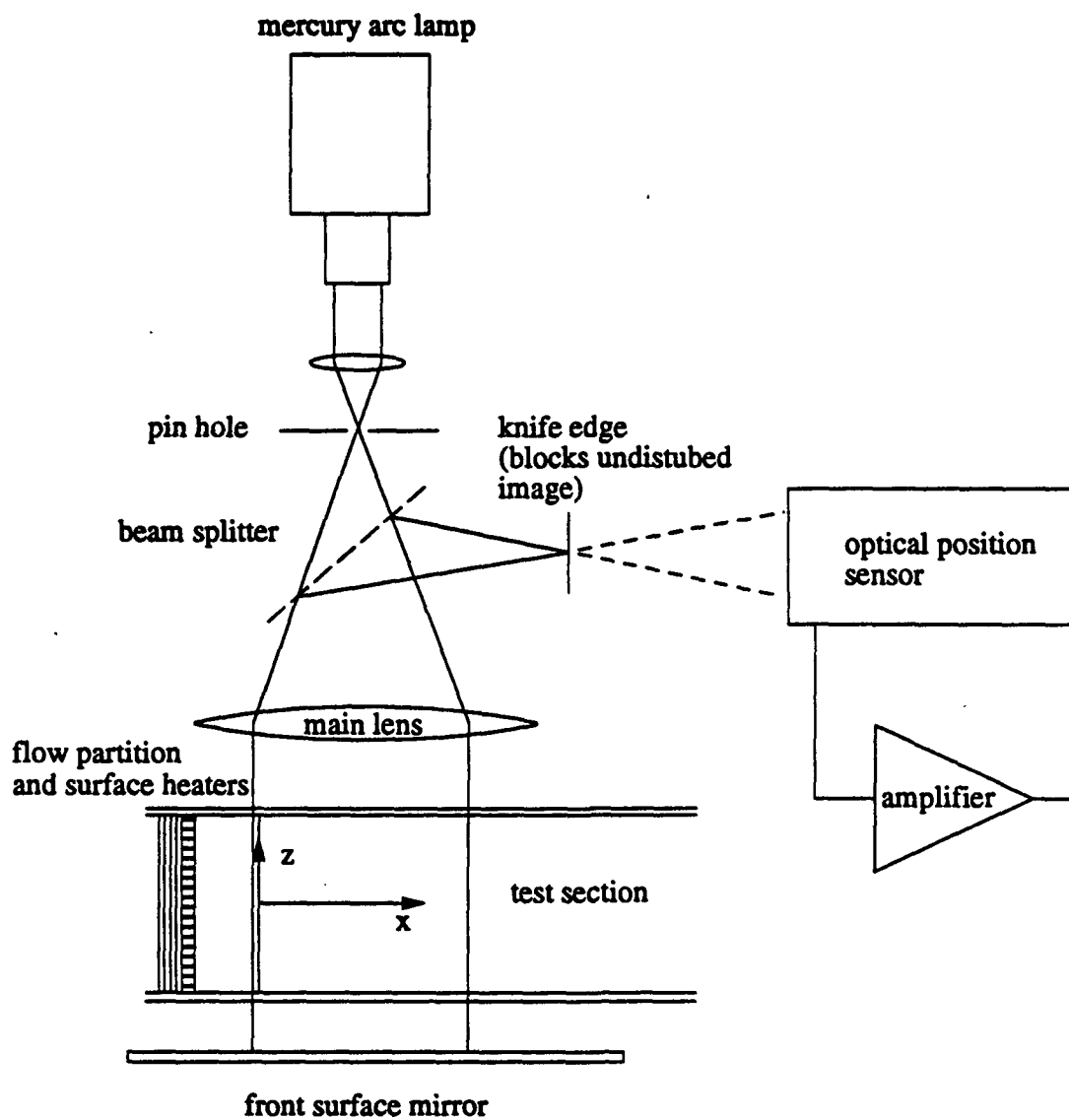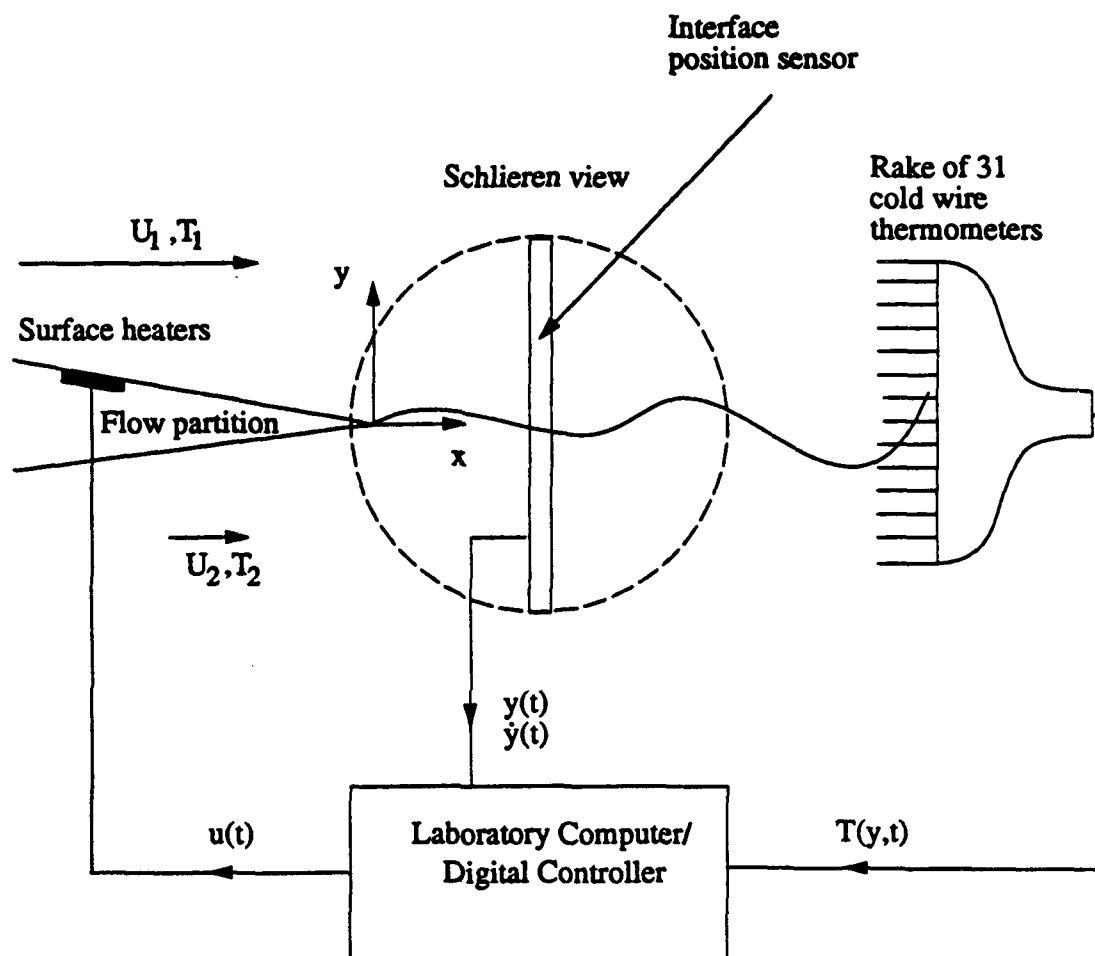
FIGURE 1. The cross-stream Schlieren system.

FIGURE 2. The control system hardware.

3. The control scheme

3.1. The system and controller

A linear feedback control system which is based on a simple model of the interface cross-stream position $y(t)$ and its time derivative $\dot{y}(t-\Delta)$ has been developed. This model applies in the streamwise domain immediately downstream of the flow partition and before the roll up of the primary vortices (in the experiments reported here at $x = 3.175$ cm). Within this streamwise domain, $y(t)$ is approximately time-harmonic which suggests modeling the interface motion as a second order system. It is also convenient to normalize $y(t)$ by $y_{r.m.s.}$ (the r.m.s. displacement of the unforced interface) so that $Y(t) = y(t)/y_{r.m.s.}$.

A nontrivial problem in the implementation of this controller is that the state which is fed back into the controller is actually the state at $t - \Delta_T$, where Δ_T is the total system delay (or the loop delay, in the terminology of Reisenthel) between the actuators and the sensors. The total system delay $\Delta_T = \Delta_N + \Delta$, where Δ_N is the convection delay of a disturbance between the actuators and the sensors, and Δ is a delay which is prescribed in software. It is clear that as Δ_T increases, the effect of the feedback is diminished.

In what follows, the procedure for calculating Δ_N is outlined. The averaged power spectrum of the interface position $S_Y(f) = |F(Y(t))|^2$ is measured when the flow is unforced. The natural frequency is found to be $f_N = 5.66$ Hz. Next, the flow is forced open-loop for the case of isothermal flow ($\Delta T = 0$) and both the forcing signal and the centerline temperature $T(x = 3.175$ cm, $y = 0.0$, $t)$ at the streamwise location of the position sensor are recorded. The cold-wire probe on the centerline is capable of measuring the small temperature fluctuations induced by the

surface heaters. Since at the surface heaters the temperature fluctuations will precisely follow the heater power u, it is possible to correlate u and $T(y = 0.0)$ at $x = 3.175$ cm and hence determine the convective delay time Δ_N between the heaters and $x = 3.175$ cm. Correlations of u and $T(y = 0)$ were done for a number of open-loop forcing frequencies. A series of frequencies were found which led to a maximum correlation at zero lag. For example, forcing the flow at 6.104 Hz leads to a maximum correlation at -.0063s (figure 3a), while forcing at 6.18 Hz results in a maximum correlation at a lag of .0125s (figure 3b). From this, it can be interpolated that the desired frequency (resulting in a maximum correlation at zero lag) is 6.129 Hz. Similarly, it can be found that other frequencies, such as 7.15 Hz, also result in maximum correlation at zero lag. Hence, assuming there are no such eigenfrequencies between 6.129 and 7.15 Hz, it can be seen that the convective delay is

$$\Delta_N = \Delta_T - \Delta = \frac{n}{\Delta f} = \frac{1}{7.15 - 6.129} = 0.979s.$$

It is also necessary to find the phase between the output of the position sensor Y and the input u at the natural frequency. When the flow is forced at 5.66 Hz, the lag between u and $T(x = 3.175$ cm, $y = 0.0)$ is (figure 3c) 0.1025s. Similarly, for $\Delta T = 3^\circ$ C, the lag between u and Y (figure 3d) is .15s. Hence, Y lags $T(y = 0.0)$ (when they are both measured at the same streamwise station, $x = 3.175$ cm) by 0.0475s. Assuming this same phase relationship holds at the surface heaters, the phase between Y and u is $\phi(Y,u) \approx -90^\circ$ (at the natural frequency).

A transfer function was developed which includes the effects of the total delay time Δ_T in the feedback. Figure 4 shows the physical significance of the

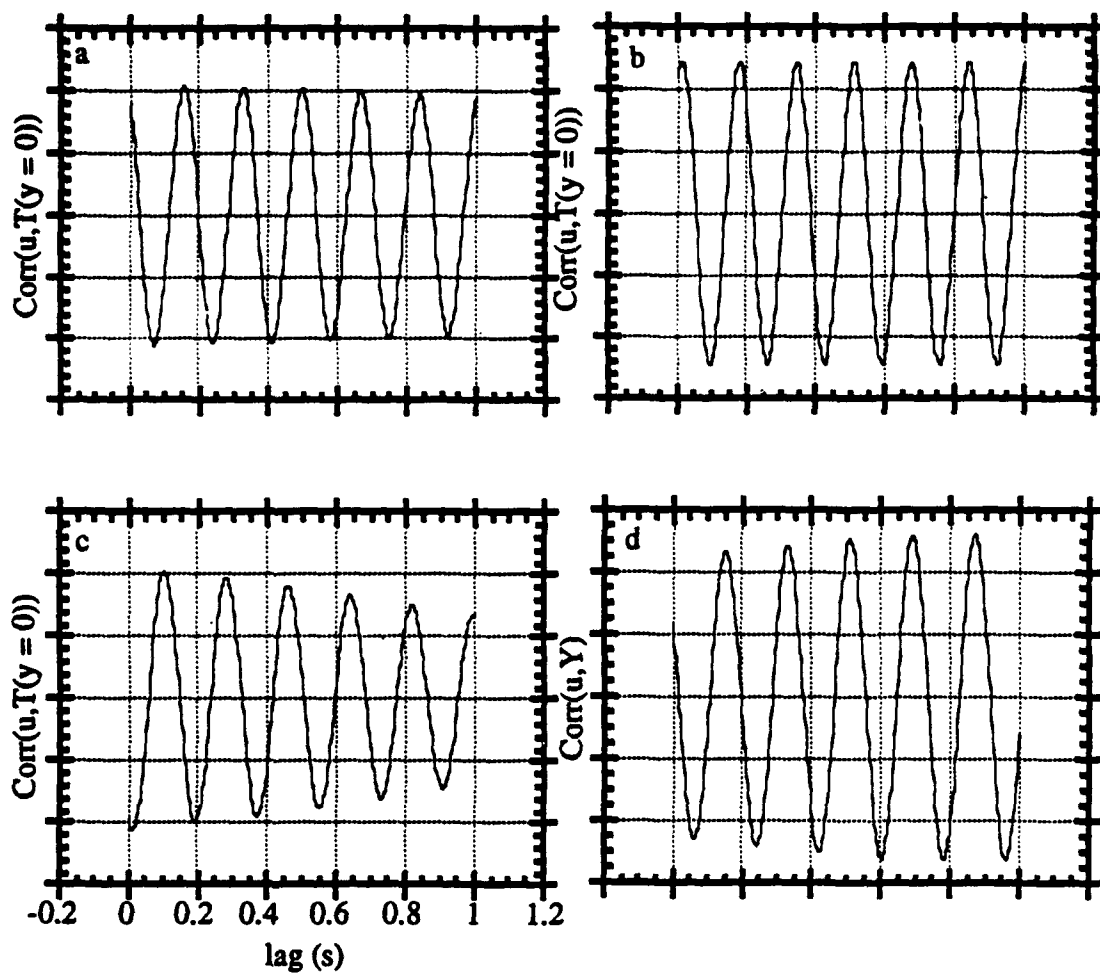transfer function. The plant consists of the flow partition downstream of the surface

FIGURE 3. Correlations used to determine delay times. Correlation between u and T(y = 0.0) for SU forcing and ΔT = 0.0 at (a) 6.104 Hz, and (b) 6.18 Hz. Correlation between u and T(y = 0.0) for SU forcing at f = 5.66 Hz with ΔT = 0 (c); and correlation between u and Y for SU forcing at 5.66 Hz with ΔT = 3 °C.
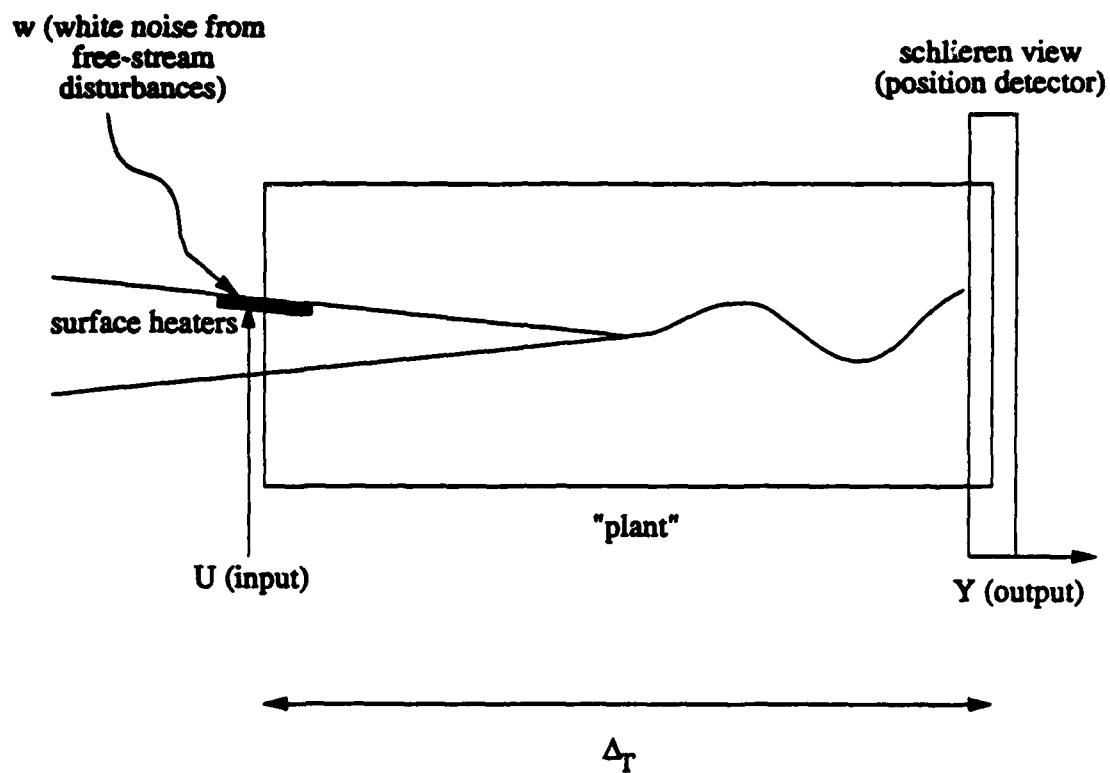
FIGURE 4. Plant for use with transfer function.

heaters through x = 3.175 cm (the location of the position sensor). Disturbances (consisting of nominally white noise from the free stream and the input r from the surface heaters) are amplified in the plant as they are convected to the position sensor in time Δ_T. In order to optimize the effectiveness of the transfer function, the software delay Δ is chosen so that the total delay $\Delta_T = \Delta_N + \Delta$ corresponds to an integer number of cycles of the flow. Since (6/5.66 Hz) = 1.06s, Δ = .08s.

The shape of the power spectrum of the unforced interface motion S_Y (figure 5a) suggests modeling the region of flow between the surface heaters and the optical position sensor as a tuned second-order amplifier, for which the transfer function

$$G(s) = G(i\omega) = \frac{(\cos(\phi), \sin(\phi))}{-\omega^2 + \frac{i\omega\omega_0}{Q} + \omega_0^2}$$

where $\omega_0 = \omega_N$ in this case. The squared magnitude of this filter $|G(f)|^2$ is shown in figure 5b. For the unforced case, u is the broad-band disturbance always present in the flow (white noise, denoted by w). As noted above, $\omega_N = 2\pi \cdot 5.66$ Hz, and henceforth G will be given in terms of ω/ω_N. Q was chosen so that G accurately modeled $S_Y(f)$ for frequencies less than or equal to ω_N. For the present experiments, Q = 4.7.

The effect of closed-loop feedback is modeled below. By letting the control u be a negative feedback of the states,

$$u(t) = -A(k_1 Y(t-\Delta_T) + k_2 \dot{Y}(t-\Delta_T)) + w$$

where A is the ratio of the disturbance introduced by the forcing to the disturbance introduced by w. The delay time Δ_T enters the equation because the feedback into the
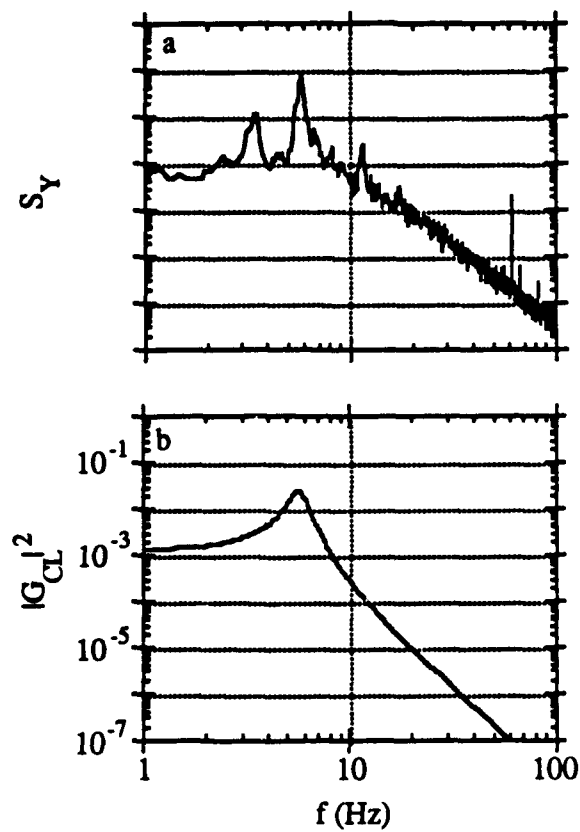
FIGURE 5. (a) The power spectrum of the unforced interface motion, and (b) analogous second-order transfer function.

heaters at any given time is a function of what is being measured at the position sensor, which was at the heaters a time Δ_T ago. Thus, taking the Fourier transform of u(t),

$$F(u) = -A(k_1 F(Y)exp(-i\omega\Delta_T) + k_2 F(Y)(i\omega)exp(-i\omega\Delta_T)) + F(w).$$

This can be inserted into the expression $F(Y) = GF(u)$ to give the closed-loop transfer function

$$G_{CL} = \frac{G}{1 + GAexp(-i\omega\Delta_T)(k_1 + k_2 i\omega)} .$$

The remaining unknown parameter A was found to be $A = 4$ (found by observations of the effect of feedback on the total power in S_Y). The next section shows the utility of $|G_{CL}|^2$ in predicting S_Y.

3.2. Controller verification

The utility of the transfer function in predicting the motion of the interface can be assessed be systematically varying the control gains k and the software delay Δ. Figure 6 shows the effect of varying k on the motion of the interface. The magnitude of the control gain $|k|$ is held constant at 1.25, the safety limit of the surface heaters. The angle between k_2 and k_1 is then varied between 0^0 and 360^0 (see figure 6a). The angle between the two components of the gain vector is defined as $\theta = tan^{-1}(k_2/k_1)$. Figure 6b shows the variation of the r.m.s. motion of the interface as predicted by the transfer function and as measured by the position detector. In this figure, $\Delta =$
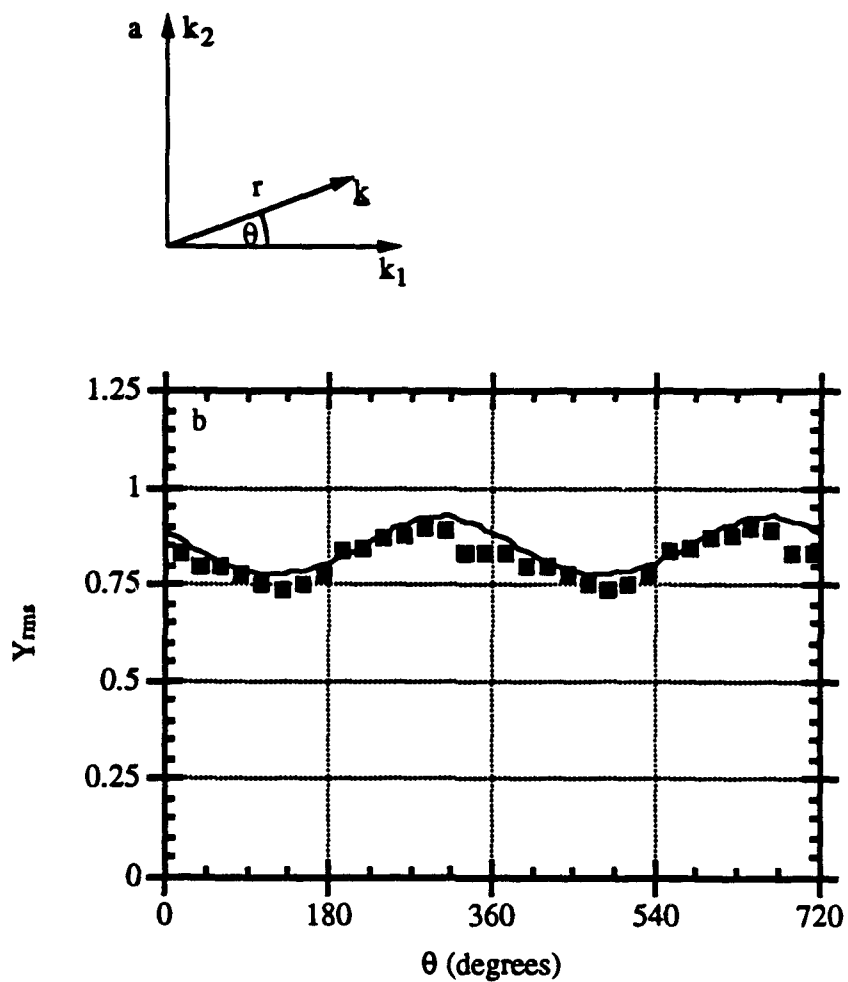
FIGURE 6. RMS displacement of the interface motion as a function of the angle θ of
$\mathbf{k}$. (a) geometry, and (b) Y_{RMS} as predicted by the transfer function (—) and Y_{RMS}
measured (■).

.08s, which gives a value of $\Delta_T = 1.06s$ (corresponding to six cycles of the natural frequency). This value of Δ is used in the bulk of the closed-loop experiments. The figure shows that the transfer function does a good job of predicting the response of the r.m.s. motion of the interface to different gains.

Similarly, figure 7 shows the rms displacement of the interface as a function of the total delay time Δ_T as Δ is varied from 0s to 1.4s (Δ_T varies from 0.979s to 2.38s) and θ is fixed at 0°. Again, the transfer function accurately predicts the motion of the interface, especially for short delay times. However, as Δ_T increases, it appears that the variation of the motion of the interface changes more with a smaller change in Δ. This also suggests that had the convective delay time Δ_N been greater, it would have been much more difficult to control the motion of the interface.

The effect of feedback is to cause "resonance" conditions (in which there is one characteristic frequency in the flow) for some values of θ and "anti-resonance" conditions (in which the characteristic frequency of the flow is constantly changing) for other values of θ. It is thus constructive to consider the spectral power at the fundamental frequency for various feedback gains. Figure 8 depicts the spectral power S_Y at the fundamental frequency f_0 ($= 5.66$ Hz). Shown are the measured spectral power and that predicted by the transfer function. Although there is some disparity in the absolute magnitude of the two (as expected since the transfer function is only of second order), the transfer function does do an accurate job of predicting the locations of the minimum and maximum of $S_Y(f_0)$. This minimum in $S_Y(f_0)$ (at k $= (0.163, 1.239)$) is the anti-resonance condition alluded to earlier, while the maximum in $S_Y(f_0)$ (at $k = (-0.163, -1.239)$) is the resonance condition. They are noted in the figure as conditions C_1 and C_2, respectively, and will be referred to repeatedly throughout the remainder of this work.
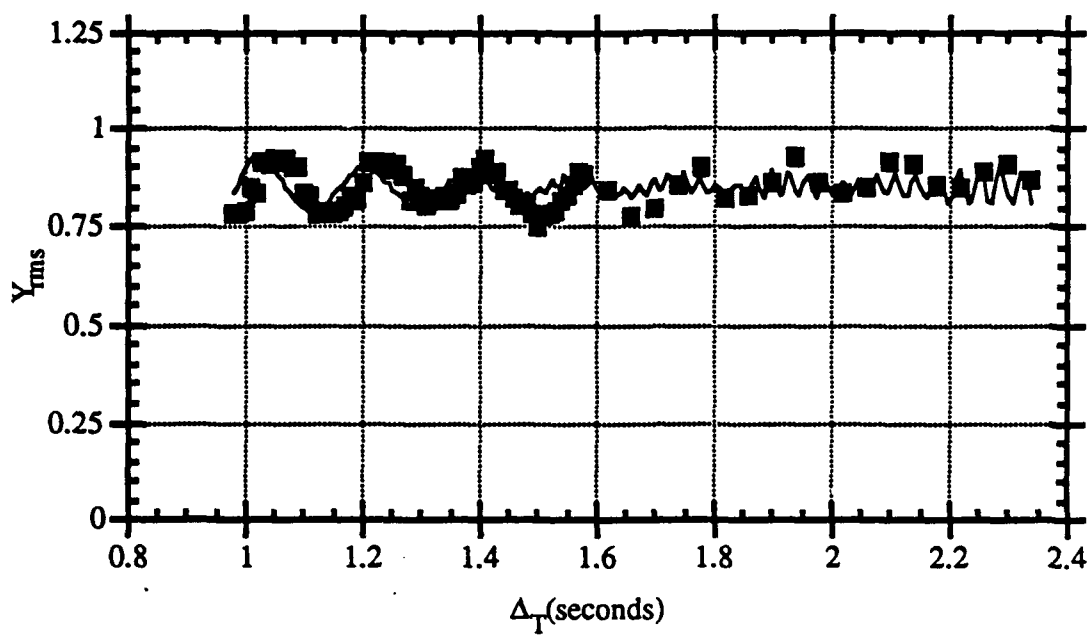
FIGURE 7. RMS displacement of the interface motion as a function of the total (convective + software) delay Δ_T for $\underline{k} = (1.25, 0.0)$. Y_{RMS} as predicted by the transfer function (—) and Y_{RMS} measured (■).
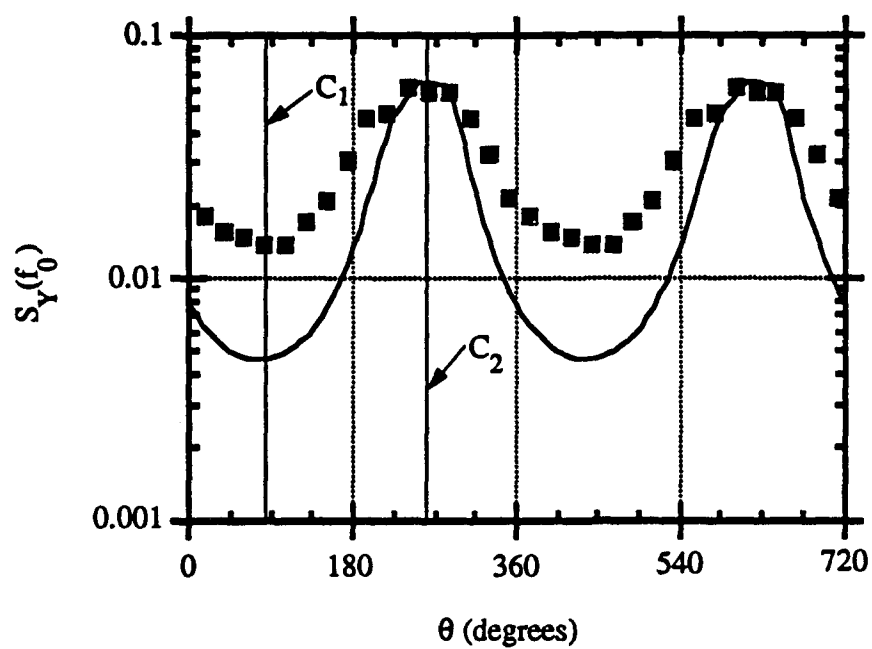
FIGURE 8. Spectral power S_Y at the natural frequency of the flow f_0: predicted (—) and measured (■).

The effect of the controller is studied by comparing the power spectrum of the interface motion $S_Y(f)$ when the flow is unforced (UF), and with feedback (F). One common feature of all the F spectra is the presence of sidebands around f_N. This is to be expected for a system with delays because the input U to the system is a function of $Y(t - \Delta_T)$ as was noted above. Therefore, since Δ is chosen such that

$$\Delta = \frac{n}{f_N} - \Delta_N$$

where n is the smallest integer such that $n \geq \Delta_N f_N$, it stands to reason that frequencies other than f_N will also be eigenfrequencies of the closed-loop system if

$$f_i = \frac{i}{\Delta_N + \Delta}$$

where i is *any* integer. As the delay time increases, more frequencies should appear in the spectrum corresponding to the eigenfrequencies observed by Reisenthel. Figure 9 illustrates this point. For a given $\underline{k} = (1.25, 0)$ $|G_{CL}|^2$ and S_Y are shown as Δ is increased from 0s (figure 9b) to 0.5s (figure 9c) to 1.0s (figure 9d). Figure 9a shows the unforced case. The power spectra support the conjecture that sidebands of f_N include discrete spectral peaks the separation of which is inversely proportional to the loop delay Δ_T.

Figure 10 shows the effect of different values of $\underline{k}$ on the squared magnitude of the model transfer function $|G_{CL}|^2$ and the power spectrum of the interface motion S_Y. The software delay Δ is held constant at a value of 0.08s, so that Δ_T is six complete cycles of the flow. The spectrum of the unforced interface shown in figure 10a is the same as in figure 5; it is shown again for reference. Figure 10b is the
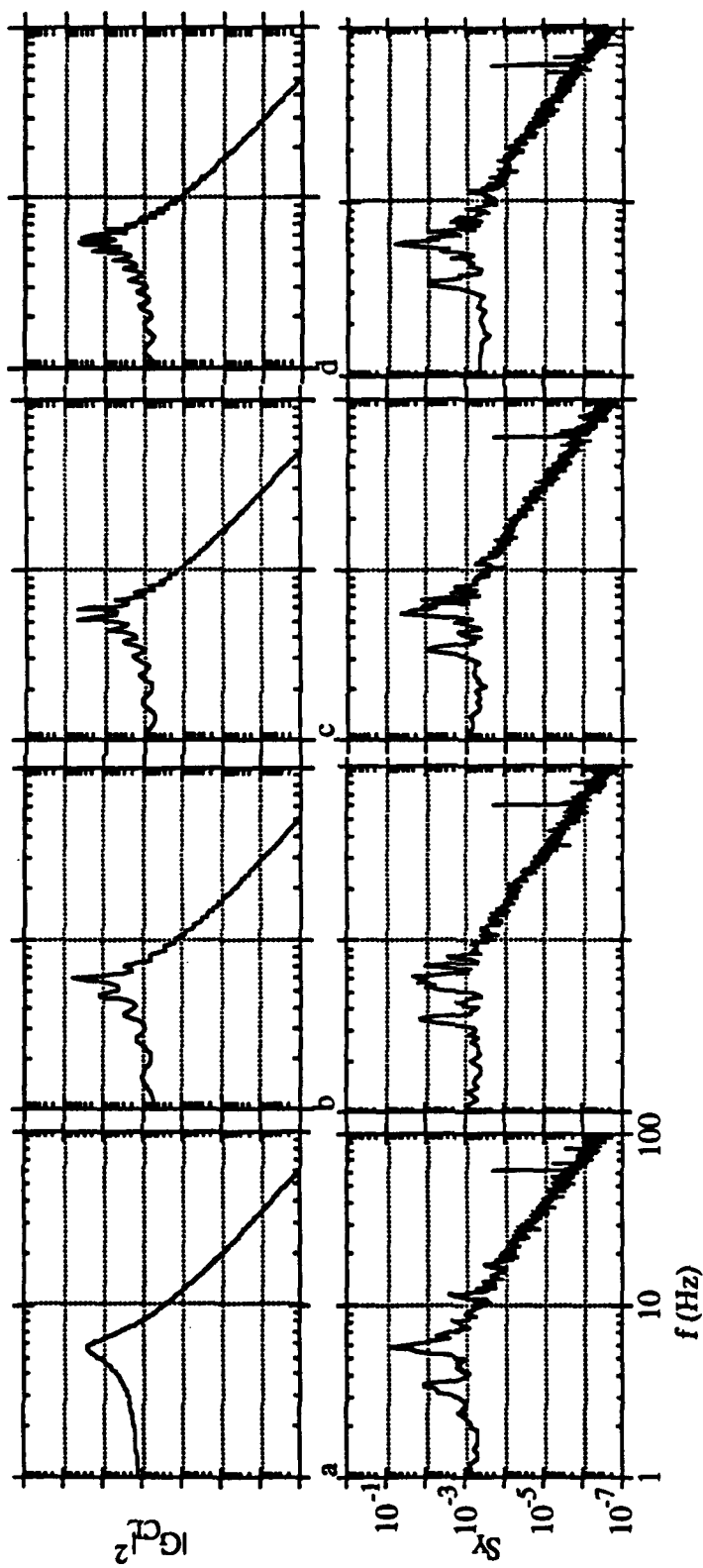
FIGURE 9. Pairs of $|G_{CL}(f)|^2$ (top) and $S_Y(f)$ (bottom) for (a) unforced, and Δ = (b) 0.0s, (c) 0.5s, and (d) 1.0s.
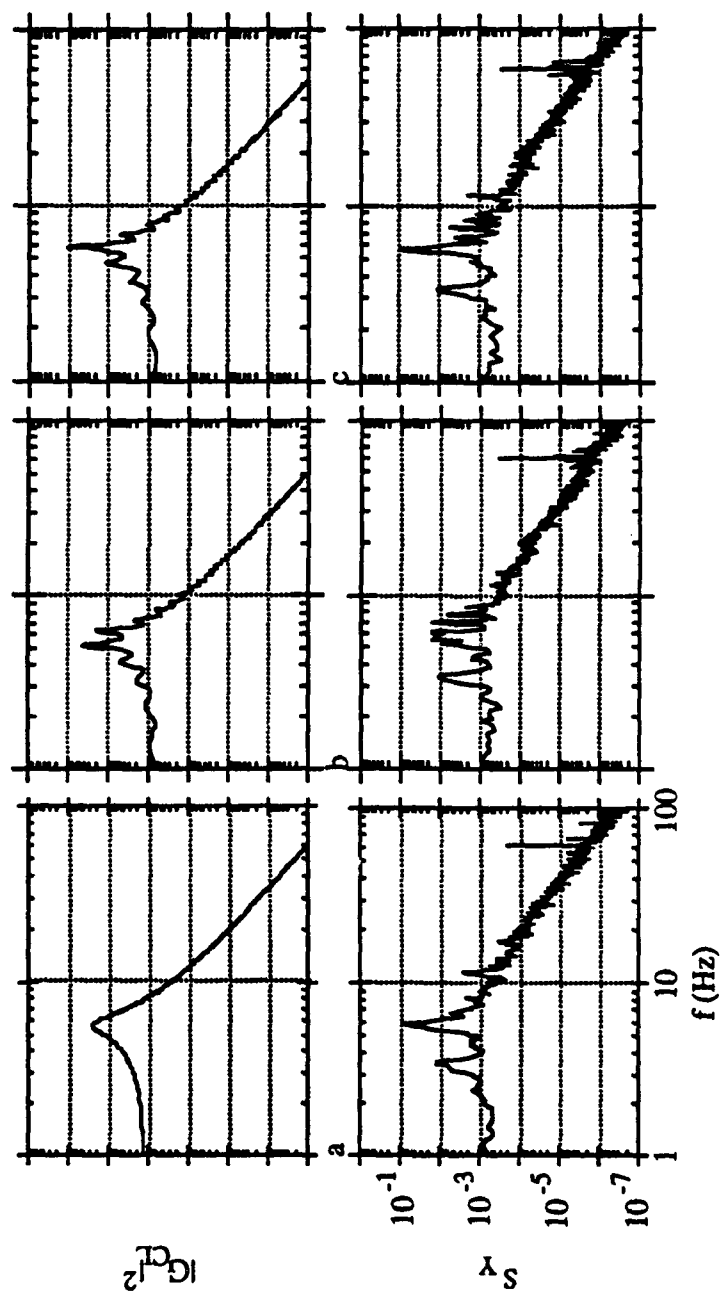
FIGURE 10. Pairs of $|G_{CL}(f)|^2$ (top) and $S_Y(f)$ (bottom) for (a) unforced, (b) feedback configuration C_1, and (c) feedback configuration C_2.

response of the interface to feedback configuration C_1, k^1 = (0.163, 1.239). This is a case which is chosen to attenuate f_N by amplifying the sidebands. Note that compared to the unforced case, there are a large number of spectral peaks around the natural frequency. The magnitude of these peaks is equal in magnitude to the peak at the natural frequency. The broadening of the spectrum in this region allows for its eventual attenuation farther downstream. This effect will be noted in §4.2 below. Figure 10c shows the case of k^2 = (-0.163, -1.239) which is chosen to amplify the natural frequency. In comparison with figure 10b, the spectral peak at f_N is larger while the spectral peaks within the side bands are considerably smaller in figure 10c. In fact, in figure 10c, the spectral peak at f_N is more than one order of magnitude larger than the spectral peaks at its sidebands.

Close examination of figure 5a shows that there is a discrete low frequency peak in the power spectrum below the natural frequency f_0. This frequency occurs at f_L = 3.40 Hz. Although this peak is roughly an order of magnitude weaker than that at f_0, under the right conditions it can have an effect on the flow. Figure 11a (also figure 5a) shows S_Y for the unforced flow. Figure 5b depicts a transfer function with f_L = 3.40 Hz and Q = 3.0. With this transfer function, it is possible to consider the effect of feedback on the low-frequency peak. Figure 12a (also figure 8) shows $S_Y(f_0)$ as measured and as predicted by the transfer function. Figure 12b shows $S_Y(f_L)$ as measured and as predicted by the transfer function. Again, although the magnitude of the peaks is inaccurate, the transfer function accurately predicts the minimum and maximum amplitude of the spectral peak at f_L. At the maximum of $S_Y(f_L)$, $S_Y(f_0)$ approaches a minimum. This suggests that θ = 15° (or k = (1.449, 0.324)) may be effective at introducing low frequencies into the flow as it attenuates f_0. This feedback configuration will hereinafter be referred to as configuration C_3.
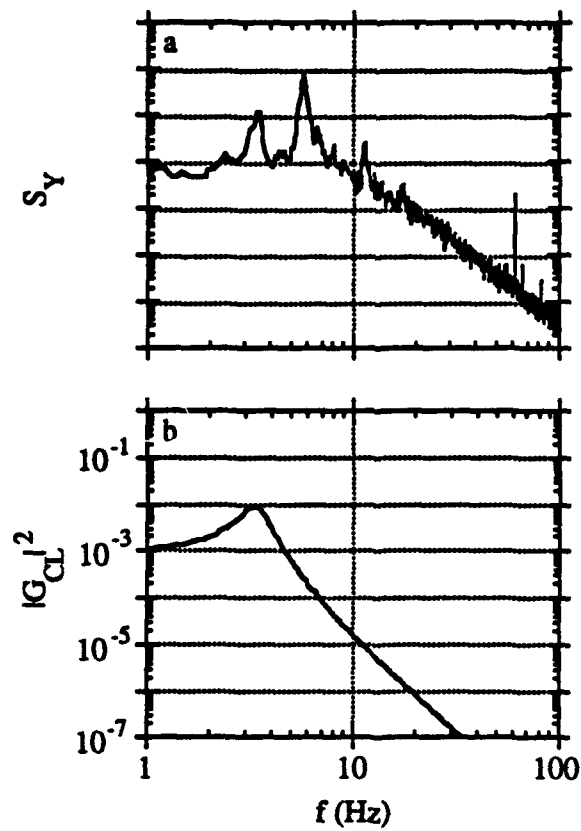
FIGURE 11. (a) The power spectrum of the unforced interface motion, and (b) analogous second-order transfer function for modelling low-frequency peak f_L.
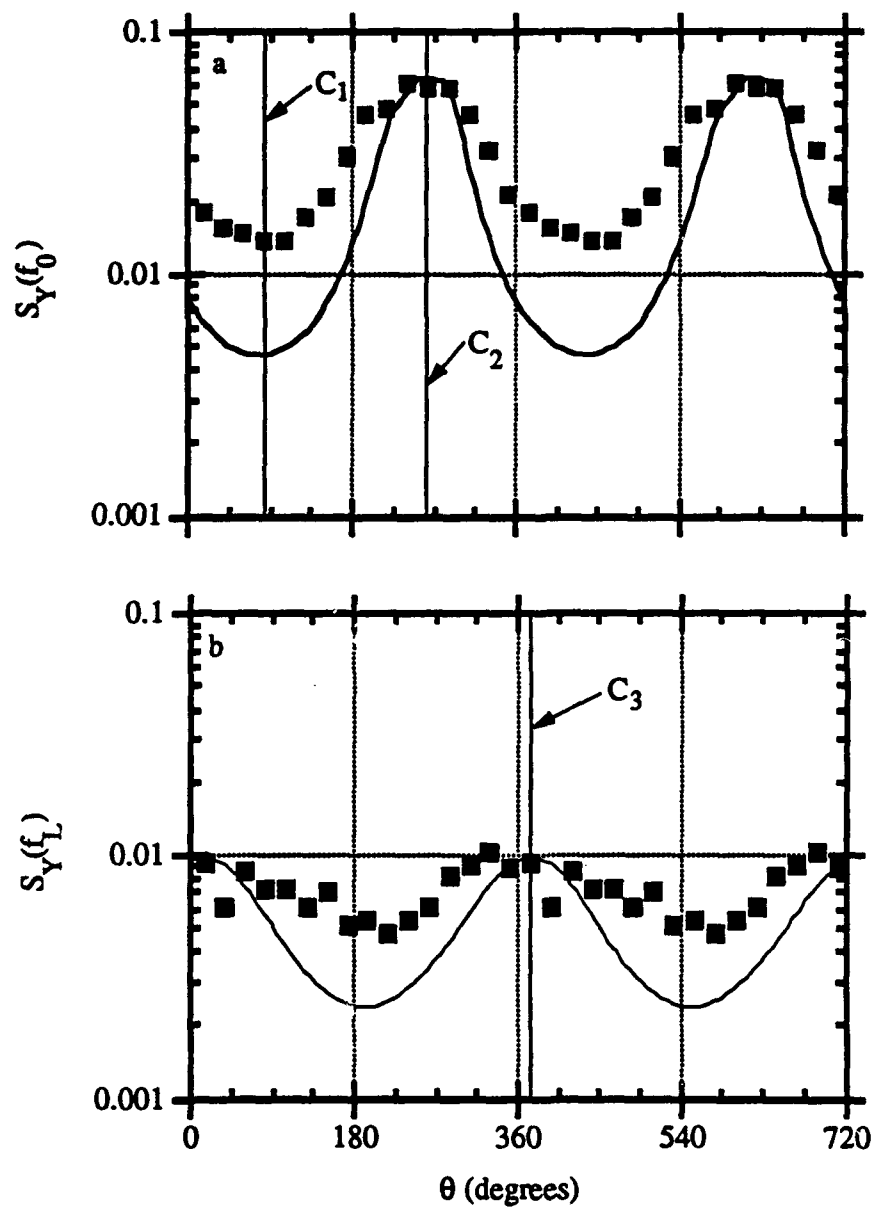
FIGURE 12. Spectral power S_Y predicted (—) and measured (■) at (a) the natural frequency f_0, and (b) the low frequency f_L.

Finally, figure 13a-b depicts pairs of the interface motion $y(t)$ and the wavelet transform of the interface motion $W(y(t))$ at a scale factor a corresponding to the natural frequency ($f_0 = 5.66$ Hz) for feedback configurations C_1 and C_2, respectively. The wavelet transform shows that configuration C_1 does attenuate the natural frequency by creating points where f_0 "drops out" of the spectrum. By contrast, figure 13b shows that configuration C_2 creates a resonance condition in which f_0 is always present. Notice that there are only three drop-out points in 40s for C_2, compared with a drop-out point every ~1.0s for C_1. The drop-out points for configuration C_1 occur at a time roughly corresponding to Δ_T, suggesting that the effect of antiresonance feedback is to set up an amplitude-modulated waveform with an envelope duration approximately that of the total system delay.
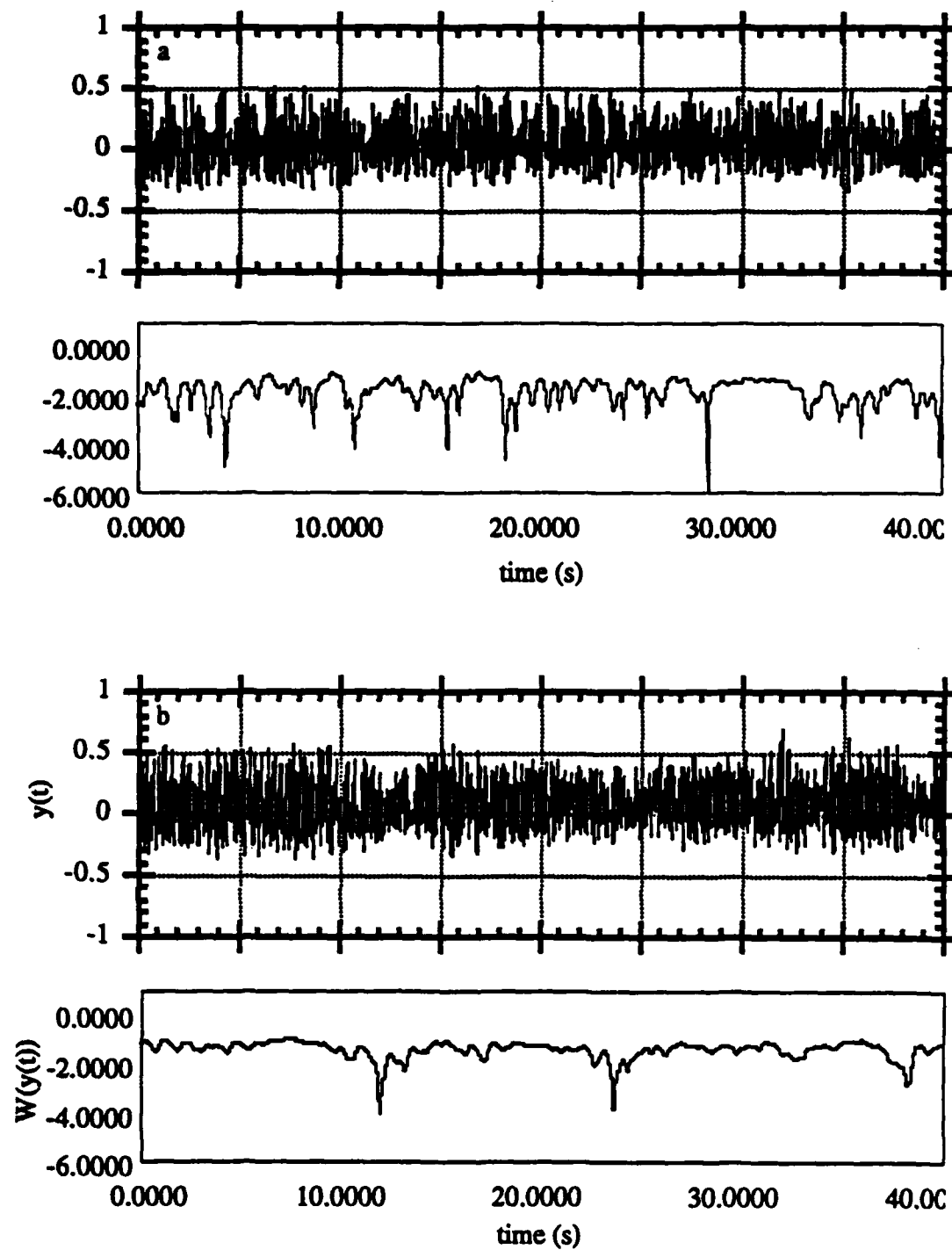
FIGURE 13. y(t) and W(y(t)) over a period of 40s for (a) configuration C_1 and (b) configuration C_2.

4. The effect of spanwise-uniform feedback on mixing

4.1. The baseline flow

To obtain a baseline for the feedback experiments, open-loop measurements were taken for the following configurations: unforced, SU, f = 5.66 Hz, and SP, f = 5.66 Hz (head and tail). The open-loop forcing frequency of f = 5.66 Hz is chosen because it is the natural frequency of the flow near the flow partition.

Figure 14a-c depicts three composites (at x = 10.16 cm, 15.24 cm, and 20.32 cm, respectively) of the average temperature profile T(y), a grayscale raster image of the instantaneous temperature distribution T(y,t) over a period of 1.28s, and a contour plot of *pdf*(T,y) plotted on a logarithmic scale (i.e., $\log_{10}(pdf(T,y))$). The contours of $\log_{10}(pdf(T,y))$ begin at -1.0 [$\log_{10}(^{\circ}C^{-1})$] with a contour increment of 0.1 [$\log_{10}(^{\circ}C^{-1})$]. The contours are sufficient to cover the maximum level of *pdf*. The flow appears to have more small-scale motions than the corresponding case (figure I.3) when the side walls are in the open-loop configuration. This manifests itself in an increase in the levels of *pdf*(T,y) at x = 15.24 cm and 20.32 cm (figures 14b-c, respectively).

This increase in mixed fluid also apparent in PM(x) for the unforced flow (figure 15a). Although the shape of the curve is similar to that in WGI figure 16a, PM ranges from 20% to 40% higher with the side walls in the closed-loop position. This is to be expected: the walls were put in this position to allow amplification over a broader band of frequencies. In addition, the flow should be more receptive to naturally-occurring three-dimensional disturbances.

Figure 15b depicts the percentage change in PM (relative to the unforced flow) for SU, f = 5.66 Hz and SP, f = 5.66 Hz (head and tail). Forcing with SU, f
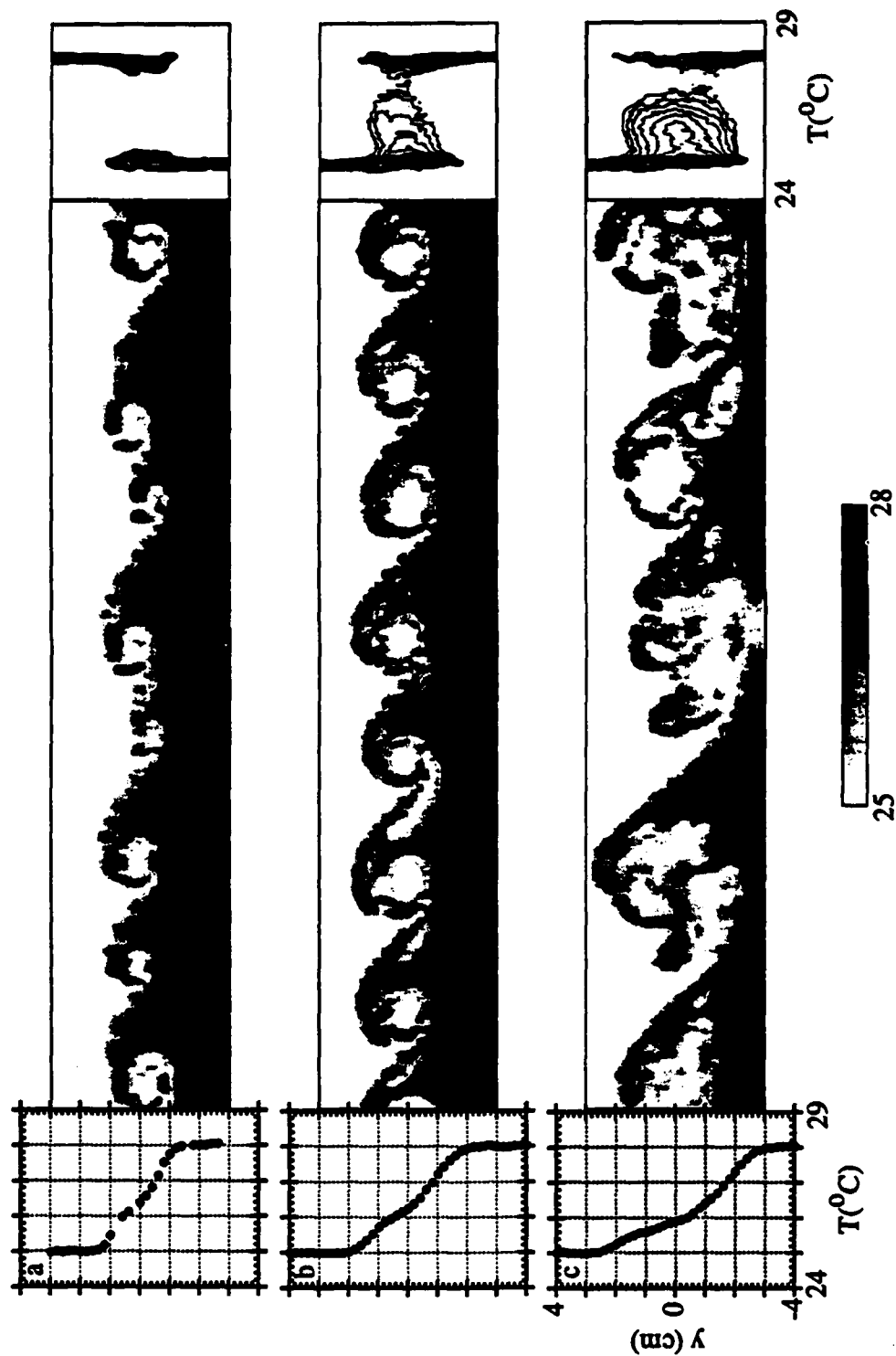
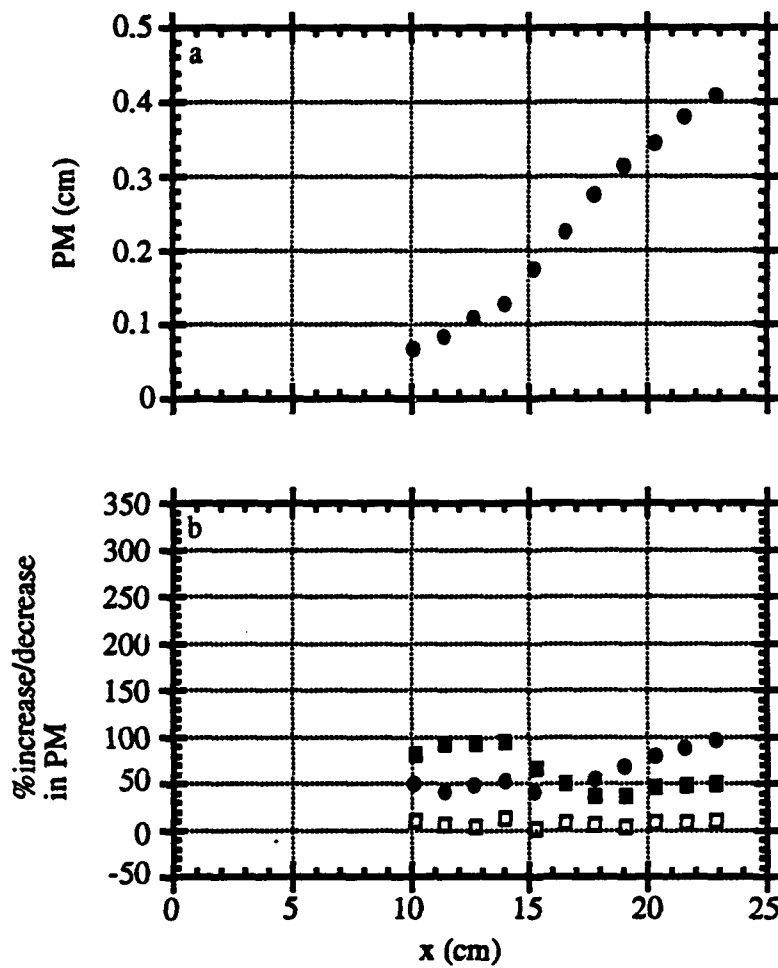FIGURE 14. T(y), T(y,t), and *pdf*(T,y) for the unforced flow at *x* = (a) 10.16 cm, (b) 15.24 cm, and (c) 20.32 cm.

FIGURE 15. (a) PM(x) for the unforced flow, (b) % increase/decrease in PM for SU, f = 5.66 Hz (□) and SP, f = 5.66 (head) (●) and (tail) (■).

= 5.66 Hz results in an increase in the performance measure of approximately 10% at all streamwise stations. When the flow is forced with SP, f = 5.66 Hz, mixed fluid is produced initially at the tail of the streamwise vortex. There is an increase of 80-90% until x ~ 14 cm, where the increase in PM levels off until it reaches a level of approximately 50% above the unforced flow at x = 22.86 cm. At the head of the streamwise vortex, PM is increased by 50% for 10.16 cm $\leq$ x $\leq$ 17.78 cm after which point the improvement reaches a value of 95% at x = 22.86 cm.

4.2. Controller effect on the flow

The power spectrum $S_{PM}(x,f) = |F(PM(x,t))|^2$ gives a good measure of the spectral components of the temperature (and possibly the velocity) field, and more specifically the frequencies associated with mixing at downstream locations. The power spectrum $S_{PM}(x = 15.24$ cm, f) is shown in figure 16 for the unforced case and for feedback programs C_1, C_2, and C_3. The unforced case (figure 16a) shows not only a strong peak at the f_N, but also a strong spectral peak at $0.6f_N$. This is consistent with the idea that the mixing layer grows with downstream distance by pairing interactions between the primary vortical structures. At this downstream location, the flow has already begun pairing and hence the amplitude of the subharmonic is of the same order as that of the fundamental.

Plots of S_{PM} show the effect of the feedback much more strongly than the plots of S_Y. For example, figure 16b corresponds to C_1 (i.e., k^1 = (0.163, 1.239)). Notice that the features of S_Y for this case (figure 10b) are essentially accentuated. The spectrum is filled with a number of spectral peaks around the natural frequency, none of which can be classified as dominant - in fact, the peaks that are there are quite weak. In contrast, figure 10c shows a very strong fundamental frequency.
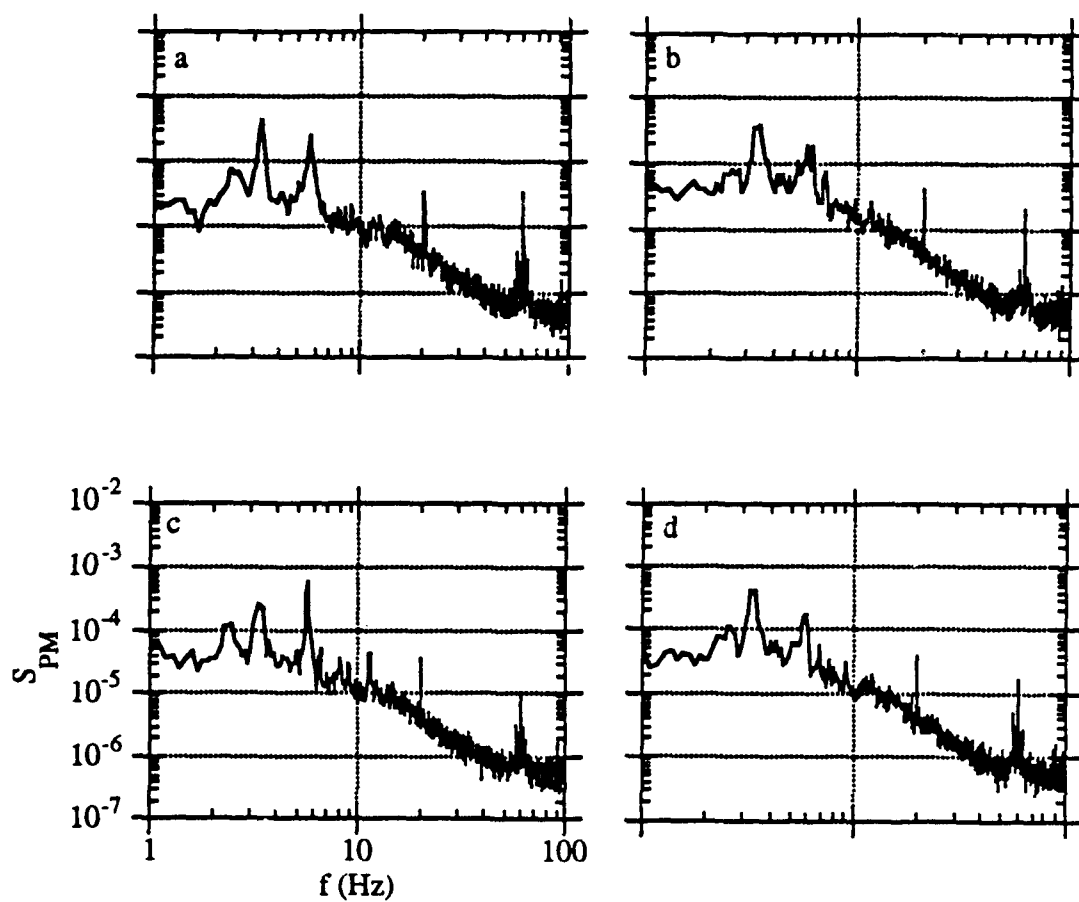
FIGURE 16. $S_{PM}(f)$ for (a) unforced, (b) C_1, (c) C_2, and C_3. $x = 15.24$ cm.

This suggests that $k^2 = (-0.163, -1.239)$ does indeed amplify the natural frequency. This peak is roughly two times that of peak at $0.6f_N$, which is a substantial increase over the unforced case, where the peak at $0.6f_N$ is slightly higher than the peak at f_N. Finally, figure 16d depicts Sp_M for feedback configuration C_3 (designed to amplify f_L and attenuate f_0). In this case, the fundamental frequency f_0 is almost completely attenuated. The subharmonic frequency $0.6f_N$, however, is amplified to a level significantly higher than f_0.

The effect of feedback on the flow can be assessed by considering plots of $T(y)$, $T(y,t)$, and $pdf(T,y)$ as was done in figure 14. In what follows, the shear layer is subjected to feedback configurations C_1 (figure 17), C_2 (figure 18), and C_3 (figure 19).

Feedback configuration C_1 is designed to attenuate the natural frequency of the flow by amplifying the sidebands. The instantaneous temperature distributions $T(y,t)$ show that the flow does indeed appear quite irregular at all streamwise stations. The size, cross-stream position, and passage frequency of the primary vortical structures all vary significantly. This irregularity also results in smoother average temperature profiles $T(y)$ than for the unforced flow. It is postulated that feedback configuration C_1 enhances mixing by creating large structures of mixed fluid (see V_1 in figure 17c). Notice that the mixed fluid in V_1 is mixed at a temperature close to the temperature of the high-speed stream T_1. The large strain rate in the fluid layers in vortices of this size result in a large surface area over which mixing can occur. The contours of $pdf(T,y)$ at $x = 15.24$ cm (figures 17b) show that, compared to the unforced flow, mixing takes place over a broader cross-stream extent. However, most of the mixed fluid appears concentrated at lower temperatures.
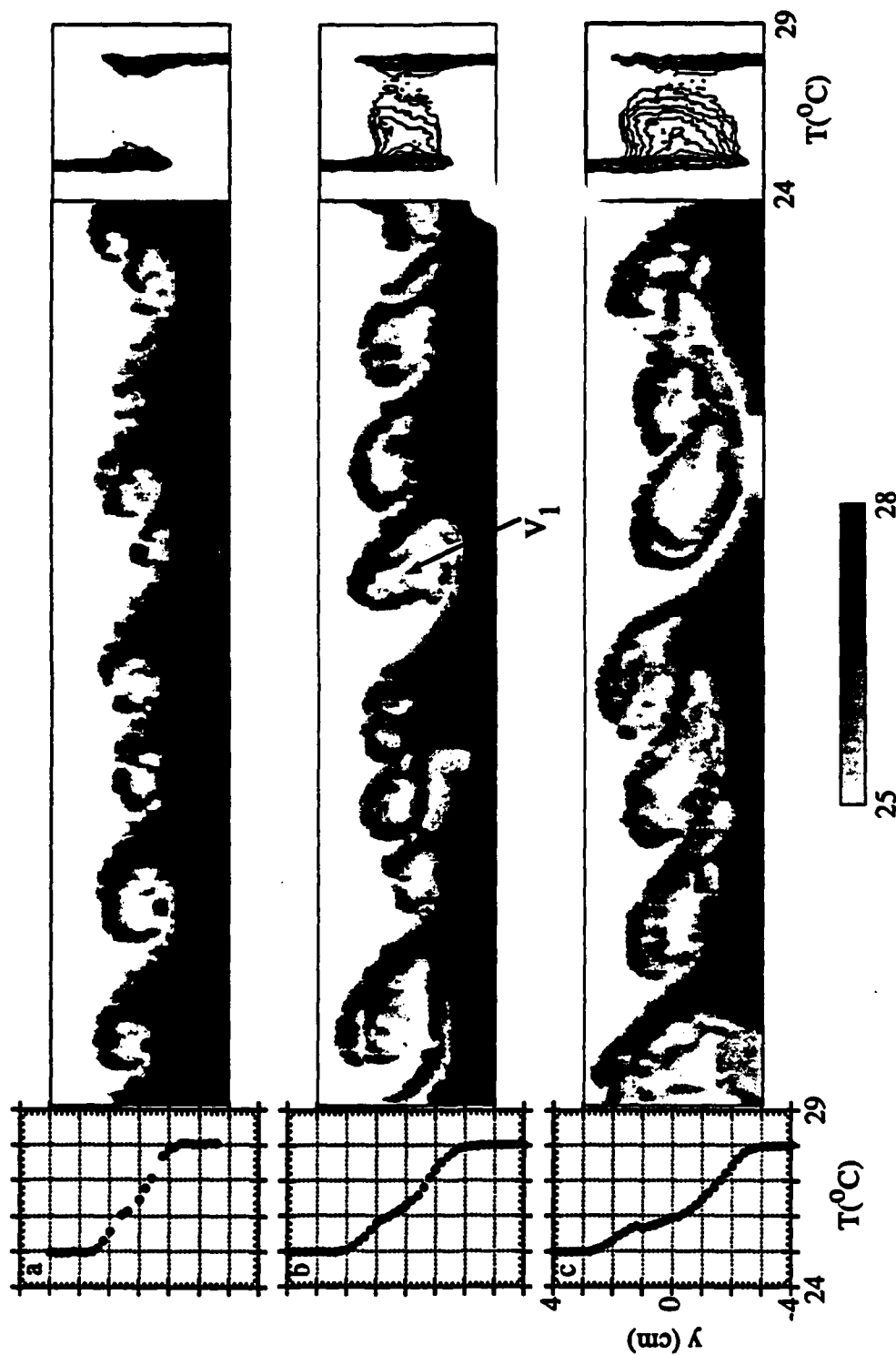
FIGURE 17. T(y), T(y,t), and *pdf*(T,y) for feedback configuration C_1 at x = (a) 10.16 cm, (b) 15.24 cm, and (c) 20.32 cm.

In strong contrast to configuration C_1, configuration C_2 (figures 18a-c) is apparently similar to strong forcing at a frequency which is close to f_N, as may be judged by the minimal variations in the size and passage frequency of the primary vortices throughout the streamwise domain of measurements. This results in sharper bends in the average temperature profiles $T(y)$ than are observed either for the unforced flow or feedback configuration C_1. Configuration C_2 enhances mixing by rolling the entrained fluid into small, tightly-wound vortices (V_2 in figure 18b). These vortices entrain fluid from both free streams and strain it into thin diffusion layers within the cores of the vortices. Mixed fluid is produced at a broader range of temperatures than in the case of C_1, which tends to mix fluid close to the high-speed temperature. The contours of $pdf(T,y)$ at $x = 15.24$ cm and $x = 20.32$ cm (figures 18b-c) reflect this. Unlike feedback configuration C_1 or the unforced flow, the lowest contour $\log_{10}(pdf(T,y)) = -1.0$ [$\log_{10}({}^\circ C^{-1})$] span the entire temperature distribution from T_1 to T_2.

Configuration C_3 (figure 19a-c) amplifies a low frequency at $f_L = 0.6f_0$, and the plots of $T(y,t)$ show that low frequencies near the subharmonic are indeed induced by this mode of feedback. Although at $x = 10.16$ cm (figure 19a) the vortices have not paired, alternating primary vortices are displaced in the cross-stream direction. By 15.24 cm, the vortices are beginning to pair, and by 20.32 cm (figure 19c) the pairing process is virtually completed. Note that approximately 4 1/2 large vortices are present over the period of 1.28s, giving a vortex passage frequency for this short time record of approximately 3.52 Hz, which is close to f_L (3.40 Hz). The plots of $pdf(T,y)$ at all streamwise stations are qualitatively very similar to those for C_1; fluid is well mixed across the cross-stream extent of the layer, but most of the mixing occurs at temperatures close to that of the high-speed stream T_1.
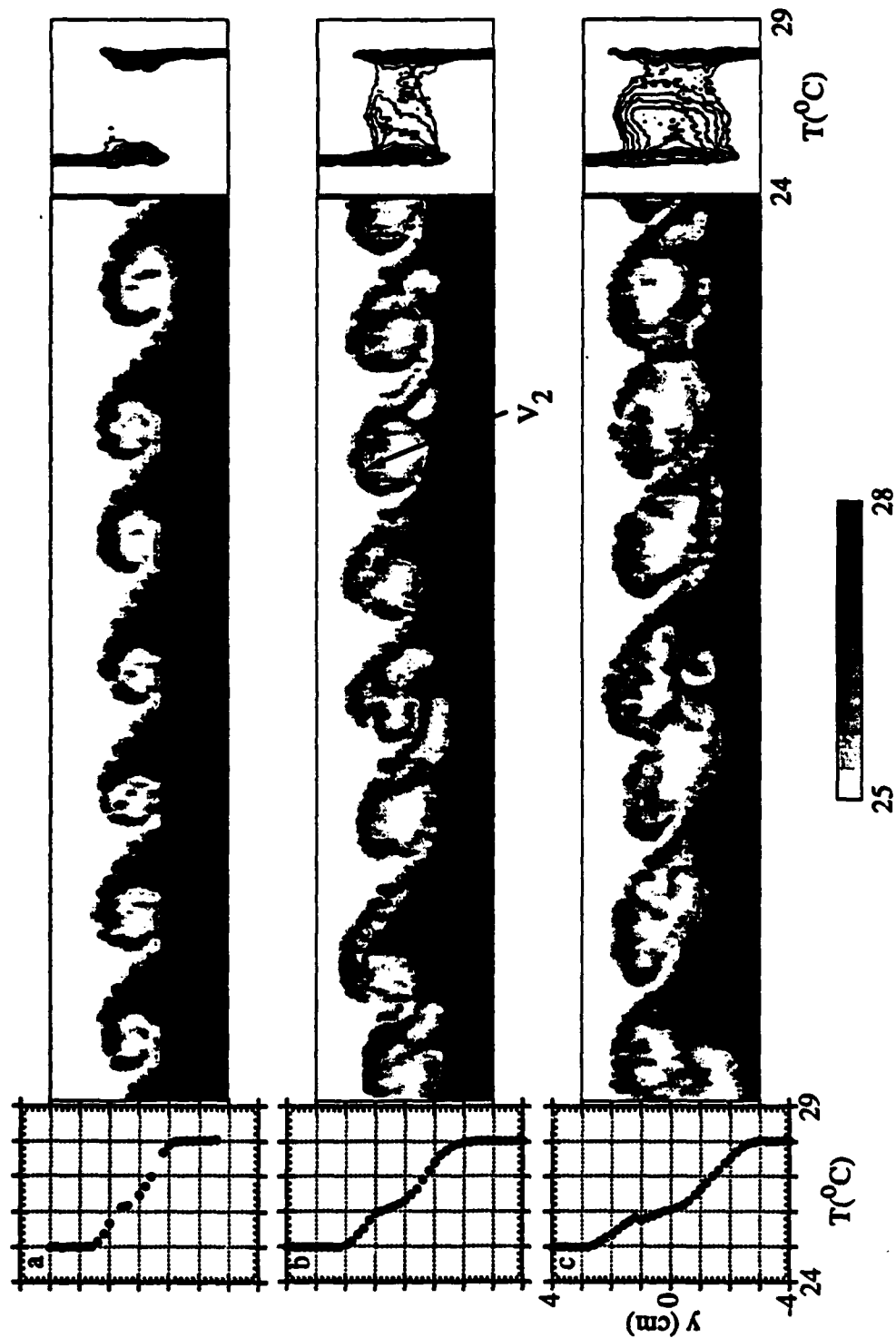
FIGURE 18. T(y), T(y,t), and *pdf*(T,y) for feedback configuration C$_2$ at x = (a) 10.16 cm, (b) 15.24 cm, and (c) 20.32 cm.
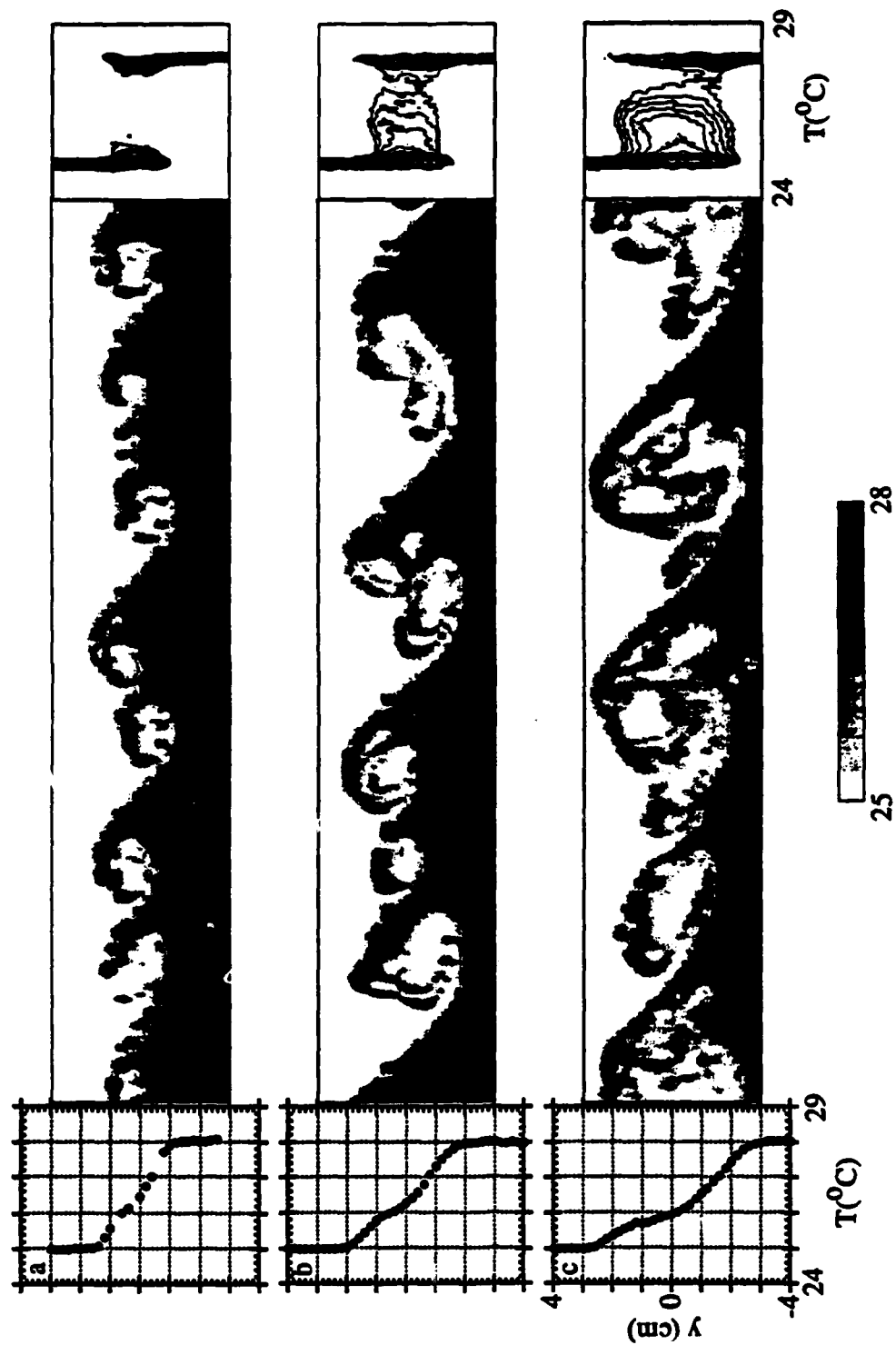
FIGURE 19. T(y), T(y,t), and *pdf*(T,y) for feedback configuration C_3 at x = (a) 10.16 cm, (b) 15.24 cm, and (c) 20.32 cm.

Figure 20a-f shows the percentage increase in PM as a function of $\theta =$ $\tan^{-1}(k_2/k_1)$ at x = 10.16 cm, 12.70 cm, 15.24 cm, 17.78 cm, 20.32 cm, and 22.86 cm, respectively. The levels obtained with SU, f = 5.66 Hz open-loop excitation are indicated by dashed lines. This figure shows two peaks corresponding to C_1 ($\theta =$ 82.5°) and C_2 ($\theta =$ 262.5°). Configuration C_1, however, appears to be most advantageous from the point of view of maximizing PM. At x = 10.15 cm (figure 20a) and x = 12.70 cm (figure 20b) C_1 results in significantly more mixed fluid than SU, f = 5.66 Hz. At x = 10.16 cm, C_1 results in and increase in PM of approximately 15% over the unforced flow, compared to 9% for SU, f = 5.66 Hz. By x = 15.24 cm (figure 20c) the effect of feedback is attenuated somewhat. Configuration C_1 results in an increase in PM of 4% over the unforced flow, compared to 2% for SU, f = 5.66 Hz. At x = 17.78 cm, 20.32 cm, and 22.8´ ⌐m (figures 20d-f), the maxima of PM are somewhat *lower* than the corresponding SU, f = 5.66 Hz. Finally, it is interesting to notice that $\theta = 150°$ (noted as configuration C_4 in figure 20a) results in minima of PM at all streamwise stations. In fact, this feedback configurations results in a level of PM either less than or approximately equal to that of the unforced flow at all x stations.

Since mixing occurs where there are strong temperature gradients, it is interesting to consider the scalar dissipation $\nabla T \cdot \nabla T(x,t)$ (i.e., Dahm, Southerland, and Buch (1991)). Since the data is in the form of $T(y,t)$, it is necessary to approximate $\nabla T \cdot \nabla T(x,t) = (\partial T/\partial y)^2 + (1/U_C)^2 (\partial T/\partial t)^2$.

Figure 21a-c shows pairs of $S_T(f;y)$ (left) and the scalar dissipation over a period of 1.28s (right) at x = 17.78 cm for the feedback configurations C_1 (figure 21a), C_2 (figure 21b), and C_4 (figure 21c). The power spectra S_T are plotted on a logarithmic scale with arbitrary units. The two contours are at $\log_{10}(S_T) = 0.0$ and
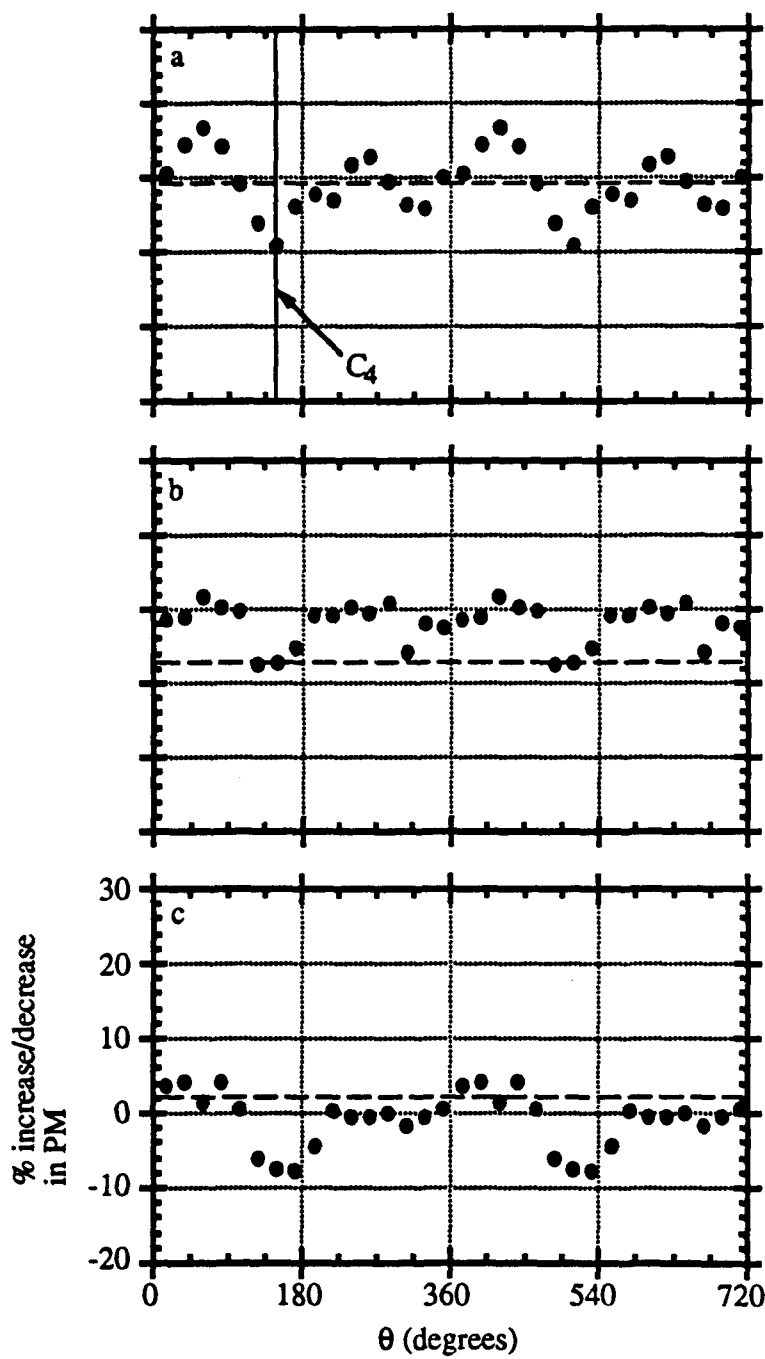
FIGURE 20. **PM**(θ) for SU feedback at x = (a) 10.16 cm, (b) 12.70 cm, and (c) 15.24 cm.
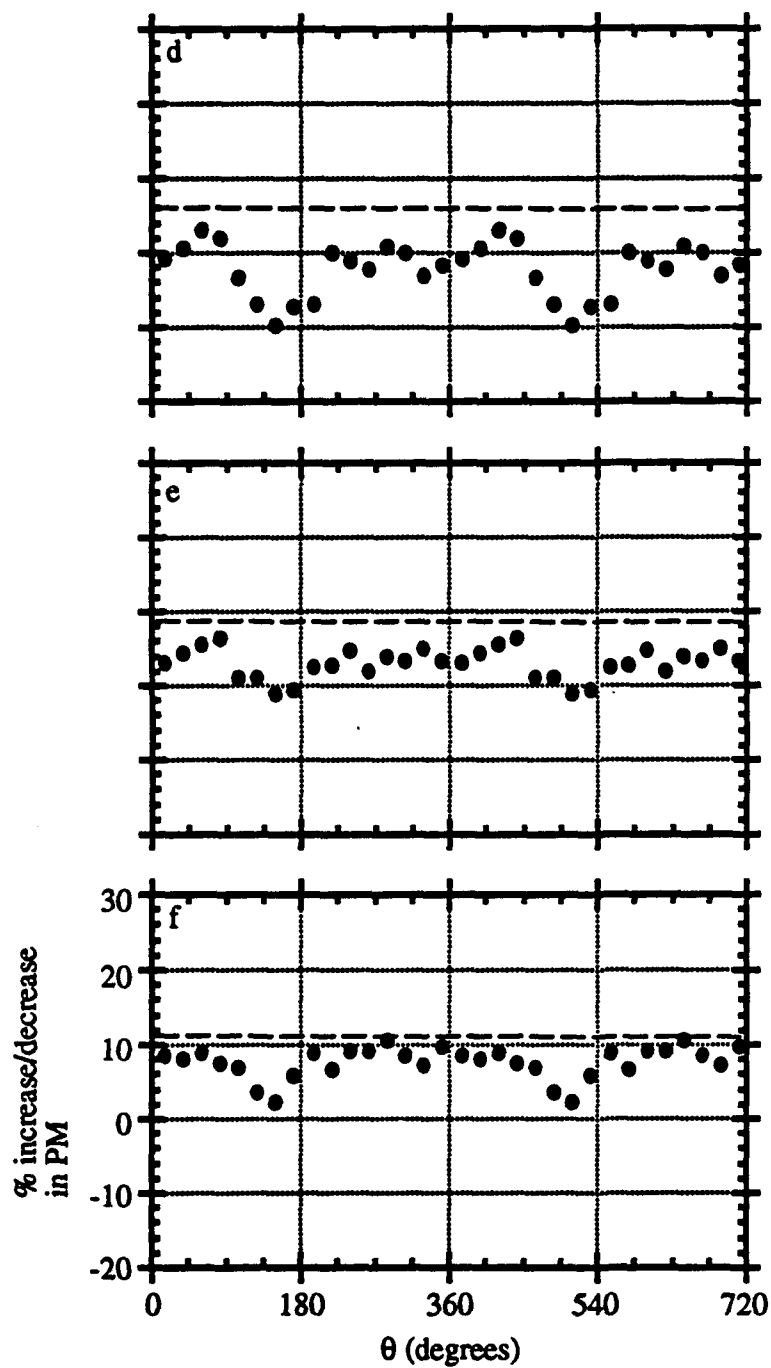
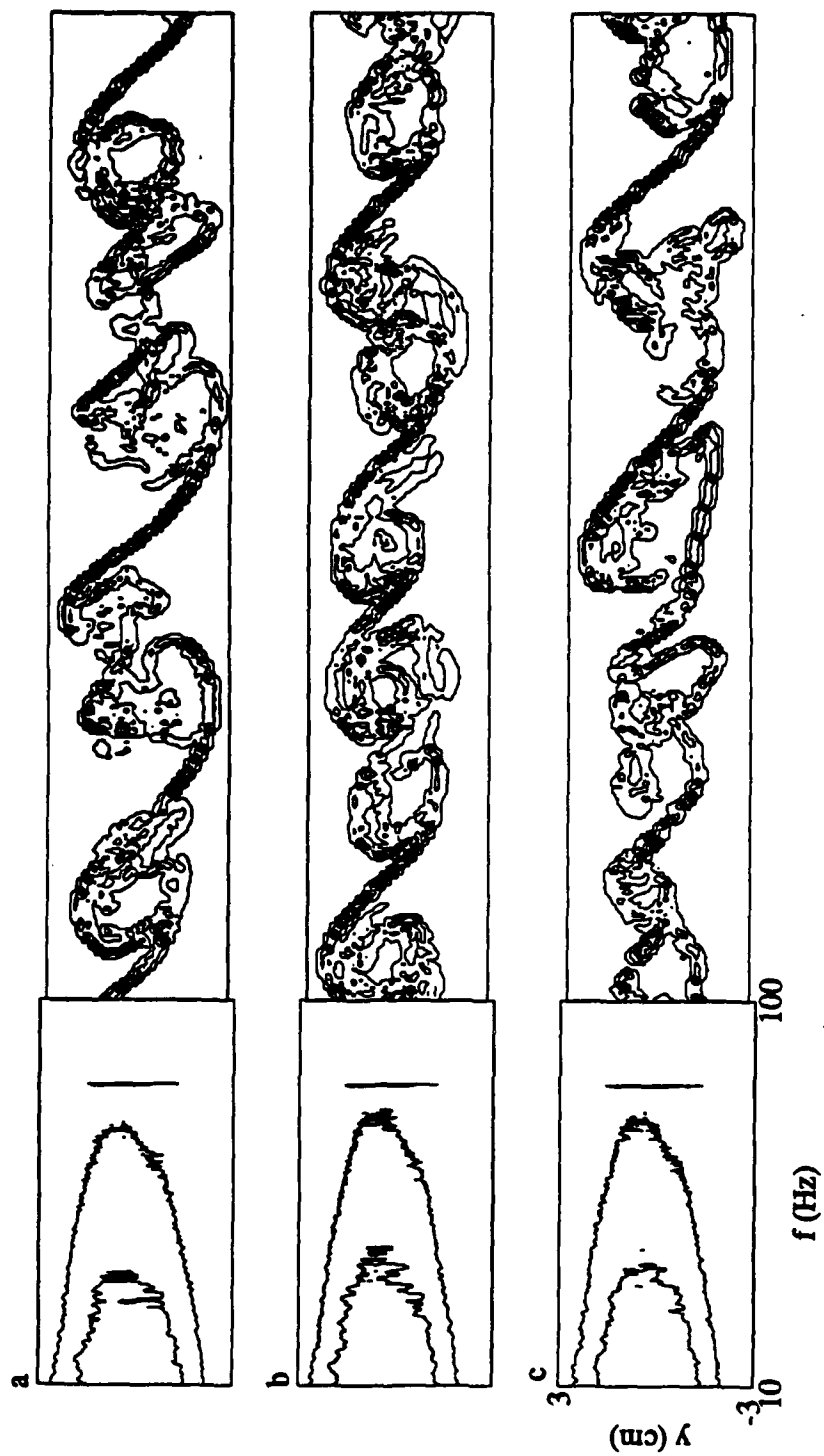FIGURE 20-*Continued.* PM(θ) for SU feedback at x = (a) 10.16 cm, (b) 12.70 cm, and (c) 15.24 cm.

FIGURE 21. Pairs of S_T (left) and scalar dissipation (right) at $x = 17.78$ cm for (a) C_1, (b) C_2, and (c) C_4.

$\log_{10}(S_T) = 0.654$. The contours of the scalar dissipation range from a minimum value of 10.0 $[^\circ C/cm]^2$ to a maximum of 210.0 $[^\circ C/cm]^2$ at a contour increment of 40 $[^\circ C/cm]^2$. As was mentioned previously, configuration C_1 enhances mixing by stretching the layer and allowing large patches of mixed fluid to form; whereas configuration C_2 concentrates rolled fluid layers into the primary vortices where mixing can occur. Comparison of $S_T(f;y)$ for these two cases shows that spectral power extends significantly further into the small-scale region for configuration C_2 (figure 21b) than for configuration C_1. By contrast, the small-scale motions occur over a larger cross-stream extent for configuration C_1. The scalar dissipation for these two cases illustrate this point: in configuration C_1, the small scales are combined into large structures, whereas in configuration C_2, the small scales are concentrated into small, regularly-spaced structures. Configuration C_4 (figure 21c), which resulted in minima of PM at all streamwise stations, depicts a cross-stream extent of $S_T(f;y)$ comparable to C_2 but an extension into high values of f that is comparable to C_1. Essentially it combines the worst features of the other two feedback configurations and hence results in a significantly lower level of PM.

Figure 22a-c depicts three composites of T(y), T(y,t), and pdf(T,y) (as in figure 14 et al) for feedback configuration C_4. The plots of pdf(T,y) at x = 15.24 cm (figure 22b) and 20.32 cm (22c) also depict the deficiency in mixing for this case. Compared with configuration C_1, configuration C_4 shows less mixed fluid towards the low-speed stream. Furthermore, configuration C_4 shows lower values of pdf at all values of T than configuration C_2.

The streamwise variation of mixedness can be inferred from the integral performance measure PM(x). Figure 23 shows a plot of the percentage change of PM (relative to the unforced flow) for SU, f = 5.66 Hz (for comparison), C_1 (which occurs at the absolute maximum of PM(θ)), C_2 (a local maximum of PM(θ)), and
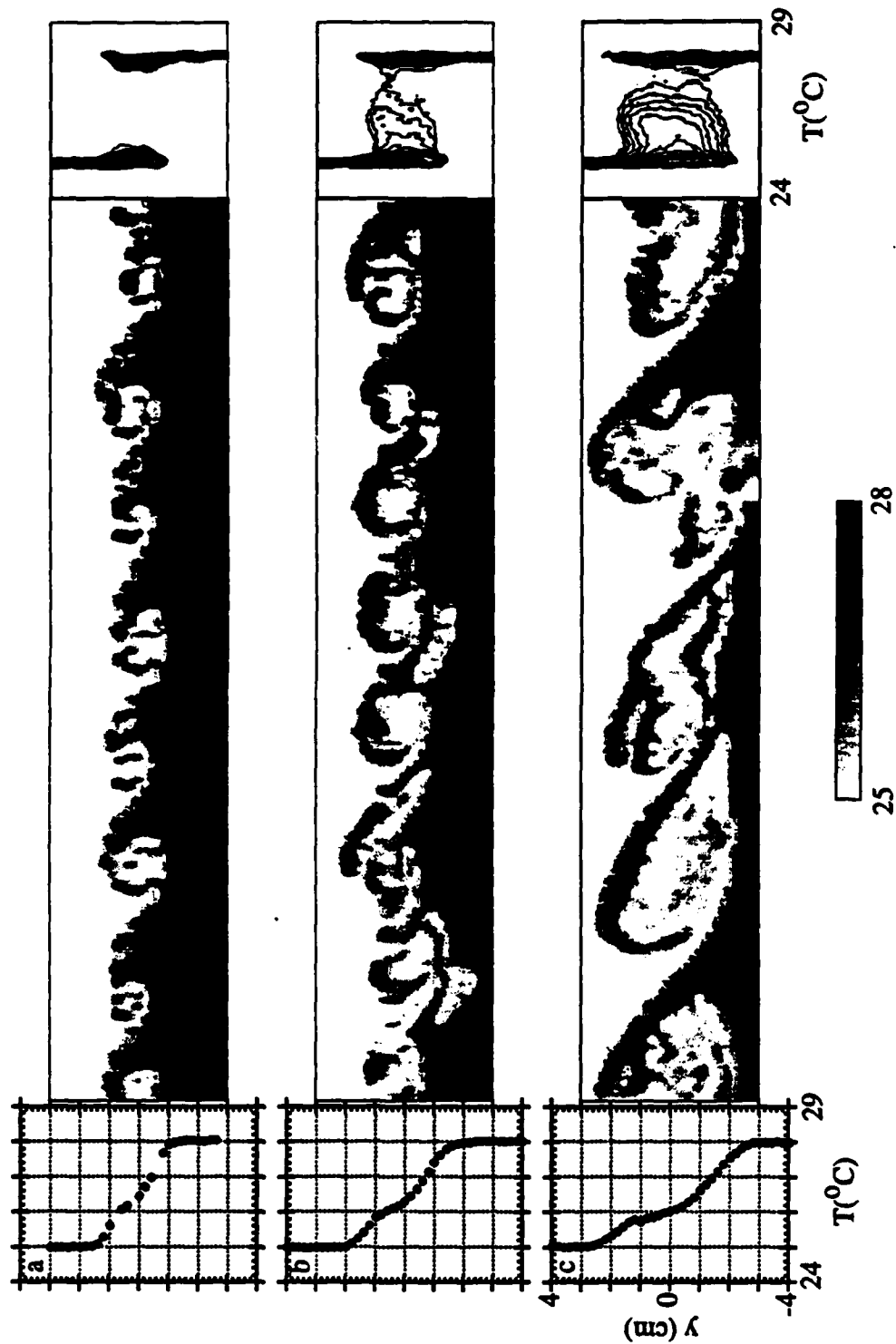
FIGURE 22. T(y), T(y,t), and *pdf*(T,y) for feedback configuration C4 at x = (a) 10.16 cm, (b) 15.24 cm, (c) 20.32 cm.
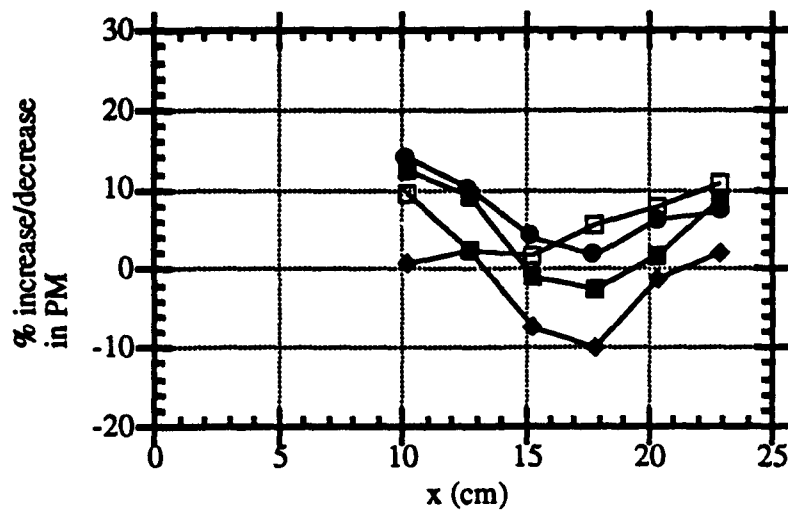
FIGURE 23. % chance in PM relative to unforced for SU, f = 5.66 (a), C_1 (●), C_2 (■), and C_4(◆).

C_4 (the local minimum of $PM(\theta)$). Notice that for the feedback cases, the percentage change in $PM(x)$ has a minimum between $x = 15$-20 cm while the open-loop case has a minimum just upstream of this location. Hence, feedback configurations C_2 and particularly C_1 can accrue a greater increase in PM than open loop forcing at streamwise stations corresponding to $x \leq 17$ cm (approximately). For $x \geq 17$ cm, SU, $f = 5.66$ Hz forcing results in a higher level of mixedness than the feedback cases. Finally, it should be noted that the curves for configurations C_1 and C_2 are nearly coincident at upstream stations but that C_1 results in a significantly higher level of PM at downstream stations. Configurations C_4 (as expected) results in a the lowest level of mixedness throughout the measurement domain.

It is instructive to consider what may broadly be construed as moments of $pdf(T,y)$. The total mixed fluid in the layer is obtained by

$$M^0 = \int_{T_1+\epsilon}^{T_2-\epsilon} \int_{-\infty}^{+\infty} pdf(T,y)\, dy\, dT.$$

The average temperature of mixed fluid within the layer is obtained by

$$T_{cent} = M_T^1 = \frac{1}{M_0} \int_{T_1+\epsilon}^{T_2-\epsilon} \int_{-\infty}^{+\infty} T\, pdf(T,y)\, dy\, dT.$$

The average y-position of mixed fluid within the layer is obtained by

$$y_{cent} = M_y^1 = \frac{1}{M_0} \int_{T_1+\epsilon}^{T_2-\epsilon} \int_{-\infty}^{+\infty} y\, pdf(T,y)\, dy\, dT.$$

And finally, it is possible to construct higher-order moments with respect to T and y in the following manner:

$$M_T^i = \frac{1}{M^0} \int_{T_1+\epsilon}^{T_2-\epsilon} \int_{-\infty}^{+\infty} (T - T_{cent})^i \, pdf(T,y) \, dy \, dT$$

and

$$M_y^i = \frac{1}{M^0} \int_{T_1+\epsilon}^{T_2-\epsilon} \int_{-\infty}^{+\infty} (y - y_{cent})^i \, pdf(T,y) \, dy \, dT.$$

For all of these integrals, $\epsilon = 0.25$ °C to ensure that the lobes of unmixed fluid do not contribute to the integral. Deemed to be of particular interest are the total mixed fluid (M_0), the average mixed fluid temperature T_{cent} (M_T^1), the average cross-stream position of mixed fluid y_{cent} (M_y^1), σ_y (($M_y^2)^{1/2}$), the skewness with respect to T skew$_T$ (M_T^3/σ_T^3), and the kurtosis with respect to T kurtosis$_T$ (M_T^4/σ_T^4).

Figure 24a-f depicts the total mixed fluid (figure 24a), T_{cent} (figure 24b), y_{cent} (figure 24c), σ_y (figure 24d), skew$_T$ (figure 24e), and kurtosis$_T$ (figure 24f) for the unforced flow. The total mixed fluid (figure 24a) follows trends similar to PM(x) (figure 15a). Figure 24b shows that the average temperature of mixed fluid in the layer changes significantly with downstream distance, declining from $T_{cent} \approx$ 26.33 °C at x = 10.16 cm to $T_{cent} \approx$ 26.13 °C at x = 22.86 cm. The average cross-stream location of mixed fluid (figure 24c) is consistent with the idea that the layer grows by entraining low-speed fluid and thus bending into this stream. The centroid y_{cent} falls linearly from y_{cent} = 0.2 cm at x = 12.70 cm to y_{cent} = -0.4 cm at x = 22.86 cm. As the layer grows with downstream distance, the cross-stream extent of mixing also increases, as indicated by σ_y(x) (figure 24d). This measure also grows linearly from x = 10.16 cm to x = 22.86 cm, from a value of σ_y = 0.65 cm to σ_y = 1.30 cm. Figure 24e shows that the mixed fluid density becomes increasingly
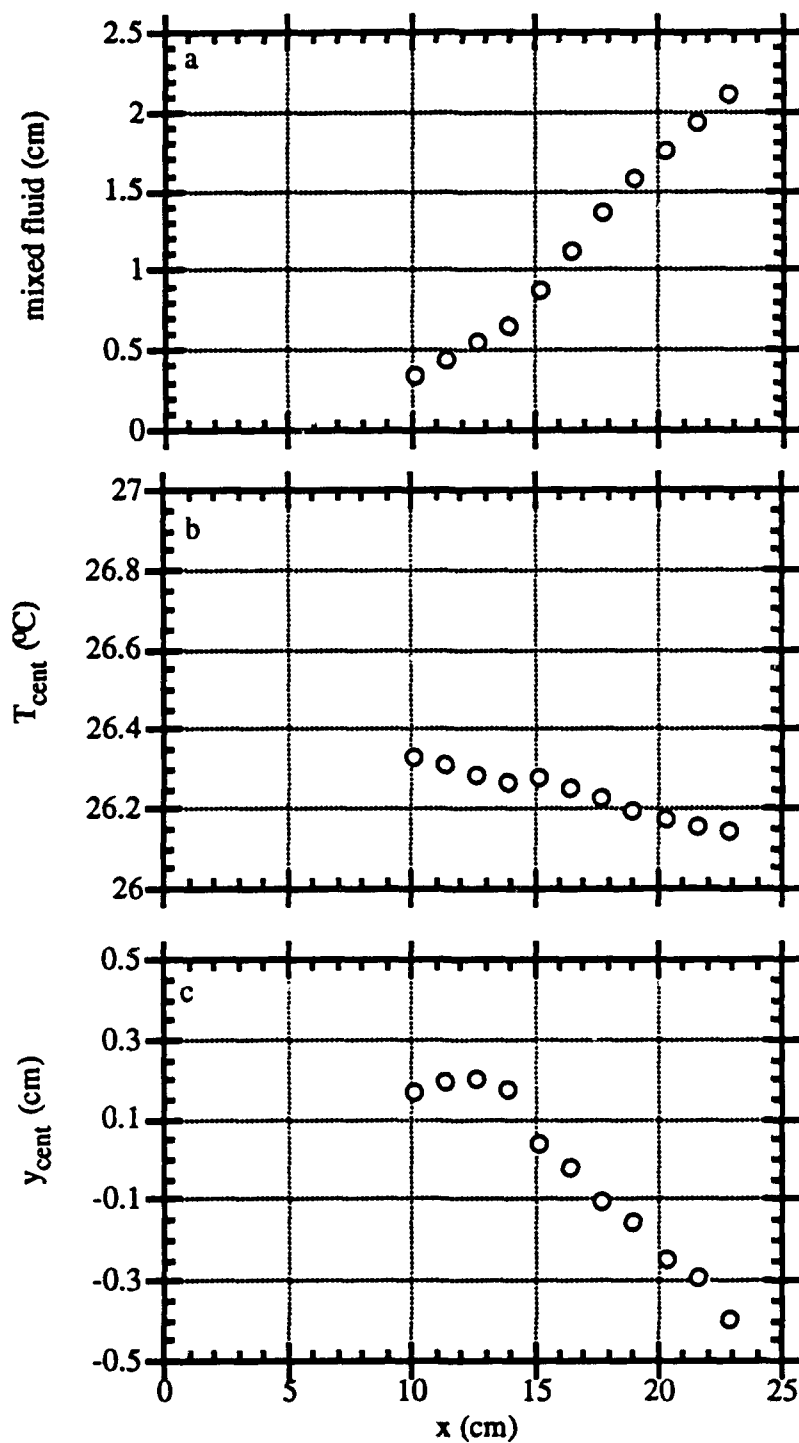
FIGURE 24. Moments of *pdf*(T,y) for the unforc\u0259d flow: (a) total mixed fluid, (b) average temperature of mixed fluid, and (c) average cross-stream height y of mixed fluid.
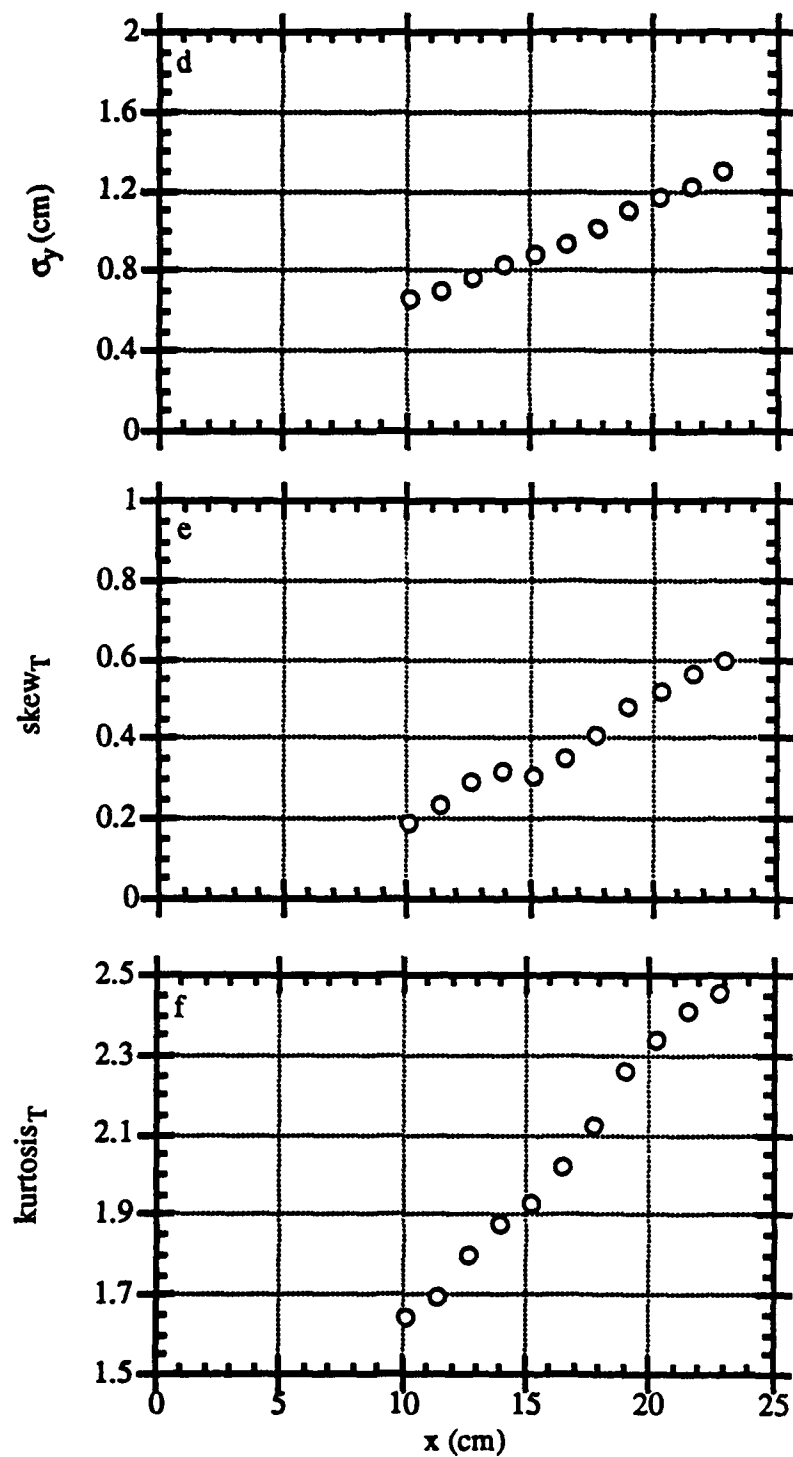
FIGURE 24-*Continued*. Moments of *pdf*(T,y) for the unforced flow: (d) σ_Y, (e) skew$_T$, and (f) kurtosis$_T$.

skewed towards higher values of T; that is, there is a long tail pointing in the direction of T_2, the temperature of the low-speed stream. And finally, the plot of kurtosis$_T$(x) shows that this measure increases with downstream distance, suggesting a flattening of pdf(T,y).

Figure 25a-f shows (at all measured streamwise stations) the variation of these moments with $\theta = \tan^{-1}(k_2/k_1)$. The curves for the total mixed fluid, T_{cent}, and σ_y are presented as the percentage change with respect to the unforced flow, and y_{cent} is given as the difference from the unforced flow. Since skew$_T$ and kurtosis$_T$ are non-dimensional by definition, they are not normalized further.

The total mixed fluid (figure 25a) again shows the same trends as PM(θ) (figure 20a-f). The plots for T_{cent} and y_{cent} (figures 25b and 25c, respectively) demonstrate the difference in mixing between C_1 and C_2. As was noted previously, C_2 enhances mixing by drawing fluid from both streams into the primary vortices, where it is strained into thin layers where mixing can occur. This configuration has the effect of drawing more fluid from the low-speed stream (at temperature T_2) into the layer, where it is mixed throughout the width of the layer. Hence, the average temperature of mixed fluid is higher in this configuration (note the peak at $\theta = 262.5°$ in figure 25b) and the fluid is mixed at an average cross-stream location y_{cent} which is further into the high-speed stream than with the other feedback gains. At the opposite extreme, configuration C_1 entrains less low-speed fluid, but mixes it effectively in large vortical structures. This is reflected in the lowest values of T_{cent} and y_{cent} of the feedback cases.

The plots of σ_y (figure 25d) suggest that feedback can either increase or decrease the cross-stream extent over which mixing occurs. Furthermore, these plots (especially at the downstream locations) have a broad peak at $\theta \_ 15°$ which suggests that feedback configuration C_3, by amplifying the low frequencies already present in

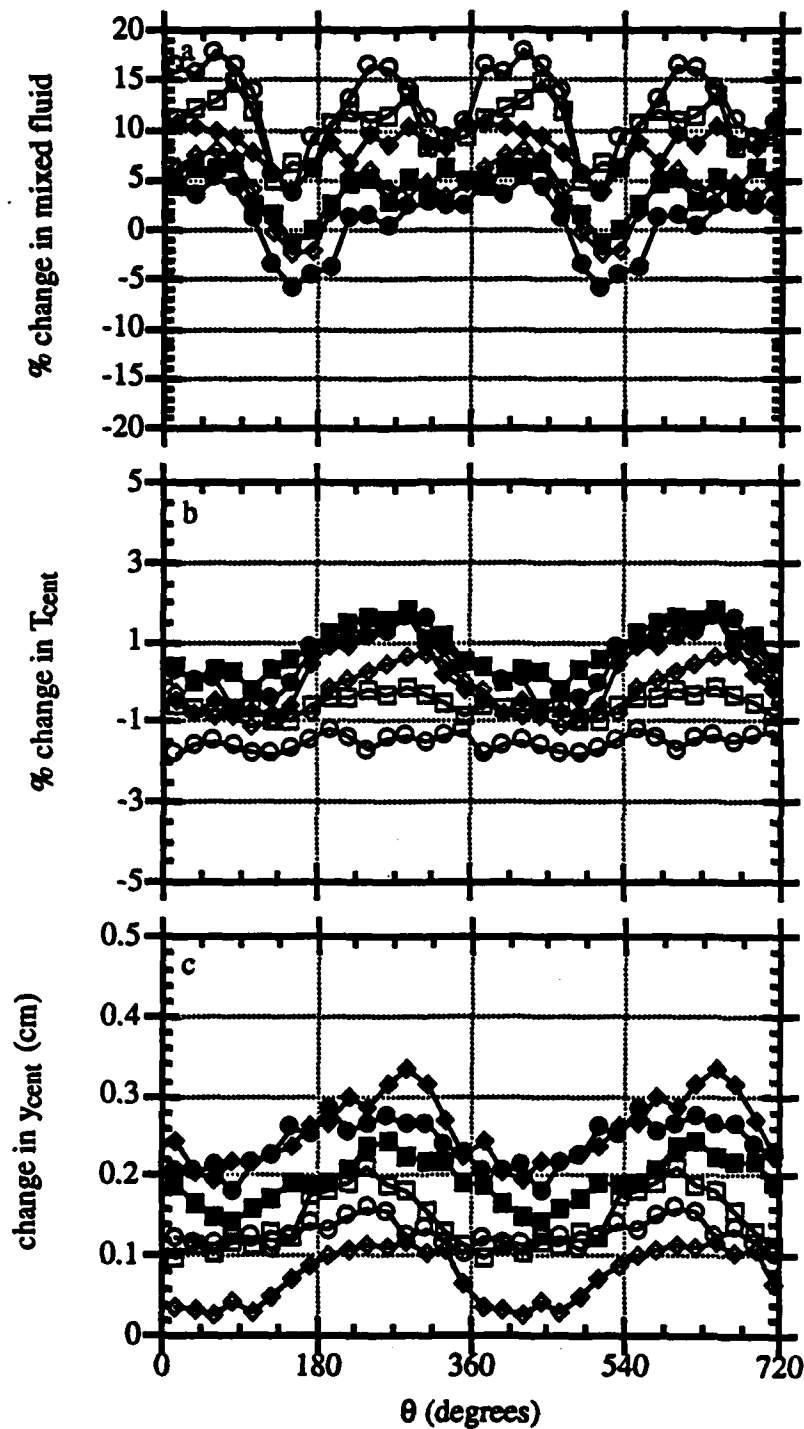FIGURE 25. Moments of *pdf*(T,y) for the flow with feedback at x = 10.16 cm (O), 12.70 cm (□), 15.24 cm (◊), 17.78 cm (●), 20.32 cm (■), and 22.86 cm (◆): (a) total mixed fluid, (b) average temperature of mixed fluid, and (c) average cross-stream height y of mixed fluid.

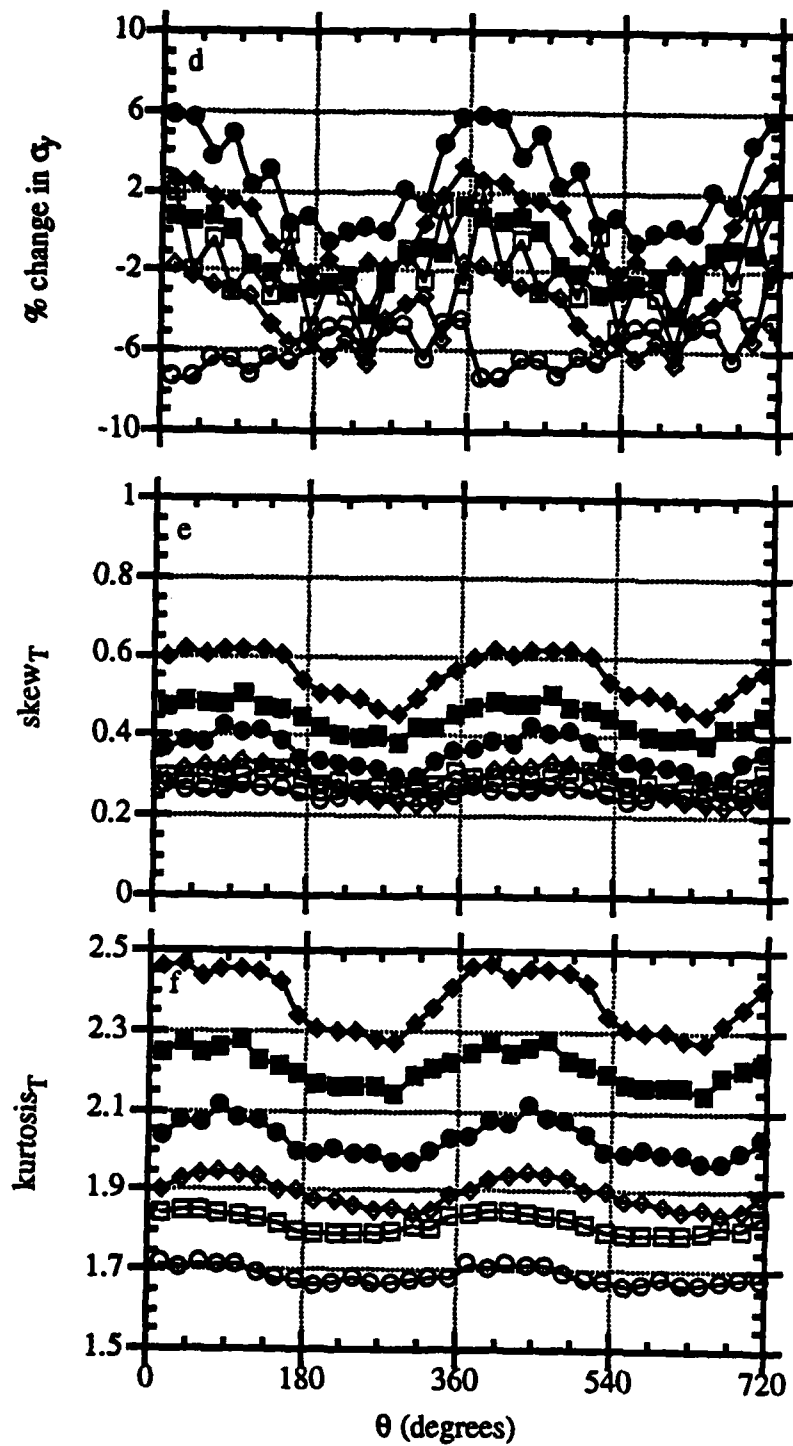**FIGURE 25-*Continued*.** Moments of $pdf(T,y)$ for the flow with feedback at x = 10.16 cm ($\bigcirc$), 12.70 cm ($\square$), 15.24 cm ($\Diamond$), 17.78 cm ($\bullet$), 20.32 cm ($\blacksquare$), and 22.86 cm ($\blacklozenge$): (d) σ_Y, (e) skew$_T$, and (f) kurtosis$_T$.

the flow, lead to an increased spreading of the layer. Finally, $skew_T(\theta)$ shows that mixing for configuration C_2 is more symmetric (less skewed toward the low-speed temperature) than C_1, which is to be expected since T_{cent} is closer to the median temperature for C_2.

4.3. Optimization of PM_{max} by adjusting θ

It is possible to optimize **PM** at a given streamwise station by adjusting θ (the angle of $\underline{k}$) in real time. This would allow a controller to optimize mixing without the operator knowing *a priori* which gains were the best to use. In addition, it is conceivable that, for example, if the speeds of the two free streams changed to a significant extent, Δ_N would change and the gains which worked before would no longer be effective.

The optimization algorithm used here is a golden section search. This method successively brackets a maximum. An initial triple of θ's (a,b,c) is chosen (from figure 20) such that $PM(b) > PM(a)$ and $PM(b) > PM(c)$. This creates two "bracketing segments", a-b and c-b. Each subsequent triple of θ's (a,b,c) is calculated from the preceding one by discarding the point (a or c) which gives the lowest value of **PM** and replacing it with a new one, such that the ratio of the length of this newer bracketing segment to that of the total bracket length a-c is a constant. This constant is the golden ratio 0.38197.

Figure 26 shows the utility of the golden segment search method to optimize PM_{max} at $x = 15.24$ cm. Figure 26a shows the convergence of θ with successive iterations. The final value of θ approaches 80^0. Similarly, figure 26b shows that the value of PM converges to a value of 4% above the unforced flow. Note, however,
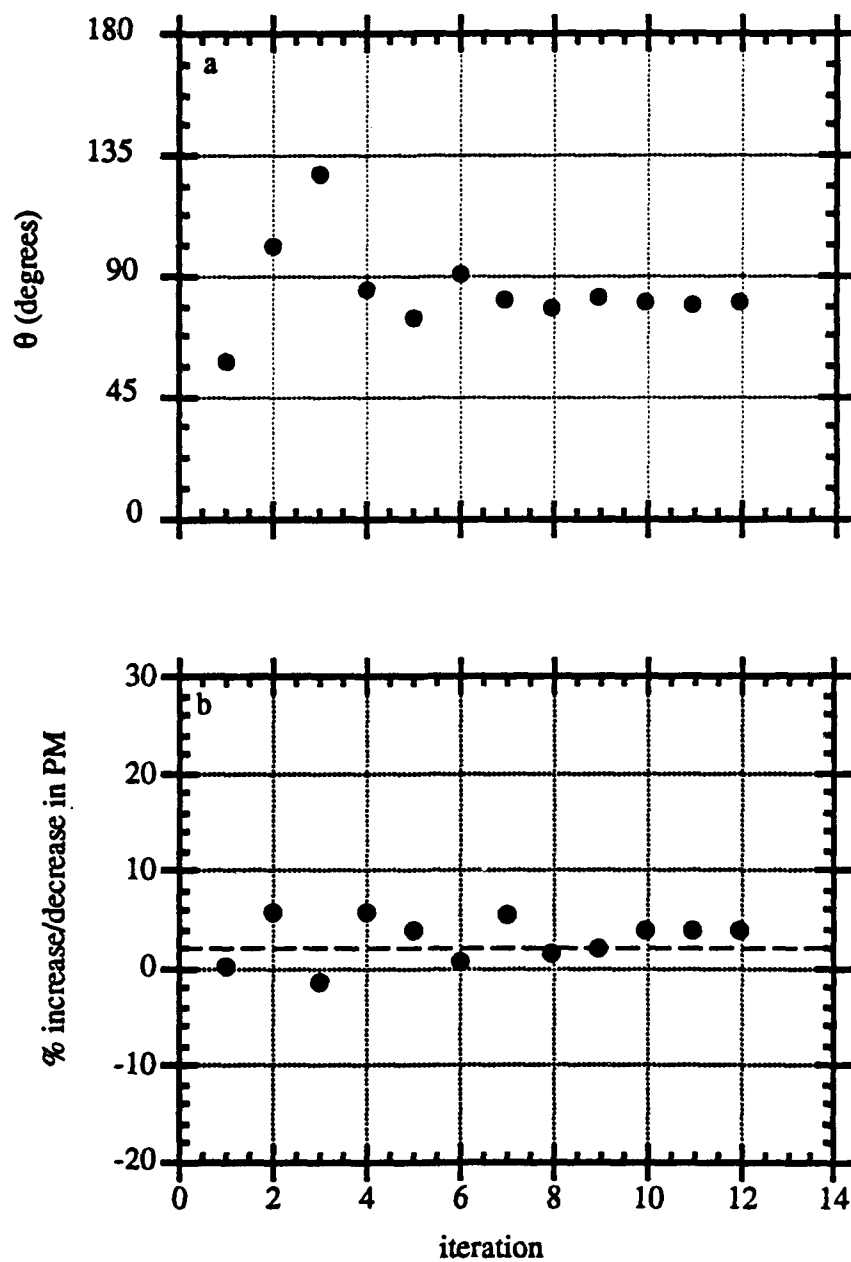
FIGURE 26. Optimization of PM_{max} by adaptively adjusting θ based on PM: (a) θ as a function of the iteration, and (b) PM as a function of the iteration. $x = 15.24$ cm.

that there are limitations to this method. Since it is based on *successively* bracketing a maximum, it depends crucially on the ability to accurately calculate PM in real time. Since this calculation is inherently noisy (due to calibration drift, slight changes in the free stream temperatures, etc.) θ can converge to the wrong value if an inaccurate value of PM is calculated at just one iteration. In addition, this method is limited to regions of the flow far enough upstream that the rake can cover the full cross-stream extent of the flow and far enough downstream that the flow reaches enough sensors that a slight drift in a few of them will not cause a significant error in the calculated value of PM. There are two possible solutions to this problem. The first is to be able to calculate PM more accurately in real time. The second is to use a more robust optimization scheme than the golden section search: one which does not permanently eliminate any values of θ from consideration based on only one measurement.

5. The effect of spanwise-periodic feedback on mixing

5.1. Modification to the transfer function

In this section, the effect of feedback in the presence of streamwise vortices is used to further enhance mixing. In the spanwise-uniform case discussed in §4, only the spanwise-uniform surface heaters are used as control actuators. In this section, the linear array of 32 small heating elements is used as well. A spanwise-periodic waveform is effected by varying $r = (k_1^2 + k_2^2)^{1/2}$ in the span. This time-invariant spanwise waveform has a spanwise wavelength of $\lambda_z = 2.66$ cm and a duty cycle of 75%. It is synthesized by a repeated pattern of four small heaters in which $r = 1.0$ on three and $r = 0.04$ on the fourth). This is analogous to the SP waveform of WGI.

Since the optical position sensor (figure 1) views an integrated image of the temperature image, it is expected that the current transfer function as described in §3.1 (with slight modification) can be used for the SP experiments in this section. The optical position sensor has been moved from $x = 3.175$ cm in the previous section to $x = 3.81$ cm. The current control scheme delays the emergence of the natural frequency of the flow making effective control impossible with the position sensor at $x = 3.175$ cm. Moving the sensor downstream attenuates the low-frequency peak in the power spectrum of the interface motion S_Y (figure 27a). Consequently, Q for the model transfer function must be reduced to $Q = 4.25$ to properly account for the low frequencies present in the interface motion (figure 27b).

Because additional surface heaters are used, and because the optical position sensor is further downstream, the natural delay time Δ_N must be determined for the new conditions. It is found to be $\Delta_N = 0.9093$s. In addition, the phase between Y and u has changed significantly, from $\phi(Y,u) = -90°$ in the SU case to $\phi(Y,u) = 0°$ in
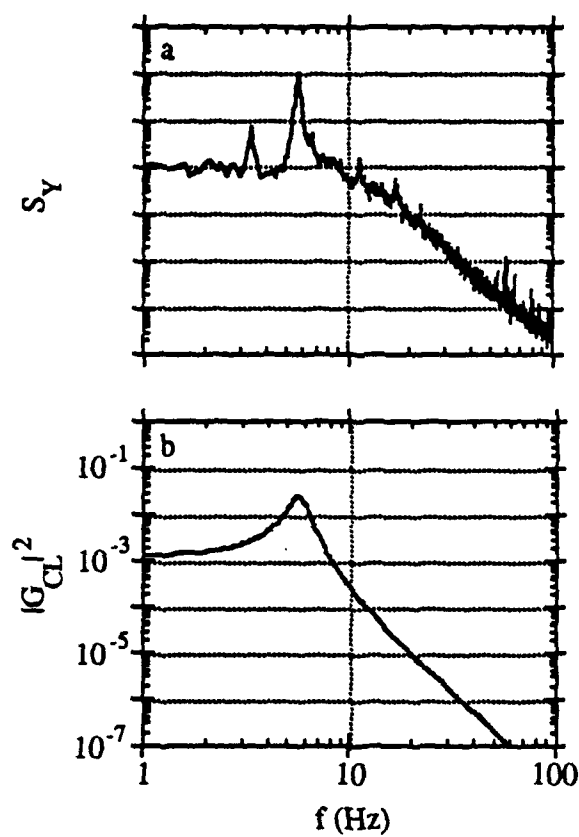
FIGURE 27. (a) The power spectrum of the unforced interface motion with the position sensor a the spanwise-periodic position (x = 3.81 cm), (b) analogous second-order transfer function (no feedback).

this case. In order to optimize the effectiveness of the transfer function, the software delay Δ is chosen so that the total delay $\Delta_T = \Delta_N + \Delta$ corresponds to an integer number of cycles of the flow. Since (6/5.66 Hz) = 1.06s, $\Delta = 0.15$s. The remaining unknown parameter A was found to be A = 4.7 (found by observations of the effect of feedback on the total power in S_Y).

The utility of the transfer function in predicting the motion of the interface for the SP case is verified in figures 28-30, the SP analogs to figures 6, 8, and 9, respectively. Figure 28 shows the effect of varying $\underline{k}$ on the motion of the interface. The magnitude of the control gain $|\underline{k}|$ is held constant at 1.0, the safety limit of the surface heaters in this case. The angle between k_2 and k_1 is then varied between 0° and 360° (see figure 28a). Figure 28b shows the variation of the rms position of the interface as predicted by the transfer function and as measured by the position detector. As was the case for SU feedback, the transfer function does a good job of predicting the rms motion of the interface for various feedback gains. The total deviation in this case appears to be slightly less, however, possibly because the interface motion is saturating more at the current location of the position sensor (x = 3.81 cm) than it was at the upstream location.

Figure 29 depicts the spectral power S_Y at the fundamental frequency f_0 (= 5.66 Hz). Shown are the measured spectral power and that predicted by the transfer function. As was the case with SU feedback, there is some disparity in the absolute magnitude of $S_Y(f_0)$ between the measured and predicted values, but the transfer function does an accurate job of predicting the minimum and maximum. The locations of the resonance condition ($\theta = 180^o$, feedback configuration C_{3D2}) and anti-resonance condition ($\theta = 0^o$, feedback configuration C_{3D1}) are noted. These occur at different values of θ than the corresponding SU cases because $\phi(Y,u)$ is different for SP feedback as was noted above.
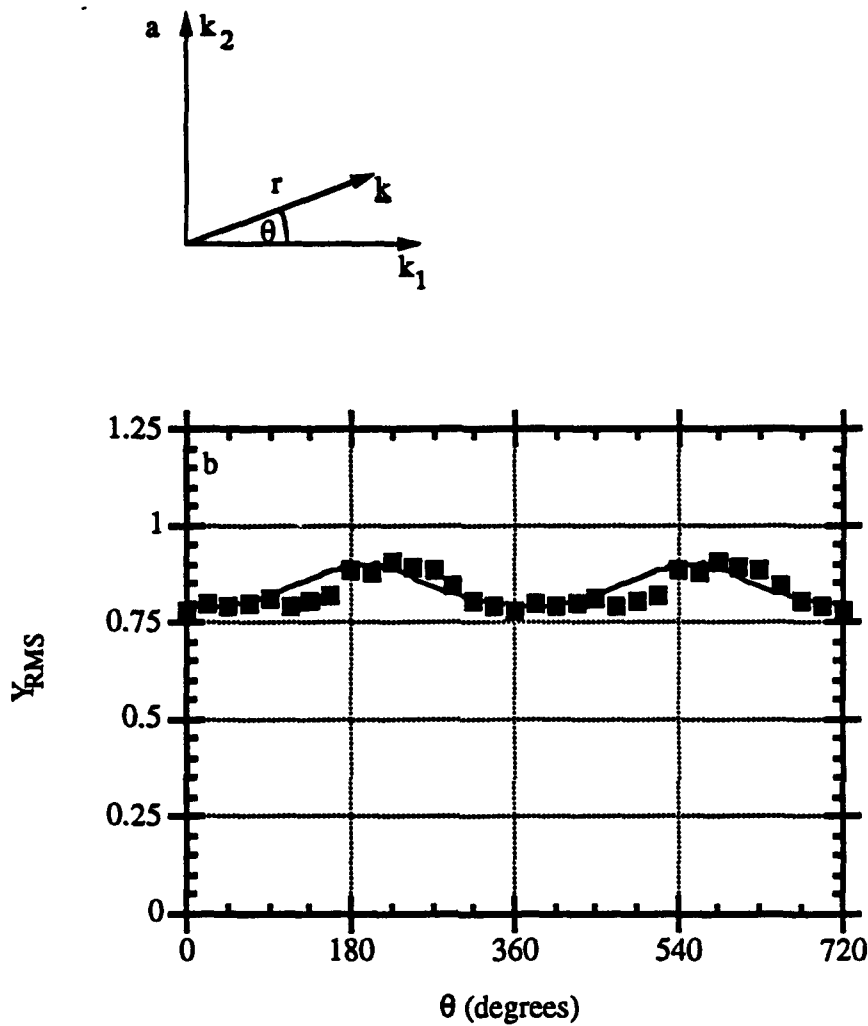
FIGURE 28. RMS displacement of the interface motion as a function of the angle θ of $\underline{k}$ for spanwise-periodic case: (a) geometry, and (b) Y_{RMS} as predicted by the transfer function (—) and Y_{RMS} measured (■).
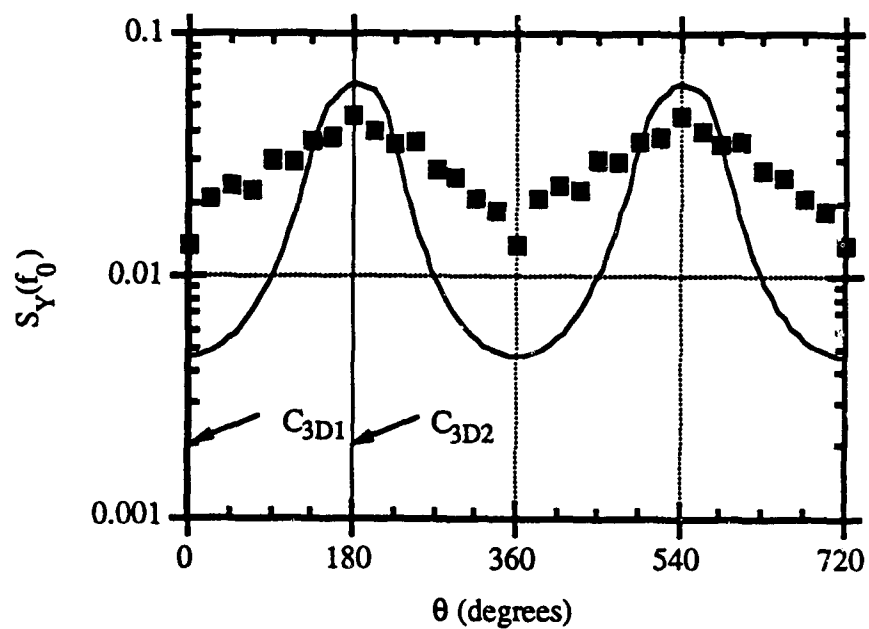
FIGURE 29. Spectral power S_Y at the natural frequency of the flow f_0 for spanwise-periodic feedback: predicted (—) and measured (■).
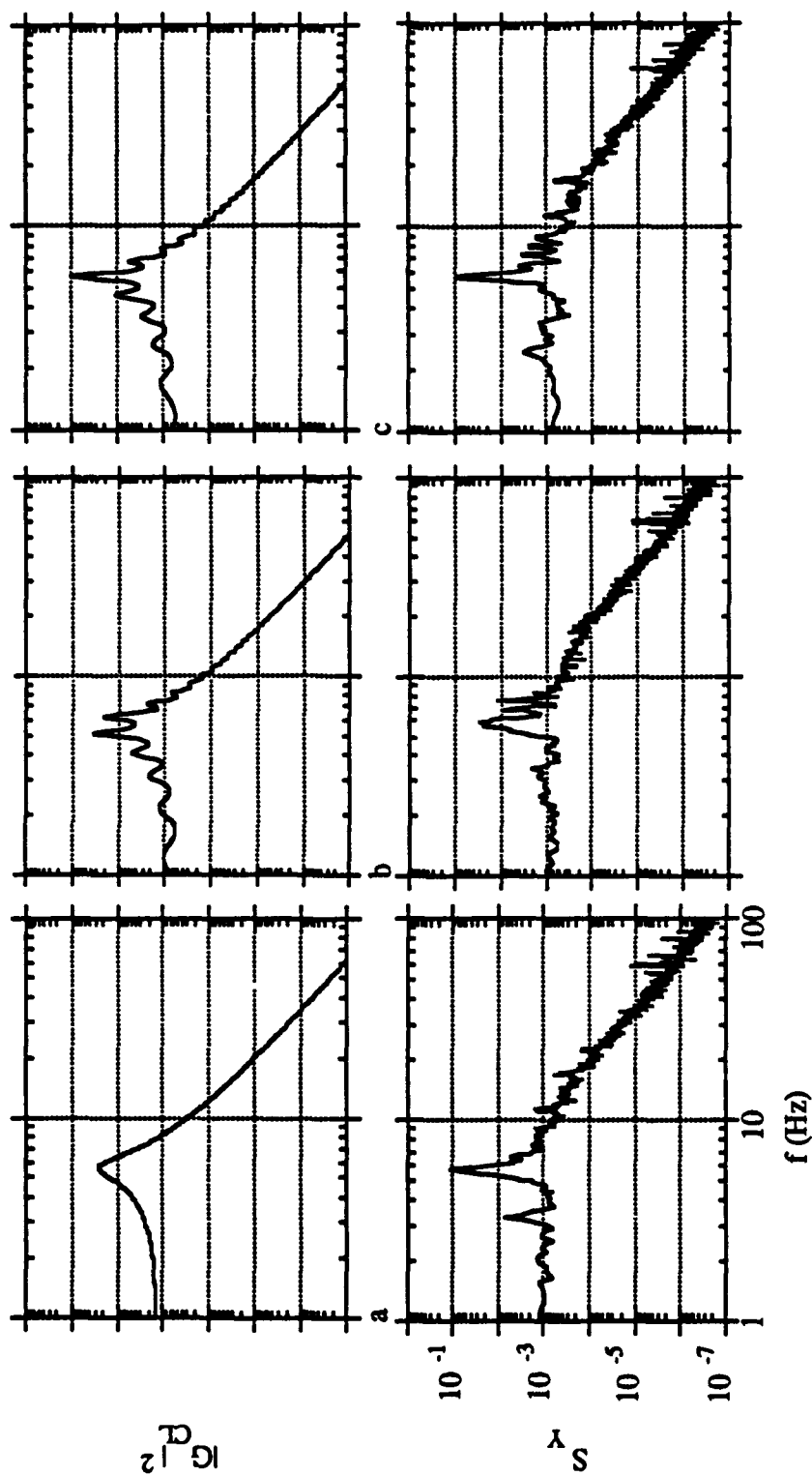
FIGURE 30. Pairs of $|G_{CL}(f)|^2$ (top) and $S_Y(f)$ (bottom) for (a) unforced, (b) feedback configuration C_{3D1}, and (c) feedback configuration C_{3D2}.

Figure 30 shows the effect of different values of $\underline{k}$ on the squared magnitude of the model transfer function $|G_{CL}|^2$ and the power spectrum of the interface motion S_Y. The software delay Δ is held constant at a value of 0.15s, so that Δ_T is six complete cycles of the flow. Figure 30b is the response of the interface to feedback configuration C_{3D1}, $\underline{k}^1 = (1.0,0.0)$. This is a case which is chosen to attenuate f_N by amplifying the sidebands. Note that compared to the unforced case, there are a number of spectral peaks around the natural frequency. The magnitude of these peaks is almost equal in magnitude to the peak at the natural frequency. Figure 30c shows the case of $\underline{k}^2 = (-1.0,0.0)$ which is chosen to amplify the natural frequency. In comparison with figure 30b, the spectral peak at f_N is larger while the spectral peaks within the side bands are considerably smaller in figure 30c. In fact, in figure 10c, the spectral peak at f_N is more than one order of magnitude larger than the spectral peaks at its sidebands.

Finally, it must be briefly noted that since the optical position sensor was deliberately placed further downstream to minimize the low-frequency peak f_L that was measured, there is no feedback configuration C_{3D3}. That is, it is no longer possible to amplify low frequencies naturally present in the flow.

5.2. Spanwise variation of r

As was shown in the open-loop experiments, the most effective way to increase the amount of mixed fluid produced is to introduce streamwise vortices into the flow. This was accomplished using a spanwise-periodic (SP) amplitude modulation of the 32 small heaters on the flow partition. As is the case for open-loop SP forcing, the head of a streamwise vortex forms at the transition between $r = 1.0$ and $r = 0.04$. The two spanwise positions which are emphasized in what follows are

$z = 0.0$ cm (the head of the streamwise vortex, which forms on the high-speed side of a primary vortex) and $z = -1.35$ cm (the tail of the streamwise vortex, which forms on the low-speed side of a primary vortex).

Figure 31 depicts S_{PM} at $x = 15.24$ cm for spanwise-periodic feedback. The two configurations considered are C_{3D1} (designed to attenuate the natural frequency) and C_{3D2} (designed to amplify the natural frequency). Shown are the response of the flow at the head of the streamwise vortex to C_{3D1} (figure 31a) and C_{3D2} (figure 31b), and at the tail of the streamwise vortex to C_{3D1} (figure 31c) and C_{3D2} (figure 31d). At the head of a streamwise vortex (figure 31a-b), the frequencies induced by the feedback are qualitatively similar to the corresponding SU cases (figure 16). By contrast, low frequencies dominate f_0 in S_{PM} measured at the tail of a streamwise vortex. In addition to $f_L \approx 3.40$ Hz (which is dominant even in the C_{3D2} case, there is an additional low frequency at $f \approx 2.4$ Hz which is almost of equal magnitude to f_L. These plots suggest that, particularly for large x, feedback may not have a significant effect on the spectral contents of the flow at the tail.

Figures 32 and 33 depict sets of $T(y)$, $T(y,t)$, and $pdf(T,y)$ at $x = 10.16$ cm, 15.24 cm, and 20.32 cm for feedback configuration C_{3D1} (the "out-of-resonance" condition) at the head and the tail of the streamwise vortex, respectively. Figures 34 and 35 show the corresponding figures for feedback configuration C_{3D2} (the "resonance" condition). and for feedback configuration C_2 (the "resonance" condition, figure 46a-c). There are significant differences in the flow at the head and the tail of the streamwise vortex. The effect of these counter-rotating vortices is to pump low-speed fluid into the layer and towards the high-speed stream at the head of the vortex. At the tail of the streamwise vortex, the pumping action is reversed: it tends to suppress entrainment of low-speed fluid as it pumps more high-speed fluid into the layer. Each pair of figures (32 and 3ɔ; 34 and 35) demonstrates this fact. In
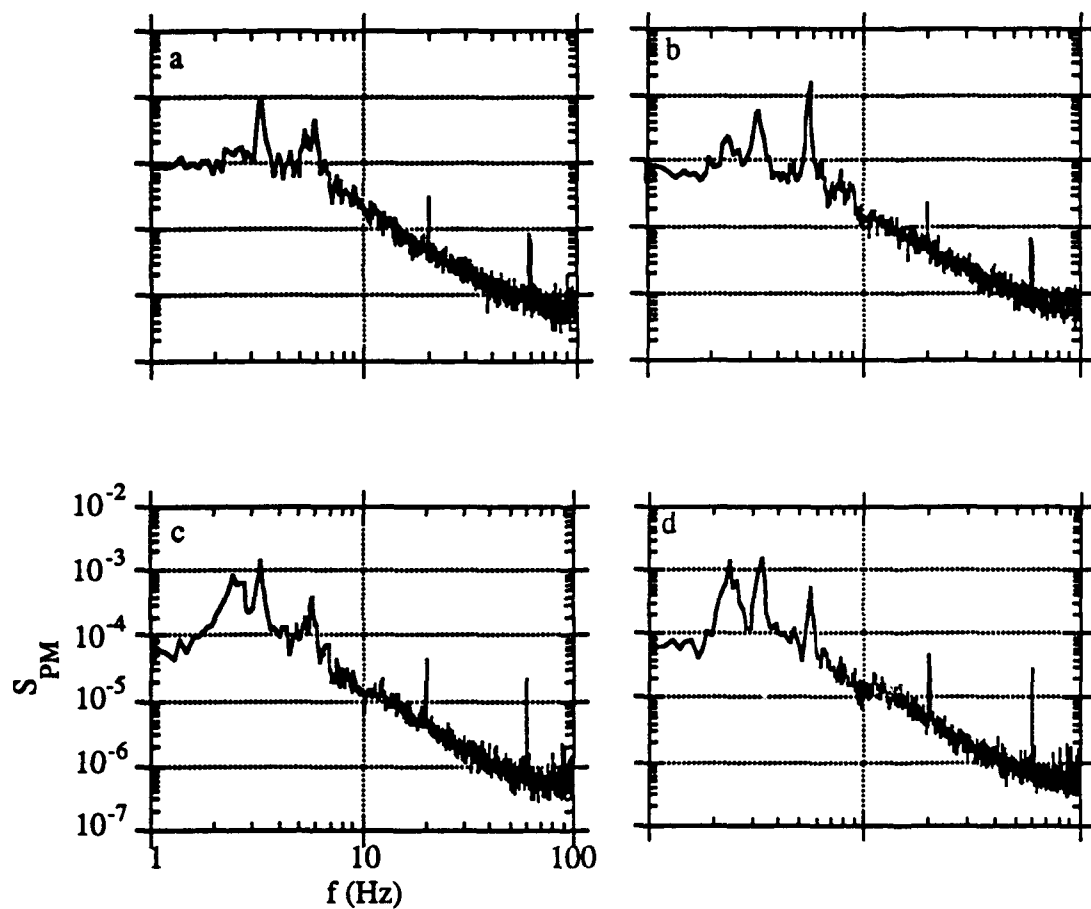
FIGURE 31. $S_{PM}(f)$ for (a) C3D1 (head), C3D2 (head), (c) C3D1 (tail), and (d) C3D2 (tail). $x = 15.24$ cm.
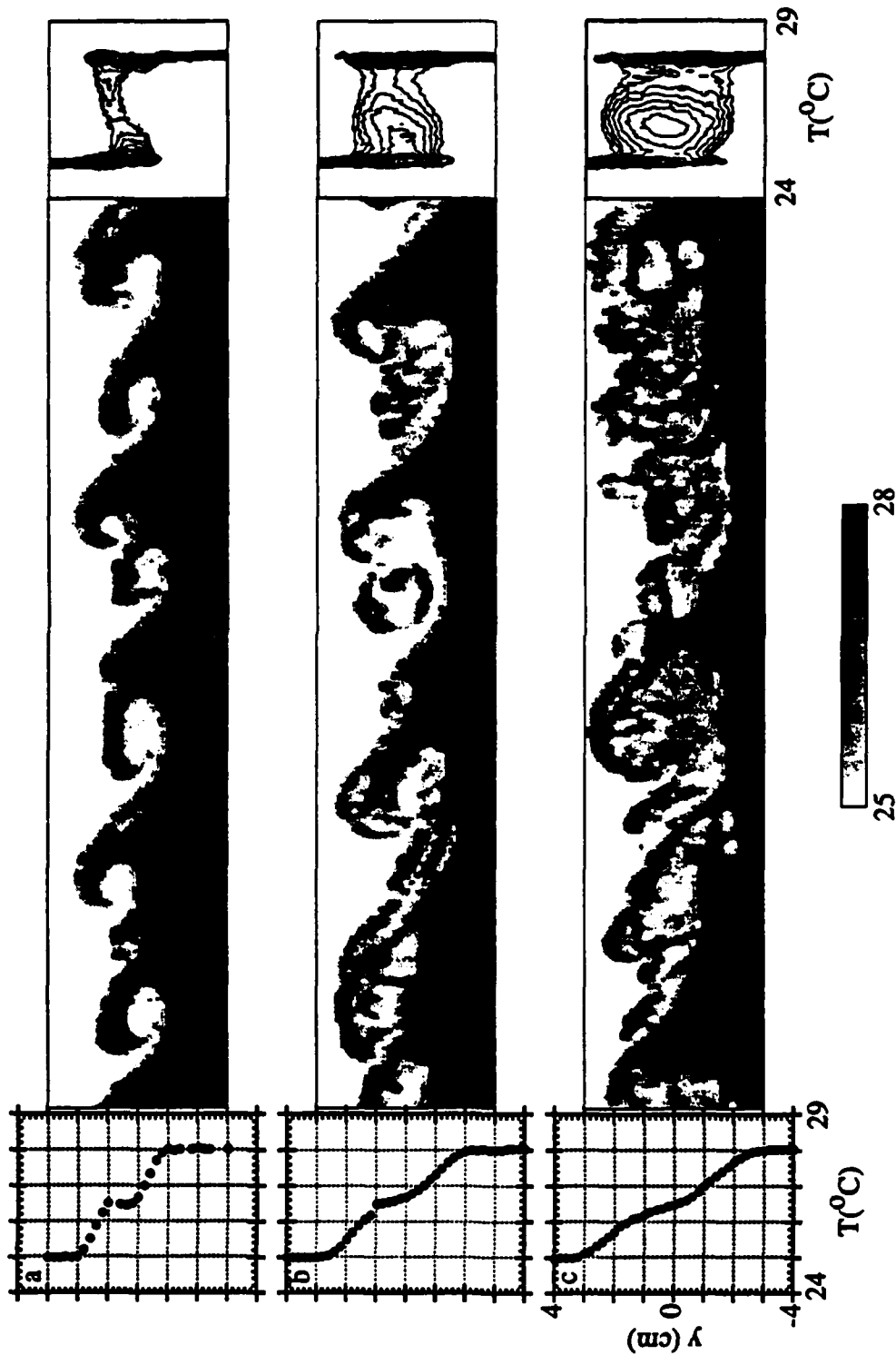
FIGURE 32. T(y), T(y,t), and *pdf*(T,y) for feedback configuration C$_{3D1}$ (head) at x = (a) 10.16 cm, (b) 15.24 cm, and (c) 20.32 cm.
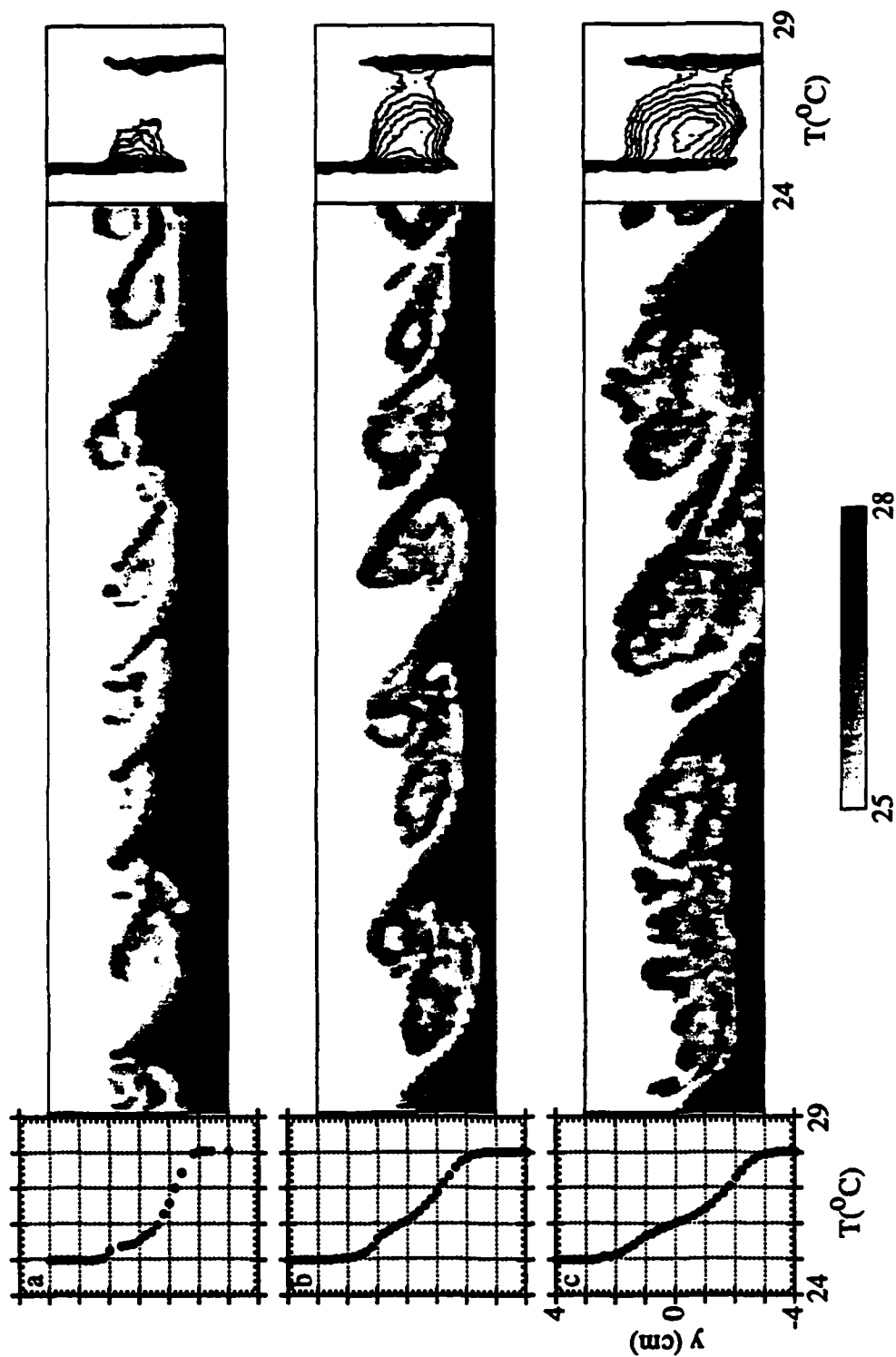
FIGURE 33. T(y), T(y,t), and *pdf*(T,y) for feedback configuration C3D1 (tail) at x = (a) 10.16 cm, (b) 15.24 cm, and (c) 20.32 cm.
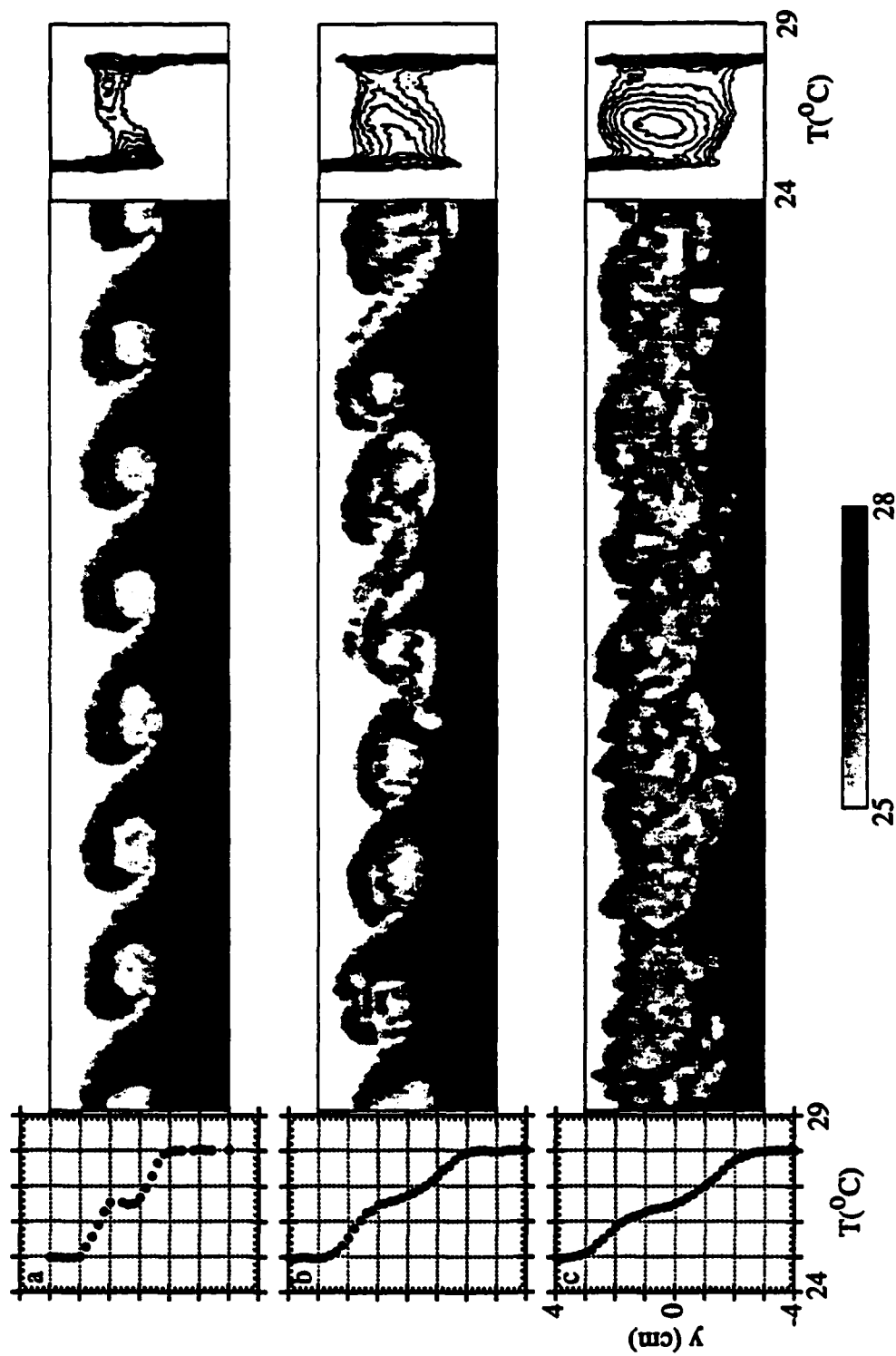
FIGURE 34. T(y), T(y,t), and *pdf*(T,y) for feedback configuration C$_{3D2}$ (head) at x = (a) 10.16 cm, (b) 15.24 cm, and (c) 20.32 cm.
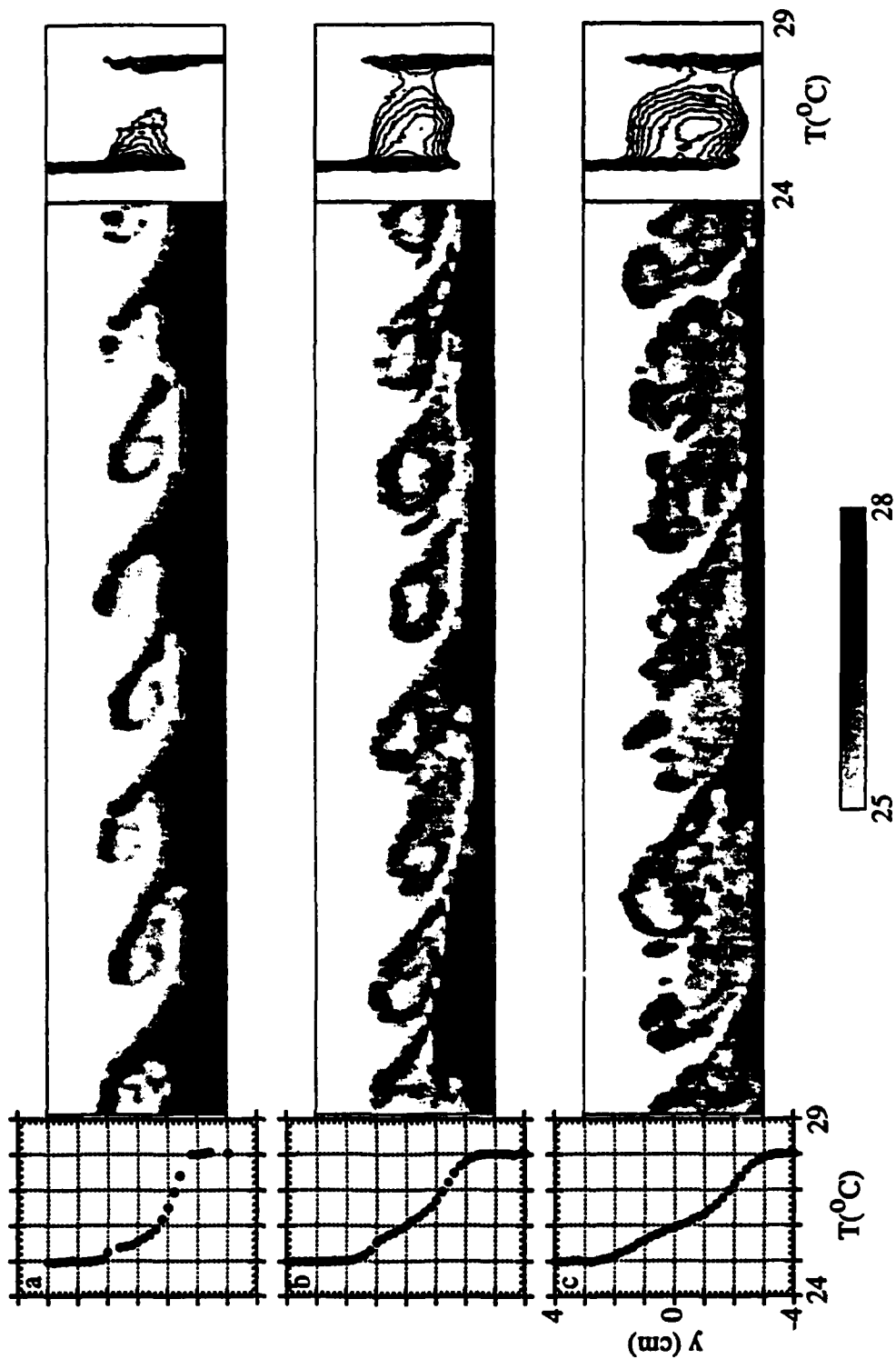
FIGURE 35. T(y), T(y,t), and *pdf*(T,y) for feedback configuration C3D2 (tail) at x = (a) 10.16 cm, (b) 15.24 cm, and (c) 20.32 cm.

the composites taken at the tail of the streamwise vortex (figures 33 and 35) the tongues of hot low-speed fluid being entrained into the layer are significantly thinner than in the corresponding composites at the head of the streamwise vortex (figure 32 and 34). Note that the small spatial scales at the tail of the streamwise vortex allow rapid mixing; however, the lack of entrainment of low-speed fluid suggests that there will be less mixed fluid further downstream. This is consistent with the plots of $PM(x)$ for SU, $f = 5.66$ Hz (figure 15) in which PM is higher at the tail of the streamwise vortex for $x \le 16.51$ cm and PM is higher at the head of the streamwise vortex for $x \ge 16.51$ cm.

The grayscale raster images of $T(y,t)$ in figures 32 and 33 show that configuration C_{3D1} does indeed attenuate the natural frequency. There is no characteristic frequency of the flow at any streamwise station at either the head or the tail of the streamwise vortex. Most of the mixed fluid is produced in large patches as in the case of C_1; however, due to the increase in small scales caused by the streamwise vortices, there is substantially more mixed fluid in $pdf(T,y)$ than in this corresponding SU case.

The grayscale images of $T(y,t)$ in figures 34 and 35 show that feedback configuration C_{3D2} creates a resonance condition which results in the natural frequency of the flow ($f_0 = 5.66$ Hz) being prevalent throughout the measurement regime. The spanwise vortices (particularly at the head, figure 34) are regular in both size and position. Note that at the tail of the streamwise vortex, there are lower frequencies present in the flow. This is to be expected from the plots of S_{PM} (figure 31d) which show that C_{3D2} is unable to produce a dominant natural frequency at the tail position of the streamwise vortex.

Figure 36a-f consists of pairs of $PM(\theta)$ for SP feedback at the head (left) and tail (right) of the streamwise vortex at $x = 10.16$ cm, 12.70 cm, 15.24 cm, 17.78
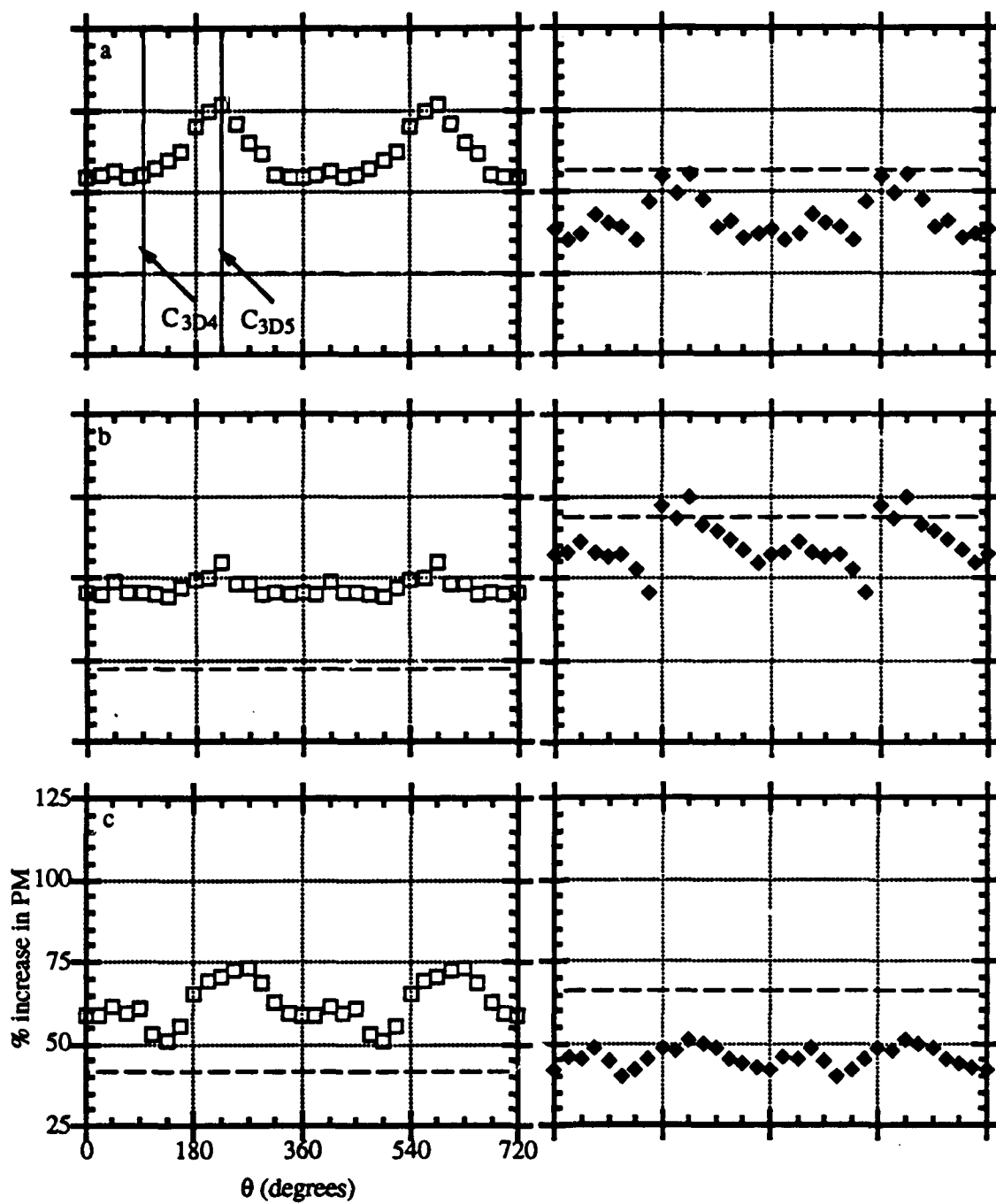
FIGURE 36. Pairs of PM(θ) for SP feedback at the head (left) and tail (right) of the streamwise vortex at x = (a) 10.16 cm, (b) 12.70 cm, and (c) 15.24 cm.
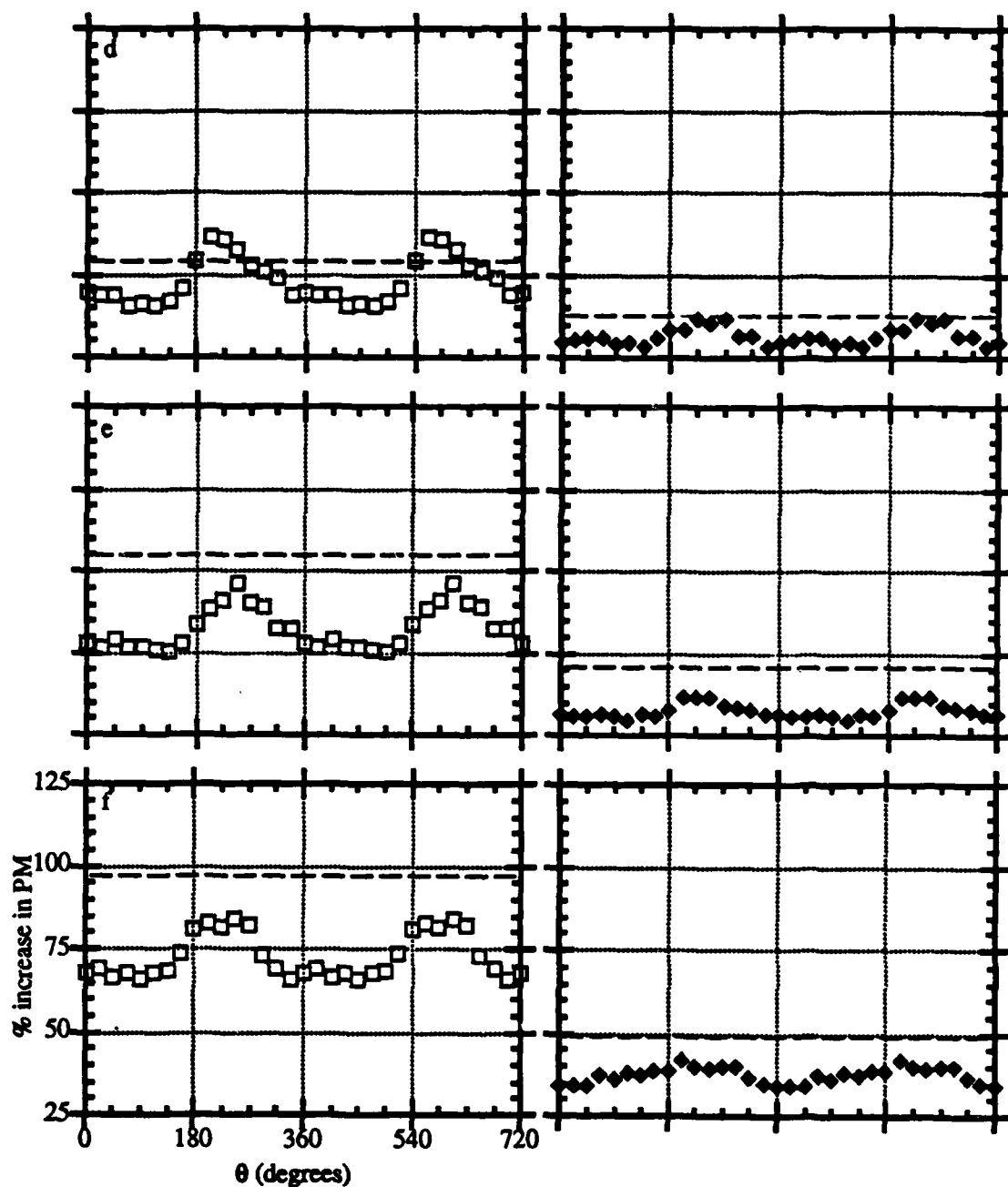
FIGURE 36-*Continued*. Pairs of PM(θ) for SP feedback at the head (left) and tail (right) of the streamwise vortex at x = (a) 17.78 cm, (b) 20.32 cm, and (c) 22.86 cm.

cm, 20.32 cm, and 22.86 cm. As anticipated, there is a substantial increase in PM relative to the unforced flow. In fact, at the head of the streamwise vortex, SP feedback can accrue gains of 40%-100% over the unforced flow at all streamwise stations. Furthermore, the excursions of $PM(\theta)$ are also significant at the head, with variations of the order of 25% of the unforced level at all streamwise stations. By strong contrast, the excursions at the tail of the streamwise vortex are negligible for x $\geq$ 15.24 cm. This is consistent with the idea that the flow is so dominated with low frequencies that feedback has very little effect. In addition, the levels of PM with feedback are somewhat lower at all streamwise stations than the levels obtained via open-loop forcing at SP, f = 5.66 Hz. Hence, if uniform mixing is desired across the span, it may be advantageous to use open-loop forcing rather than feedback.

If, however, large amounts of mixed fluid are desired and the spanwise distribution is irrelevant, it certainly is possible to feedback gains which significantly increase PM over that attainable with S, f = 5.66 Hz forcing. For x $\leq$ 15.24 cm, choice of the proper θ can result in improvements over the unforced PM level *twice* as high as SP, f = 5.66 Hz.

Finally, it should be noted that the maxima in $PM(\theta)$ occur not at C_{3D1} or C_{3D2} (as was the case for SU feedback) but at $\theta = 225^\circ$. Likewise, instead of the sharp minima that were present in the SU case (figure 20), there are broad valleys centered at approximately $\theta = 90^\circ$. These two cases are designated as C_{3D5} and C_{3D4}, respectively. This suggest that a different mechanism is responsible for mixing enhancement in this case. It is postulated herein that this mechanism is the strengthening of the streamwise vortices for certain feedback gains.

Figure 37 depicts the difference in the average height of mixed fluid Δy_{cent} between the head and the tail positions. Curves are shown for all six streamwise stations. Since the streamwise vortices pump low-speed fluid into the layer at the
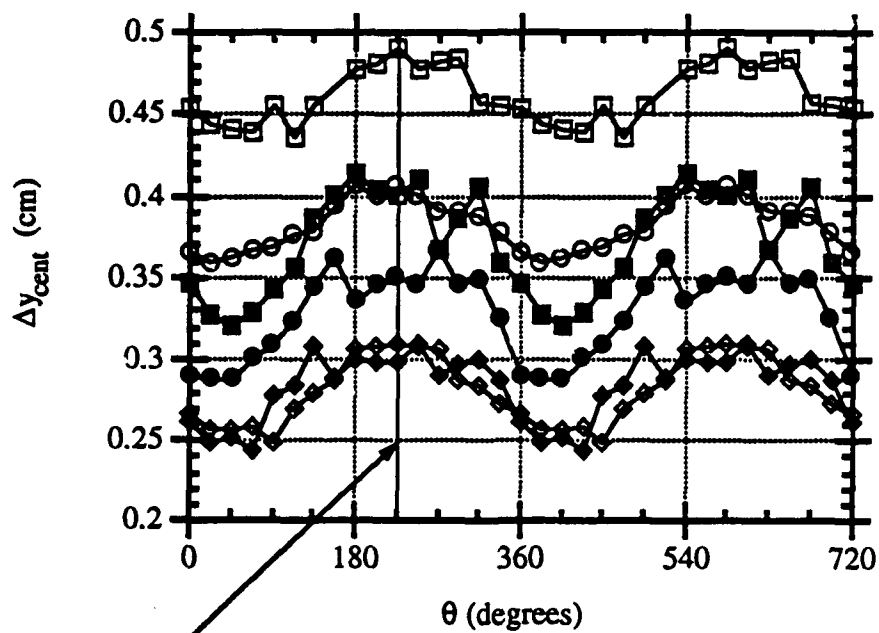
strongest streamwise vortices

FIGURE 37. Difference in average cross-stream position of mixed fluid at the head and the tail for SP feedback at x = 10.16 cm (O), 12.70 cm (□), 15.24 cm (◊), 17.78 cm (●), 20.32 cm (■), and 22.86 cm (◆).

head, they tend to increase y_{cent} at this station. Similarly, this pumping action at the tail tends to suppress entrainment of low-speed fluid and hence lower y_{cent}. Thus, the difference in y_{cent} at the head and the tail may give an indication of the strength of the streamwise vortices as a function of the feedback gain angle θ. Figure 37 shows a broad peak at $\theta = 225^\circ$, which also corresponds to the maxima of PM. In addition, the minima in these curves at $\theta = 90^\circ$ also correlates well with configuration $C_{3}D_{4}$.

Figure 38 shows the percentage increase in PM(x) relative to the unforced flow for $C_{3}D_{5}$ (which maximizes PM) and $C_{3}D_{4}$ (which minimizes PM) at the head (figure 38a) and the tail (figure 38b). Also shown for reference is the open-loop case SU, f = 5.66 Hz. As was noted above, feedback does not result in as large an increase in PM at the tail of the streamwise vortex as does open-loop forcing. However, figure 38a show how significantly feedback can increase PM at the head of the streamwise vortex. For $x \leq 15.24$ cm, feedback configuration $C_{3}D_{5}$ virtually doubles the increase in PM attained with SP, f = 5.66 Hz. At x ≈ 17 cm, however, the curve for SP, f = 5.66 Hz passes that for $C_{3}D_{5}$. For x $\geq$ 17 cm, SU, f = 5.66 Hz forcing results in higher values of PM than the feedback cases.

Figures 39 and 40 are composites of T(y), T(y,t), and pdf(T,y) at x = 10.16 cm, 15.24 cm, and 20.32 cm for $C_{3}D_{4}$ at the head and the tail, respectively. Figures 41 and 42 are the corresponding plots for $C_{3}D_{5}$. Comparison of the two feedback configurations at the head of the streamwise vortex (figures 39 and 41) shows that configuration $C_{3}D_{5}$ enhances mixing by creating mixed fluid at temperatures near the median of the two streams and above the (y) centerline of the layer (as can be inferred from pdf(T,y) at x = 15.24 cm and 20.32 cm). This is consistent with the idea that mixing is enhanced for $C_{3}D_{5}$ (relative to $C_{3}D_{4}$) by strengthening the streamwise vortices.
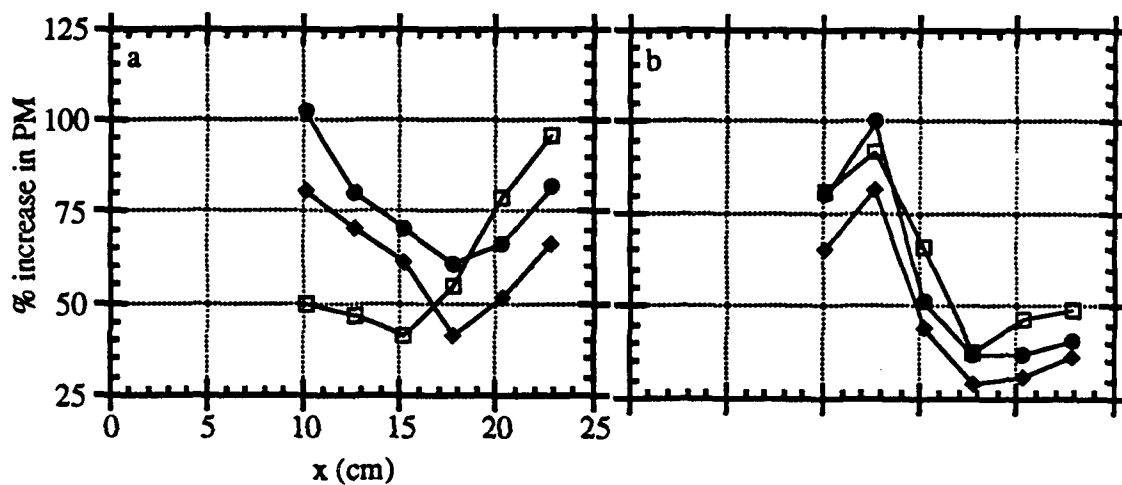
FIGURE 38. % increase in PM relative to unforced at (a) head, and (b) tail of streamwise vortex for SP, f = 5.66 Hz (▲), C3D4 (□), and C3D5 (●).
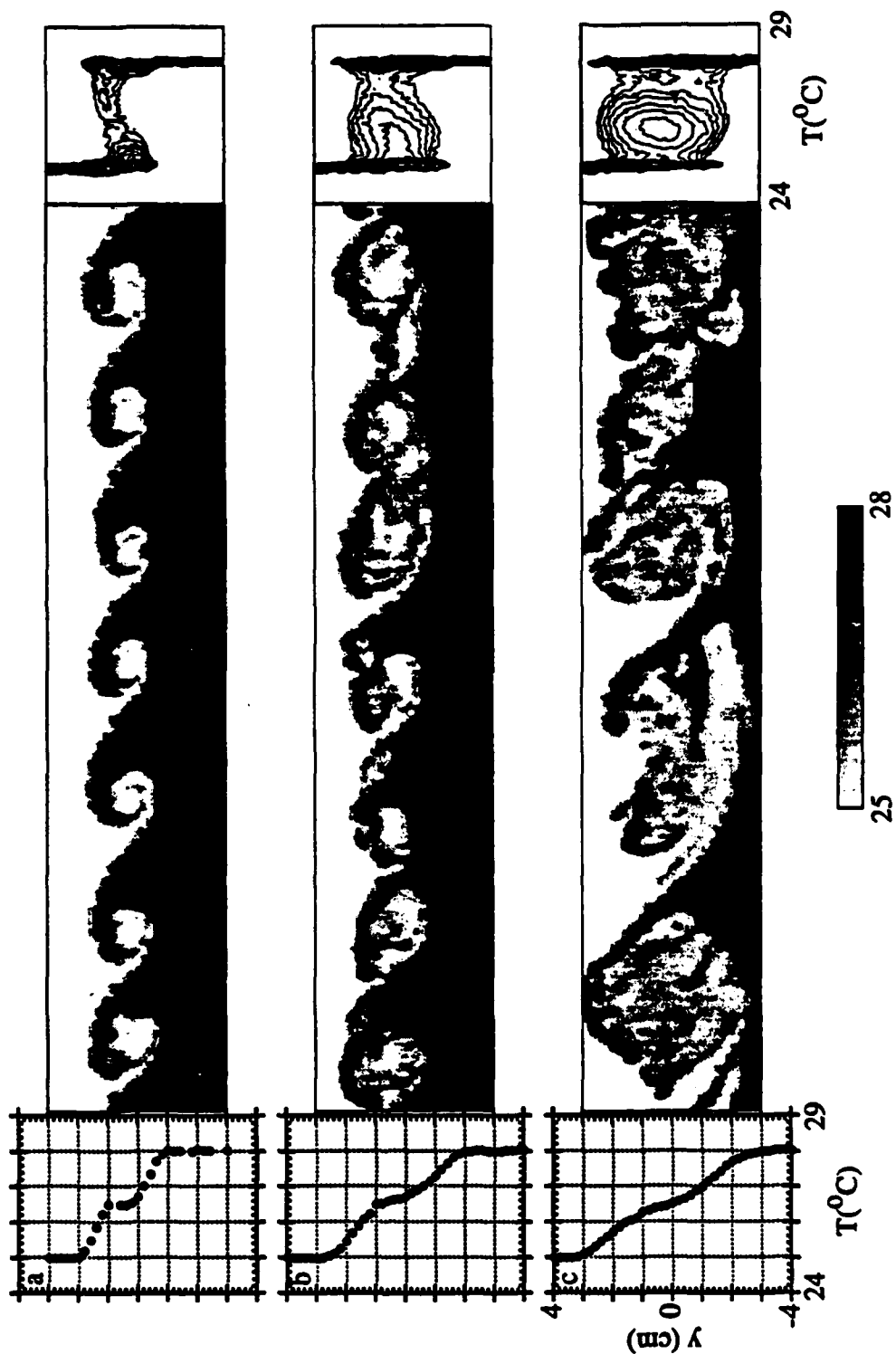
FIGURE 39. $T(y)$, $T(y,t)$, and $pdf(T,y)$ for feedback configuration C_3D_4 (head) at x = (a) 10.16 cm, (b) 15.24 cm, and (c) 20.32 cm.
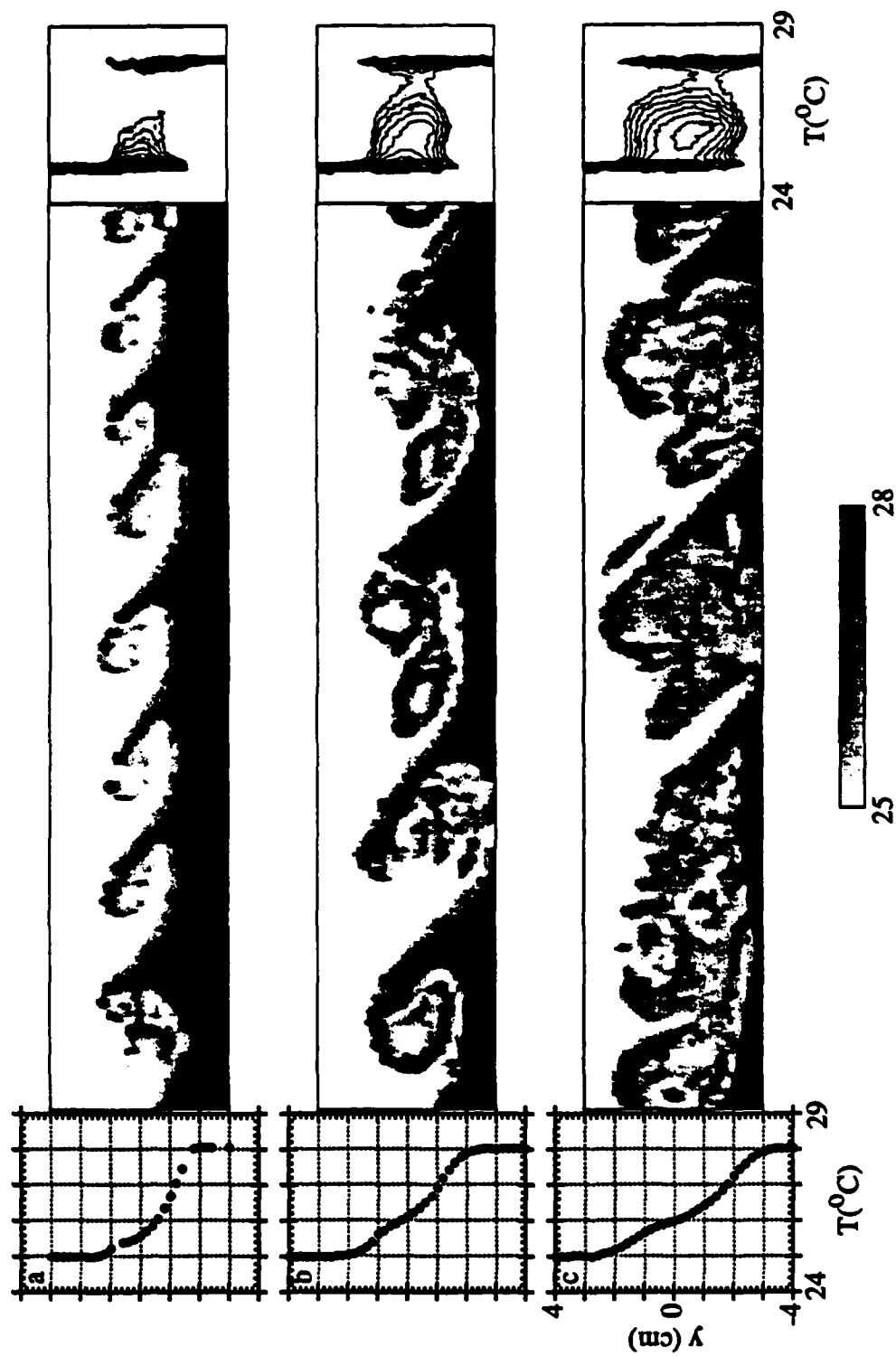
FIGURE 40. T(y), T(y,t), and *pdf*(T,y) for feedback configuration C_3D_4 (tail) at x = (a) 10.16 cm, (b) 15.24 cm, and (c) 20.32 cm.

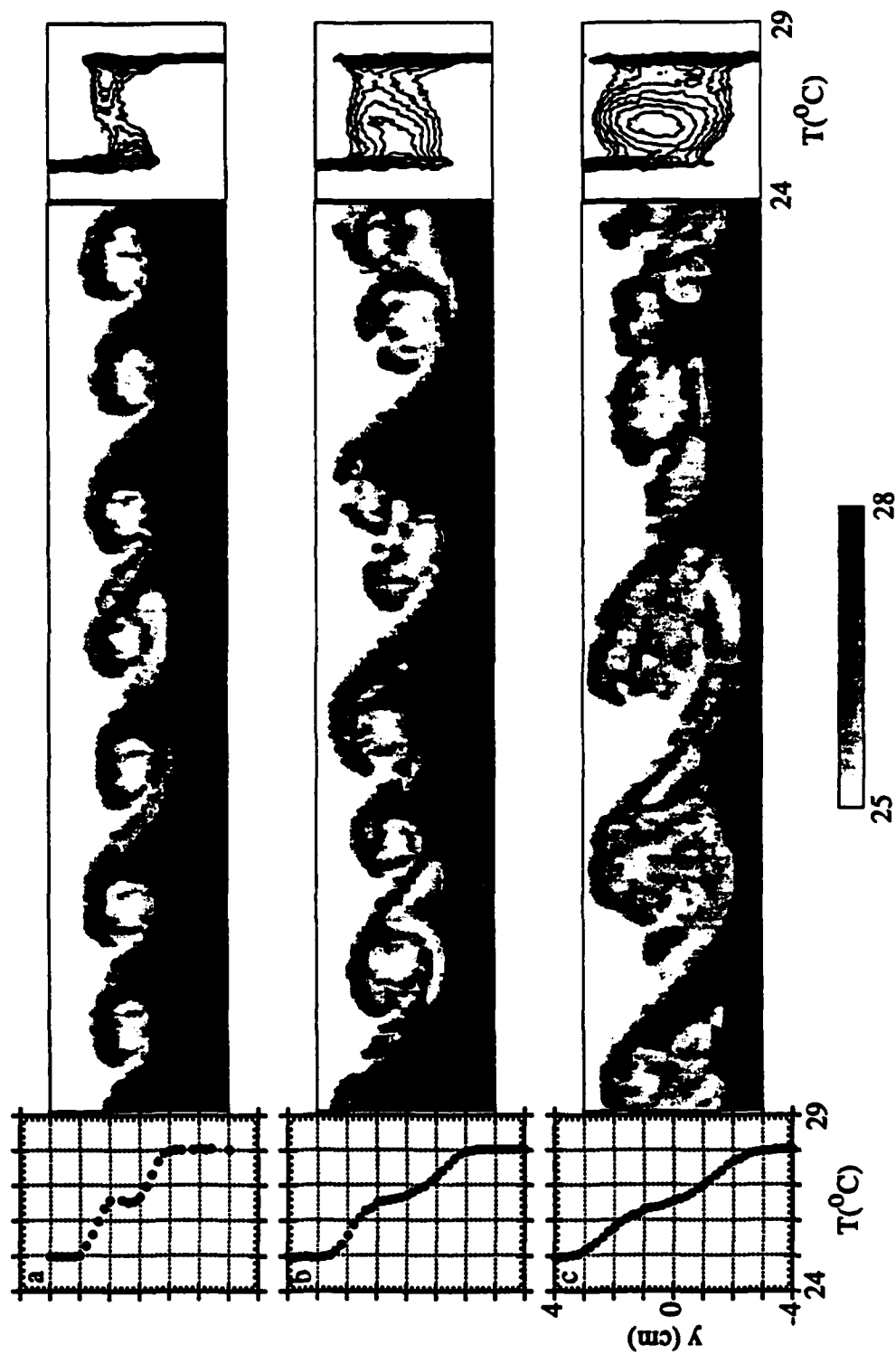FIGURE 41. T(y), T(y,t), and *pdf*(T,y) for feedback configuration C₃D5 (head) at x = (a) 10.16 cm, (b) 15.24 cm, and (c) 20.32 cm.

Similarly, at the tail of the streamwise vortex (figures 40 and 42 for C_{3D4} and C_{3D5}, respectively) the peak of $pdf(T,y)$ occurs at a lower value of y and a higher value of T for C_{3D5} than for C_{3D4}. In both of these feedback configurations $T(y,t)$ shows a dearth of unmixed low-speed fluid at x = 20.32 cm. This suggests that further downstream there may be only a minimal gain in PM since there is no unmixed fluid in the layer to be mixed.

Finally, figures 43 and 44 show the moments of $pdf(T,y)$ (as in figure 25 for the SU case) at the head and the tail of the streamwise vortex, respectively. The total mixed fluid (figures 43a and 44a) shows trends similar to $PM(\theta)$. There are clear peaks at $\theta = 225^{\circ}$, corresponding to feedback configuration C_{3D5}. Again, there are broad minima at $\theta = 90^{\circ}$ corresponding to feedback configuration C_{3D4}. There is a significant variation of the average temperature of mixed fluid at the head of the streamwise vortex (figure 43b) but only minimal excursions at the tail (figure 44b). This suggest that the effect of feedback is minimal at the tail. Furthermore, it is important to note that the percentage change in T_{cent} is positive at the head and negative at the tail due to the pumping action of the streamwise vortices. The change in the average cross-stream location of mixed fluid (figures 43c and 44c) show a positive change (towards the high-speed stream) at the head and a negative change (towards the low-speed stream) at the tail. There is more variation of y_{cent} with θ at the tail of the streamwise vortex, and it shows (as expected) that y_{cent} moves towards the low-speed stream for feedback configuration C_{3D5}.

The other moments (σ_y, skew$_T$, and kurtosis$_T$) show little variation with θ. However, it is instructive to compare the values of these moments at the head and the tail. The skewness skew$_T$ is quite low at the head of the streamwise vortex, suggesting that the mixing is symmetric. It is slightly more positive at the tail, suggesting a "tail" which intrudes into the low-speed temperatures. This is to be
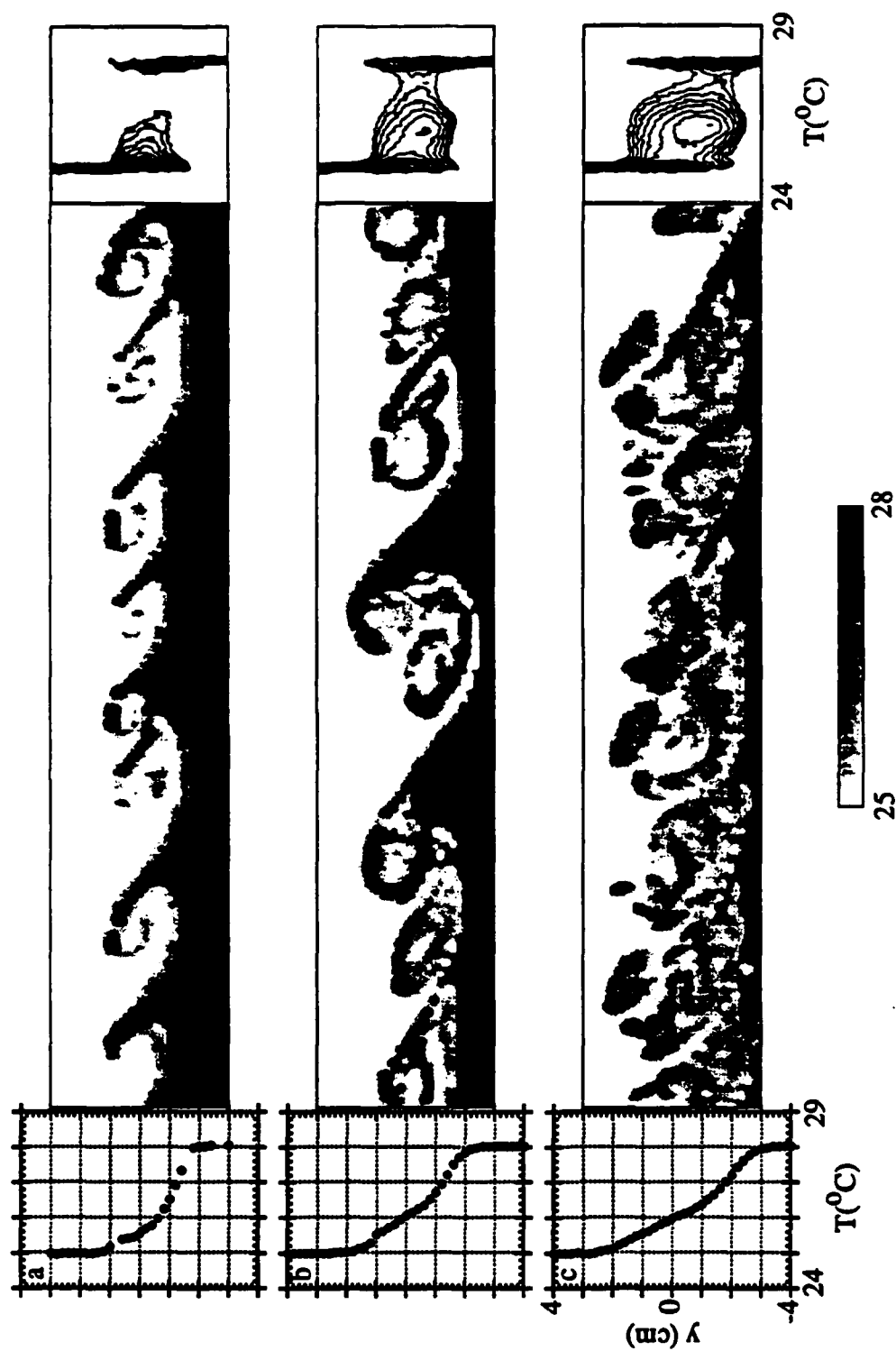
FIGURE 42. T(y), T(y,t), and *pdf*(T,y) for feedback configuration C$_{3D5}$ (tail) at x = (a) 10.16 cm, (b) 15.24 cm, and (c) 20.32 cm.

FIGURE 43. Moments of *pdf*(T,y) for the flow with feedback (measured at the head of a streamwise vortex) at x = 10.16 cm (O), 12.70 cm (□), 15.24 cm (◊), 17.78 cm (●), 20.32 cm (■), and 22.86 cm (◆): (a) total mixed fluid, (b) average temperature of mixed fluid, and (c) average cross-stream position y of mixed fluid.
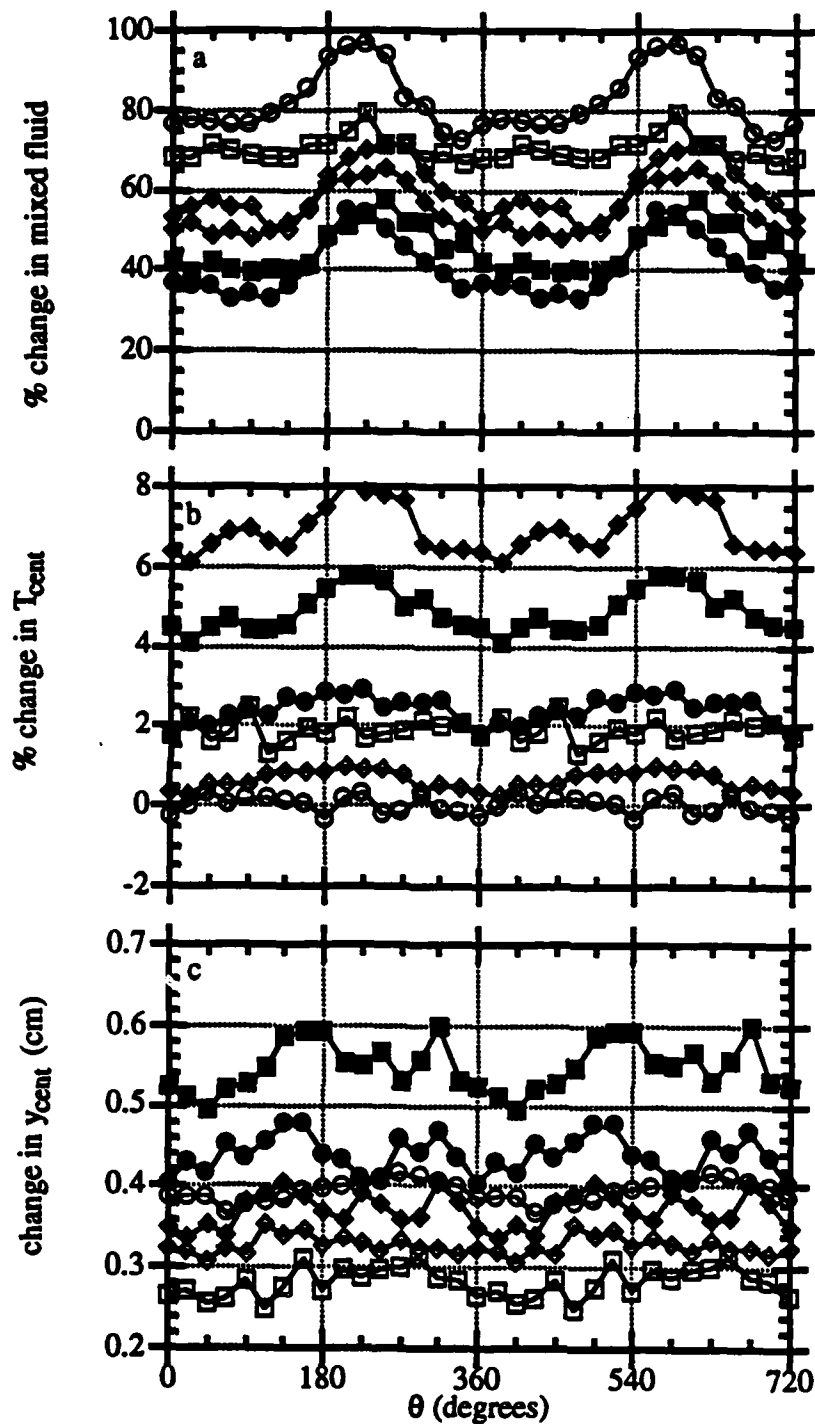
FIGURE 43-*Continued.* Moments of *pdf*T,y) for the flow with feedback (measured at the head of a streamwise vortex) at x = 10.16 cm (O), 12.70 cm (□), 15.24 cm (◊), 17.78 cm (●), 20.32 cm (■), and 22.86 cm (◆): (d) σ_Y, (e) skew$_T$, and (f) kurtosis$_T$.

FIGURE 44. Moments of $pdf(T,y)$ for the flow with feedback (measured at the tail of a streamwise vortex) at $x = 10.16$ cm (O), 12.70 cm (□), 15.24 cm (◊), 17.78 cm (●), 20.32 cm (■), and 22.86 cm (◆): (a) total mixed fluid, (b) average temperature of mixed fluid, and (c) average cross-stream position y of mixed fluid.

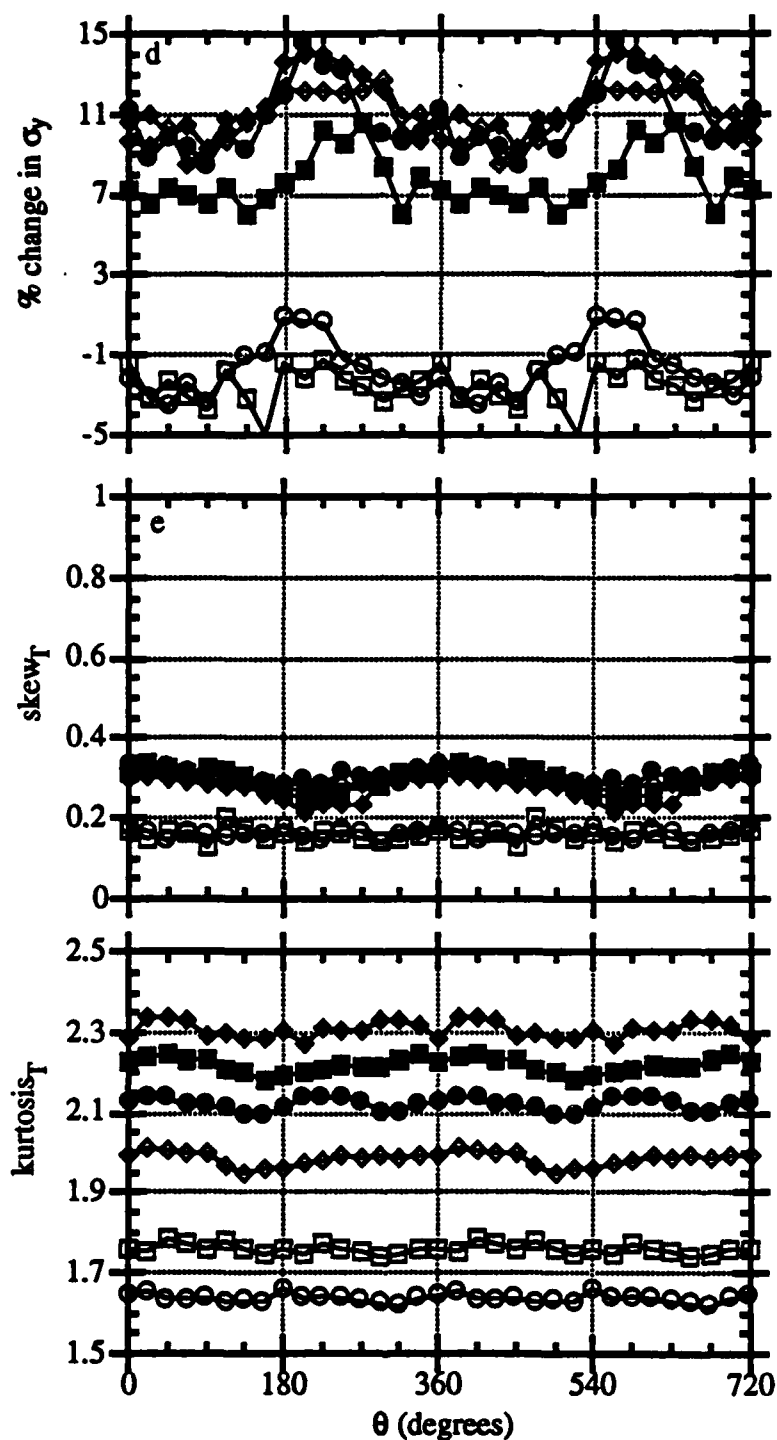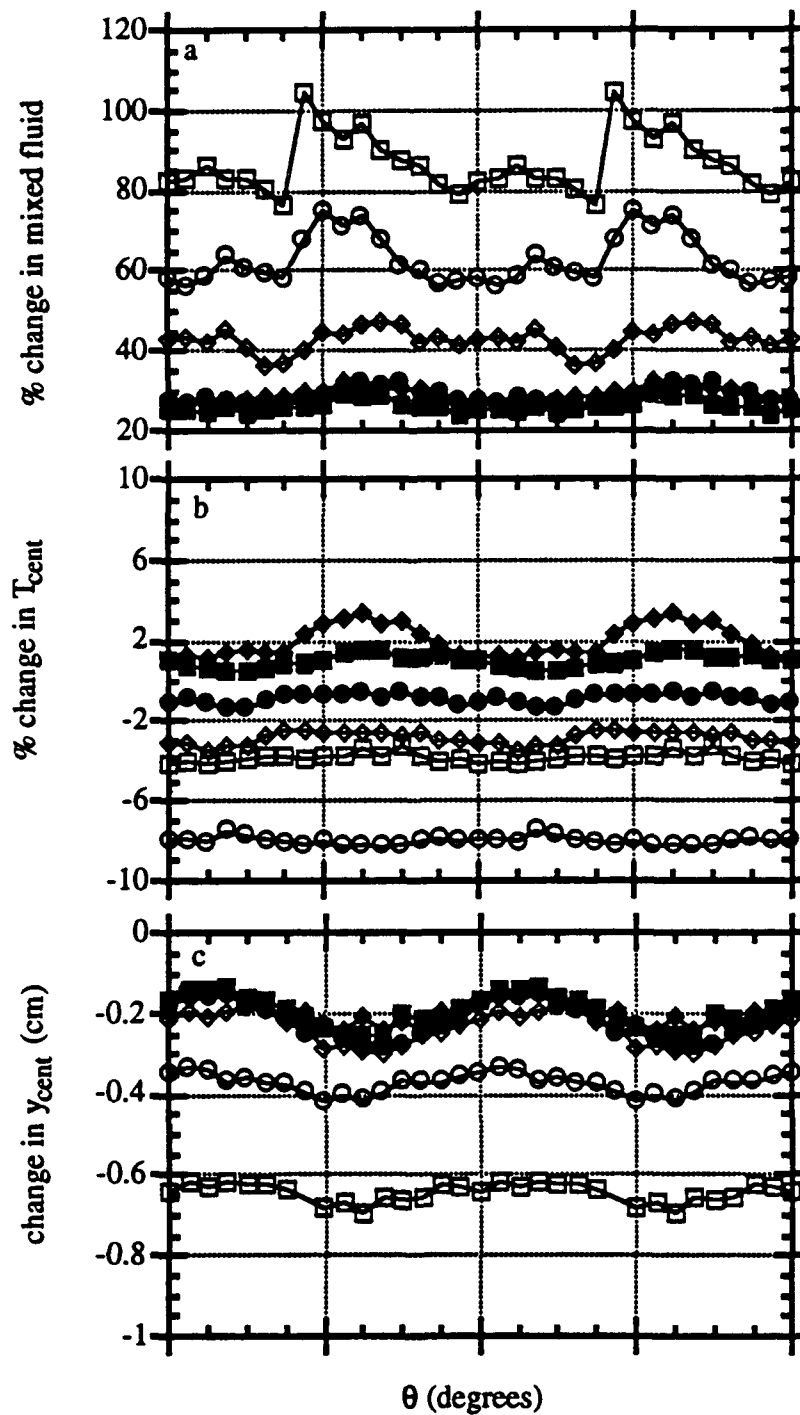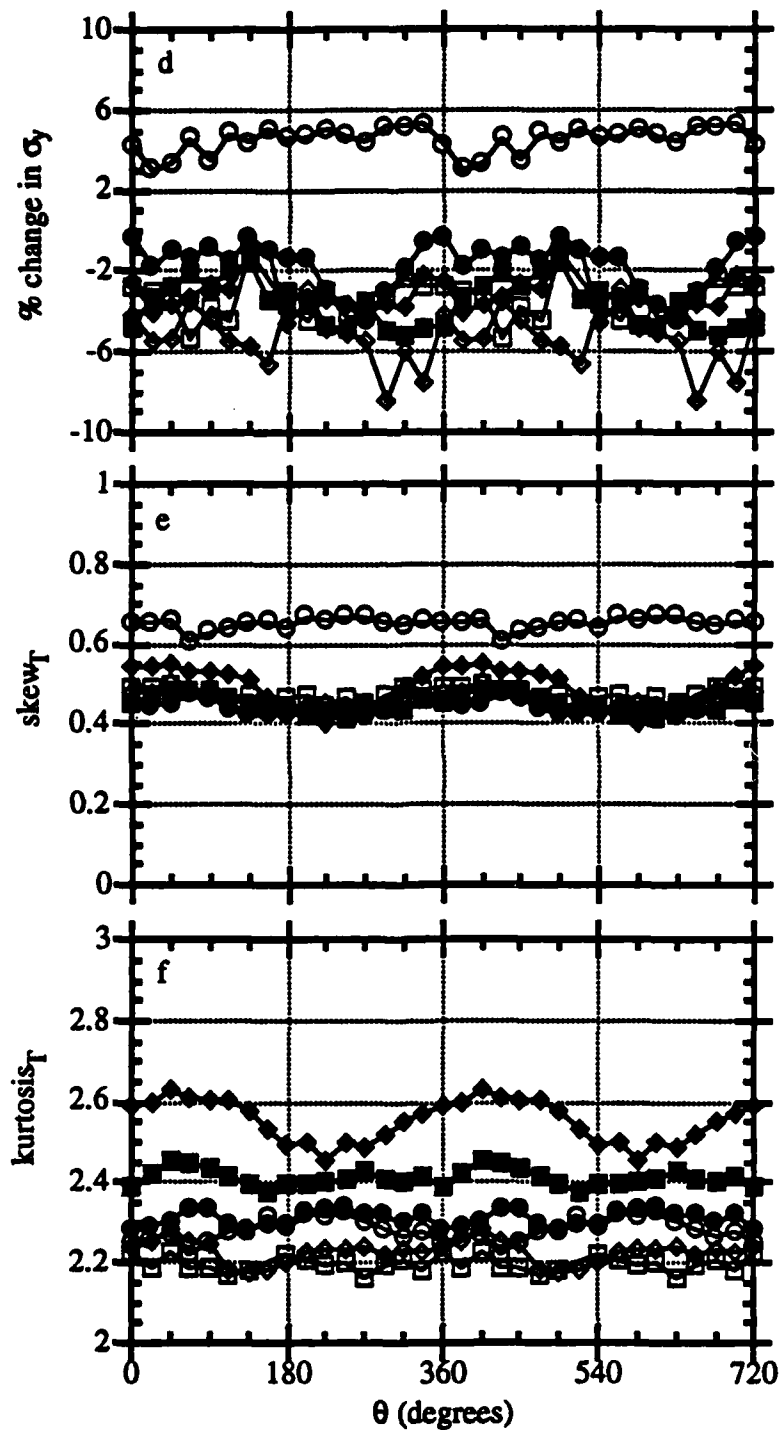FIGURE 44-*Continued.* Moments of *pdf*T,y) for the flow with feedback (measured at the tail of a streamwise vortex) at x = 10.16 cm (O), 12.70 cm (□), 15.24 cm (◊), 17.78 cm (●), 20.32 cm (■), and 22.86 cm (◆): (d) σY, (e) skewT, and (f) kurtosisT.

expected since T_{cent} is closer to the median temperature of the free streams at the head than at the tail.

5.3. Optimization of PM_{max} by adjusting θ (SP)

Figure 45 shows the utility of the golden segment search method to optimize PM_{max} at $x = 10.16$ cm for SP feedback at the head of the streamwise vortex. Initially, three bracketing values of θ are chosen from figure 36a. Figure 45b shows that PM converges to a value that is 80% higher than that for the unforced flow. Note, however, that this is less than the maximum shown in figure 36a (100%). The reason for this is the principle shortcoming in the use of the golden section search with noisy data. Figure 46a shows that θ converges to a final value of $\theta = 250^\circ$, whereas figure 36a shows that the maximum should occur at $\theta = 225^\circ$. Consider iterations 3, 4, and 5. Iteration 3 appears to give an inaccurately low value of PM. Hence, this value of θ is discarded and the new bracket becomes $235^\circ < \theta < 258^\circ$. The scheme from this point on in incapable of reaching the optimal θ. However, within this new bracket the scheme does converge to $\theta = 240^\circ$, which still significantly enhances mixing.
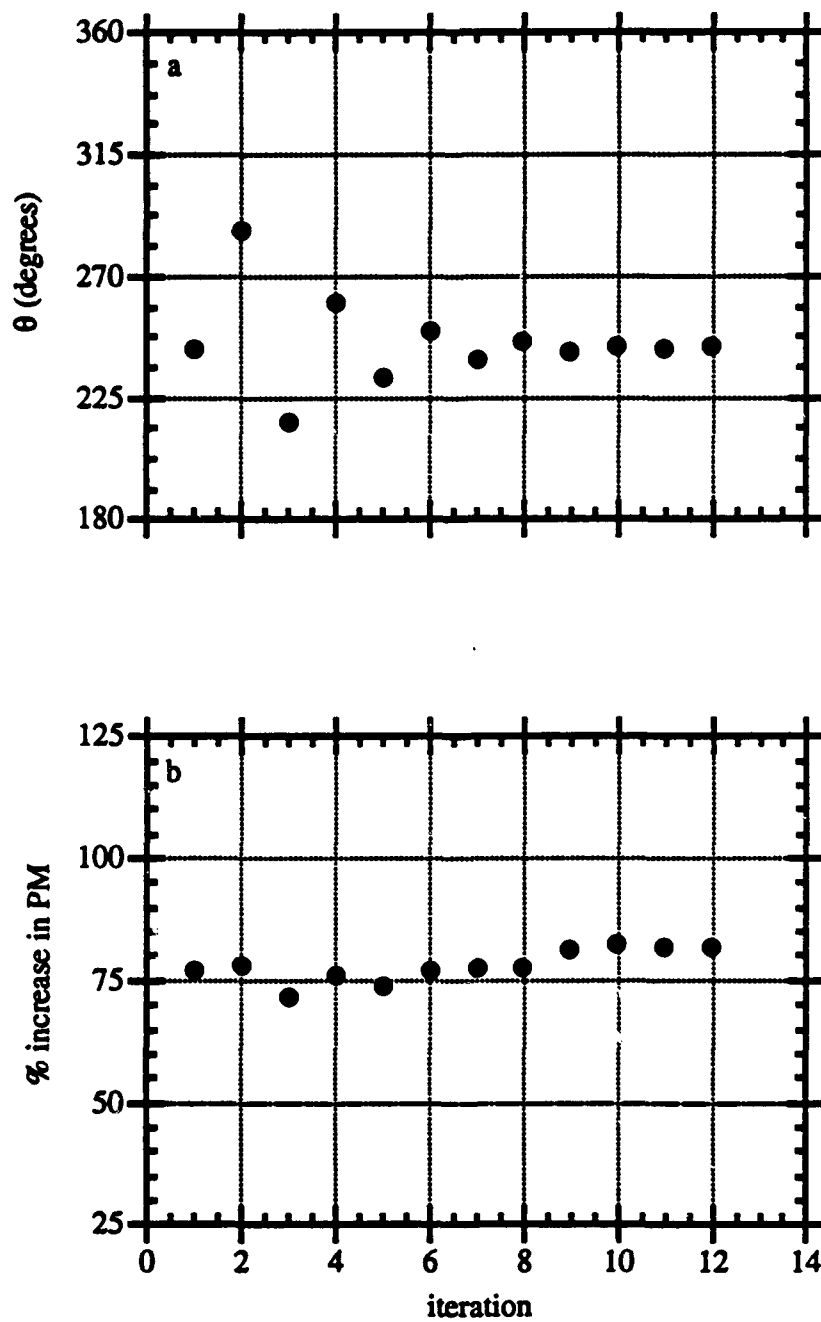
FIGURE 45. Optimization of PM_{max} by adaptively adjusting θ based on PM: (a) θ as a function of the iteration, and (b) PM as a function of the iteration. $x = 10.16$ cm, SP feedback (head).

6. Summary and conclusions

The present work is concerned with the development and implementation of feedback control systems for the enhancement and regulation of mixing in a plane shear layer. The work focuses on a plane shear layer in which, far upstream of the flow partition, the high- and low-speed streams have uniform, steady temperatures differing by 3° C. Downstream of the flow partition, the temperature distribution is sensed and controlled. Because the work is a study of mixing of a passive scalar in a nonreacting flow, this experiment can be conducted in a closed-return water facility.

Any feedback control system is comprised of three elements in addition to the plant: actuators, sensors, and a controller. The actuators are chosen as surface film heaters flush-mounted on the high-speed side of the flow partition. The heaters are arranged in an array consisting of four spanwise-uniform and elements upstream of a 32-element spanwise row. The spanwise-uniform heaters provide the control authority for influencing the nominally two-dimensional rollup and entrainment in the shear layer. The 32-element spanwise nonuniform array provides the capability to introduce a high degree of three-dimensionality into the flow.

The sensors consist of a rake of 31 equally-spaced cold wire thermometers (for measuring the temperature distribution at various streamwise stations, and thus ascertaining the amount of mixed fluid) and an optical position sensor (for measuring the location of the temperature interface of the two streams upstream of the first rollup of the primary vortices). All sensors are sampled virtually simultaneously by the laboratory computer.

A controller was developed in which the interface between the two streams of the plane mixing layer upstream of the first rollup of the primary vortices is modeled as a second-order transfer function. By proper selection of the feedback gains, the

spectral response of the flow can be altered. The results presented above show that the feedback gains can be adjusted to beneficially enhance mixing. The case of spanwise-uniform feedback is found to accrue modest increases in mixing performance measures over open-loop forcing at the natural frequency. Closed-loop feedback in the presence of streamwise is found to increase the mixing performance measure by 75-100% over the unforced flow for upstream locations, an improvement almost twice that attainable with open-loop forcing at the natural frequency.

Information from the rake of cold-wire thermometers can be used to adjust the feedback gains in real time. It was shown that this form of on-line optimization allows the controller to increase mixing at a given streamwise station, potentially even when not all the flow parameters are known *a priori*.

References

Batt, R.G. 1977 Turbulent mixing of passive and chemically reacting species in a low-speed shear layer. *J. Fluid Mech.* **82**, 53-95.

Bernal, L.P. 1981 The Coherent Structure of Turbulent Mixing Layers. *Ph.D. Thesis, California Institute of Technology.*

Bernal, L.P. & Roshko, A. 1986 Streamwise vortex structure in plane mixing layers, *J. Fluid Mech.* **170**, 499-525.

Breidenthal, R. 1980 Response of plane shear layers and wakes to strong three-dimensional disturbances. *Phys. Fluids* **23**(10), 1929-1934.

Breidenthal, R. 1981 Structure in turbulent mixing layers and wakes using a chemical reaction. *J. Fluid Mech.* **109**, 1-24.

Broadwell, J.E. & Breidenthal, R.E. 1982 A simple model of mixing and chemical reaction in a turbulent shear layer. *J. Fluid Mech.* **125**, 397-410.

Broadwell, J.E. & Mungal, M.G. 1988 Molecular Mixing and Chemical Reactions in Turbulent Shear Layers. *Twenty-Second Symposium (International) on Combustion/The Combustion Institute*, 579-587.

Buch, K.A. & Dahm, W.J.A. 1991 Fine scale structure of conserved scalar mixing in turbulent shear flows: Sc » 1, Sc ≈ 1 and implications for reacting flows. *Report No. 026779-5, The University of Michigan.*

Buell, J.C. & Mansour, N.N. 1989 Asymmetric Effects in Three-Dimensional Spatially-Developing Mixing Layers. *Seventh Symposium on Turbulent Shear Flows, Stanford University, August 21-23, 1989*, 9.2.1-9.2.6.

Dahm, W.J.A., Southerland, K.B., & Buch, K.A. 1991 Direct, high resolution, four-dimensional measurements of the fine scale structure of Sc >> 1 molecular mixing in turbulent flows. *Phys. Fluids A* **3** (5), 1115-1127.

Dimotakis, P.E. 1986 Two-Dimensional Shear-Layer Entrainment. *AIAA J.* **24**, 1791-1796.

Dimotakis, P.E. 1989 Turbulent Free Shear Layer Mixing. AIAA Paper 89-0262. *AIAA 27th Aerospace Sciences Meeting, January 9-12, 1989, Reno, Nevada.*

Gaster, M. 1986 A Non-Linear Transfer Function Description of Wave Growth in a Boundary Layer. Proceedings of the Fourth International Conference on Boundary and Interior Layers, July 7-11, 1986, Novosibirsk, USSR, 107-114.

Jimenez, J. 1983 A spanwise structure in the plane shear layer. *J. Fluid Mech.* **132**, 319-336.

Katch, G.J. & Kochesfahani, M.M 1993 Mixing of Species in a Two-Stream Shear Layer Forced by an Oscillating Airfoil. AIAA Paper 93-0444. *AIAA 31st Aerospace Sciences Meeting, January 11-14, 1993, Reno, Nevada.*

Kerstein, A.R. 1989 Linear-eddy modeling of turbulent transport. II: Application to shear layer mixing. *Combustion and Flame* **75**, 397-413.

Konrad, J.H. 1977 An experimental investigation of mixing in two-dimensional turbulent shear flows with applications to diffusion-limited chemical reactions. Ph.D. thesis, California Institute of Technology.

Koochesfahani, M.M. & Dimotakis, P.E. 1986 Mixing and chemical reactions in a turbulent liquid mixing layer. *J. Fluid Mech.* **170**, 83-112.

Koochesfahani, M.M. & MacKinnon, C.G. 1991 Influence of forcing on the composition of mixed fluid in a two-stream shear layer. *Phys. Fluids A* **3** (5), 1135-1142.

Lasheras, J.C. & Choi, H. 1988 Three-dimensional instability of a plane free shear layer: an experimental study of the formation and evolution of streamwise vortices. *J. Fluid Mech.* **189**, 53-86.

Liepmann, H. W. & Nosenchuck, D. M. 1982 Active control of laminar-turbulent transition. *J. Fluid Mech.* **118**, 201-204.

Liepmann, H. W., Brown, G. L. & Nosenchuck, D. M. 1982 Control of laminar instability waves using a new technique. *J. Fluid Mech.* **118**, 187-200.

Matsutani, S.M. & Bowman, C.T. 1986 The structure of a chemically reacting plane mixing layer. *J. Fluid Mech.* **172**, 93-126.

Metcalfe, R.W., Orszag, S.A., Brachet, M.E., Menon, S. & Riley, J.J. 1987 Secondary instability of a temporally growing mixing layer. *J. Fluid Mech.* **184**, 207-243.

Moser, R.D. & Rodgers, M.M. 1991 Mixing transition and the cascade to small scales in a plane mixing layer. *Phys. Fluids A* **3** (5) 1128-1134.

Moser, R.D. & Rodgers, M.M. 1993 The three-dimensional evolution of a plane mixing layer: pairing and transition to turbulence. *J. Fluid Mech.* **247**, 275-320.

Nosenchuck, D.M. 1982 Passive and Active Control of Boundary Layer Transition. *Ph.D. Thesis, California Institute of Technology.*

Nygaard, K. J. & Glezer, A. 1991 Evolution of streamwise vortices and generation of small-scale motion in a plane shear layer. *J. Fluid Mech.* **231**, 257-301.

Oster, D. & Wygnanski, I. 1982 The forced mixing layer between parallel streams. *J. Fluid Mech.* **123**, 91-130.

Park, K.-H., Metcalfe, R.W. & Hussain, F. 1994 Role of Coherent Structures in and Isothermally Reacting Mixing Layer. Accepted by *Phys. Fluids A.*

Reisenthel, P. 1988 Hybrid instability in an axisymmetric jet with enhanced feedback. *Ph.D. dissertation, Illinois Institute of Technology, Chicago.*

Riley, J.J., Metcalfe, R.W. & Orszag, S.A. 1986 Direct numerical simulations of chemically reacting turbulent mixing layers. *Phys. Fluids* 29 (2), 406-422.

Roberts, F.A. 1985 Effects of a Periodic Disturbance on Structure and Mixing in Turbulent Shear Layers and Wakes. *Ph.D. Thesis, California Institute of Technology.*

Roberts, F. A. & Roshko, A. 1985 Effects of periodic forcing on mixing in turbulent shear layers and wakes. *AIAA Shear Flow Control Conference, March 12-14, Boulder, Colorado.*

Rodgers, M.M & Moser, R.D. 1992 The three-dimensional evolution of aplane mixing layer: the Kelvin-Helmholtz rollup. *J. Fluid Mech.* 243, 183-226.

Rodgers, M.M. & Moser, R.D. 1993 Spanwise scal selection in plane mixing layers. *J. Fluid Mech.* 247, 321-337.

Roshko, A. 1981 The plane mixing layer; flow visualization results and three-dimensional effects. In *The Role of Coherent Structures in Modelling Turbulence and Mixing* (ed. J. Jimenez). Lecture Notes in Physics, vol. 136, pp.208-217. Springer.

Tennekes, H. & Lumley, J.L. 1972 **A First Course in Turbulence.** The MIT Press.

Wehrmann, O. H. 1965a Reduction of velocity fluctuations in a Karman vortex street by a vibrating cylinder. *Phys. Fluids* 8, 760-761.

Wehrmann, O.H. 1965b Tollmien-Schlichting waves under the influence of a flexible wall. *Phys. Fluids* 8, 1389-1390.

Wehrmann, O. H. 1967a The influence of vibrations on the flow field behind a cylinder. *Document D1-82-0619.* Boeing Scientific Research Laboratories.

Wehrmann, O. H. 1967b Self-adjusting feedback loop for mechanical systems to influence flow in transition; part I. *Document D1-82-0632.* Boeing Scientific Research Laboratories

Wiltse, J. M. & Glezer, A. 1994a Control of mixing in a nonreactive plane shear layer. Part I. Open-loop control. (To be submitted).

Wiltse, J. M. & Glezer, A. 1994b Control of mixing in a nonreactive plane shear layer. Part II. Feedback control. (To be submitted).

Winant, C.D. & Browand, F.K. 1974 Vortex pairing: the mechanism of turbulent mixing-layer growth at moderate Reynolds number. *J. Fluid Mech.* 63(2), 237-255.

Witte, A.B., Broadwell, J.E., Shackleford, W.L., Cummings, J.C., Trost, J.E., Whiteman, A.S., Marble, F.E., Crawford, D.R., and Jacobs, T.A. 1974 Aerodynamic reactive flow studies of the H_2/F_2 laser - II. *Technical Report No. AFWL-TR-74-78*, Air Force Weapons Laboratory, Kirtland Air Force Base, New Mexico.